QUANTUM CHEMICAL CHARACTERISATION OF MOLECULAR MAGNETISM IN ACTINIDE COMPLEXES

A thesis submitted to the University of Manchester
for the degree of Doctor of Philosophy
in the Faculty of Science and Engineering

2023

Austin William Lloyd
School of Natural Sciences, Department of Chemistry

Contents

List of Tables

List of Figures

The University of Manchester

Austin William Lloyd
Doctor of Philosophy
Quantum Chemical Characterisation of Molecular Magnetism in Actinide Complexes
2023/04/03

The prediction of paramagnetic NMR (pNMR) chemical shifts in molecules containing heavy atoms presents a significant challenge to computational quantum chemistry. The importance of meeting this challenge lies in the central role that NMR plays in the structural characterisation of chemical systems. Hence there is a need for reliable assignment and prediction of chemical shifts. We have developed code in MATLAB that facilitates this, based on the decomposition of the magnetic moment matrices by irreducible tensor operators (ITO) as outlined in the work of van den Heuvel and Soncini.[1]

This work firstly presents a published paper[2] that studies the effect of zero-field-splitting (ZFS). It is shown that the inclusion of ZFS can produce substantial shifts in the predicted chemical shifts. The computations presented are typically sufficient to enable assignment of experimental spectra. However for one case, in which the peaks are closely clustered, the inclusion of ZFS re-orders the chemical shifts making assignment quite difficult. We also observe, and echo, the previously reported importance of including the paramagnetic spin-orbit hyperfine interaction for ^{13}C and ^{29}Si atoms, when these are directly bound to a heavy element and thus subject to heavy-atom-light-atom (HALA) effects.

Then we study the magnetic properties of U(DOTA), where DOTA = 1,4,7,10-tetrazacyclodecane-1,4,7,10-tetraacetate and three axially substituted variants, [U(DOTA)H_2O], [U(DOTA)OH]$^-$ and [U(DOTA)F]$^-$. This is achieved by calculating the main magnetic matrices and paramagnetic NMR (pNMR) spectra. U(DOTA) has two suggested assignments for its ^{1}H spectra,[3,4] and our calculations allow a definitive assignment. The complications due to large spin-orbit coupling (SOC) and the interchange between the square antiprism (SAP) and twisted square antiprism (TSA) conformers are discussed. The axial symmetry of the molecule allows the tensor decomposition technique to be used to model the Zeeman contribution, and this results in strong correlation between calculated and experimental results. Experimental assignments for the axially substituted variants do not distinguish between protons attached to the same carbon atom,[5] and we are able to separate these. The binding of a water ligand has little effect on the calculated spectra, but binding an anionic ligand results in a compression of the spectral range which our results duplicate. Binding an anionic ligand also causes the anisotropy axis to rotate by 90°. These effects are examined with reference to spin density. Finally ^{13}C spectra are predicted for future experimental verification.

The applicability of the new method of calculating paramagnetic NMR shifts is extended to another class of very heavy element compounds — some substituted actinocene complexes. The initial results aimed at assigning published experimental NMR data are presented and our implementation of the ITO model is considered as promising.

Declaration

No portion of the work referred to in the thesis has been submitted in support of an application for another degree or qualification of this or any other university or other institute of learning.

Copyright Statement

i. The author of this thesis (including any appendices and/or schedules to this thesis) owns certain copyright or related rights in it (the "Copyright") and s/he has given The University of Manchester certain rights to use such Copyright, including for administrative purposes.

ii. Copies of this thesis, either in full or in extracts and whether in hard or electronic copy, may be made **only** in accordance with the Copyright, Designs and Patents Act 1988 (as amended) and regulations issued under it or, where appropriate, in accordance with licensing agreements which the University has from time to time. This page must form part of any such copies made.

iii. The ownership of certain Copyright, patents, designs, trade marks and other intellectual property (the "Intellectual Property") and any reproductions of copyright works in the thesis, for example graphs and tables ("Reproductions"), which may be described in this thesis, may not be owned by the author and may be owned by third parties. Such Intellectual Property and Reproductions cannot and must not be made available for use without the prior written permission of the owner(s) of the relevant Intellectual Property and/or Reproductions.

iv. Further information on the conditions under which disclosure, publication and commercialisation of this thesis, the Copyright and any Intellectual Property and/or Reproductions described in it may take place is available in the University IP Policy (see http://documents.manchester.ac.uk/DocuInfo.aspx?DocID=487), in any relevant Thesis restriction declarations deposited in the University Library, The University Library's regulations (see http://www.manchester.ac.uk/library/aboutus/regulations) and in The University's Policy on Presentation of Theses.

Acknowledgements

I'd like to give my sincere gratitude to Joe McDouall for his support wisdom, advice and patience with my many many idiosyncrasies, especially with my insistence in using LaTeX to produce this work, for which I apologise. I have missed talking in the same room, and I miss us sharing MATLAB demonstrating sessions. I'd also like to thank David Collison for his kindness, advice and for taking over following Joe's retirement. Both have given useful feedback on this work. In a similar vein, I'd like to thank Louise Natrajan for her advice on NMR and feedback on Chapter 5. I'd especially like to thank these three good people for their help on the third year presentation, without which I would not have been awarded a section prize. I am also grateful to my father-in-law Geoffrey Jobbins for proofreading, even if this somehow proved to be even more abrupt and disjointed than for my MPhil. I still joke that maths is my first language, so I apologise to my proofreaders for any corrections that I have still somehow missed or misunderstood.

I'd like to thank Andrew Kerridge and Neil Burton for a productive and mostly enjoyable viva, and for valuable suggestions which have improved this work.

I am very grateful to DSTL for funding my work.

I'd like to thank Phil Riby, Neil Burton and Carl Poree for the graduate teaching assistant opportunities that I have thoroughly enjoyed, even if it sometimes seemed to involve more IT support then chemistry. Before Covid, Nicholas Beattie gave useful feedback to practice presentations, for which I am grateful. I am extremely grateful to Kath Baddeley, an asthma nurse, for suggesting a bone scan.

I owe every achievement to my parents, who have unfailingly supported me throughout my life. Without their love, I doubt I would have ever prospered. My sister is my oldest friend, and despite the distance she is missed daily. She and my nephew, George, remain a valued source of Lego and fun.

Finally my wife, Leah, is the centre of my world, and I would not have dared to attempt this journey without her love and support. I thank her keeping me mostly sane during Covid. She remains forever my soulmate, to love, honour and annoy.

Better together.

Research is a neverending process, so this work is necessarily incomplete, but this thesis is respectfully dedicated to my wife and my parents.

Peace and love, Austin

Chapter 1

Introduction

Actinide chemistry remains an interesting and relatively unexplored area of chemistry, and the use of actinides for energy production and in radiotherapy provides considerable incentive to understand their chemistry better. Due to the commonality of unpaired electrons, paramagnetic NMR (pNMR) is a valuable probe of their chemical nature. However, the radioactive nature of actinides can confound more complex NMR experiments and thereby make assignment of their spectra challenging. While computational chemistry can be utilised to achieve such assignments, the rich electronic structure and the importance of relativistic effects in such compounds present profound computational problems.

This work focuses on the assignment and prediction of pNMR spectra for a number of actinide and lanthanide compounds and on probing their magnetochemistry and electronic structure. Chapters 2 and 3 build the general and magnetic theory necessary to achieve this. Chapter 4 contains a published exploration of the pNMR of six spin 3/2 compounds and highlights the importance of including zero-field splitting (ZFS) effects, Chapter 5 performs a similar study for the U(DOTA) complex [DOTA is a tetraazadodecane tetraacetate ligand] and some axially substituted variants (F^-, OH^-, H_2O). Chapter 6 looks at a set of substituted actinocenes and assesses the use of higher order Zeeman correction terms. The final chapter summaries the limitations of this work, and outlines future possibilities to improve the accuracy of the assignments that we have made.

1.1 Notation

The notation used in this work is shown below.

η	Primitive gaussian type function.	$\mathbb{N}$	The natural numbers, $1, 2, 3, \ldots$
ϕ	Atomic orbital.	$\mathbb{N}_0$	Non negative integers, $0, 1, 2, 3, \ldots$
ψ	Molecular orbital.	$\mathbb{Z}$	Integers.
Ψ	Single determinant function.	$\mathbb{R}$	Real numbers.
Φ	Multiple determinant function.	$\mathbb{C}$	Complex numbers.
$\Phi^{(n)}$	The n^{th} order correction to Φ.		
$\hat{\mathcal{H}}$	Hamiltonian.	k_B	Boltzmann constant.
$\hat{\mathcal{L}}$	Angular momentum operator.	μ_B	Bohr magneton.
$\hat{\mathcal{S}}$	Spin operator.	μ_n	Nuclear magneton.
$\hat{\mathcal{T}}$	Kinetic energy operator.	g_e	Free electron g-factor.
$\hat{\mathcal{V}}$	Potential energy operator.	g_n	Nuclear g-factor.
$\hat{\mathcal{P}}$	Momentum operator.	α	Fine structure constant.
$\hat{\mathcal{I}}$	Identity operator.	c	Speed of light.
$\hat{p}$	1-electron momentum operator.	$\mathbf{r}$	Spatial coordinates.
$\hat{\ell}$	1-electron angular momentum.	σ	Spinor.
$\hat{s}$	1-electron spin.	$\mathbf{x}$	Combined coordinates $(\mathbf{r}, \sigma)$.
ρ	Electron density.	Z_A	Atomic number of nucleus A.
$\boldsymbol{\rho}$	Density matrix.	A_κ	κ^{th} co-ordinate of nucleus A.
$\boldsymbol{\sigma}_\kappa$	Pauli matrix.	r_{iA}	Distance: electron i to nucleus A.
i, j	Iterator, electrons.	E	Energy.
A, B	Iterator, atoms, eigenvectors.	S^2	Expectation value of $\hat{\mathcal{S}}^2$.
κ, υ	Iterator, cartesian coordinates.	m_s	Expectation value of $\hat{\mathcal{S}}_z$.
$\boldsymbol{\sigma}$	Orbital shielding matrix.	${}^N C_M$	Binomial coefficient.
$\mathbf{g}$	Zeeman matrix.	$\mathbf{I}_n$	$n \times n$ identity matrix.
$\mathbf{A}$	Hyperfine coupling matrix.	$\mathbf{0}_n$	$n \times n$ zero matrix.
$\mathbf{D}$	Zero-field splitting tensor.	$\hat{\nabla}$	$\left(\frac{\partial}{\partial x}, \frac{\partial}{\partial y}, \frac{\partial}{\partial z}\right)$.
$\mathbf{G}$	Abragam-Bleaney tensor, $\mathbf{g} \cdot \mathbf{g}^T$	$\hat{\nabla}^2$	$\frac{\partial^2}{\partial x^2} + \frac{\partial^2}{\partial y^2} + \frac{\partial^2}{\partial z^2}$.
$\boldsymbol{\mu}_\kappa$	Magnetic moment.	$f^{(n)}(a)$	The n^{th} derivative of f at a.

1.2 Abbreviations

The abbreviations used in this work are shown below.

AO	Atomic Orbital.
aZORA	Atomic Zeroth-Order Regular Approximation.
BSE	Basis Set Exchange.
CASCI	Complete Active Space Configuration Interaction.
CASPT2	Complete Active Space Perturbation Theory (2nd order).
CASSCF	Complete Active Space, Self-Consistent Field (theory).
CF	Crystal Field.
CI	Configuration Interaction.
CISD	CI Single and Double (excitations).
CIPSI	CI by Perturbation with multiconfigurational zeroth-order wavefunctions Selected by Iterative process.
COT	1,3,5,7-Cyclo**oct**atetraene
CSF	Configuration State Functions.
DFT	Density Functional Theory.
DKH	Douglas-Kroll-Hess (theory).
DOTA	tetraaza**do**decane **t**etraacetic **a**cetate
EPR	Electron Paramagnetic Resonance.
FCI	Full Configuration Interaction.
GGA	Generalized Gradient Approximation (functional).
GTO	Gaussian Type Orbital.
HALA	Heavy-Atom Light-Atom (effect).
HF	Hartree-Fock (theory).
HOMO	Highest Occupied Molecular Orbital.
ITO	Irreducible Tensor Operator
LSDA	Local Spin Density Approximation.
LUMO	Lowest Unoccupied Molecular Orbital.
LYP	Lee-Yang-Parr (functional).
MO	Molecular Orbital.

NEVPT	N-Electron Valence State Perturbation Theory.
NMR	Nuclear Magnetic Resonance.
NRBO	Non-Relativistic Born-Oppenheimer (approximation).
ODE	Ordinary Differential Equation.
PAS	Principal Axis System.
PBE	Perdew-Burke-Ernzerhof (functional).
PBE0	Hybrid Perdew-Burke-Ernzerhof (functional).
PDE	Partial Differential Equation.
pNMR	Paramagnetic Nuclear Magnetic Resonance.
PSO	Paramagnetic Spin-Orbit.
QDPT	Quasi-Degenerate Perturbation Theory.
QRO	Quasi-Restricted Orbital.
RASSCF	Restricted Active Space, Self-Consistent Field (theory).
RHF	Restricted Hartree Fock (theory).
RI	Resolution of the Identity.
ROHF	Restricted Open-shell Hartree Fock (theory).
RME	Reduced Matrix Element.
SA-CASSCF	State-Averaged Complete Active Space Self-Consistent Field (theory).
SARC	Segmented All-electron Relativistically Contracted (basis).
SCF	Self-Consistent Field (theory).
SOC	Spin-Orbit Coupling.
SOMF	Spin-Orbit Mean Field.
STO	Slater Type Orbital.
TISE	Time-Independent Schrödinger Equation.
TPSS	Tao-Perdew-Staroverov-Scuseria (functional).
UHF	Unrestricted Hartree Fock.
UKS	Unrestricted Kohn-Sham.
UNO	Unrestricted Natural Orbital.
ZFS	Zero-Field Splitting.
ZORA	Zeroth-Order Regular Approximation.

Chapter 2

Theory

2.1 The wavefunction

Wave-particle duality is based on the observation that very small objects behave either as particles or as waves depending on experimental context. Consider a molecule comprising of M atoms and N electrons. Chemistry is dominated by the behaviour of electrons, so the corresponding N-electron system can be mathematically modelled by the electronic wavefunction, $\Psi(\mathbf{r}_1\boldsymbol{\sigma}_1...\mathbf{r}_N\boldsymbol{\sigma}_N, \mathbf{R}_1 Z_1...\mathbf{R}_M Z_M)$, which is a function of the spatial, $\mathbf{r}_i = (x_i\ y_i\ z_i)^T$, and spin, $\boldsymbol{\sigma}_i$, coordinates of each electron, and also the spatial coordinates, $\mathbf{R}_j$, and charges, Z_j of each nucleus. The nuclei are fixed for the following discussion. Typically the electronic coordinates are combined as $\mathbf{x}_i = \{\mathbf{r}_i, \boldsymbol{\sigma}_i\}$. While the spatial coordinates are from the well-known Euclidean three-dimensional vector space, $\mathbb{R}^3$, the spin coordinate is more abstract. The spinors $\boldsymbol{\alpha} = (1\ 0)^T$ and $\boldsymbol{\beta} = (0\ 1)^T$ relate to a two-dimensional vector space referred to as the special unitary[*] group of degree two, SU(2), which maps to the group of 2×2 unitary matrices with determinant $+\ 1$. Unlike $\mathbb{R}^3$, a 2π rotation of this space changes the sign of the spinor, while a 4π rotation is needed to return the spinor to its original orientation.

For an electronic wavefunction to be physically plausible it must satisfy a number of boundary conditions, for example, the wavefunction must be continuous. Considering a spinless one-electron wavefunction, then the electron probability density is $\rho(\mathbf{r}) = |\Psi(\mathbf{r})|^2 = \Psi(\mathbf{r})^*\Psi(\mathbf{r})$. The Born interpretation,[6] implies that $\rho(\mathbf{r})\delta\mathbf{r}$ represents the probability of an electron being in the cube $\delta\mathbf{r} = \delta x\delta y\delta z$ centred on $\mathbf{r} = (x, y, z)$ as

---

[*] A unitary matrix satisfies $\mathbf{U}^*\mathbf{U} = \mathbf{U}\mathbf{U}^* = \mathbf{U}\mathbf{U}^{-1} = \mathbf{I}_3$ where $\mathbf{U}^*$ is the conjugate transpose of $\mathbf{U}$ and $\mathbf{I}_3$ is the 3×3 identity matrix.

$\delta\mathbf{r}$ becomes arbitrarily small. The integral of ρ must equal the probability of finding an electron in the region of integration, so, for a valid one-electron wavefunction, the integral over all space must equal one, *i.e.*

$$\int_{\mathbb{R}^3} \Psi^*(x, y, z)\Psi(x, y, z)\,\mathrm{d}x\,\mathrm{d}y\,\mathrm{d}z = \int_{\mathbb{R}^3} \rho(\mathbf{r})\,\mathrm{d}\mathbf{r} = 1 < \infty. \tag{2.1}$$

Similarly for an N-electron wavefunction, the corresponding integral (for all electronic co-ordinates) must equal N. This implies that the radial part of the wavefunction must tend to zero as the radial distance becomes arbitrarily large. It is the imposition of these boundary conditions that lead to quantisation.

2.2 Lagrangian mechanics

Lagrangian mechanics was introduced in 1788 by Joseph-Louis Lagrange as a reformulation of classical mechanics[7] to facilitate solving problems that were difficult to solve in cartesian coordinates. The abstract concept of an action functional $\hat{\mathcal{L}}[L]$ was introduced describing the evolution of a system (a functional is an operator that takes a function and maps it to a scalar), and so the action of the system is given by the functional

$$\hat{\mathcal{L}}[L] = \int_{t=a}^{t=b} L(t, \mathbf{s}(t), \dot{\mathbf{s}}(t))\,\mathrm{d}t, . \tag{2.2}$$

where $\mathbf{s}$ is a set of generalised coordinates (*e.g.* the distance along a bent string), the overdot notation indicates differentiation with respect to time, and t is a time coordinate. While an abstract quantity, the action is defined as a scalar to allow for the evolution of a system to be measurable, and can be used to model the effect of small changes to $\mathbf{s}$ and $\dot{\mathbf{s}}$, and most importantly allows these functions to be optimised.[8] The function, L, is called the Lagrangian and for systems of particles it is defined by

$$L(t, \mathbf{x}(t), \dot{\mathbf{x}}(t)) = T(t, \mathbf{x}(t), \dot{\mathbf{x}}(t)) - V(t, \mathbf{x}(t), \dot{\mathbf{x}}(t)), \tag{2.3}$$

where T and V represent the potential and kinetic energy of the system. The principle of least action states[8] that the solutions to the equations of motion for such a system are the ones that minimise this action functional,[†] and as a result the functional can

---

[†] Strictly speaking the solutions only need to be stationary points.

be minimised by solving the associated Euler-Lagrange equation. This approach can be mirrored for quantum systems with the wavefunction $\Psi(t)$ representing the state of the system.[6,9]

2.2.1 Noether's theorem

Noether's theorem[10] was a landmark theorem for theoretical physics. Essentially it implies that if a physical system has a continuous symmetry, there must be a corresponding quantity that is conserved. This remarkable theorem implies that in a system that is time-symmetric (does not change with time) energy must be conserved as a mathematical consequence of this symmetry. Similarly translational and rotational symmetries imply that linear and angular momentum must be conserved. Of significance for this work is that the underlying mathematics of magnetism involves the definition of an electrostatic and vector potential, and a magnetic system is not affected by a change of reference potential providing the underlying field does not change. This is called gauge invariance and implies that the charge of the system must be conserved. Unfortunately modelling magnetic properties may include approximations that break this physical requirement, and require additional work to counteract the resulting gauge dependence.

2.3 The Schrödinger equation

Considering an electron with constant momentum, p. The corresponding one-dimensional wavefunction, as a function of position x along the axis of motion, and time t, can be written as

$$\Psi(x,t) = e^{i(\kappa x - \omega t - \phi)}, \quad \kappa = 2\pi/\lambda \tag{2.4}$$

where λ is the wavelength, κ is the (angular) wavenumber, ω is the angular frequency, and ϕ is a phase factor which can be ignored for the following discussion. Note that if the wavefunction is smooth and continuous it can be represented as a Fourier series, *i.e.* a linear combination of functions of Eq. 2.4, so this approach can be generalised. The energy of the wave, E, is given by $E = \hbar\omega$ where $\hbar = h/(2\pi)$ and h is the Planck constant. The momentum of the electron is given by the de Broglie relation,[11] $p = h/\lambda = \hbar\kappa$. Form these relations Eq. 2.4 can be rewritten as

$$\Psi(x,t) = e^{i(px-Et)/\hbar}. \tag{2.5}$$

Partially differentiating Eq. 2.5 with respect to time gives

$$\frac{\partial}{\partial t}\Psi(x,t) = \frac{-iE}{\hbar}e^{i(px-Et)/\hbar} = \frac{1}{i\hbar}E\Psi(x,t), \tag{2.6}$$

and from this, the one-dimensional time dependent Schrödinger equation is given by

$$i\hbar\frac{\partial}{\partial t}\Psi(x,t) = E\Psi(x,t). \tag{2.7}$$

If the underlying system does not change in time, then Noether's theorem implies that energy is constant and therefore a time independent wavefunction, $\Psi(x)$, can be built from Eq. 2.5, *i.e.*

$$\Psi(x,t) = \Psi(x)e^{-iEt/\hbar} \tag{2.8}$$

and the time independent Schrödinger equation (TISE) is written as

$$\hat{\mathcal{H}}\Psi(x) = E\Psi(x), \tag{2.9}$$

where $\hat{\mathcal{H}}$ is the Hamiltonian operator which can be formed using the correspondence principle. This principle was introduced by Bohr[12] and implies that any quantum mechanical system must produce the same results as a classical mechanical system when the system becomes macroscopic, and as in classical mechanics, the total energy is given by the sum of kinetic and potential energy operators. That is

$$\hat{\mathcal{H}}\Psi = \hat{\mathcal{T}}\Psi + \hat{\mathcal{V}}\Psi. \tag{2.10}$$

Applying this to a hydrogen atom, again we concentrate on electronic part of the system, and for simplicity, the following discussion ignores the purely nuclear components of the Hamiltonian, treating the nuclei as static. This approximation is justified by noting that the proton is 1836 times more massive than the electron and moves much more slowly. This is known as the Born-Oppenheimer approximation.

For an isolated and static hydrogen atom at the origin of a coordinate system, the electronic Hamiltonian operator can be expressed in SI units as

$$\hat{\mathcal{H}}\Psi = \frac{\hbar^2}{2m_e}\hat{p}\Psi \cdot \hat{p}\Psi - \frac{q_e q_n}{4\pi\epsilon_0 r_e}\Psi, \tag{2.11}$$

where we introduce an electronic momentum operator $\hat{p}$. The quantities m_e, q_e and r_e are the electron's mass, charge[‡] and distance from the proton respectively, q_n is proton's charge the and ϵ_0 is the electric permittivity of a vacuum. To simplify this equation we introduce a system of atomic units; this system defines the reduced Planck constant ($\hbar$), the mass and charge of an electron, and the expectation value of the electron-proton distance as one,[13] the latter quantity is called the Bohr radius, $a_0 = \langle r_e \rangle$. From this it follows that $4\pi\epsilon_0 = 1$. The atomic unit of energy, the hartree (E_h), is given by the Coulombic energy of two electrons separated by the Bohr radius, $1E_h = q_e^2/(4\pi\epsilon_0 a_0) = 27.2$ eV. In this system, Eq. 2.11 becomes

$$\hat{\mathcal{H}}\Psi = \frac{1}{2}\hat{p}\Psi \cdot \hat{p}\Psi - \frac{1}{r_e}\Psi. \tag{2.12}$$

Partially differentiating Eq. 2.5 with respect to x (in atomic units) gives

$$\frac{\partial}{\partial x}\Psi(x,t) = ipe^{i(px-Et)} = ip\Psi, \tag{2.13}$$

and since the electronic momentum operator is defined by $\hat{p}\Psi = p\Psi$ it follows that it is given by

$$\hat{p} = -i\frac{\partial}{\partial x}. \tag{2.14}$$

In three dimensions this generalises to the vector differential operator, $\hat{\nabla}$, which is the sum of the partial derivatives with respect to each dimension. Therefore, the Schrödinger equation for the hydrogen atom (Eq. 2.12) can be written as

$$\hat{\mathcal{H}}\Psi = -\frac{1}{2}\hat{\nabla}^2\Psi - \frac{1}{r_e}\Psi, \tag{2.15}$$

where $\hat{\nabla}^2 = \hat{\boldsymbol{\nabla}} \cdot \hat{\boldsymbol{\nabla}}$.

[‡] Strictly the magnitude of the charge, for simplicity the sign is contained in Eq. 2.11.

For a N-electron atom, these one-electron terms are summed over all N electrons, but the potential energy operator has two terms, the above one-electron nuclear-attraction energy operator, $\hat{\mathcal{V}}_n$ and a two-electron electron-repulsion energy operator, $\hat{\mathcal{V}}_e$. The corresponding Schrödinger equation is given by

$$\hat{\mathcal{H}}\Psi = -\frac{1}{2}\sum_{i}^{\text{electrons}} \hat{\nabla}_i^2\Psi - \sum_{i}^{\text{electrons}} \frac{Z}{r_i}\Psi + \hat{\mathcal{V}}_e\Psi \tag{2.16}$$

$$= -\frac{1}{2}\sum_{i}^{\text{electrons}} \hat{\nabla}_i^2\Psi - \sum_{i}^{\text{electrons}} \frac{Z}{r_i}\Psi + \sum_{\substack{i,\\ j>i}}^{\text{electrons}} \frac{1}{r_{ij}}\Psi, \tag{2.17}$$

where the $\hat{\nabla}_i^2$ operator acts on electron i, Z is the charge on the nucleus (*i.e.* the atomic number), r_i is the distance between the nucleus and electron and r_{ij} is the distance between electrons, i and j. For a molecule it is necessary to additionally sum the nuclear-attraction term over all nuclei, in which case the Schrödinger equation is

$$\hat{\mathcal{H}}\Psi = -\frac{1}{2}\sum_{i}^{\text{electrons}} \hat{\nabla}^2\Psi - \sum_{A}^{\text{nuclei}}\sum_{i}^{\text{electrons}} \frac{Z_A}{r_{Ai}}\Psi + \sum_{\substack{i,\\ j>i}}^{\text{electrons}} \frac{1}{r_{ij}}\Psi, \tag{2.18}$$

where Z_A is the charge on the nucleus A, and r_{Ai} is the distance between nucleus A and electron i.

2.4 The variational principle

Because the Hamiltonian is a transformed Lagrangian,[14] the Schrödinger equation is a transformed Euler-Lagrange equation. This means that solving the Schrödinger is equivalent to minimising the action functional equation and acts as a strict lower bound for the associated energy, E_{exact}. This is an attractive property: Any valid normalised trial wavefunction Ψ_t must have an energy E_t that is necessarily equal to or above this lower bound, *i.e.*

$$E_t = \langle\Psi_t|\hat{\mathcal{H}}|\Psi_t\rangle \geqslant E_{\text{exact}}. \tag{2.19}$$

Furthermore, if $E_t = E_{\text{exact}}$, then the trial wavefunction is one of the lowest energy eigenstates of the Hamiltonian. This implies that the TISE can be minimised iteratively to find an appropriate solution. This is referred to as the variational principle and is a cornerstone of computational quantum chemistry. However, the most accurate models of all but the simplest chemical systems produce mathematically intractable equations, so approximations must be used. Many of these obey the variational principle, but the solution only represents the lowest bound of the model used.

2.5 Basis sets

It is considerably easier to think of the complicated and unknown wavefunction as a linear combination built from a set of known, simple functions. This section briefly discusses the underlying mathematics required to achieve this and the following sections discuss the construction of a trial wavefunction.

A group is a set of objects $\{G\}$ combined with a binary operation, $\circ$, which together satisfy four properties:

- Closure: Combining two elements produces a member of the group, $\forall g, h \in G : g \circ h \in G$.
- Associativity: The outcome of combining three elements is independent of the order in which the operation is applied, $\forall f, g, h \in G : (f \circ g) \circ h = f \circ (g \circ h)$.
- Identity element: There is an identity element, 0, that when combined with any other element produces the other element. $\exists 0 \in G : \forall g \in G : g \circ 0 = g$.
- Inverse element: For every element, there exists an inverse element that when the two are combined produces the identity element, $\forall g, \exists g^{-1} : g \circ g^{-1} = 0$

A vector space takes a group with the binary operation of addition and also includes an additional binary operation, multiplication by a complex scalar, $a \in \mathbb{C}$. This multiplication must also satisfy the closure, associativity and identity relationships,[§] and must also satisfy the following two distributivity relationships.

- $\forall a \in \mathbb{C}, \forall g, h \in G : a(g + h) = ag + ah$.
- $\forall a, b \in \mathbb{C}, \forall g \in G : (a + b)g = ag + bg$,

Often a 'distance' or measure of the space is added. A basis $\{e\}$ is a set of linearly independent elements from the vector space that can generate any member of the

---

[§] 0 is a scalar so the inverse property does not hold.

group; it is said to span the vector space. Elements are linearly independent if and only if they cannot be linearly combined to form the identity element (without multiplying by 0): this implies that no one element of the basis can be constructed from the others.

The simplest example of a vector space is the set of two-dimensional vectors from a fixed point. The group identity element is the origin and a basis is any pair of position vectors, e_1, e_2 that are not parallel (or anti-parallel); parallel vectors are linearly dependent. Note the underlying basis is not unique. The appropriate measure of such a space is the dot product. If these two vectors are perpendicular, then $e_1 \cdot e_2 = 0$ and this is an example of an orthogonal basis. If unit vectors are used, then $e_1 \cdot e_1 = e_2 \cdot e_2 = 1$ and the basis is said to be normalised. An orthonormal basis has both these properties, and often an orthonormal basis is considerably simpler to use.

The idea can be expanded to a vector space of functions. For instance any periodic sequence can be expressed as a Fourier series, that is a linear combination of a potentially infinite set of sine and cosine functions. Hence this infinite set of functions forms a basis for the vector space of all periodic functions. Quantum chemistry relates to spaces with a defined inner product, analogous to the dot product, an example of which is shown below for a set of functions $g, h \in G$ of one dimension,

$$\langle g|h\rangle = \int_{-\infty}^{\infty} g^* h \, \mathrm{d}x \tag{2.20}$$

From this the same concepts of orthogonality and normalisation follow. A vector space with an inner product measure is called a Hilbert space.

2.6 Orbitals: one-electron-functions

The electronic TISE in spherical co-ordinates can be exactly solved for the hydrogen atom. The imposition of boundary conditions results in an infinite discrete set of eigenstates that are labelledby a set of quantum numbers; n, the principal quantum number, l, the orbital angular momentum quantum number and m, the magnetic quantum number. The addition of a spin quantum number, s is needed to fully describe an electronic state and account for the Zeeman effect (see Section 3.1). Studies of atomic spectra can be rationalised using these quantum numbers, however it is also necessary to introduce the Pauli principle which states that:[6] “The total wavefunction must be antisymmetric under the interchange of any pair of identical fermions and symmetrical under the interchange of any pair of identical bosons.” This further implies the Pauli exclusion principle, that is:[6] “no two electrons can occupy the same state.” Hence no two electrons can have the same set of quantum numbers.

The TISE is solved by separating the equation into two partial differential equations (PDE), one radial, one angular. The angular PDE also needs to separated into polar and azimuthal angle PDEs. The resulting three PDEs can be solved by treating them as ordinary differential equations (ODEs). The radial PDE can be solved using the Frobenius method[15] and the solutions, $R_{n,l}(r)$ can be written as a product of a polynomial and a real exponential term. After a change of variable, the polar PDE produces a series of associated Legendre polynomials in the cosine of the polar angle. The azimuthal PDE trivially integrates to an imaginary exponential function. The combination of the angular components are the spherical harmonics $Y_{l,m}$. $R_{n,l}(r)$ and $Y_{l,m}$ are orthogonal over a one-dimensional line and the surface of a sphere respectively. They are commonly normalised, *i.e.*

$$\int_{-\infty}^{\infty} Y_{l,l'}(\theta,\phi) Y^*_{m,m'}(\theta,\phi)\,\mathrm{d}r = \delta_{ll'}\delta_{mm'}, \tag{2.21}$$

where δ_{ij} is the Kronecker delta. The normalised product of these, $R_{n,l}(r)Y_{l,m}$ are the beautiful atomic orbitals that all chemists are familiar with (Figure 2.1).

The hydrogen atomic orbitals (AOs) are orthonormal functions of $\mathbb{R}^3$. They are linearly independent and span the L^2 (complex) vector space of three-dimensional square-integrable functions,[¶] and can therefore be used as a basis for all such functions. From Eq. 2.1, any physical one-electron wavefunction is a L^2 function, so can be represented by a potentially infinite linear combination of the infinite set of atomic orbitals on a single centre. This justifies the use of such a combination to form atomic orbitals, $\phi_i(\mathbf{r})$. Obviously, in practice a truncated set is used.

Molecular bonding is represented by the linear combination of atomic orbitals model, that is, by constructing the one-electron molecular orbitals (MOs), $\psi_a(\mathbf{r})$, via

$$\psi_a(\mathbf{r}) = \sum_i^{\mathrm{AO}} c_{ai}^{\mathrm{MO}} \phi_i(\mathbf{r}), \tag{2.22}$$

where c_{ij}^{MO} are the MO coefficients of the linear expansion. The practical use of such

---

[¶] $\forall f \in L^2$, $\sqrt{\langle f|f\rangle}$ exists. This quantity is referred to as its norm.

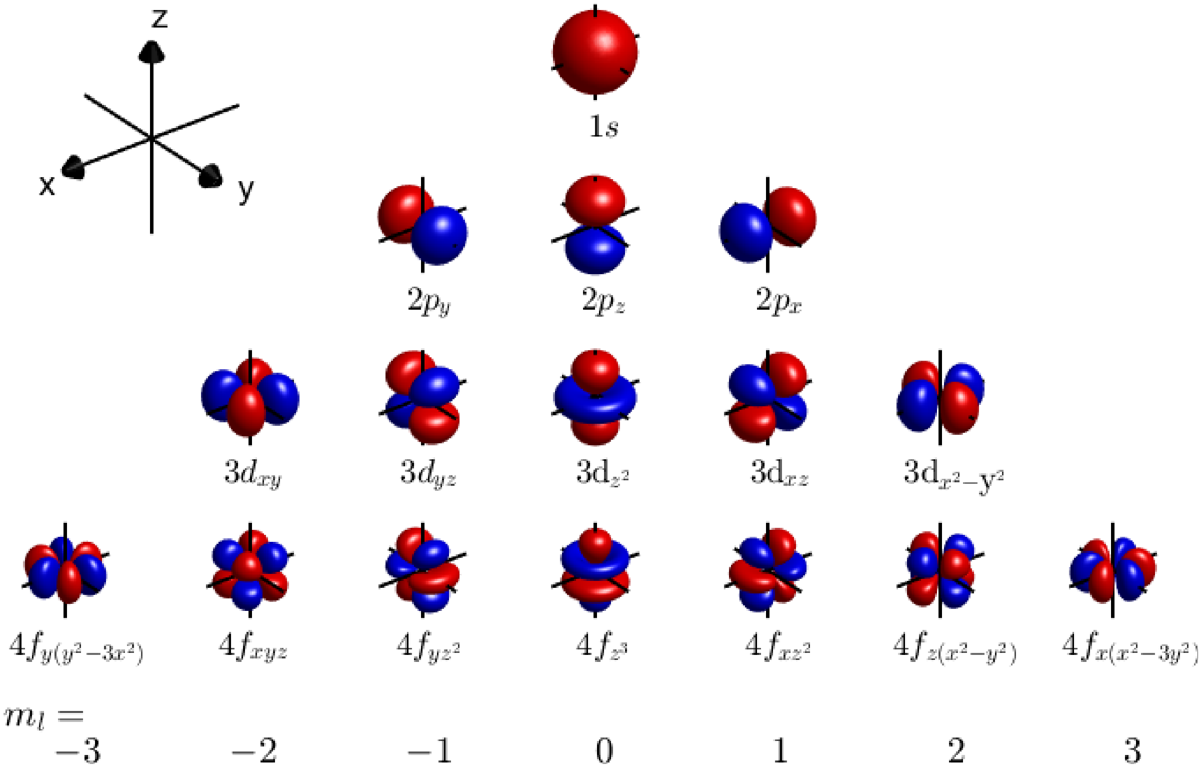

Figure 2.1: Atomic orbitals of the hydrogen atom.

orbitals is discussed below. For an infinite set of AOs on each nucleus, the resulting infinite set of MOs still spans L^2.

However an MO is an one-electron function. For an N-electron wavefunction it is necessary to combine the orbitals in product form. The simplest method is to form a Hartree product, $|\Psi_{\text{HP}}\rangle$, multiplying molecular orbitals together, *i.e.*

$$\Psi_{\text{HP}} = \prod_{a}^{MOs} \psi_a. \tag{2.23}$$

Each orbital has an independent set of coordinates, so it follows that these products can be integrated sequentially, hence a Hartree product formed from N independent infinite sets of AOs or MOs spans L^2 over $3N$-dimensional space. This mathematically justifies using Hartree products to represent an N-electron wavefunction.

As real quantity and an observable, the electron (probability) density, $\rho(\mathbf{r}) = |\Psi(\mathbf{r})|^2$ can be more easily discussed than the wavefunction. It can be obtained from

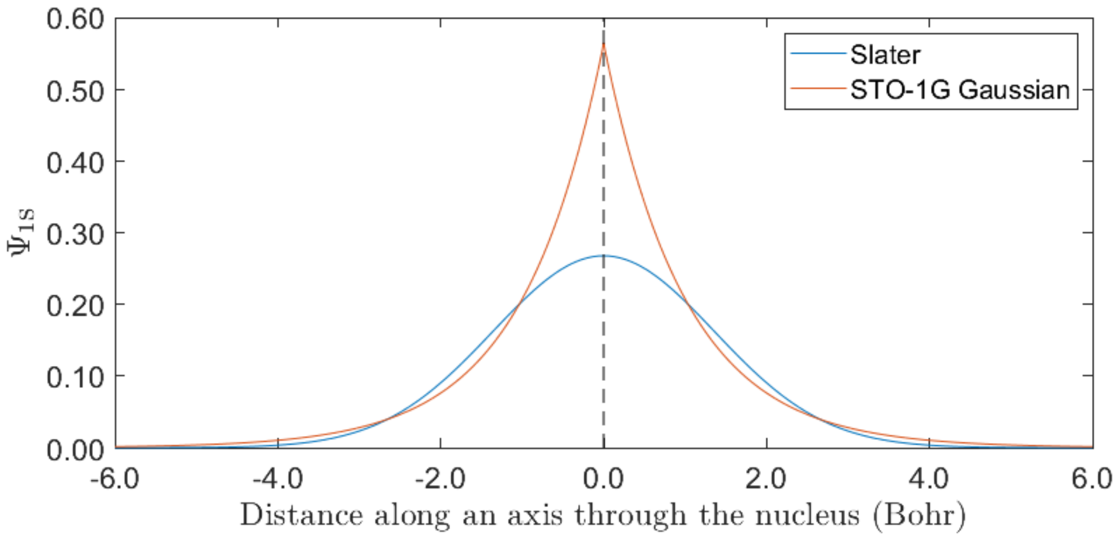

Figure 2.2: The Slater and STO-1G[17] $1s$ orbitals for hydrogen, plotted along an axis through the nucleus.

a N-electronic wavefunction using the corresponding $\hat{\rho}$ operator, *i.e.*

$$\langle\Psi|\hat{\rho}|\Psi\rangle = \left\langle\Psi\middle|\sum_{i=1}^{\text{electrons}}\delta(\mathbf{r}-\mathbf{r}_i)\middle|\Psi\right\rangle, \qquad \delta(\mathbf{r}) = \begin{cases} 1 & \mathbf{r} = (0\ 0\ 0)^T \\ 0 & \text{otherwise.} \end{cases} \tag{2.24}$$

δ is called a Dirac delta function. Considering only the spatial part of the wavefunction, the above equation can be explicitly written as

$$\rho(\mathbf{r}) = \int_{\mathbb{R}^3}\cdots\int_{\mathbb{R}^3}\Psi^*(\mathbf{r}_1\ldots\mathbf{r}_N)\sum_{i=1}^{\text{electrons}}\delta(\mathbf{r}-\mathbf{r}_i)\Psi(\mathbf{r}_1\ldots\mathbf{r}_N)\ \ \mathrm{d}\mathbf{r}_1\cdots\mathrm{d}\mathbf{r}_N, \tag{2.25}$$

and, since electrons are indistinguishable particles, this can be simplified to

$$\rho(\mathbf{r}) = N\int_{\mathbb{R}^3}\cdots\int_{\mathbb{R}^3}\Psi^*(\mathbf{r}_1\ldots\mathbf{r}_N)\Psi(\mathbf{r}_1\ldots\mathbf{r}_N)\ \ \mathrm{d}\mathbf{r}_2\cdots\mathrm{d}\mathbf{r}_N. \tag{2.26}$$

The electron density has a cusp, a discontinuous derivative, at any nucleus. Considering a hydrogenic atom with nuclear charge Z, then the electron density must satisfy Kato's cusp condition;[16]

$$Z = -\left[\frac{1}{2\rho(\mathbf{r})}\frac{\mathrm{d}\rho(\mathbf{r})}{\mathrm{d}r}\right]_{r\to 0}. \tag{2.27}$$

The electron density of, for example, a $1s$ orbital, ϕ_{1s}, is simply given by $\rho_{1s}(\mathbf{r}) = |\phi_{1s}(\mathbf{r})|^2$, since orbitals are one-electron functions. Similar results follow for all other orbitals.

Slater type orbitals (STOs) are based on a radial function of $r^{n-1}e^{-\alpha r}$ where α is a constant called the exponent, in this case, the effective nuclear charge. Such functions satisfy the cusp condition and correctly model the exponential decay of the electron density (Figure 2.2), but the evaluation of their multi-centre integrals is computationally expensive.[18,19] This led to the introduction[20] of Gaussian type orbitals (GTOs), $\eta(\mathbf{r})$. These can be linear combinations of Gaussian functions, or primitives, of the electronic position $\mathbf{r} = \{x, y, z\}$ with the latter functions defined by

$$\eta(\mathbf{r}; \mathbf{R}, \mathbf{l}, \alpha) = x_A^{l_x} y_A^{l_y} z_A^{l_z} e^{-\alpha|\mathbf{r}_A|^2}, \tag{2.28}$$

$$\text{where } \mathbf{r}_A = \mathbf{r} - \mathbf{R}_A = \{x_A, y_A, z_A\} = \{x - X_A, y - Y_A, z - Z_A\}. \tag{2.29}$$

The parameters are, α, the exponent, $\mathbf{R}_A = \{X_A, Y_A, Z_A\}$, the centre of the Gaussian (normally at a nucleus, here labelled A), and $\mathbf{l} = \{l_x, l_y, l_z\}$, the angular momentum components (with $|\mathbf{l}| = l$). The main advantage of using Gaussian functions comes from the "Gaussian product rule": The product of two Gaussian functions is itself a Gaussian.[17] This makes evaluating multi-centre integrals considerably simpler. However a single Gaussian function is a poor model for a hydrogenic atomic orbital because it does not have a cusp at the nucleus and its asymptotic behaviour is qualitatively incorrect. To attenuate this problem, linear combinations are used to form atomic orbitals (AOs), ϕ_i, where the exponents vary but, in most cases, the other parameters are the same. *i.e.*

$$\phi_i(\mathbf{r}; \mathbf{R}, \mathbf{l}, \boldsymbol{\alpha}) = \sum_j^{Gaussian} c_{ij}^{AO} \eta_j(\mathbf{r}; \mathbf{R}, \mathbf{l}, \alpha_j). \tag{2.30}$$

where c_{ij}^{AO} are the AO coefficients of the linear expansion. A further linear combination is often necessary for $l \geqslant 2$, *i.e.* for d,f,g,... orbitals to convert these cartesian AOs to a spherical form, *e.g.* to reduce six cartesian d-orbitals, $d_{x^2}, d_{y^2}, d_{z^2}, d_{xy}, d_{xz}, d_{yz}$, to five spherical d-orbitals, $d_{x^2-\mathrm{y}^2}, d_{z^2}, d_{xy}, d_{xz}, d_{yz}$.

The spherical orbitals are the smallest basis that spans L^2. Mathematically this is called a minimal basis, but the common unrelated term, minimal basis set, refers to a basis with enough orbitals to represent each occupied shell (*e.g.* the 1s and 2sp shells for carbon). Cartesian orbitals remain a valid basis, but use a larger number of functions so are not mathematically minimal. STOs produce more accurate results, but using additional GTO based AOs in a basis set dramatically improves basis set performance: parity in accuracy between a STO or GTO calculation can be achieved with a surprisingly small proportional increase of GTO functions.[19]

2.6.1 The taxonomy of basis sets

A minimal basis set is one that that has enough AOs to represent each occupied shell. The simplest minimal basis sets are the STO-nG family. These fit n Gaussian functions to the corresponding STO. These sets are limited in both the representation of the AO and in flexibility to respond to neighbouring atoms when involved in bonding.

One method of increasing flexibility in the atomic basis is to add an additional set of AOs, leading to a 'double-zeta' or DZ basis set, so a double-zeta carbon basis set would have ten functions instead of five. A compromise can be made where only the valence shell is doubled leading to 'split-valence' basis sets with SV indicating a double valence shell. This can be extended to triple, quadruple, quintuple basis sets (TZ,QZ,5Z respectively) as far as necessary. However to model the polarisation of the electron density due to neighbouring atoms, it is typical to add polarisation functions in the form of a shell of higher angular momentum orbitals, so for carbon d orbitals are added. Such a basis set is represented by adding a P to their shorthand form, or PP if two polarisation shells are used. Additionally it is sometimes useful to improve the modelling of the long tail of the orbitals to better represent long-range behaviour. This is done by adding small exponent or diffuse shells, and this is represented by a D suffix. Combining these labels gives a large number of possible basis sets, and as an example, TZVPPD is a triple-zeta valence atomic basis set with two polarisation shells and a diffuse shell. Although much less common, sometimes it is useful to improve the nuclear cusp representation of the s orbitals, especially when properties that explicitly depend on the electron density close to the nucleus are being modelled, such as the hyperfine matrix. This can be done by introducing a simple geometrical progression of s functions based on the set of largest exponent s functions in the underlying basis, referred to as adding sharp functions. This can be done manually as in this work.

There has been decades of work on improving basis sets, and we cannot possibly do the subject justice, so only directly relevant sets are discussed further. Basis Set Exchange (BSE)[21] is an invaluable online repository of basis sets and has an open-source github repository.

On a sample 61 day period,[21] Karlsruhe group's def2-TZVP basis set[22,23] was the most popularly downloaded set from the BSE and the 'def2' family was reported to show improved performance in density functional theory and post-Hartree-Fock methods,[22] and analysis of the calculations of geometries and relative energies demonstrate that these basis sets to provide "reasonable options that balance calculational cost and accuracy."[24] Bursch *et al.* consider def2-TZVP as "sufficient" for calculations of molecular geometry,[25] although note that larger basis sets may be useful for studying conformational change. Pankratyev *et al.* estimated the error inherent in closed shell NMR calculations using TZVP-based gauge-including atomic orbitals (GIAO) and DFT (PBE functional):[26] Over 263 ^{1}H shifts and 308 ^{13}H shifts the estimated error was ±0.35 ppm and ±6.05 ppm respectively for a 95% confidence interval. The estimated basis error for ^{1}H shifts is an order of magnitude smaller than the errors for open-shell molecules presented in this thesis. Finally the basis set was used to investigate our inhouse aZORA scalar-relativistic model[27] and the calculation of a number of Zeeman matrices.[28] Due to these considerations, this is the basis set we favour for lighter atoms.

Relativistic effects make the construction of basis sets for heavy atoms increasingly difficult as they must also have the flexibility to model such effects. We prefer the segmented all-electron relativistically contracted (SARC) basis sets,[29–31] including the published single polarisation functions (g shell). These are also VTZP basis sets. Designed for the scalar-relativistic ZORA and DKH Hamiltonians discussed at the end of this chapter, this set was reported to have improved performance in DFT and CCSD(T) calculations and is recommended for electron paramagnetic resonance (EPR) calculations.[32] Segmented basis sets do not share primitive functions between basis functions, and this reduces the computational effort in generating electron-repulsion integrals.

Gauge-including atomic orbitals (GIAO)

This thesis focuses on the calculation of magnetic properties, and due to the approximations that we are forced to employ, the calculation of these properties is often unphysically dependent on the definition of the co-ordinate system, *i.e.* do not obey gauge invariance. In particular the orbitals that are defined in this section are explicitly centred on an atomic nucleus.

To resolve this issue, gauge-including atomic orbitals (GIAOs) where developed, sometimes called London orbitals.[33] This orbitals include the gauge as a phase term, *e.g.* the London form of a the gaussian primitive, $\eta(\mathbf{r};\mathbf{R},\mathbf{l},\alpha)$ centred on a nucleus at $\mathbf{R}$ is given by

$$\eta_{\text{London}}(\mathbf{r};\mathbf{R},\mathbf{l},\alpha)) = e^{-i\mathbf{A}(\mathbf{R})\cdot(\mathbf{r}-\mathbf{R})}\eta(\mathbf{r};\mathbf{R},\mathbf{l},\alpha) \tag{2.31}$$

where $\mathbf{A}(\mathbf{R})$ is the value of a defined vector field at the nucleus. These orbitals are sometimes (incorrectly) called gauge-invariant atomic orbitals, but contain the gauge in the definition of $\mathbf{A}(\mathbf{R})$, and as such are gauge-variant. However, all chemical properties calculated with these functions involve integrals (*i.e.* are the expectation values of operators), and it can be shown that integrals of these orbitals are gauge-invariant, hence all properties calculated using London orbitals are also gauge-invariant.

2.7 Slater determinants: N-electron functions

A Hartree product cannot satisfy the antisymmetry principle — exchanging two electrons does not produce a change in the sign of the Hartree product. Models of multielectron behaviour must address this constraint. A common assumption for closed shell systems is that the spatial form of the MOs is independent of their spin-coordinate, so only N spatial orbitals are needed to model a $2N$-electron wavefunction, this is the case for the restricted Hartree-Fock model discussed later. The necessary antisymmetry is typically accounted for by using a determinant constructed from all occupied molecular orbitals over all $2N$ electrons *i.e.*

$$|\Psi\rangle = \frac{1}{\sqrt{N!}} \begin{vmatrix} \psi_1(\mathbf{r}_1,\alpha) & \psi_2(\mathbf{r}_1,\alpha) & \dots & \psi_N(\mathbf{r}_1,\alpha) & \psi_1(\mathbf{r}_1,\beta) & \dots & \psi_N(\mathbf{r}_1,\beta) \\ \psi_1(\mathbf{r}_2,\alpha) & \psi_2(\mathbf{r}_2,\alpha) & \dots & \psi_N(\mathbf{r}_2,\alpha) & \psi_1(\mathbf{r}_2,\beta) & \dots & \psi_N(\mathbf{r}_2,\beta) \\ \dots & \dots & \dots & \dots & \dots & \dots & \dots \\ \psi_1(\mathbf{r}_{2N},\alpha) & \psi_2(\mathbf{r}_{2N},\alpha) & \dots & \psi_N(\mathbf{r}_{2N},\alpha) & \psi_1(\mathbf{r}_{2N},\beta) & \dots & \psi_N(\mathbf{r}_{2N},\beta) \end{vmatrix},$$

where $\psi_i(\mathbf{r}_j,\alpha)$ refers to the i^{th} spin-orbital, occupied by the j^{th} electron and having spin α. This is equivalent to building an antisymmetrised linear combination of all Hartree products, *e.g.* Considering the above determinant; if row 1 and row 2 of the determinant are exchanged, then this is equivalent to exchanging two electrons (with positions $\mathbf{r}_1$ and $\mathbf{r}_2$), and the new determinant has the same functional form as the original determinant, but the opposite sign.

Slater determinants can also be built for open-shell systems, however while these are eigenfunctions of $\hat{\mathcal{S}}_z$, they are not necessarily eigenfunctions of $\hat{\mathcal{S}}^2$; this effect is called spin contamination. To solve this issue the wavefunction can be represented by a linear combination of Slater determinants, and such a construction is called a configuration state function (CSF).

A simple example of a CSF is given by the open-shell singlet form of the excited state of the helium atom, $1s^1 2s^1$, where the two electrons are spin-paired but are in different spatial orbitals. An appropriate antisymmetric wavefunction is given by[34]

$$\Psi_{{}^1\text{He},\,1s^1 2s^1} = \tfrac{1}{2}[\psi_{1s}(\mathbf{r}_1)\psi_{2s}(\mathbf{r}_2) - \psi_{2s}(\mathbf{r}_1)\psi_{1s}(\mathbf{r}_2)][\alpha(\sigma_1)\beta(\sigma_2) - \alpha(\sigma_2)\beta(\sigma_1)]. \quad (2.32)$$

This wavefunction cannot be represented by a single determinant built from spin-orbitals, but can be represented by a linear combination of determinants, *i.e.* a CSF.

2.8 Hartree-Fock theory

Within the non-relativistic, Born-Oppenheimer approximation of the time-independent Schrödinger equation and considering a single determinant wavefunction, Ψ, then the variational principle implies that we want to determine the constituent molecular orbitals that minimise the electronic energy, E_0.

$$E_0 = \left\langle \Psi|\hat{\mathcal{H}}|\Psi \right\rangle = \sum_{i}^{electrons} \left\langle \Psi|\hat{\mathscr{h}}(i)|\Psi \right\rangle + \sum_{i,j<i}^{electrons} \left\langle \Psi|\hat{\mathscr{g}}(i,j)|\Psi \right\rangle, \quad (2.33)$$

where $\hat{h}(i)$ gathers the one-electron operators for electron i, representing the kinetic and nuclear-electron attraction energies.

$$\hat{h}(i) = -\tfrac{1}{2}\hat{\nabla}^2 - \sum_{a}^{nuclei} \frac{Z_a}{|\mathbf{r}_i - \mathbf{R}_a|}, \tag{2.34}$$

and $\hat{g}(i,j)$ is the two-electron operator representing electron-electron repulsion energies.

$$\hat{g}(i,j) = \frac{1}{|\mathbf{r}_i - \mathbf{r}_j|} = \frac{1}{r_{ij}} \tag{2.35}$$

Electrons are indistinguishable particles, so without loss of generality we only need to consider $\hat{h}(1)$ and $\hat{g}(1,2)$ explicitly. Applying the Slater determinant to Eq. 2.33 leads to a set of one-electron integro-differential eigenvalue equations

$$\hat{f}_i(1)\psi_i(1) = \left[\hat{h}_i(1) + \sum_{j\neq i}^{orbitals} \hat{g}_{ij}(1,2)\right]\psi_i(1) = \epsilon_i\psi_i(1) \tag{2.36}$$

where subscripts relate to the molecular orbitals. The overall one-electron operator $\hat{f}_i$ is called the Fock operator. The energy of the i^{th} solution, ϵ_i is called the orbital energy. The two-electron operator is transformed into a pair of averaged one-electron operators, the Coulomb, $\hat{j}_j$, and exchange $\hat{k}_j$ operators,

$$\hat{g}_{ij}(1,2)\psi_i(1) = \hat{j}_j(1)\psi_i(1) + \hat{k}_j(1)\psi_i(1). \tag{2.37}$$

These result from an integration over the second electron in $\mathbb{R}^3$ and spin space;

$$\hat{j}_j(1)\psi_i(1) = \left[\int \frac{\psi_j^*(2)\psi_j(2)}{r_{12}}\,\mathrm{d}\mathbf{x}_2\right]\psi_i(1) \tag{2.38}$$

$$\hat{k}_j(1)\psi_i(1) = \left[\int \frac{\psi_j^*(2)\psi_{\color{red}i}(2)}{r_{12}}\,\mathrm{d}\mathbf{x}_2\right]\psi_{\color{red}j}(1) \tag{2.39}$$

the exchange operator switches the orbital labels within and outside the integral (shown in red) and is a result of the spin antisymmetry of the electron. Electron labels can now be safely omitted.

Considering Eq. 2.36 and expanding the Slater determinant wavefunction in its finite orbital basis allows the Hartree-Fock equations to relate the variational parameters, the MO coefficients, C_{aj} to the set of molecular orbital eigenvalue equations

$$\hat{f}_j \sum_{a}^{\text{AOs}} C_{aj}\phi_j = \epsilon_j \sum_{a}^{\text{AOs}} C_{aj}\phi_j. \tag{2.40}$$

Integrating these equations over the AOs allows the Hartree-Fock equations to be written in matrix form, as the Roothaan-Hall[35,36] equations

$$\mathbf{FC} = \mathbf{SC}\boldsymbol{\epsilon}, \tag{2.41}$$

where

$$\mathbf{F}_{ij} = \int \phi_i \hat{f}_j \phi_j \,\mathrm{d}\mathbf{r}, \tag{2.42}$$

$$\mathbf{S}_{ij} = \int \phi_i \phi_j \,\mathrm{d}\mathbf{r}, \tag{2.43}$$

$$\boldsymbol{\epsilon} = \delta_{ij}\epsilon_j \tag{2.44}$$

and **C** is the matrix of MO coefficients. The orbitals are typically orthogonalised by a unitary transform, so that the overlap matrix **S** becomes an identity matrix. The Roothaan-Hall matrix formulation has the form of an eigenvalue equation, but it is non-linear because of the dependence of the Coulomb and exchange operators on the MO coefficients. It is necessary to use an iterative process to find the eigenvectors that produce a self-consistent solution. By finding the lowest energy solution, the "best" non-relativistic Hartree-Fock wavefunction is produced as constrained by the atomic orbital basis set. The finite nature of the basis set is another approximation of this method. In principle, as the basis set is expanded and improved, the wavefunction evolves towards a better approximation of the true wavefunction, within the model. This change can be studied, and the convergence of the wavefunction towards that of the infinite basis set is called the basis set limit.

For a closed shell system, it is often assumed that the spatial parts of the spin-orbitals are independent of their spin coordinate, and therefore only one set of orbitals is needed to represent alpha and beta spin-orbitals. This is called restricted Hartree-Fock theory.

If this assumption is relaxed, then two sets of orbitals are needed, one for each spin coordinate. This is called unrestricted Hartree-Fock theory (UHF). In UHF theory orbital energies can differ with spin coordinate and typically the lower energy orbitals are considered to have alpha spin.

For an open shell system, there is a further possibility that replaces RHF theory. In this, restricted open shell Hartree-Fock (ROHF) theory, a single set of M orbitals is used and for a system with N electrons with spin, S, the first $(N-2S)/2$ are doubly

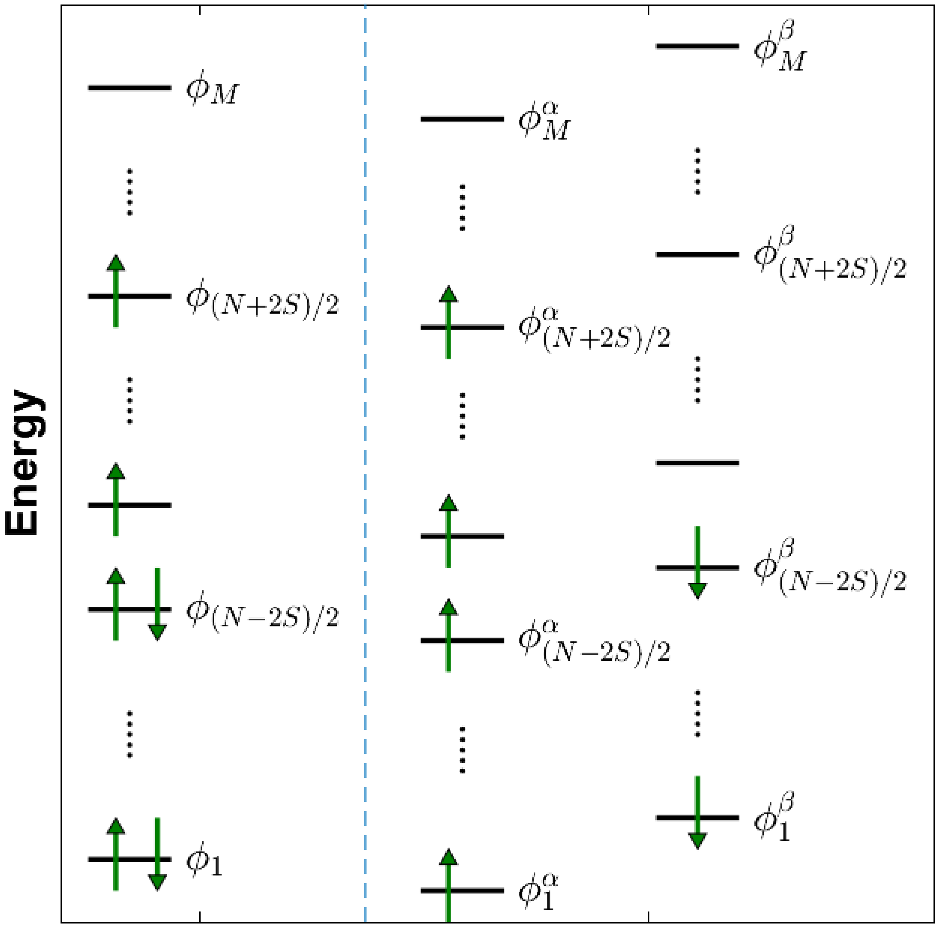

Figure 2.3: ROHF (left) and UHF (right) molecular orbital energies (not to scale).

filled, the next $2S$ are singly filled and the remaining orbitals are vacant. These two schemes are shown in Figure 2.3.

Unfortunately ROHF molecular orbital energies are poorly defined[37] and unlike UHF do not obey Koopmans' theorem.[38] Koopmans' theorem states that the first ionisation energy of a molecule should be equal to the negative value of the highest occupied molecular orbital (HOMO) energy. Furthermore using the same set of orbitals for α and β spin state results in the exchange interactions of these spin states to be identical. Hence ROHF is typically unsuitable for spin-dependent properties.[39]

Conversely UHF is a single determinant method where the spatial form of an orbital is explicitly linked to its spin-coordinate. This means that a construction separating spatial and spin coordinates (*e.g.* as shown in Eq. 2.32) is not possible, hence CSFs cannot be used, and UHF wavefunctions are not eigenfunctions of $\hat{\mathcal{S}}^2$.

2.8.1 Canonical and natural orbitals

Orbitals can present a valuable qualitative insight into chemistry, but because the orbitals form a basis for the wavefunction, any linear combination of these orbitals that remains a valid basis will recover the same wavefunction.[40] As a result, their physical interpretation is highly dependent on the context. The canonical orbitals are eigenfunctions of the Fock operator, and as such satisfy Koopmans' theorem. They therefore can relate orbital energies to ionisation energies. However, they may be delocalised and can be poor representations of the bonding in the molecule. Natural orbitals diagonalise (and thereby represent) the electron density. For an unrestricted calculation, they can be used to quantify the average electron distribution of degenerate and nearly degenerate orbitals and tend to be qualitatively more valuable in understanding bonding. However the corresponding orbital energies have less physical significance, because they are not eigenfunctions of an energy (*i.e.* the Fock) operator. Natural orbitals from an unrestricted calculation are called unrestricted natural orbitals (UNOs).

The spin-contamination present in canonical or natural orbitals from an unrestricted calculation can cause convergence problems and cause inaccuracies in single-reference calculations on spin-dependent properties.[32] To address this, Neese developed quasi-restricted orbitals (QROs).[41] These are formed from three sets of orbitals, firstly a set of UNOs with occupations close to 2.0 which are set to be doubly occupied, then the set of UNOs with an exact occupation of 1. These are set to be singly occupied. Finally orbitals with an occupation close to 0. These are considered to be virtual orbitals. Determinants built from this set of wavefunctions are spin-eigenfunctions, and represent a state that is a close approximation to the restricted solution. Furthermore these orbitals can be assigned well defined orbital energies via the Fock operator.

2.9 Electron correlation

Beyond the limitations of the finite one-electron basis, the Hartree-Fock approximation of the wavefunction suffers from two additional problems.

Firstly, the approximation assumes that the N-electron wavefunction can be represented by a single determinant built from the MOs. This is referred to as static correlation. The simplest example of the importance of static correlation occurs when attempting to model the dissociation of the hydrogen molecule via RHF. In this case, using a single determinant results in an ionic dissociation where both of the electrons are on one of the two hydrogen atoms. This is clearly unphysical; RHF cannot model bond breaking.[42]

Secondly, the approximation represents the electron-electron interaction as an interaction between a single electron and the mean field due to the other electrons, however electrons repel each other locally, so if one electron is considered to be at $\mathbf{r}_1$, all other electrons are less likely to be at (or close to) $\mathbf{r}_1$, and an averaged field cannot capture this behaviour. This is called dynamic correlation. Some dynamic correlation is recovered by the exchange operator, since using an antisymmetric wavefunction means that electrons with the same spin function cannot have the same spatial function (Fermi correlation).

In practice, both types of correlation are present and a simple separation into static and dynamic effects may not be possible.[43] The non-relativistic correlation energy E_{corr} is defined as

$$E_{\text{corr}} = E_{\text{exact}} - E_{\text{HF}}^{\infty} \tag{2.45}$$

where E_{exact} is the exact non-relativistic energy within the Born-Oppenheimer approximation, and E_{HF}^{∞} is the Hartree-Fock energy that would result from using an infinite basis set. This represents the largest-source of error in computational chemistry for many species only consisting of lighter nuclei, however relativistic effects scale with atomic number and also become critical to model for heavier elements (see Section 2.16).

2.10 Density functional theory

The electronic Schrödinger equation (Eq. 2.17) for a N-electron molecule can be written as

$$\hat{\mathcal{H}}\Psi = \hat{\mathcal{T}}\Psi + \hat{\mathcal{V}}_n\Psi + \hat{\mathcal{V}}_e\Psi. \tag{2.46}$$

The only operator within this which is explicitly dependent on the arrangement of the nuclei is the nuclear-attraction potential energy operator, $\hat{\mathcal{V}}_n$. This operator can be represented by the summation of one-electron operators, $\hat{v}_{\text{ext}}(\mathbf{r}_i)$,[44] corresponding to the electrons experiencing an "external potential," $\hat{\mathcal{V}}_{\text{ext}}(\mathbf{r})$. Explicitly this is written as

$$\hat{\mathcal{H}}\Psi = \hat{\mathcal{T}}\Psi + \sum_i^{electrons} \int_{\mathbb{R}} \mathrm{d}\mathbf{r}_i \; \hat{v}_{\text{ext}}(\mathbf{r}_i)\Psi + \hat{\mathcal{V}}_e\Psi. \tag{2.47}$$

or

$$\hat{\mathcal{H}}\Psi = \hat{\mathcal{T}}\Psi + \int_{\mathbb{R}} \mathrm{d}\mathbf{r} \; \hat{\mathcal{V}}_{\text{ext}}(\mathbf{r})\Psi + \hat{\mathcal{V}}_e\Psi. \tag{2.48}$$

The N-electron wavefunction is an unknown function of $3N$-spatial and N-spin coordinates, and as such rapidly becomes more complex as the number of electrons increases. The spinless one-electron density (Eq. 2.26) is always a three-dimensional function, and as such is simpler and conceptually more intuitive.

Density functional theory[45] (DFT) is based on two Hohenberg-Kohn theorems. The first Hohenberg-Kohn theorem establishes that there is a one-to-one mapping between a non-degenerate ground-state wavefunction and the corresponding external potential, $\hat{v}_{\text{ext}}(\mathbf{r}_i)$. Similarly there is a one-to-one mapping between a non-degenerate ground-state wavefunction and the ground-state electron density. Together this implies that the external potential energy is a unique functional of the ground-state electronic density (to within a constant). This implies that the true density must be representable by the external potential, this property is called v-representability.[46] A similar property of the true density, N-representability, is that the density must equal the number of electrons when it is integrated over all space (as in Eq. 2.1).

The second Hohenberg-Kohn theorem proves that there exists a universal functional of the density, $E[\rho]$, which can be used variationally to find the exact energy minimum and density.[47]

In principle, this energy functional can be divided into functionals representing the kinetic energy, $T[\rho]$, the nuclear-attraction potential energy, $V_n[\rho]$ and the electron-attraction potential energy, $V_n[\rho]$; that is, the universal functional can be written as

$$E[\rho] = T[\rho] + V_n[\rho] + V_e[\rho], \tag{2.49}$$

or

$$E[\rho] = T[\rho] + \int_{\mathbb{R}} \mathrm{d}\mathbf{r}\ \rho(\mathbf{r})\hat{\mathcal{V}}_{\text{ext}}(\mathbf{r}) + V_e[\rho], \tag{2.50}$$

however this form is intractable. Kohn-Sham theory[48] starts by modelling an auxiliary system of non-interacting atoms. This can be written as

$$E[\rho] = T_s[\rho] + \int_{\mathbb{R}} \mathrm{d}\mathbf{r}\ \rho(\mathbf{r})\hat{\mathcal{V}}_{\text{ext}}(\mathbf{r}) + V_e[\rho] + E_{xc}[\rho], \tag{2.51}$$

where the non-interacting kinetic energy functional, $T_s[\rho]$, is given by

$$T_s[\rho] = -\int_{\mathbb{R}} \mathrm{d}\mathbf{r}\ \hat{\nabla}^2\rho(\mathbf{r}), \tag{2.52}$$

and the non-interacting electron-electron repulsion energy functional, $E_e[\rho]$, is given by

$$E_e[\rho] = \frac{1}{2}\int_{\mathbb{R}} \mathrm{d}\mathbf{r}_1 \int_{\mathbb{R}} \mathrm{d}\mathbf{r}_2\ \frac{\rho(\mathbf{r}_1)\rho(\mathbf{r}_2)}{|\mathbf{r}_1 - \mathbf{r}_2|}. \tag{2.53}$$

The remaining functional, $E_{xc}[\rho]$, is called the exchange-correlation functional which is defined by Eq. 2.51. The theory is typically used in a single determinant form similar to that used for Hartree-Fock theory, and the above equations can be converted, using variational methods,[44] to the one-electron Kohn-Sham equations shown below. The one-electron equations can be used in a similar way to the Roothaan-Hall equations (Eq. 2.44).

$$\left[-\nabla^2 + \hat{\mathcal{V}}_{\text{ext}}(\mathbf{r}) + \int \mathrm{d}\mathbf{r}_2\ \frac{\rho(\mathbf{r}_2)}{|\mathbf{r}_1 - \mathbf{r}_2|} + \frac{\partial E_{xc}}{\partial \rho(\mathbf{r})}\right]\phi_i(\mathbf{r}_1) = \epsilon_i\phi_i(\mathbf{r}_1). \tag{2.54}$$

where the eigenvalues ϵ_i represent the Kohn-Sham orbital 'energies.'

The exchange-correlation functional corrects three sources of error in the non-interacting model, these are:

1. The difference between the interacting and the non-interacting kinetic energy (*i.e.* $T[\rho] - T_s[\rho]$).

2. The $E_e[\rho]$ term only models the coulombic part of electronic repulsion (cf. Eq. 2.37). The exchange term, due to Pauli repulsion must be modelled.
3. Like Hartree-Fock theory, DFT is a mean field theory, and therefore dynamic correlation must be modelled.

Like Hartree-Fock theory, restricted, restricted-open and unrestricted Kohn-Sham approaches exist. In principle, density functional theory scales with the cube of the number of electrons $O(n^3)$ which compares favourably with other correlated techniques and accounts for its popularity.

A large number of functionals has been developed. The first functionals developed started from the local spin density approximation (LSDA),[48] which takes the known[49] exchange-correlation functional, $\epsilon_{\mathrm{xc}}^{\mathrm{UEG}}$, of the uniform electron gas as applied to a pair of spin-densities, ρ_α, ρ_β applied locally in infinitesimal regions, so the corresponding DFT exchange-correlation energy, $E_{\mathrm{xc}}^{\mathrm{LSDA}}$ is represented by

$$E_{\mathrm{xc}}^{\mathrm{LSDA}}[\rho_\alpha, \rho_\beta] = \int_{\mathbb{R}^3} \epsilon_{\mathrm{xc}}^{\mathrm{UEG}}[\rho_\alpha, \rho_\beta]\, \mathrm{d}\mathbf{r} \tag{2.55}$$

In practice, the infinitesimal regions are often approximated by splitting space (to a finite limit) into a three-dimensional (radial and angular) grid, *i.e.* by numerical quadrature,[32] with each region representing a uniform density. LSDA functionals were found to represent regular solid surfaces well, and benefit from a fortunate cancellation of errors; it tends to underestimate the exchange-energy and overestimate the correlation-energy. However it was insufficient for the calculation of many properties, *e.g.* it tends to overestimate atomisation energies. One solution was to introduce a functional dependence on the gradient of the density, referred to as a generalised gradient (GGA) functional. An early exchange functional developed by Becke,[50] was parameterised using a set of exact Hartree-Fock exchange-energies. A similar parameterised functional is the correlation LYP[51] functional. The combined BPE[52] functional is an example of a functional that is not parameterised. A possible refinement of the functional is to include a dependence on the Laplacian of the density (or the kinetic energy) such as the TPSS[53] functional. The increasing sophistication of the functionals is sometimes referred to climbing a “Jacob’s ladder” of functionals to the dream of a perfect functional.[53,54]

A final refinement to the functional is based on the observation that it is possible to define a parameterised many-body Hamiltonian that bridges Kohn-Sham and Hartree-Fock theory. This is written as[44]

$$\hat{\mathcal{H}}_\lambda = \sum_{i}^{\text{electrons}} \left[-\tfrac{1}{2}\hat{\nabla}_i^2 + v_\lambda \right] + \lambda \sum_{\substack{i=1,\\ j>i}}^{\text{electrons}} \hat{g}(i,j). \tag{2.56}$$

Note that $\hat{\mathcal{H}}_\lambda$ is dependent on a single parameter, $\lambda \in [0,1]$, which is sometimes called the coupling constant. $\hat{g}(i,j)$ is the two-electron electron-repulsion energy operator defined in Eq. 2.35 for Hartree-Fock theory.

When $\lambda = 1$ then the one-electron potential, $v_\lambda = \hat{v}_{\text{ext}}(\mathbf{r}_i)$, and $\hat{\mathcal{H}}_1$ is the Hartee-Fock Hamiltonian; this Hamiltonian applied to a Slater determinant will have an 'exact' exchange energy, E_{x}^{HF}, due to the determinant's antisymmetry. When $\lambda = 0$ then the one-electron potential is the Kohn-Sham non-interacting one-electron potential and $\hat{\mathcal{H}}_0$ is the Kohn-Sham Hamiltonian.

It follows that for every values of λ on the continuous interval $[0,1]$, by the first Hohenberg-Kohn theorem, we can establish a mapping between v_λ and the electron density, such that the eigenfunction of the Hamiltonian produces the ground-state density. In principle we can consider starting at the Kohn-Sham density and infinitesimally (adiabatically) reducing λ so that the ground-state density does not change. This is sometimes called the "adiabatic connection" and it is exploited in hybrid functionals that have been developed such as PBE0.[55] The PBE0 functional is based on the PBE functional and defines $\lambda = 1/4$. It has been shown to reproduce the molecular properties of heavy metals more effectively than many competing functionals[56–58] and it is the functional that this work favours.

In general, the exchange-correlation energy, $E_{\text{xc}}^{\text{hybrid}}$ for a hybrid functional is

$$E_{\text{xc}}^{\text{hybrid}} = E_{\text{xc}}^{\text{GGA}} + \lambda(E_{\text{x}}^{\text{HF}} - E_{\text{x}}^{\text{GGA}}), \tag{2.57}$$

where $E_{\text{xc}}^{\text{GGA}}$ and $E_{\text{x}}^{\text{GGA}}$ is the exchange-correlation and the exchange energy of the GGA.

2.11 Second quantisation

Second quantisation presents a more efficient technique for directly including the effects of the antisymmetry principle in the generation of wavefunctions. It is equivalent to building a Slater determinant, but allows a more concise notation for modifying such determinants. Defining a creation operator $\hat{\alpha}_i^\dagger$ that adds an occupied spin-orbital to the N-electron determinant, and can thereby create any determinant of a set of spin-orbitals from a vacuum state, $|vac\rangle = 1$, *i.e.*

$$\hat{\alpha}_i^\dagger|vac\rangle = |\alpha_i\rangle \tag{2.58}$$

This operator has the property that if it attempts to create a spin-orbital that is already present in the determinant, then the wavefunction is destroyed and no future operations are possible. similarly, a destruction operator α_i is defined that eliminates a spin-orbital from the determinant, *e.g.*

$$\hat{\alpha}_1|\alpha_1\alpha_2\cdots\alpha_N\rangle = |\alpha_2\cdots\alpha_N\rangle \tag{2.59}$$

similarly if the destruction operator attempts to delete a spin-orbital that is not present, then the wavefunction is destroyed. The two operators only affect the first column of the determinant, so the columns must be exchanged to allow their operation and maintain parity. Each column exchange switches the sign of the determinant, *e.g.*

$$\hat{\alpha}_3|\alpha_1\alpha_2\alpha_3\rangle = -\hat{\alpha}_3|\alpha_1\alpha_3\alpha_2\rangle = \hat{\alpha}_3|\alpha_3\alpha_1\alpha_2\rangle = |\alpha_1\alpha_2\rangle \tag{2.60}$$

An excited determinant, Ψ_r^a, can be generated from the original state, Ψ_0, by exciting an electron from the (occupied) a^{th} orbital to the (virtual) r^{th} orbital, *i.e.*

$$\Psi_r^a = (-1)^{r-a}\hat{\alpha}_r^\dagger\hat{\alpha}_a\Psi_0 \tag{2.61}$$

the parity term preserves the ordering of the determinant. This can be extended to produce doubly excited determinants, Ψ_{rs}^{ab}, triply excited determinants, Ψ_{rst}^{abc}, and higher excited terms only limited by the number of electrons and orbitals.

2.12 Configuration interaction (CI)

A fully correlated wavefunction, Φ_{FCI}, can be produced by forming a linear combination of the reference determinant and a series of excited determinants, to form the full configuration interaction (FCI) wavefunction:

$$\Phi_{FCI} = c_0\Psi_0 + \sum_{r>a}^{orbitals} c_a^r \Psi_a^r + \sum_{\substack{r>a,\\ s>b}}^{orbitals} c_{ab}^{rs} \Psi_{ab}^{rs} + \sum_{\substack{r>a,\\ s>b,\\ t>c}}^{orbitals} c_{abc}^{rst} \Psi_{abc}^{rst} + \ldots \tag{2.62}$$

where $c_0, c_a^r, c_{ab}^{rs}, c_{abc}^{rst}$ are the CI coefficients, constrained so the resultant wavefunction is normalised. This wavefunction can be modified variationally in these coefficients, so the lowest energy solution corresponds to the best wavefunction. The addition of excited states allows more correlation to be recovered via the exchange term, and in principle for an infinite basis set, the resulting wavefunction is exact within the non-relativistic Born-Oppenheimer approximation.[17]

Obviously this is not practical. Within a finite basis, using a fully expanded ansatz is referred to as a full CI calculation. Unfortunately, the number of determinants scales factorially; the number of determinants, $n_{\det}(N, M)$ that can be formed from N electrons in M orbitals (that allow double occupation) is given by the binomial theorem as;

$$n_{\det}(N, M) = \frac{(2M)!}{N!(2M-N)!}. \qquad M \leqslant N \tag{2.63}$$

this is also clearly impractical for all but the smallest molecules. To combat this, the expansion is typically truncated. For example, the CI single and double (CISD) technique uses the expansion to second order (only single and double excitations). It is not possible to only include the single excitations due to Brillouin's theorem: Singly excited determinants do not mix with the ground state Hartree-Fock wavefunction.[17]

One issue with truncated CI methods is that they are not size consistent (or extensive), *i.e.* the CI energy of a set of infinitely separated (and therefore non-interacting) molecules is not the same as the sum of their individual energies, and by extension, the CI energy does not scale with a number of identical non-interacting molecules. This is an artifact of the truncation; not all excitations in a single molecule are represented in the expanded system.

2.13 Perturbation theory

Perturbation theory offers a systematic method of improving the wavefunction and unlike configuration interaction it is size consistent, but it is no longer variational. The central idea is derived from the concept of a Taylor series. Consider a function, $f(x)$, that is perfectly smooth[†] at a point a. Then the Taylor series of this function about a is given by

$$f(x) = f(a) + \sum_{n=1}^{\infty} \frac{1}{n!} \left. \frac{\mathrm{d}^n f(x)}{\mathrm{d}x^n} \right|_{x=a} (x-a)^n \tag{2.64}$$

For conciseness, the n^{th} derivative of $f(x)$ at a is denoted by $f^{(n)}(a)$. Consider a perturbation operator $\Delta\hat{\mathcal{H}}$, with corresponding TISE given by

$$\hat{\mathcal{H}}_\lambda \Phi_\lambda = [\hat{\mathcal{H}} + \lambda \Delta\hat{\mathcal{H}}]\Phi_\lambda = E_\lambda \Phi_\lambda, \qquad \lambda \in (0,1) \tag{2.65}$$

where λ is a continuous parameter used to control the perturbation. Provided the perturbation is sufficiently small, that is less than the radius of convergence for the series, a convergent Taylor series can be formed about λ;

$$\Phi_\lambda = \Phi^{(0)}(0) + \sum_{n=1}^{\infty} \Phi^{(n)}(0) \frac{\lambda^n}{n!}. \tag{2.66}$$

By convention, the notation is simplified to

$$\Phi_\lambda = \Phi^{(0)} + \sum_{n=1}^{\infty} \Phi^{(n)} \lambda^n, \tag{2.67}$$

(where the $n!$ factorial terms have been absorbed). Similarly the energy of the perturbed system is

$$E_\lambda = E^{(0)} + \sum_{n=1}^{\infty} E^{(n)} \lambda^n \tag{2.68}$$

The next technique exploits the resolution of the identity (RI) property that applies to any finite orthonormal basis, $\{\phi\}$, that spans a Hilbert space. This is

$$\sum_{n=1}^{\text{basis}} |\phi_n\rangle\langle\phi_n| = \hat{\mathcal{I}} \tag{2.69}$$

[†] A function's smoothness at a point is measured by the number of continuous derivatives it has, a perfectly smooth function is infinitely differentiable.

where $\hat{\mathcal{I}}$ is an identity operator. Any observable must be representable by a Hermitian matrix, and the eigenvalues of a Hermitian[‡] matrix are always orthogonal. From this it can be shown that the infinite set of eigenfunctions from a Hartree-Fock calculation are orthonormal, and span L^2. Therefore

$$\left[\hat{\mathcal{H}} + \Delta\hat{\mathcal{H}}\right] |\Phi^{(0)}\rangle = E^{(0)} \left|\Psi_0^{(0)}\right\rangle + \sum_{n=1}^{\text{Excited states}} |\Psi^{(n)}\rangle\langle\Psi^{(n)}|\Delta\hat{\mathcal{H}}|\Phi^{(0)}\rangle. \tag{2.70}$$

From this the first order corrections can be derived

$$|\Phi^{(1)}\rangle = \sum_{n=1}^{\text{Excited states}} \frac{\left\langle \Psi_0^{(0)} \middle| \Delta H \middle| \Psi_n^{(0)} \right\rangle}{E_n - E_0^{(0)}}, \tag{2.71}$$

$$E_0^{(1)} = \left\langle \Psi_0^{(0)} \middle| \Delta H \middle| \Psi_0^{(0)} \right\rangle, \tag{2.72}$$

and higher order corrections can similarly be formed.

The Hellmann-Feynman theorem states that the first-order derivative of the energy with respect to a small, continuous perturbation is given by

$$E^{(1)} = \left[\frac{\partial E_\lambda}{\partial \lambda}\right] = \left\langle \Phi_\lambda \middle| \frac{\mathrm{d}\hat{\mathcal{H}}_\lambda}{\mathrm{d}\lambda} \middle| \Phi_\lambda \right\rangle. \tag{2.73}$$

This theorem has the significant advantage that it is not dependent on derivatives of the wavefunction and allows perturbation theory to model external perturbations, such as a magnetic field, $\mathbf{B}$. When there are two separate perturbations involved the technique can be further extended and this is called double perturbation theory, which is typically restricted to first order. The time independent sum-over-states expression for the contribution resulting from the first-order application of two perturbations is;[59]

$$\mathbb{E}^{(1,1)} = 2\ \text{Real} \left[\sum_{n=1}^{\text{Excited states}} \frac{\left\langle \Phi_n^{(0)} \middle| \hat{\mathcal{B}} \middle| \Phi_0^{(0)} \right\rangle \left\langle \Phi_n^{(0)} \middle| \hat{\mathcal{A}} \middle| \Phi_0^{(0)} \right\rangle}{E_n - E_0^{(0)}} \right] \tag{2.74}$$

Where $\hat{\mathcal{A}}$ and $\hat{\mathcal{B}}$ are the perturbing operators. This is equivalent to calculating a mixed derivative. One mixed derivative of particular interest is the Zeeman matrix (see Section 3.3) and it is given by the partial derivative of the energy with respect to the magnetic field and electronic spin in each cardinal direction, *i.e.* the $\mathbf{k}^{\text{th}}$ element of the matrix, $g_{\kappa\upsilon}$ is

$$g_{\kappa\upsilon} = \frac{1}{\mu_B}\left[\frac{\partial^2 E}{\partial B_\kappa\, \partial S_\upsilon}\right]. \tag{2.75}$$

[‡] The ij^{th} and ji^{th} elements of a Hermitian matrix satisfy $\sigma_{ij} = \sigma_{ji}^*$ where z^* is the conjugate of z.

2.13.1 Quasi-degenerate perturbation theory (QDPT)

A major drawback of using perturbation theory occurs when two states are degenerate (or nearly degenerate), *i.e.* $E_n \approx E_0^{(0)}$. The corresponding term in the Taylor series becomes unphysically large (or singular) and the calculation diverges. Quasi-degenerate perturbation theory (QDPT) addresses this by taking a manifold of states and constructing a matrix of their interactions. Consider a Hamiltonian, $\hat{\mathcal{H}}_S$, that contains a spin dependent operator and its operation on the following electronic states; two singlet states written as

$$|A;\ S=0\ m_s=0\rangle,\ |B;\ S=0\ m_s=0\rangle,$$

and two sets of triplet states written as

$$\begin{gathered}|A;\ S=1\ m_s=-1\rangle,\ |A;\ S=1\ m_s=0\rangle,\ |A;\ S=1\ m_s=1\rangle,\\ |B;\ S=1\ m_s=-1\rangle,\ |B;\ S=1\ m_s=0\rangle,\ |B;\ S=1\ m_s=1\rangle.\end{gathered}$$

Then introducing the notation for the matrix element between the A^{th} and B^{th} state with the labelled spin state:

$$\langle A;\ S=S_A\ m_s=m_{S_A}|\,\hat{\mathcal{H}}_S\,|B;\ S=S_B\ m_s=m_{S_B}\rangle = \left[\begin{array}{c|c|c}\mathbf{S}_A & \mathbf{A} & \mathbf{S}_B\\ m_{S_A} & \mathbf{B} & m_{S_B}\end{array}\right]. \tag{2.76}$$

If the Hamiltonian has the selection rule $|\delta m_s| \leqslant 1$, then the resulting matrix is partitioned as

$$\left(\begin{array}{cc|cc|cc|cc}
\left[\begin{array}{c|c|c}\mathbf{0}&\mathbf{A}&\mathbf{0}\\0&\mathbf{A}&0\end{array}\right] & 0 & \left[\begin{array}{c|c|c}\mathbf{0}&\mathbf{A}&\mathbf{1}\\0&\mathbf{A}&1\end{array}\right] & \left[\begin{array}{c|c|c}\mathbf{0}&\mathbf{A}&\mathbf{1}\\0&\mathbf{B}&1\end{array}\right] & \left[\begin{array}{c|c|c}\mathbf{0}&\mathbf{A}&\mathbf{1}\\0&\mathbf{A}&0\end{array}\right] & \left[\begin{array}{c|c|c}\mathbf{0}&\mathbf{A}&\mathbf{1}\\0&\mathbf{B}&0\end{array}\right] & \left[\begin{array}{c|c|c}\mathbf{0}&\mathbf{A}&\mathbf{1}\\0&\mathbf{A}&-1\end{array}\right] & \left[\begin{array}{c|c|c}\mathbf{0}&\mathbf{A}&\mathbf{1}\\0&\mathbf{B}&-1\end{array}\right]\\
0 & \left[\begin{array}{c|c|c}\mathbf{0}&\mathbf{B}&\mathbf{0}\\0&\mathbf{B}&0\end{array}\right] & \left[\begin{array}{c|c|c}\mathbf{0}&\mathbf{B}&\mathbf{1}\\0&\mathbf{A}&1\end{array}\right] & \left[\begin{array}{c|c|c}\mathbf{0}&\mathbf{B}&\mathbf{1}\\0&\mathbf{B}&1\end{array}\right] & \left[\begin{array}{c|c|c}\mathbf{0}&\mathbf{B}&\mathbf{1}\\0&\mathbf{A}&0\end{array}\right] & \left[\begin{array}{c|c|c}\mathbf{0}&\mathbf{B}&\mathbf{1}\\0&\mathbf{B}&0\end{array}\right] & \left[\begin{array}{c|c|c}\mathbf{0}&\mathbf{B}&\mathbf{1}\\0&\mathbf{A}&-1\end{array}\right] & \left[\begin{array}{c|c|c}\mathbf{0}&\mathbf{B}&\mathbf{1}\\0&\mathbf{B}&-1\end{array}\right]\\
\hline
\left[\begin{array}{c|c|c}\mathbf{1}&\mathbf{A}&\mathbf{0}\\1&\mathbf{A}&0\end{array}\right] & \left[\begin{array}{c|c|c}\mathbf{1}&\mathbf{A}&\mathbf{0}\\1&\mathbf{B}&0\end{array}\right] & \left[\begin{array}{c|c|c}\mathbf{1}&\mathbf{A}&\mathbf{1}\\1&\mathbf{A}&1\end{array}\right] & 0 & \left[\begin{array}{c|c|c}\mathbf{1}&\mathbf{A}&\mathbf{1}\\1&\mathbf{A}&0\end{array}\right] & \left[\begin{array}{c|c|c}\mathbf{1}&\mathbf{A}&\mathbf{1}\\1&\mathbf{B}&0\end{array}\right] & 0 & 0\\
\left[\begin{array}{c|c|c}\mathbf{1}&\mathbf{B}&\mathbf{0}\\1&\mathbf{A}&0\end{array}\right] & \left[\begin{array}{c|c|c}\mathbf{1}&\mathbf{B}&\mathbf{0}\\1&\mathbf{B}&0\end{array}\right] & 0 & \left[\begin{array}{c|c|c}\mathbf{1}&\mathbf{B}&\mathbf{1}\\1&\mathbf{B}&1\end{array}\right] & \left[\begin{array}{c|c|c}\mathbf{1}&\mathbf{B}&\mathbf{1}\\1&\mathbf{A}&0\end{array}\right] & \left[\begin{array}{c|c|c}\mathbf{1}&\mathbf{B}&\mathbf{1}\\1&\mathbf{B}&0\end{array}\right] & 0 & 0\\
\hline
\left[\begin{array}{c|c|c}\mathbf{1}&\mathbf{A}&\mathbf{0}\\0&\mathbf{A}&0\end{array}\right] & \left[\begin{array}{c|c|c}\mathbf{1}&\mathbf{A}&\mathbf{0}\\0&\mathbf{B}&0\end{array}\right] & \left[\begin{array}{c|c|c}\mathbf{1}&\mathbf{A}&\mathbf{1}\\0&\mathbf{A}&1\end{array}\right] & \left[\begin{array}{c|c|c}\mathbf{1}&\mathbf{A}&\mathbf{1}\\0&\mathbf{B}&1\end{array}\right] & \left[\begin{array}{c|c|c}\mathbf{1}&\mathbf{A}&\mathbf{1}\\0&\mathbf{A}&0\end{array}\right] & 0 & \left[\begin{array}{c|c|c}\mathbf{1}&\mathbf{A}&\mathbf{1}\\0&\mathbf{A}&-1\end{array}\right] & \left[\begin{array}{c|c|c}\mathbf{1}&\mathbf{A}&\mathbf{1}\\0&\mathbf{B}&-1\end{array}\right]\\
\left[\begin{array}{c|c|c}\mathbf{1}&\mathbf{B}&\mathbf{0}\\0&\mathbf{A}&0\end{array}\right] & \left[\begin{array}{c|c|c}\mathbf{1}&\mathbf{B}&\mathbf{0}\\0&\mathbf{B}&0\end{array}\right] & \left[\begin{array}{c|c|c}\mathbf{1}&\mathbf{B}&\mathbf{1}\\0&\mathbf{A}&1\end{array}\right] & \left[\begin{array}{c|c|c}\mathbf{1}&\mathbf{B}&\mathbf{1}\\0&\mathbf{B}&1\end{array}\right] & 0 & \left[\begin{array}{c|c|c}\mathbf{1}&\mathbf{B}&\mathbf{1}\\0&\mathbf{B}&0\end{array}\right] & \left[\begin{array}{c|c|c}\mathbf{1}&\mathbf{B}&\mathbf{1}\\0&\mathbf{A}&-1\end{array}\right] & \left[\begin{array}{c|c|c}\mathbf{1}&\mathbf{B}&\mathbf{1}\\0&\mathbf{B}&-1\end{array}\right]\\
\hline
\left[\begin{array}{c|c|c}\mathbf{1}&\mathbf{A}&\mathbf{1}\\-1&\mathbf{A}&-1\end{array}\right] & \left[\begin{array}{c|c|c}\mathbf{1}&\mathbf{A}&\mathbf{1}\\-1&\mathbf{B}&-1\end{array}\right] & 0 & 0 & \left[\begin{array}{c|c|c}\mathbf{1}&\mathbf{A}&\mathbf{1}\\-1&\mathbf{A}&0\end{array}\right] & \left[\begin{array}{c|c|c}\mathbf{1}&\mathbf{A}&\mathbf{1}\\-1&\mathbf{B}&0\end{array}\right] & \left[\begin{array}{c|c|c}\mathbf{1}&\mathbf{A}&\mathbf{1}\\-1&\mathbf{A}&-1\end{array}\right] & 0\\
\left[\begin{array}{c|c|c}\mathbf{1}&\mathbf{B}&\mathbf{1}\\-1&\mathbf{A}&-1\end{array}\right] & \left[\begin{array}{c|c|c}\mathbf{1}&\mathbf{B}&\mathbf{1}\\-1&\mathbf{B}&-1\end{array}\right] & 0 & 0 & \left[\begin{array}{c|c|c}\mathbf{1}&\mathbf{B}&\mathbf{1}\\-1&\mathbf{A}&0\end{array}\right] & \left[\begin{array}{c|c|c}\mathbf{1}&\mathbf{B}&\mathbf{1}\\-1&\mathbf{B}&0\end{array}\right] & 0 & \left[\begin{array}{c|c|c}\mathbf{1}&\mathbf{B}&\mathbf{1}\\-1&\mathbf{B}&-1\end{array}\right]
\end{array}\right)$$

Note that that in the absence of a spin operator, the states are orthonormal so matrix elements with the same spin are non-zero if and only if they are between the same state (*i.e.* on the diagonal), and its value is unchanged by the spin-dependent operator. The zero 2×2 blocks result from the selection rule.

2.14 The complete active space self-consistent field method

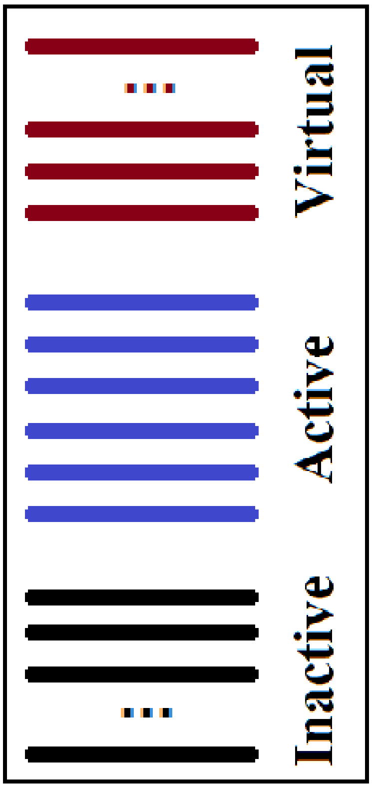

Figure 2.4: CASSCF partition

The complete active space SCF (CASSCF) method[60,61] is based on partitioning molecular orbitals into three sets (see Figure 2.4). Two sets are non-active orbitals, the inactive orbitals (black) and the virtual orbitals (red). The inactive orbitals are always doubly occupied and present in all determinants, the virtual orbitals are always unoccupied and absent in all determinants. The CASSCF wavefunction is built by combining the inactive orbitals, with every possible combination of the remaining n_{act} active electrons in the m_{act} active orbitals (blue). This is commonly referred to as a CASSCF(n_{act}, m_{act}) calculation.

The CASSCF wavefunction is a truncated full CI wavefunction, with only determinants that satisfy the prescribed orbital partition remaining. Like full CI, the calculation scales factorially, but with respect to the number of active electrons and orbitals instead of the full set, and therefore allows calculation for much larger systems. Nevertheless the number of determinants n_{DET} involved can be very large, and the resulting CASSCF matrix is a $n_{\text{DET}} \times n_{\text{DET}}$ real symmetric matrix. Instead of diagonalising the full matrix, iterative techniques such as the Davidson method[62] exist to find a smaller set of the lowest eigenvalues and corresponding eigenvectors. These are commonly referred to as roots. As a further complication, determinants may not match the space/spin symmetry of the system under investigation, and a set of configuration state functions, each formed from a linear combination of determinants, is used as a basis for the CI expansion.

The most important and subtle part of a CASSCF calculation is the selection of the active space. The simplest approach is to perform a UHF/UKS calculation and form the natural orbitals (by diagonalising the density matrix). From this occupation numbers can be calculated. As a rule of thumb, occupation numbers below 0.02 imply an unoccupied virtual orbital and above 1.98 imply a doubly occupied inactive orbital, so the remaining orbitals form the active space. However for multiconfigurational systems, single reference occupation numbers may be misleading and additional active orbitals may be needed.[63]

During the calculation both the molecular orbital coefficients and the CI coefficients are variationally optimised. It is necessary to choose which roots are used in this process. The natural choice is to use the lowest root (the ground CAS state), however often a set of degenerate (or near degenerate) roots more properly represent the ground state of the molecule, and as such the orbitals need to be optimised over these states. Such an approach is called state averaging. Furthermore many chemical properties, including the magnetic properties this work is interested in, depend on state energies and interactions; optimising for the ground state may lead to a poor description of important excited states. To account for this it is necessary to expand state averaging to include significant excited states. For a state-averaged calculation there is trade-off between the quality of orbital description of all included roots and the description of the ground state. It is possible to include weighting functions in the calculation to favour or exclude roots in the orbital optimisation process.

Because of its subtleties, CASSCF is not a black box technique and has some important disadvantages. It only includes dynamic correlation within the active space. This must be corrected perturbationally as discussed in the following section, it is highly dependent on the active space used, and because the optimisation process is inherently non-linear, it may optimise to a local energy minimum.[64] Furthermore SA-CASSCF is not necessarily size intensive.[65]

A CASSCF calculation without orbital optimisation is termed a CASCI (complete active space configuration interaction) calculation and can be useful to generate excited states without changing the optimised orbitals.

The RASSCF method

CASSCF is based on full CI and as such scales factorially with the size of the active space. This presents a significant barrier in the study of f-element compounds due to the increased number of orbitals that have canonical energies close together and may therefore be partially occupied and involved in multiconfigurational behaviour. Realistically either a truncated active space must be used, or the configurations produced during the CI process must be reduced. A compromise that features both approaches is called RASSCF (Restricted Active Space Self-Consistent Field). This technique partitions a larger active space into three smaller subsets. The lowest energy subset (RAS1) represents an extension of the active orbitals into the CASSCF inactive space, and consists of mostly doubly occupied orbitals. A fixed number of excitations are allowed out of this space. The next subset (RAS2) corresponds to the active orbitals of a CASSCF calculation. The final subset (RAS3) consists of largely vacant orbitals with a fixed number of electrons allowed into this space. This has the benefit of expanding the active space, but like CASSCF, this is not a black box technique. The additional partition of the active space into three subspaces introduces a further, subjective decision on the relative importance of orbitals that may hide unusual chemical behaviour.

2.14.1 ICE theory

Assessing the orbitals for inclusion in an active space requires chemical intuition, however such intuition is necessarily fallible. As a result we would like to assess and improve the quality of our active space. Ideally using an approach that concentrates on safely truncating the CI expansion without constraints on active orbital occupations. Such an approach is available in ORCA using the ICE (Iterative-Configuration Expansion) approach,[32] itself based on the CIPSI[†] technique.[66] This process scales polynomially instead of factorially with the size of active space.

ICE is based upon a partition of configuration space (here configurations can be thought of as a set of occupation numbers and maps to CSFs[32]) into a dominant (or

---

[†] Configuration Interaction by Perturbation with multiconfigurational zeroth-order wavefunctions Selected by Iterative process

generator) subspace, an interacting subspace and the remaining subspace. The latter does not significantly interact with the dominant subspace and is absent from the calculation.

It is also based on the observation that, for the non-relativistic Hamiltonian, states can only interact if they differ in orbital occupations by two electrons or less. The implication being that single and double excitations from the configurations of the dominant subspace can be used to form an interacting subspace covering the most important components of the wavefunction. Furthermore, any configuration that does not interact with the dominant subspace can safely be removed. Hence the ICE procedure can be described as follows:

1. A starting subspace of configurations subspace is formed.
2. Single and double excitations form the interacting subspace.
3. The interacting subspace is truncated using second order perturbation theory and the interaction with the starting dominant subspace.
4. The configuration interaction problem is solved using the dominant and interacting subspaces. This step is repeated until the energy converges using iteratively generated subspaces. *i.e.*
    (a) The new dominant subspace is formed (using the CI coefficients).
    (b) The new interacting subspace is formed from single and double excitations.
    (c) The interacting subspace is truncated (using the interaction with the dominant subspace).

The partition of the configuration space is iteratively defined by two thresholds. The first controls the cut-off for the CI coefficients to find the generators. The second controls the cut-off for the interaction with the dominant subspace to truncate the interacting subspace. The cut-offs that this work uses are discussed in the relevant chapter.

2.15 N-electron valence state perturbation theory

Unlike single reference perturbation theories such as MP2, N-electron valence state perturbation theory (NEVPT) starts from a multireference zero-order wavefunction such as that supplied by a CASSCF calculation, such as that represented by

$$\left|\Psi^{(0)}\right\rangle = \sum_{i}^{states} C_i \left|\Psi_i\right\rangle . \tag{2.77}$$

Directly applying QDPT to a CAS wavefunction produces divergent behaviour due to intruder state problems, and other perturbation approaches do not preserve size consistency; even CASPT2 only partially resolves the former by introducing shift techniques.[67] Thus NEVPT theory was developed to resolve this problem, preserving size consistency and ensuring that the wavefunction remains invariant to rotations of the active space.[68]

For simplicity, we'll consider single determinant reference states. If $\left|\Psi^{(0)}\right\rangle$ comes from a CAS calculation, it follows that this wavefunction already fully models the second-order interactions between electrons in the active space, *i.e.* those based on

$$\sum_{\substack{r>a,\\ s>b}}^{active} \hat{\alpha}_r^\dagger \hat{\alpha}_s^\dagger \hat{\alpha}_a \hat{\alpha}_b |\Psi_0\rangle. \tag{2.78}$$

However, consider two single reference states from the CAS calculation, $|\Psi_1\rangle$, $|\Psi_2\rangle$ which differ by two orbitals in the active space. Labelling the different orbitals, κ_i, υ_i, where i indicates which wavefunction contains the orbital, we can define a common determinant, $|l\rangle$ such that

$$|\Psi_1\rangle = \hat{\alpha}_{\kappa_1}^\dagger \hat{\alpha}_{\upsilon_1}^\dagger |l\rangle, \qquad |\Psi_2\rangle = \hat{\alpha}_{\kappa_2}^\dagger \hat{\alpha}_{\upsilon_2}^\dagger |l\rangle \tag{2.79}$$

It follows that if both states experience the same double excitation from the doubly occupied inactive (or core for clarity) orbitals in $|l\rangle$ to the active space[‖] then the interaction between the resulting pair of states will still differ by the same two active orbitals. These additional second-order interactions are not considered in CASSCF,[68] and the Slater-Condon rules[17] imply that two-electron operators acting on determinants differing by two orbitals may have non-zero integrals, so such interactions are

---

[‖] or experience the same double excitation from the active space to the virtual orbitals potentially important. The aim of NEVPT is to represent the effect of these interactions on the CASSCF wavefunction.

NEVPT introduces a "perturber function"[68–70] that is classified by the number of electrons exchanged from the non active space (*i.e.* doubly occupied and virtual orbitals) and the active space orbitals and a set of common determinants. For a single reference state, $|\Psi_{\text{single}}\rangle$, $S_l^{(2)}$ is the set of determinants which have had two electrons excited from the doubly occupied core orbitals to the active space, *i.e.*

$$S_l^{(2)} = \{\alpha_{\mathrm{r}}^{\dagger}\alpha_{\mathrm{s}}^{\dagger}\alpha_{\mathrm{a}}\alpha_{\mathrm{b}}|\Psi_{\text{single}}\rangle\} = \{\alpha_{\mathrm{r}}^{\dagger}\alpha_{\mathrm{s}}^{\dagger}\{|l\rangle\}\} \begin{cases} \forall a > b, & \text{core orbital} \\ \forall r > s, & \text{active space orbital} \end{cases} \tag{2.80}$$

and $S_l^{(-2)}$ is the corresponding set of determinants where two electrons are excited from the active space to the virtual space. If the full CASCSF wavefunction is then taken, then $S_l^{(2)}$ represents a subspace of the full CI wavefunction, based on a set of common determinants, $\{|l\rangle\}$, and all possible double excitations from the core to the active space. This can be generalised to $S_l^{(k)}$ for $k \geqslant 2$, but the commonly used approach, NEVPT2, limits the excitations to second order.

A full explanation of NEVPT2 is beyond the scope of this work, and details vary depending on the treatment of the zero-order Hamiltonian[71] and the truncation of the NEVPT2 space. Figure 2.5[68,72] shows the matrix representation of the NEVPT2 Hamiltonian used in three common approaches, differentiated by the level of truncation used: The totally uncontracted approach (UC-NEVPT) diagonalises the Hamiltonian over the entire space, while the most efficient "strongly-contracted" approach (SC-NEVPT) only produces a single representative function for each perturbation operator's action on each function in $|\Psi^{(0)}\rangle$, producing a subspace of S_l^k labelled $\tilde{S}_l^k$. Due to the resulting improved efficiency, this is the approach that is used in this work. Partially contracted approaches (PC-NEVPT) lie between these extremes.

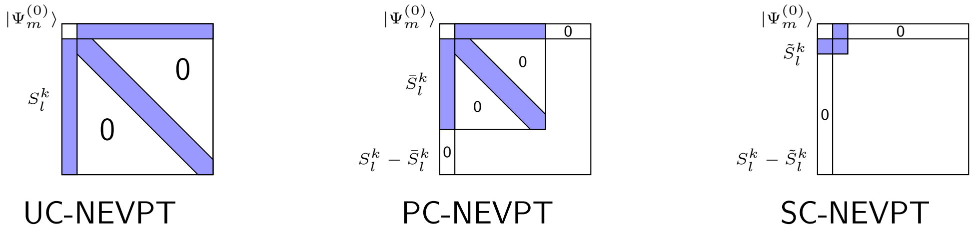

Figure 2.5: Truncation of the NEVPT2 matrix.[68]

2.16 Relativistic quantum chemistry

Considering an atom with nuclear charge, Z, and a single bound electron. The virial theorem states that two isolated particles bound only by a spherical potential with an inverse square dependence on their distance must satisfy

$$\langle T \rangle = -\tfrac{1}{2}\langle V \rangle, \tag{2.81}$$

where $\langle T \rangle$ and $\langle V \rangle$ are the average kinetic and potential energy respectively. The average total energy, $\langle E \rangle$, is therefore[39]

$$\langle E \rangle = \langle T \rangle + \langle V \rangle = \langle T \rangle - 2\langle T \rangle = -\langle T \rangle. \tag{2.82}$$

The energy of the n^{th} state is given by

$$E_n = -\frac{Z^2}{2n^2}\mu_{\mathrm{red}}, \qquad \mu_{\mathrm{red}} = \frac{m_e m_n}{m_e + m_n} \approx 1, \tag{2.83}$$

where m_{n} is the mass of the nucleus and μ_{red} is the reduced mass of the system. The latter can be approximated by unity since $m_{\mathrm{n}} \geqslant 1836 m_e$; the nucleus must contain at least one proton and the mass of the proton is $1836 m_e$. It follows that since $\langle T \rangle = \frac{1}{2} m_e \langle \dot{r}^2 \rangle$, the energy of the 1s orbital is given by

$$E_1 = \tfrac{1}{2}\langle \dot{r}^2 \rangle \approx -\tfrac{1}{2} Z^2. \tag{2.84}$$

This implies that, in the non-relativistic limit, the root-mean-square speed of this electron scales with the atomic number. The speed of light, c, is ≈ 137 (a.u.), hence for U^{91+}, the electron is predicted to be moving at 67% of the speed of light. This implies that the unshielded 1s electron in uranium is moving at an appreciable fraction of the speed of light.

Naively, chemistry seems to be determined by shielded valence electrons that experience weaker potential fields and move considerably more slowly than light, implying that relativistic effects can be safely neglected.[73] However relativistic effects on the innermost electrons of the actinides have a profound effect on their properties.

The relativistic mass of an electron, m_{rel}, is given by

$$m_{\text{rel}} = \frac{m_e}{\sqrt{1 - \dot{r}^2 c^{-2}}} = \frac{1}{\sqrt{1 - \dot{r}^2 \alpha^2}}, \tag{2.85}$$

where $\alpha = c^{-1}$ is the fine structure constant, originally introduced while studying atomic hydrogen spectra.[74] An electron moving at $0.67c$ would experience a 35% increase in mass. The average electron-nucleus distance is inversely proportional to its mass, which implies that the size of the uranium 1s orbital is reduced by 26%. This is in addition to the normal reduction due to the increased atomic charge: the non-relativistic expectation value of the nucleus-electron distance for a hydrogenic orbital with quantum numbers n, l, m is given by[75]

$$\langle r \rangle = \frac{1}{2Z}(2n^2 - l(l+1)). \tag{2.86}$$

Due to electron-electron repulsion, electrons in valence orbitals of a N-electron atom ($N \geqslant 3$) experience a smaller electrostatic potential from the nucleus, hence these electrons are said to be 'shielded' by the electrons in the core orbitals from the nucleus. An effective nuclear charge is often used to empirically model this effect.

All spherical hydrogenic AOs are orthogonal by construction, so they do not interact under the hydrogenic one-electron Hamiltonian. However the additional electron-electron repulsion term in the Hamiltonian for N-electron atoms means that the commonly used hydrogenic AOs are only a very good approximation to electronic behaviour. It is precisely this term that leads to screening and prevents analytic solutions.

The potency of the screening effect can be qualitatively assessed by examining the AO's radial distribution. Figure 2.6 shows the radial probability densities of the first four s orbitals of the hydrogen atom. Note all four orbitals have electronic density within 1 a.u. of the nucleus. The radial component of a ns orbital, R_{ns}, has the form[76]

$$R_{\text{ns}} = Z^{3/2} e^{-Zr} \sum_{i=0}^{n-1} a_i (Zr)^i, \tag{2.87}$$

where $a_i (\neq 0)$ are coefficients dependent on the orbital. This implies that, for all s orbitals, the electron density at the nucleus is non-zero (the angular component is isotropic). An orbital of angular momentum l has radial component, R_{nl}, with the form[76]

$$R_{nl} = Z^{3/2} e^{-Zr} \sum_{i=0}^{n-l-1} a_i (Zr)^{i+l}. \tag{2.88}$$

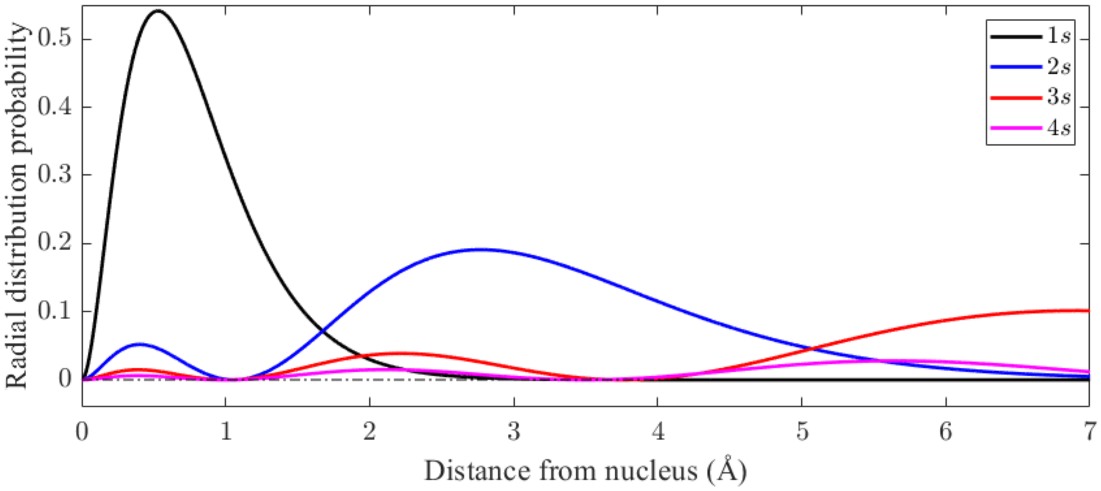

Figure 2.6: Radial probability density functions for the first four s orbitals of the hydrogen atom.

All terms are powers of r^l or higher, so for $l \geqslant 1$ there is no electron density at the nucleus. Therefore s orbitals penetrate the atom more deeply than orbitals with higher angular momentum, and shield electrons more effectively. The penetration and screening efficiency of orbitals decreases with increasing angular momentum. Overall s and p orbitals experience a relativistic contraction corresponding to a stabilisation of these orbitals. Conversely d and f orbitals experience increased screening from the contracted s and p orbitals,[77] leading to a relativistic expansion and are destabilised.

The relativistic stabilisation/destabilisation of AOs has profound effects on the later transition metals, the actinides and the lanthanides. As an example, gold has the electronic structure configuration [Xe] $4f^{14}5d^{10}6s^1$. The $6s$ orbitals are stabilised, but the $5d$ orbitals are destabilised. Therefore the $5d \rightarrow 6s$ transition energy is reduced and gold absorbs visible light. Relativistic effects are responsible for gold's unique colour.

A further complication of relativistic calculations is that the nature of linear transformations between reference frames (space/time coordinate systems) must be modified. Intuitively we are familiar with the Galilean framework where linear transformations between a starting reference frame $(\mathbf{r}, t)$ to a new reference frame $(\mathbf{r}', t')$ preserves relative motion. Such transformations are composed of up to three components, a translation, a rotation and a boost:[78]

Translation	$(\mathbf{r}, t) \rightarrow (\mathbf{r} + \mathbf{a}, t + \delta t)$	where $\mathbf{a}$ is a real constant vector and δt is a constant.
Rotation	$(\mathbf{r}, t) \rightarrow (\mathbf{R}\mathbf{r}, t)$	where $\mathbf{R}$ is a fixed rotation matrix.
Boost	$(\mathbf{r}, t) \rightarrow (\mathbf{r} + \mathbf{v}t, t)$	where $\mathbf{v}$ is a constant velocity.
General	$(\mathbf{r}, t) \rightarrow (R\mathbf{r} + \mathbf{v}t + \mathbf{a}, t + \delta t)$.	

The progression of time is always the same, only the starting time changes. Classical mechanics implicitly uses this reference frame and the metric for this space is simply the distance, r.

As an example, consider two observers in a vacuum each defining a reference frame, the first static and the second reference frame moving away from the first by a constant speed, v along the x-axis, *i.e.* a boost transformation exists between the two frames. Then consider a photon, observed from the static frame, moving at the speed of light, c, along the negative x-axis. According to the Galilean framework, the second observer should observe this photon moving at $c + v$.

The special theory of relativity implies that the speed of light in a vacuum is a constant and that this speed cannot be exceeded, so the second observation is impossible; it can only be accommodated if the progression of time is no longer the same in all reference frames. A transform consistent with this constraint is called a Lorentz transform and the quantity $(r^2 - c^2t^2)$ is constant through all frames, and acts as the measure of distance. Defining $\mathbf{s} = \{x, y, z, t\}$ the general transform is given by $(\mathbf{s}) \rightarrow (\mathbf{R}\mathbf{s} + \mathbf{s}_1)$ where $\mathbf{R}$ is a constant and real 4×4 matrix and $\mathbf{s}_1$ is a constant and real (x, y, z, t) vector. This implicitly puts the time coordinate on the same footing as the spatial coordinates.

The time dependent Schrödinger equation has a first-order derivative with respect to time, but second-order derivatives with respect to spatial coordinates. This implies that it is not invariant to a Lorentz transform,[78] which is required by the special theory of relativity. It is not Lorentz covariant.[**] Hence it cannot be used for relativistic calculations.

[**] covariance implies that it varies in correlation with a change in basis and contravariance implies a transformation in correlation with change of coordinates, the inverse of covariance.

The relativistic free electron energy, E_{rel}, of an electron with momentum, p, is given by the energy-momentum equation[78]

$$E_{\text{rel}} = \sqrt{m_e^4 c^4 + c^2 p^2}. \tag{2.89}$$

This represented a major development in physics since the square root term implies that there are two solutions, one positive and one negative, introducing the concept of 'anti-particles.' For the time-dependent Schrödinger equation, the energy operator is $-i\partial/\partial t$ and applying this gives the Klein-Gordon equation.[78]

$$i\frac{\partial}{\partial t}\Psi_{\text{rel}} = \left[\sqrt{-m_e^2 c^2 \boldsymbol{\nabla}^2 + c^4}\right]\Psi_{\text{rel}} \tag{2.90}$$

This equation can be written in Lorentz covariant form, but unfortunately applying this equation results in a wavefunction that cannot model probability density due to the second-order derivative with respect to time. Correcting this creates a symmetric wavefunction that does not obey the Pauli principle.[14,78–80] Feynmann showed that the equation could be employed to represent a spinless particle.[81]

The relativistic momentum of an electron is given by

$$p = \frac{\dot{r}}{\sqrt{1-\dot{r}^2}}, \tag{2.91}$$

and the energy of an electron in a potential V, in atomic units ($m_e = 1$), is

$$E = V + c^2\left[\sqrt{1 + p^2/c^2}\right]. \tag{2.92}$$

The form of this equation suggests that a Taylor series (See Eq. 2.64) may be used provided that p^2/c^2 is sufficiently small.[††] Rearranging Eq. 2.91 implies that provided that $\dot{r}^2 < \frac{1}{2}c^2$, $p^2/c^2 < 1$. Qualitatively, from Eq. 2.84 this is true for the expected momentum of the 1s orbitals of all known atoms (since we need $Z < c \approx 137$), although there will always be a small region around the nucleus where this does not apply.[82] Assuming this condition is met, the series is convergent and applying this gives

$$E = V + \tfrac{1}{2}p^2 - \frac{p^4}{8c^2} + c^2\sum_{n=3}^{\infty}(-1)^{n-1}\frac{(2n-3)!!}{2^n n!}\frac{p^{2n}}{c^{2n}}. \tag{2.93}$$

By inspection the first two terms are equivalent to the potential and non-relativistic kinetic energy respectively. The next term is called the mass-velocity term.[82] Provided

---

[††] The radius of convergence for the Taylor series of the generalised binomial expression, $(1+x)^r$ is well known[15] to be $|x| < 1, r \in \mathbb{R}$.

that p/c is small the remaining terms can be ignored. Furthermore, the p^4 term can produce non- L^2 functions, *i.e.* unphysical wavefunctions, so it is a poorly defined operator.[82]

2.16.1 The Dirac equation

The Lorentz covariance requirement and the difficulty of forming a physically suitable wavefunction prompted Dirac to explore a relativistic equation that was first order in both space and time coordinates.[14] The approach needed to find an operator $\hat{\mathcal{A}}$ equivalent to the square root operator, *i.e.*

$$\left[\hat{\mathcal{A}} \cdot \left\{\frac{\partial}{\partial x}, \frac{\partial}{\partial y}, \frac{\partial}{\partial z}, \frac{i}{c}\frac{\partial}{\partial t}\right\}\right]^2 \equiv \hat{\nabla}^2 - \frac{1}{c^2}\frac{\partial^2}{\partial t^2} = c^2. \tag{2.94}$$

The four-dimensional nature of the problem implied that the operator could be represented by a set of 4 × 4 matrices which can be expressed in terms of the 2 × 2 Pauli matrices, *i.e.*

$$\boldsymbol{\sigma}_x = \begin{pmatrix} 0 & 1 \\ 1 & 0 \end{pmatrix}, \quad \boldsymbol{\sigma}_y = i\begin{pmatrix} 0 & -1 \\ 1 & 0 \end{pmatrix}, \quad \boldsymbol{\sigma}_z = \begin{pmatrix} 1 & 0 \\ 0 & -1 \end{pmatrix}. \tag{2.95}$$

The Pauli matrices are a minimal basis of the SU(2) group (half-spin space). From the definition of the SU(2) group as the set of all complex unitary matrices with determinant +1, *i.e.*

$$\left\{\begin{pmatrix} ae^{i\theta_1} & be^{i\theta_2} \\ -be^{-i\theta_2} & ae^{-i\theta_1} \end{pmatrix} : \quad a, b \in [-1, 1], \theta_1, \theta_2 \in [-\pi, \pi), a^2 + b^2 = +1\right\}, \tag{2.96}$$

it follows that each member has three independent parameters (four parameters, one constraint) so it follows that their basis needs at least three elements. The spinors for a single electron are eigenvectors of the spin-squared matrix $\mathbf{s}^2 = \frac{\mathbf{1}}{\mathbf{2}}\boldsymbol{\sigma} \cdot \frac{\mathbf{1}}{\mathbf{2}}\boldsymbol{\sigma}$, and spin-$z$ matrix $\mathbf{s}_z = \frac{1}{2}\boldsymbol{\sigma}_z$ and behave as members of SU(2), but are not a basis for it. Rotation in this space is complex and represented by $e^{-i\theta/2}$, so a 4π rotation is needed to return the spinor to its original orientation (see Section 2.1).

Dirac derived the following equation[14] that satisfies the covariance requirement:[78]

$$E\Psi = i\frac{\partial \Psi}{\partial t} = \left[\mathbf{B}c^2 + c\sum_{\mathbf{k}}^{\{x,y,z\}} A_\kappa \frac{\partial}{\partial \kappa}\right]\Psi = [Bc^2 + c\mathbf{A} \cdot \hat{\boldsymbol{\nabla}}]\Psi, \tag{2.97}$$

where $\mathbf{A}$ and $\mathbf{B}$ are built from the Pauli matrices and a combination of identity and zero matrices

$$\mathbf{A_k} = \begin{pmatrix} \mathbf{0}_2 & \boldsymbol{\sigma}_\mathbf{k} \\ \boldsymbol{\sigma}_\mathbf{k} & \mathbf{0}_2 \end{pmatrix}, \qquad \mathbf{B} = \begin{pmatrix} \mathbf{I}_2 & \mathbf{0}_2 \\ \mathbf{0}_2 & -\mathbf{I}_2 \end{pmatrix}. \tag{2.98}$$

This implies that the wavefunction has a vector form, referred to as a 4-spinor, and can be split into two components, each consisting of a two component vector. The most significant part, $\boldsymbol{\Psi}^+$, corresponds to the positive energy solutions, the other part, $\boldsymbol{\Psi}^-$ corresponds to negative energy solutions. Early theories postulated the existence of an (infinite) sea of electrons in the negative energy levels which were unobservable.[83] However, it was a major advance in physics as it accurately predicted the existence of anti-matter, in this case positrons, the anti-particle equivalent of electrons. This success comes at a price, attempting to solve Dirac's equation variationally fails as it finds positronic solutions, of which there are infinitely many. Therefore the Dirac equation does not have a lower bound. This effect is called variational collapse. Restricting the wavefunction can alleviate this[39] but at significant computational expense.

For quantum chemistry the components of the positive energy solutions had profound implications: they represent α and β spin solutions and this was the first rationalisation of electron spin, previously only added to the Schrödinger ansatz to accommodate observations. Spin is a natural consequence of the Dirac formulation.

Ultimately it is the positive energy solutions that are of interest to chemists and the structure of the matrix as consisting of blocks of submatrices suggest that it might be possible to approximate the calculation by factorising the matrices into the electron and positron solutions, called the Pauli approximation. Furthermore for consistency it is necessary to reflect that the energy datum for the electron in a relativistic framework is given by Einstein's mass-energy equivalence equation,[84] $E = m_e c^2$, which is achieved by subtracting 1 from the diagonal elements of $\mathbf{B}$ (Eq. 2.98). Adding a nuclear-attraction operator and factorising the Dirac equation gives two coupled equations[39]

$$\left[\hat{\mathcal{V}}^{\text{nuc.att.}} \begin{pmatrix} 1 & 0 \\ 0 & 1 \end{pmatrix} + c^2 \begin{pmatrix} 0 & 0 \\ 0 & -2 \end{pmatrix} + ic\boldsymbol{\sigma}_\kappa \cdot \hat{\nabla}_\kappa \begin{pmatrix} 0 & 1 \\ 1 & 0 \end{pmatrix}\right] \begin{pmatrix} \Psi^+ \\ \Psi^- \end{pmatrix} = E \begin{pmatrix} \Psi^+ \\ \Psi^- \end{pmatrix}, \tag{2.99}$$

solving this gives the Pauli Hamiltonian expressible as a combination of a non-relativistic Hamiltonian, $\hat{\mathcal{H}}^{\text{non.rel.}}$, and three relativistic corrections

$$\hat{\mathcal{H}}^{\text{Pauli}} = \hat{\mathcal{H}}^{\text{non.rel.}} + \sum_{i}^{\text{electrons}} \hat{\mathcal{H}}_i^{\text{MV}} + \left[\sum_{A}^{\text{nuclei}} \hat{\mathcal{H}}_{iA}^{\text{Darwin}} + \hat{\mathcal{H}}_{iA}^{\text{SOC}} \right]. \tag{2.100}$$

The $\hat{\mathcal{H}}^{\text{MV}}$ term is the mass-velocity correction (see Eq. 2.93). The $\hat{\mathcal{H}}^{\text{Darwin}}$ term is a correction for the very rapidly moving electrons near the nucleus, called the Darwin term, and is proportional to the Dirac delta function, which can make its use problematic.[82] Finally the $\hat{\mathcal{H}}^{\text{SOC}}$ term is the spin-orbit coupling correction and is proportional to the cube of the inverse distance $1/r_A^3$ and $\mathbf{l} \cdot \mathbf{s}$. Due to these additional terms the Pauli approximation is not variational and becomes ineffective when spin-orbit coupling is strong.

Unfortunately the Dirac equation is limited to one-electron systems. Adding the standard non-relativistic electron-electron repulsion term, $\hat{\mathcal{V}}^{\text{e.rep.}}$ to the Dirac equation gives the Dirac-Coulomb equation.

$$\left[\hat{\mathcal{V}}^{\text{nuc.att.}} + \hat{\mathcal{V}}^{\text{e.rep.}} + \mathbf{B}c^2 + ic\mathbf{A} \cdot \hat{\boldsymbol{\nabla}} \right] \Psi = E\Psi. \tag{2.101}$$

The repulsion term is simply the sum of the two electron repulsion operator, $\hat{g}_{ij} = r_{ij}^{-1}$ (see Eq. 2.35), over all unique electron pairs. Unfortunately this term is not correct in a relativistic framework, since electron-electron interaction is not instantaneous, the repulsion cannot exceed the speed of light and is therefore delayed in a relativistic framework. An additional operator derived by Darwin[85] was adjusted leading to the Breit operator,[39] $\hat{\mathcal{V}}^{\text{Breit}}$, which acts as a relativistic correction to the two-electron energy. The overall equation is called the Dirac-Coulomb-Breit equation:

$$\left[\hat{\mathcal{V}}^{\text{nuc.att.}} + \hat{\mathcal{V}}^{\text{e.rep.}} + \hat{\mathcal{V}}^{\text{Breit}} + \mathbf{B}c^2 + ic\mathbf{A} \cdot \hat{\boldsymbol{\nabla}} \right] \Psi = E\Psi. \tag{2.102}$$

An alternative approach to reducing the four-component Dirac equation to two component form is to try to find a unitary transformation, $\mathbf{U}$, that converts the Dirac equation to block diagonal form, *i.e.* representing the matrix form of the Dirac operator as $\mathbf{D}$, then the transformation must satisfy

$$\mathbf{D}^{\text{BD}} = \mathbf{U}\mathbf{D}\mathbf{U}^{\dagger} = \begin{pmatrix} \mathbf{D}^{+} & \mathbf{0}_2 \\ \mathbf{0}_2 & \mathbf{D}^{-} \end{pmatrix} \qquad \mathbf{U}\mathbf{U}^{\dagger} = \mathbf{I}_2. \tag{2.103}$$

The Foldy-Wouthuysen transformation,[86] which when applied to the Dirac-Coulomb-Breit Hamiltonian, allows the formation of the Breit-Pauli equation.[87]

$$\left[\hat{\mathcal{H}}^{\text{Pauli}} + \sum_{i,j}^{\text{Unique electron pairs}} \hat{\mathcal{g}}_{ij}^{\text{BP2}}\right]\Psi = E\Psi. \tag{2.104}$$

where $\hat{\mathcal{g}}^{\text{BP2}}$ is a combination of additional operators that represent spin/same orbital, spin/other orbital, spin/spin and orbital/orbital angular momentum interactions and an additional, two electron Darwin term proportional to $\delta(r_{ij})$. The majority of the coupling terms have an inverse-cube dependent term (r_{ij}^{-3}), however the spin-spin coupling term has a $\delta(r_{ij})$ and shorter-range (r_{ij}^{-5}) term, and the orbital/orbital term has a longer range $\delta(r_{ij}^{-1})$ term. In practice the spin-orbit terms are the most significant,[88,89] so a truncated form of the operator that only includes these terms is often used.

2.16.2 The zeroth order regular approximation (ZORA)

The divergence of the expansion (Eq. 2.93) for electrons that are very close to the nucleus led to the development of an alternative 'regular' approximation (ZORA), valid for any momentum, and in particular to the zeroth order regular approximation. Introducing a shorthand $K = 2c^2 - V$, the new expansion assumes that the energy is less than K which is true in all Coulombic potentials[82] and rearranges Eq. 2.92, with a change of datum, from

$$E = \sqrt{c^4 + p^2c^2} + V - c^2 = \sqrt{c^4 + p^2c^2} - K + c^2 \tag{2.105}$$

to

$$E = \frac{p^2c^2}{K(1 + E/K + V)}. \tag{2.106}$$

This quadratic form gives an additional negative energy solution which can be discarded.[82] Expanding this in $K/E < 1$ gives a zeroth order expression

$$E_0 = \frac{p^2c^2}{2c^2 - V} + V, \tag{2.107}$$

and an improved expression can be obtained by expanding in $(2c^2 - 2V)/E < 1$, representing a reduced perturbation. The four component form can then be reduced to a two-component form via the Foldy-Wouthuysen transformation.

$$\hat{\mathcal{H}}^{\text{ZORA}} = V + \boldsymbol{\sigma} \cdot \hat{p} \left(\frac{c^2}{K}\right) \boldsymbol{\sigma} \cdot \hat{p}. \tag{2.108}$$

Despite being zeroth order this Hamiltonian is relativistic and efficiently corrects for the regions close to nucleus[78] without containing the problematic singularity introduced by the Darwin term. The approximation can also be used variationally. However by introducing a non-linear dependence on the potential, it is not gauge-invariant. Atomic ZORA (aZORA)[27] is a version of ZORA that transforms the one-electron Hamiltonian in atomic blocks, minimising this problem. It is used for all geometry optimisations in this work.

2.16.3 Douglas-Kroll-Hess theory

The block diagonal form of the Dirac equation (Eq. 2.78) can be expressed as an infinite expansion of terms of the Coulomb potential, V,[78] Douglas-Kroll-Hess theory is based on performing a potentially infinite series of unitary transforms of the Dirac equation, each of which is designed to sequentially reduce off-diagonal terms in the potential. In principle, for an infinite series of these transformations, the technique is exact. The first order DKH Hamiltonian is given by[90]

$$\hat{\mathcal{H}}^{(1)}_{\mathrm{DKH}} = \sum_i E_p - c^2 + A_p \hat{\mathcal{V}} A_p + A_p R_P (\boldsymbol{\sigma} \cdot \mathbf{p}) \hat{\mathcal{V}} (\boldsymbol{\sigma} \cdot \mathbf{p}) A_p R_P \tag{2.109}$$

where E_p is the relativistic kinetic energy and A_p and R_p are kinetic operators. To correctly model these terms the matrix elements need to be transformed into momentum space. This is achieved by diagonalising the non-relativistic kinetic energy to obtain the momentum eigenvalues. Following the evaluation of the DKH Hamiltonian in momentum space, the operators are back transformed to position space. The technique has the virtue of collecting all spin-free relativistic correction terms and unlike ZORA, as it starts from a linear potential, it is gauge-invariant. It has been described as “much cleaner” than the regular Hamiltonian.[32] For this reason it is our preferred scalar-relativistic Hamiltonian.

Chapter 3

Magnetism

The force, $\mathbf{F}$, on a charge, q, moving at velocity, $\dot{\mathbf{r}}$, in an electric field, $\mathbf{E}$, and a magnetic field, $\mathbf{B}$, is called the Lorentz force. In SI units it is given by

$$\mathbf{F} = q\left(\mathbf{E} + \dot{\mathbf{r}} \times \mathbf{B}\right), \tag{3.1}$$

and this acts as a practical definition for the two fields. The underlying mathematical basis for magnetism can be derived from the charge continuity equation (Eq. 3.2) in conjunction with the four Maxwell equations (Eqs. 3.3–3.6), which are briefly stated below.[91] The continuity equation states that in the absence of an electric current density, $\mathbf{J}$, (defined over a surface), charge is conserved, *i.e.*

$$\hat{\boldsymbol{\nabla}} \cdot \mathbf{J} = -\frac{\partial q}{\partial t}. \tag{3.2}$$

Gauss's two laws imply that charge is the monopolar source of electric fields, but no monopolar source of magnetism exists. These equations are

$$\hat{\boldsymbol{\nabla}} \cdot \mathbf{E} = \frac{q}{\epsilon_0}, \tag{3.3}$$

$$\hat{\boldsymbol{\nabla}} \cdot \mathbf{B} = 0. \tag{3.4}$$

Faraday's Law and the Ampère-Maxwell law quantify the interaction between changing electric and magnetic fields. These equations are

$$\hat{\boldsymbol{\nabla}} \times \mathbf{E} = -\frac{\partial \mathbf{B}}{\partial t}, \tag{3.5}$$

$$\hat{\boldsymbol{\nabla}} \times \mathbf{B} = \mu_0 \mathbf{J} + \epsilon_0 \mu_0 \frac{\partial \mathbf{E}}{\partial t}. \tag{3.6}$$

where ϵ_0 and μ_0 are the dielectric permittivity and magnetic permeability (of a vacuum) respectively. From these it can be shown that both the electric and magnetic field can be uniquely defined by the scalar potential, ϕ_{scalar}, and the vector potential $\mathbf{A}_{\text{vector}} = (A_x, A_y, A_z)$, encapsulating magnetic behaviour within these four functions of position and time,

$$\mathbf{E} = -\hat{\nabla}\phi_{\text{scalar}} - \frac{1}{c}\frac{\partial \mathbf{A}_{\text{vector}}}{\partial t}, \qquad \mathbf{B} = \hat{\boldsymbol{\nabla}} \times \mathbf{A}_{\text{vector}}. \tag{3.7}$$

Because these are differential equations, both **E** and **B** are defined with respect to the position of a gauge, this being conceptually equivalent to a constant of integration. The scalar and vector potentials are examples of gauge potentials.[78]

Current is the motion of charged particles, and the motion of protons and electrons in an electric field generates a magnetic field. In all molecules, the application of an external magnetic field induces an opposing magnetic field. This correlates with the macroscale effect of inducing a current by moving a magnet near a coil. This diamagnetic effect causes the molecule to be weakly repelled from the field.

However, the spin angular momentum of an unpaired electron generates a magnetic field as does any overall orbital angular momentum. As a result, most molecules with unpaired electrons have a magnetic dipole moment that will align with an applied field. This paramagnetic effect causes the molecule to be weakly attracted to the field.[*]

In a closed shell molecule, the paring of electrons results in no net magnetic dipole so there is no paramagnetic effect. Such compounds are called diamagnetic. While most open shell molecules experience both effects, the paramagnetic effect dominates. This work studies these paramagnetic molecules.

---

[*] Ferromagnetism is a macroscopic effect creating a permanent magnetic field and results from a field-free alignment of these dipoles. It is associated with materials consisting of atoms or molecules with multiple unpaired electrons and having large Pauli-exchange energies.

3.1 Angular momentum and irreducible tensor operators (ITOs)

Considering the spin-operator, $\hat{\mathcal{S}}^2$ and the set of first-order cartesian spin-operators $\hat{\boldsymbol{\mathcal{S}}} = \{\hat{\mathcal{S}}_x, \hat{\mathcal{S}}_y, \hat{\mathcal{S}}_z\}$, then a spin-eigenfunction, $|S, m_S\rangle$, must satisfy

$$\hat{\mathcal{S}}^2|S, m_S\rangle = S(S+1)|S, m_S\rangle, \quad \text{and} \tag{3.8}$$

$$\hat{\mathcal{S}}_z|S, m_S\rangle = m_s|S, m_S\rangle. \tag{3.9}$$

The spin-operators $\hat{\mathcal{S}}_x$ and $\hat{\mathcal{S}}_y$ do not commute with $\hat{\mathcal{S}}_z$. The commutators of the cartesian spin-operators are

$$\left[\hat{\mathcal{S}}_x, \hat{\mathcal{S}}_y\right] = i\hat{\mathcal{S}}_z, \quad \left[\hat{\mathcal{S}}_y, \hat{\mathcal{S}}_z\right] = i\hat{\mathcal{S}}_x, \quad \left[\hat{\mathcal{S}}_z, \hat{\mathcal{S}}_x\right] = i\hat{\mathcal{S}}_y \tag{3.10}$$

For a given S, the spin matrices in a basis of $\{|S, m_s = -S\rangle, ..., |S, m_s = -S\rangle\}$ eigenfunctions can be constructed via the equations[92]

$$\left\langle m_s = m_1|\hat{\mathcal{S}}_x|m_s = m_2\right\rangle = \tfrac{1}{2}\left(\delta_{m_1,m_2+1} + \delta_{m_1+1,m_2}\right)\sqrt{S(S+1) - m_1 m_2} \tag{3.11}$$

$$\left\langle m_s = m_1|\hat{\mathcal{S}}_y|m_s = m_2\right\rangle = \tfrac{1}{2i}\left(\delta_{m_1,m_2+1} - \delta_{m_1+!,m_2}\right)\sqrt{S(S+1) - m_1 m_2} \tag{3.12}$$

$$\left\langle m_s = m_1|\hat{\mathcal{S}}_y|m_s = m_2\right\rangle = \delta_{m_1,m_2} m_1 \tag{3.13}$$

where the S label has been dropped for conciseness. The cartesian spin operators are related to the first order spherical spin-operators $\{\hat{\mathcal{S}}^{(1)}_\kappa : \kappa = -1, 0, 1\}$, via

$$\hat{\mathcal{S}}^{(1)}_1 = \hat{\mathcal{S}}_x + i\hat{\mathcal{S}}_y, \tag{3.14}$$

$$\hat{\mathcal{S}}^{(1)}_0 = \hat{\mathcal{S}}_z, \tag{3.15}$$

$$\hat{\mathcal{S}}^{(1)}_{-1} = \hat{\mathcal{S}}_x + i\hat{\mathcal{S}}_y. \tag{3.16}$$

$\hat{\mathcal{S}}^{(1)}_1$ and $\hat{\mathcal{S}}^{(1)}_{-1}$ are sometimes called ladder operators. The spherical spin operators are examples of irreducible tensor operators which are discussed in the following section. There are differing definitions of these operators, largely based on whether the underlying Wigner-Eckart theorem (section 3.1.1) uses Wigner-3j or Clebsch-Gordon coefficients; readers are advised to check which convention is being used.

3.1.1 Tensors and tensor operators

The effect of applying a rotation matrix to any three-dimensional vector is equivalent to rotating a position vector.[93†] This idea can be extended to multi-index arrays, such as a matrix with two-indices and to N-dimensional vectors. A rank k tensor of dimension N is a k-index array which transforms under rotation according to the rules corresponding to the transformation of a position vector in real space.[94] A scalar is a rank 0 tensor, and all vectors are rank 1 tensors, however not all matrices are tensors because of the rotational transformation requirement.

The underlying basis for the N-dimensional vector space determines the form a given tensor.[95] This work will assume for simplicity that the basis is orthonormal. By definition, a rank-one tensor $\mathbf{T}$, upon rotation represented by orthogonal matrix $\mathbf{R}$ must satisfy

$$\mathbf{T}'_\kappa = \sum_i \mathbf{R}_{\kappa i} T_i, \tag{3.17}$$

and a rank-two tensor $\mathbf{T}$ must satisfy

$$\mathbf{T}'_{\kappa\upsilon} = \sum_{ij} \mathbf{R}_{\kappa i} \mathbf{R}_{\upsilon j} T_{ij} = \left[\mathbf{R}^T \mathbf{T} \mathbf{R}\right]_{\kappa\upsilon} \tag{3.18}$$

A rank-k tensor operator $T^{(k)}$ is an operator that obeys the same transformation rules.[96] Tensors using a cartesian basis are called cartesian tensors, and tensors using a spherical basis are called spherical tensors. An important distinction is that a rank 2 cartesian tensor has nine elements (*i.e.* $xx, xy, xz, yx, yy, xz, yz, zz$), six of which are unique, allowing it to be represented by a symmetric 3×3 matrix, whereas a rank 2 spherical tensor has five elements (*i.e.* $-2, -1, 0, 1, 2$). It must be possible to form a tensor in either basis, so it follows that cartesian tensors of rank $\geqslant 2$ are reducible. It can be shown that spherical tensors are not, and as a result they are a common form of irreducible tensor operators (ITOs). The spin-operator can be thought of as a rank-1 spherical tensor operator.

There are many different forms that have been used for the spin-operators, and large numbers of notational forms exist.[97] This work will use angular momentum operators which transform in the same way as spherical tensors, as first suggested by Buckmaster[98] and codified by Smith and Thornley.[99]

[†] A earlier version of section 3.1.1 and 3.1.2 appeared in the Author's MPhil Thesis.

Generating higher order tensors can be achieved using Theorem (3.10.27) of Sakurai's work,[96] specifically

$$\hat{\mathcal{T}}^{(k)}_q = \sum_{q_1}^{-k_1 ... k_1} \quad \sum_{q-q_1}^{-k_2 ... k_2} \langle k_1, k_2; q_1, q_2 | kq \rangle \hat{\mathcal{T}}^{(k_1)}_{q_1} \hat{\mathcal{T}}^{(k_1)}_{q_2}$$

where $\langle k_1 k_2; q_1 q_2 | kq \rangle$ is a Clebsh-Gordon coefficient. This coefficient is zero if $k \neq k_1 + k_2$ or $q \neq q_1 + q_2$. By using this relationship and other properties of the coefficients, it can be shown that $\hat{\mathcal{T}}^{(k)}_k = \langle k-1, 1; q-1, 1 | kq \rangle \hat{\mathcal{T}}^{(k-1)}_{k-1} \hat{\mathcal{T}}^{(1)}_1$. In this work we are interested in rank k spin tensors. Using $\mathbf{S}^{(k)}$ as the matrix representation of the spin tensor $\hat{\mathcal{S}}^{(k)}$ for a spin S in the basis $|S, -S\rangle \dots |S, S\rangle$. then for $k > 2S$, $\mathbf{S}^{(k)}_q = \mathbf{0}$. However for all other k, the $\mathbf{S}^{(k)}_k$ matrix can be calculated. This enables the remaining $\mathbf{S}^{(k)}_q$ matrix representations to be calculated using the Wigner-Eckhart theorem as outlined in the following subsection.

3.1.2 The Wigner-Eckart theorem

The Wigner-Eckart theorem allows the expression of individual matrix elements of rank k spherical tensor operators $\hat{\mathcal{T}}^k_q$ in a space-spin eigenfunction basis, (*i.e.* the CI wavefunctions) as a product of a spin-independent term called the reduced matrix element (RME) and an operator-independent term. It is expressed as[87]

$$\left\langle A(S_A, M_A) | \hat{\mathcal{T}}^k_q | B(S_B, M_B) \right\rangle = (-1)^{S_A - M_A} \omega^{S_A, k, S_B}_{-M_A, q, M_B} \langle A(S_A) \| T^k \| B(S_B) \rangle \tag{3.19}$$

where $\omega^{S_A, k, S_B}_{M_A, q, M_B}$ is a Wigner-3j symbol, an operator-independent term that only depends on the quantum numbers. It is more commonly written in the less compact notation

$$\omega^{S_A, k, S_B}_{-M_A, q, M_B} \equiv \begin{pmatrix} S_A & k & S_B \\ -M_A & q & M_B \end{pmatrix} \tag{3.20}$$

The Wigner-3j selection rules and associated symmetries[100] make the computational use of Wigner-Eckart theory easier to implement and use than the more commonly known Clebsch-Gordon coefficients $\langle S_A k M_A q | S_A k S_B M_B \rangle$, which they are related to via

$$\langle S_A k M_A q | S_A k S_B M_B \rangle = (-1)^{S_A - k - M_B} \sqrt{1 + 2S_B} \begin{pmatrix} S_A & k & S_B \\ -M_A & q & M_B \end{pmatrix} \tag{3.21}$$

3.2 The Zeeman effect

The spectral lines from a sodium flame split when that flame is exposed to an external field.[101] This effect results from interactions between the field and the atom's magnetic dipole moment, the latter split into orbital and spin moments and it can be used to study the coupling between the two.

Considering the ground state of the sodium atom. In the absence of a magnetic field, this consists of two degenerate states, $m_s = \{|-\frac{1}{2}\rangle, |\frac{1}{2}\rangle\}$. This is consistent with Kramers' theorem which states that the energy levels of any system with an odd number of fermions are at least doubly degenerate in the absence of a magnetic field. Such a pair of states is called a Kramers' pair.[78] When a magnetic field, $\mathbf{B}$, is applied to this atom, the degeneracy is lifted, and the effect on the energy levels is given by the Hamiltonian,

$$\hat{\mathcal{H}}_{Zeeman}|\tfrac{1}{2}\rangle = -\mathbf{B} \cdot \hat{\boldsymbol{\mu}}|\tfrac{1}{2}\rangle, \tag{3.22}$$

where $\hat{\boldsymbol{\mu}}$ is the electronic magnetic moment operator for the atom. For a system with total angular momentum operator, $\hat{\mathcal{J}}$, the magnetic moment operator is given by[102]

$$\hat{\boldsymbol{\mu}} = \mu_B g \hat{\boldsymbol{\mathcal{J}}}, \tag{3.23}$$

where $\mu_B = e\hbar/m_e = \frac{1}{2}$ is the Bohr magneton and g is called the g-factor, a dimensionless constant of proportionality. The g-factor for an isolated electron, denoted g_e, is predicted via Dirac's equation to be 2, however extremely precise experiments showed the actual value to be 2.0023193043617(152)[103,104] The deviation from two corresponds to quantum electrodynamics corrections. For a system where there is no orbital angular momentum, the Hamiltonian can be explicitly written as

$$\hat{\mathcal{H}}_{Zeeman} = -\mu_B \mathbf{B} \cdot \mathbf{g} \cdot \hat{\boldsymbol{\mathcal{S}}} = -\mu_B \begin{bmatrix} B_x & B_y & B_z \end{bmatrix} \begin{bmatrix} g_{xx} & g_{xy} & g_{xz} \\ g_{yx} & g_{yy} & g_{yz} \\ g_{zx} & g_{zy} & g_{zz} \end{bmatrix} \begin{bmatrix} \hat{S}_x \\ \hat{S}_y \\ \hat{S}_z \end{bmatrix}, \tag{3.24}$$

where the matrix that couples the spin to the magnetic field is often called the "g-tensor." This unfortunate terminology is discussed in Section 3.7.1, and it will be referred to as the Zeeman matrix from this point forward.

For a bound electron, the magnetic moment operator is given by

$$\hat{\boldsymbol{\mu}} = \mu_B(g_l \hat{\boldsymbol{\mathcal{L}}} + g_e \hat{\boldsymbol{\mathcal{S}}}), \tag{3.25}$$

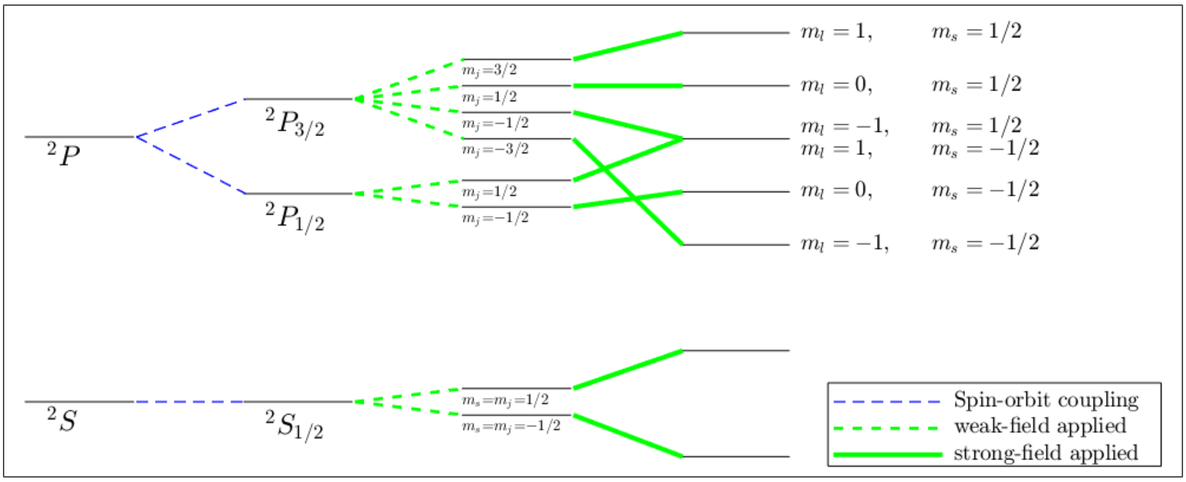

Figure 3.1: Spin-orbit coupling and the Zeeman effect on a sodium atom (not to scale).[87]

where the orbital g-factor, $g_l = 1$.[102] Note that spin-orbit coupling implies that $\hat{\boldsymbol{\mu}}$ is not a scalar multiple of $\hat{\mathcal{S}}$. The Zeeman Hamiltonian can be written in terms of the Zeeman matrix as

$$\hat{\mathcal{H}}_{Zeeman} = -\mathbf{B} \cdot \hat{\boldsymbol{\mu}} \approx -\mu_B \mathbf{B} \cdot \mathbf{g} \cdot \hat{\tilde{\boldsymbol{\mathcal{S}}}}, \tag{3.26}$$

where $\hat{\tilde{\boldsymbol{\mathcal{S}}}}$ is the effective spin, or pseudospin operator. This is discussed in Section 3.8, Figure 3.1 demonstrates the effect further. For a theoretical atom of sodium, in the absence of spin orbit coupling (SOC), the atom can exist in two states, the ^2S state, where the valence electron is in the $3s$ orbital, and the ^2P state where it is in a $3p$ orbital. This would result in a single emission line for sodium ($^2P \rightarrow {}^2S$). However, due to SOC, in the ^2P state, the orbital angular momentum, $l = 1$, couples with the spin angular momentum, $s = \frac{1}{2}$.

The total angular momentum quantum number for a single electron, j, must be an integer or half-integer that satisfies the inequality

$$|l - s| \leqslant j \leqslant |l + s| : 2j \in \mathbb{N}_0. \tag{3.27}$$

This inequality allows two values for the ^2P state, $j \in \{\frac{1}{2}, \frac{3}{2}\}$, resulting in the ^2P state splitting into two states; in the lowest state,$^2P_{1/2}$, the spin opposes the orbital angular momentum, $j = l - s$, whereas in the other state, $^2P_{3/2}$, the two are aligned, $j = l + s$.

This leads to the two ‘D-lines’observed in sodium’s emission spectra at 589.2 and 589.8 nm, this split being evidence of spin-orbit coupling.[11]

When a static magnetic field is applied, this doublet is further split into a doublet and quartet; the ${}^2P_{1/2}$ state is split into a set of $m_j = \{-\frac{1}{2}, \frac{1}{2}\}$ levels and the ${}^2P_{3/2}$ state is split into a set of $m_j \in \{-\frac{3}{2}, -\frac{1}{2}, \frac{1}{2}, \frac{3}{2}\}$ levels, and the ${}^2S_{1/2}$ state is similarly split into a doublet.[†]

Applying a strong magnetic field overcomes the spin-orbit coupling, so that the orbital and spin dipoles are affected separately. This is called the Paschen-Back effect. This leads to a set of six energy levels corresponding to the three possible values of m_l and two possible values of m_s. The $m_l = -1$, $m_s = \frac{1}{2}$ and $m_l = 1$, $m_s = -\frac{1}{2}$ levels are degenerate.[‡]

3.3 The Zeeman effect on nuclei

Like electrons, protons and neutrons have their spin quantised as $I = \frac{1}{2}$. The overall spin of a nucleus depends on its composition and each particular isotope has a fixed spin, $I = n/2 : n \in \mathbb{N}_0$. If the nuclear spin is not zero, then the nucleus will also experience a Zeeman effect, governed by the equation

$$\hat{\mathcal{H}}^{nuclear}_{Zeeman}|I = n/2\rangle = \mu_N g_N \hat{\boldsymbol{\mathcal{I}}}|I = n/2\rangle = \gamma_N \hat{\boldsymbol{\mathcal{I}}}|I = n/2\rangle, \tag{3.28}$$

where $\hat{\boldsymbol{\mathcal{I}}}$ is the nuclear spin operator and μ_N is the nuclear magneton. This is commonly combined with nucleus' g-factor, g_N, to give the nucleus' gyromagnetic ratio, γ_N, and it is this phenomenon that is the basis for nuclear magnetic resonance spectroscopy (NMR). The surrounding electrons are also affected by the magnetic field and are induced to oppose or reinforce it. Diamagnetic induction is associated with spherical charge distributions,[105] while the paramagnetic reinforcement effect is associated with charge distributions from orbitals of higher angular momentum ($l \geqslant 1$). Both effects are present in diamagnetic ($S = 0$) and paramagnetic ($S \geqslant \frac{1}{2}$) molecules, but the NMR shift in paramagnetic molecules is also affected by the unpaired spin, meaning that both the electronic Zeeman effect and spin-orbit-coupling must be considered. The nuclear and electronic spin also interact (hyperfine coupling, Section 3.4) and for a

---

[†] Selection rules imply that each ${}^2P$ state has one allowed transition to ${}^2S_{1/2}$. The energy-level separation is proportional to the magnetic field strength, *i.e.* there are degenerate emissions from ${}^2P_{3/2}$ to ${}^2S_{1/2}$, and only four spectral lines are observed.[87]

[‡] Strictly speaking they are only nearly degenerate since $g_e \approx 2g_l$.

molecule with multiple unpaired electrons, the individual electronic spin dipoles couple (zero-field splitting, Section 3.5). These effects typically have the largest influence on paramagnetic NMR (pNMR) shifts. Higher-order terms are not considered in this work.

This orbital shielding effect has a corresponding Hamiltonian given by

$$\gamma_{\text{nuc}}\mathbf{B} \cdot \boldsymbol{\sigma}^{\text{orb}} \cdot \hat{\boldsymbol{\mathcal{I}}}, \tag{3.29}$$

where $\boldsymbol{\sigma}^{\text{orb}}$ is called the chemical shielding (or orbital) matrix. Experimentally the resulting isotropic shielding effect σ is typically measured as a shift, δ, from that of a reference molecule, σ_{ref}, *i.e.*

$$\delta = \sigma_{\text{r}ef} - \sigma. \tag{3.30}$$

Shielding effects shift the resonance signal either 'upfield' or to higher frequencies, deshielding shifts 'downfield' or to lower frequencies. Since the shielding is subtracted from the reference, the reported shift is in the opposite direction and as a result, NMR spectra are often presented on a reversed frequency axis.

3.4 Hyperfine coupling

The magnetic moment of the nucleus also couples with that of the electron and the total angular momentum quantum number for the atom, K, must be an integer or half-integer number that satisfies the inequality

$$|J - I| \leqslant K \leqslant |J + I| : 2K \in \mathbb{N}_0. \tag{3.31}$$

A full description of the nuclear shell model is beyond the scope of this work, but a cursory outline is described below. The nuclear shell model for a static nucleus in a vacuum is similar to the electron shell model for a hydrogenic atom, but has a different central potential, $V(r_N)$, called the Saxon-Woods model,[106] which is given by

$$V(r_N) \propto \frac{1}{1 - e^{ar_N}}, \tag{3.32}$$

where r_N is the distance from the centre of the nucleus and a is a constant. The resulting solutions are similar to the hydrogenic model (each solution is a product of a radial solution and a spherical harmonic), and can be labelled by a principal quantum number, n, an orbital angular momentum, l, a the magnetic quantum number,

m. However but the orbital angular momentum is not constrained to be less than the principal quantum number. Protons and neutrons have different sets of energy levels, and as fermions obey the Pauli exclusion principle. Considering the sodium-23 nucleus, then this has a proton configuration of $1s^2 1p^6 1d^3$ and a neutron configuration of $1s^2 1p^6 1d^4$.

All of the neutrons, and all but one of the protons are spin paired. Hence only the third $1d$ proton is magnetically active. Applying spin-orbit coupling, this proton is in $1d_{5/2}$ orbital. There are three $1d_{5/2}$ orbitals corresponding to $m_{5/2} = \{\pm\frac{5}{2}, \pm\frac{3}{2}, \pm\frac{1}{2}\}$. In this case the energy increases with decreasing $|m_{5/2}|$, so the $m_{5/2} = \pm\frac{5}{2}$ proton level is doubly occupied. This implies that the magnetically active proton is in a $m_{5/2} = \frac{3}{2}$ orbital, which corresponds to the observed "spin" quantum number, $I = \frac{3}{2}$.[106]

An idealised energy-level splitting for sodium is shown in Figure 3.2. Starting with the $^2S_{1/2}$ state, then there are two possible atomic angular momentum quantum numbers, $K \in \{1, 2\}$, which can be thought as the electronic spin being opposed to or aligned with the nuclear spin respectively. These are split by approximately 0.3 microhartree,[107] smaller than the SOC splitting (over 200 hartree), but significant for magnetic radiofrequency experiments. A similar analysis holds for the $^2P_{1/2}$ state. The coupling for the $^2P_{3/2}$ state is more complex and there are four possible atomic angular momentum quantum numbers, $K \in \{0, 1, 2, 3\}$. Hence the state is split into four levels with the gaps between them increasing as K increases.

The Hamiltonian for the sodium-23 hyperfine interaction is given by[107]

$$\hat{\mathcal{H}} = 2\pi A \left[\hat{\mathcal{I}} \cdot \hat{\mathcal{J}}\right] + 2\pi B \left[\frac{3(\hat{\mathcal{I}} \cdot \hat{\mathcal{J}})^2 + \frac{3}{2}\hat{\mathcal{I}} \cdot \hat{\mathcal{J}} - (\hat{\mathcal{I}} \cdot \hat{\mathcal{I}})(\hat{\mathcal{J}} \cdot \hat{\mathcal{J}})}{2I(2I-1)(2J-1)}\right], \qquad (3.33)$$

where A and B are the magnetic dipole and electronic quadrupole coupling constants in atomic units. The latter term is only present for nuclei with two or more unpaired protons/neutrons,(*i.e.* $I \geqslant 1$). This work focuses on nuclei with $I = 1/2$, so the quadrupole term is not present from this point forward.

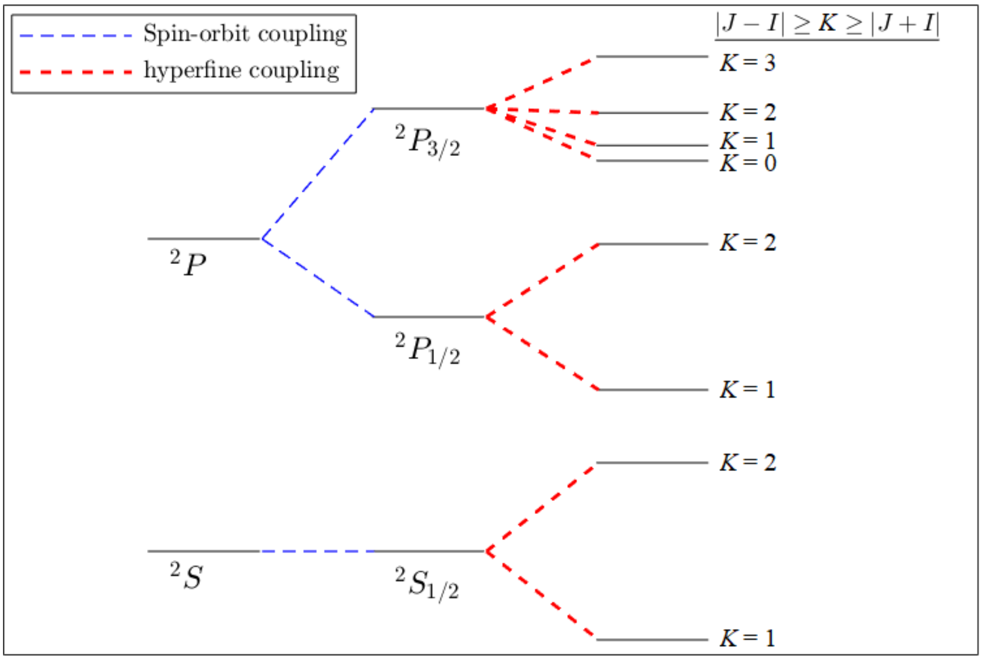

Figure 3.2: Hyperfine coupling in the sodium atom, $I = 3/2$. (not to scale). J is given in the term symbol subscript.

3.5 Zero-field splitting

Consider an isolated atom, with two active electrons that can occupy one of two non-degenerate spin-orbitals of different symmetry. This system can adopt one possible singlet and three possible triplet configurations as shown below

$$\begin{aligned}
\mathbf{S}_0^0 &= \frac{1}{\sqrt{2}}(|\uparrow\downarrow\rangle + |\downarrow\uparrow\rangle) \\
\mathbf{T}_1^1 &= |\uparrow\uparrow\rangle \\
\mathbf{T}_0^1 &= \frac{1}{\sqrt{2}}(|\uparrow\downarrow\rangle - |\downarrow\uparrow\rangle) \\
\mathbf{T}_{-1}^1 &= |\downarrow\downarrow\rangle
\end{aligned}$$

So for $\mathbf{T}_0^1$ exchanging two electrons has the effect of switching the sign of spatial part of the wavefunction, without changing the spin-part of the wavefunction.

In the absence of a magnetic field, the three triplet configurations are degenerate. Assuming that the three states are polarised along the x,y,z directions only, and labelled, $\mathbf{T}_x$, $\mathbf{T}_y$, $\mathbf{T}_z$, then applying a spherical field affects the electron density equally; the triplet states remain degenerate.

If an axial field is applied then the state polarised in the direction of the field will

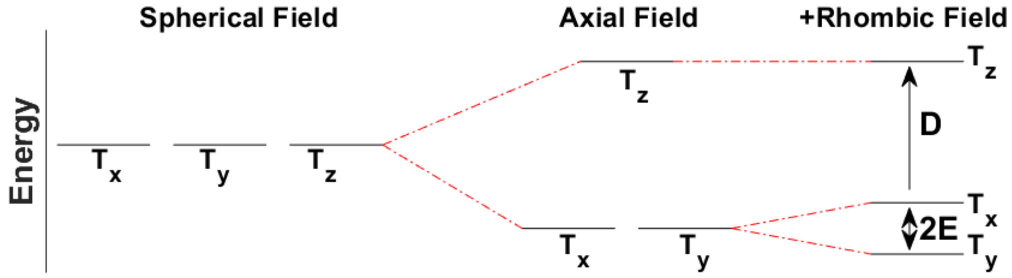

Figure 3.3: Energy levels of three isolated orbitals $\mathbf{T}_x$, $\mathbf{T}_y$, $\mathbf{T}_z$ resulting from zero-field splitting. For this example D is negative.

be either raised or lowered (labelled T_z), while the other two states remain degenerate but are lowered/raised respectively. If a further orthogonal (or rhombic) field is present than the remaining degeneracy is broken. One possible case is shown in Figure 3.3.

When this phenomenon occurs due to an internal field (*e.g.* a metal complex) this is referred to as zero-field splitting. This splitting is modelled by the dipolar ZFS Hamiltonian given by

$$\hat{\mathcal{H}}_{\mathrm{ZFS}} = \hat{\mathcal{S}} \cdot \mathbf{D} \cdot \hat{\mathcal{S}}, \tag{3.34}$$

where $\mathbf{D}$ is the zero-field splitting tensor. This tensor is symmetric and traceless and it is commonly reported using the parameters shown in Figure 3.3 (D and E) and the ratio E/D. The above Hamiltonian can be written as

$$\hat{\mathcal{H}}_{\mathrm{ZFS}} = D\left[\hat{\mathcal{S}}_z^2 - S(S+1)/3\right] + E\left[\hat{\mathcal{S}}_x^2 - \hat{\mathcal{S}}_y^2\right]. \tag{3.35}$$

It is therefore possible to verify a calculated ZFS tensor from the experimental splittings obtained via electron paramagnetic resonance (EPR) spectroscopy.

3.6 The spin Hamiltonian

The Hamiltonian corresponding to the nuclear Zeeman effect is given by

$$\hat{\mathcal{H}}_{\texttt{Nuclear Zeeman}} = -\gamma_K \mathbf{B} \cdot \left[\sum_K^{\text{nuclei}} (\mathbf{1}_3 - \boldsymbol{\sigma}_K^{\text{orb}}) \cdot \hat{\boldsymbol{\mathcal{I}}}_K \right], \tag{3.36}$$

where $\boldsymbol{\sigma}_K^{\text{orb}}$ is the chemical shielding matrix for the K^{th} nuclei. For a diamagnetic molecule additional interactions exist including direct nuclear dipole-dipole coupling and indirect nuclear spin-spin coupling. For nuclei with spin $\geqslant 1$, there are quadrupole coupling interactions. In this work these higher order terms are ignored.

For a paramagnetic system, typically the most important interactions are the Zeeman interaction, the hyperfine coupling between the electronic and nuclear spin, and where there are two or more unpaired electrons, the electron dipole-dipole coupling modelled by the ZFS tensor. The corresponding paramagnetic NMR spin Hamiltonian is given by[102,108–110]

$$\hat{\mathcal{H}}_{\texttt{pNMR}} = \mu_B \mathbf{B} \cdot \mathbf{g} \cdot \hat{\tilde{\boldsymbol{\mathcal{S}}}} - \gamma_K \sum_K^{\text{nuclei}} \mathbf{B} \cdot (\mathbf{1}_3 - \boldsymbol{\sigma}_K^{\text{orb}}) \cdot \hat{\boldsymbol{\mathcal{I}}}_K + \hat{\tilde{\boldsymbol{\mathcal{S}}}} \cdot \mathbf{D} \cdot \hat{\tilde{\boldsymbol{\mathcal{S}}}} + \sum_K^{\text{nuclei}} \hat{\tilde{\boldsymbol{\mathcal{S}}}} \cdot \mathbf{A}_K \cdot \hat{\boldsymbol{\mathcal{I}}}_K. \tag{3.37}$$

where the magnetic matrices are further discussed below and also in Section 4.3.[§]

3.6.1 The chemical shielding matrix

The $\kappa\upsilon^{\text{th}}$ ($\kappa, \upsilon \in \{x, y, z\}$, *i.e.* cartesian components) matrix element of the chemical shielding matrix for a nucleus K is formally defined by the partial derivative of the electronic energy, E, with respect to κ^{th} component of the magnetic moment of the nucleus and υ^{th} component of the magnetic field,[111] *i.e.* ,

$$\left[\boldsymbol{\sigma}_K^{\text{orb}}\right]_{\kappa\upsilon} = \left. \frac{\partial^2 E}{\partial [\boldsymbol{\mu}_K]_\kappa \, \partial B_\upsilon} \right|_{\delta \boldsymbol{\mu}_K, \delta \mathbf{B} = \mathbf{0}} . \tag{3.38}$$

This matrix is asymmetric since its left side refers to the three components of the magnetic moment whereas the right side refers to the magnetic field, however the diamagnetic contribution is symmetric. Diagonalising the symmetric part of the chemical shielding matrix gives the principal axis system (PAS) of the matrix with three eigenvalues, $\sigma_{K,i}^{orb}$ and the corresponding three orthonormal eigenvectors.

[§] In this thesis we follow the **BgS**, $\mathbf{B}\boldsymbol{\sigma}\mathbf{I}$ and **SAI** convention for the ordering of cartesian indices.[32]

The matrix can be decomposed into a diamagnetic, *i.e.* shielding and paramagnetic, *i.e.* deshielding parts. It can be shown[105] that the diamagnetic part of the shielding matrix, $\boldsymbol{\sigma}^{\mathrm{d}}_K$, is solely dependent on the ground-state wavefunction, $|\Psi_0\rangle$, and its components are given by

$$[\boldsymbol{\sigma}^{\mathrm{d}}_K]_{\kappa\upsilon} = \frac{1}{2c^2}\left\langle \Psi_0 \right| (\mathbf{r}\cdot\mathbf{r}_K\delta_{\kappa\upsilon} - r_\kappa r_{K_\upsilon})\, r^{-3} \left|\Psi_0\right\rangle . \tag{3.39}$$

where $\mathbf{r}_K$ is the vector from the K^{th} nucleus to the electron.

The paramagnetic part of the shielding matrix, $\boldsymbol{\sigma}^{\mathrm{p}}_K$, and its components are given by a sum over states (SOS) formulism between the ground state and the set of electronic excited states, $\{|\Psi_n\rangle\}$, *i.e.*

$$[\boldsymbol{\sigma}^{\mathrm{p}}_K]_{\kappa\upsilon} = -\frac{1}{2c^2}\sum_{\{|\Psi_n\rangle\}}^{\text{excited states}} \frac{\langle\Psi_0|L_\kappa|\Psi_n\rangle \left\langle\Psi_n|r_K^{-3}L_{K,\upsilon}|\Psi_0\right\rangle}{E_n - E_0}, \tag{3.40}$$

where $\mathbf{L}$ and $\mathbf{L}_K$ are the angular momentum matrices of the electron with respect to the origin and to the nucleus respectively.

3.7 The Zeeman matrix

The $\kappa\upsilon^{\mathrm{th}}$ matrix elements of the Zeeman matrix and the ZFS-tensor are defined by the partial derivatives

$$g_{\kappa\upsilon} = \left.\frac{\partial^2 E}{\partial\mu_\kappa\,\partial B_\upsilon}\right|_{\delta\boldsymbol{\mu},\delta\mathbf{B}=\mathbf{0}} . \qquad \text{and} \qquad D_{\kappa\upsilon} = \left.\frac{\partial^2 E}{\partial\boldsymbol{\mu}_\kappa\,\partial\boldsymbol{\mu}_\upsilon}.\right|_{\delta\boldsymbol{\mu}=\mathbf{0}} . \tag{3.41}$$

One approach to calculating this property uses effective Hamiltonian theory. For the calculation of the $\mathbf{g}$ matrix from a set of multiconfigurational states $0, A, B ...$, it can be shown from perturbation theory[59] that the $\kappa\upsilon^{\mathrm{th}}$ component of the shift of the $\mathbf{g}$ matrix $\Delta g_{\kappa\upsilon} = g_{\kappa\upsilon} - g_e\delta_{\kappa\upsilon}$ for a non-degenerate spin-free ground state is given by[112]

$$\Delta g_{\kappa\upsilon} = \frac{1}{2S_0}\sum_{A\neq 0}\frac{L_\kappa^{0A}\Omega_\upsilon^{A0} + L_\kappa^{A0}\Omega_\upsilon^{0A}}{\Delta E_A}\delta_{S_0,S_A}, \tag{3.42}$$

$$L_\kappa^{AB} = \left\langle A\left|\sum_i^{\text{electrons}} \hat{\ell}_\kappa(i)\right|B\right\rangle \qquad \Omega_\kappa^{AB} = \left\langle A\left|\sum_i^{\text{electrons}} \hat{h}_\kappa^{SO}(i)s_z(i)\right|B\right\rangle . \tag{3.43}$$

In the above formulae, S_A is the total spin of state A, ΔE_A is the energy difference between state A and the ground state. $\hat{\ell}$,$\hat{s}$ and $\hat{h}^{SO}$ are the one electron angular momentum, spin and spin-orbit operators respectively. Extensions exist to handle degenerate states, and spin-orbit adapted states can be modelled via a unitary transform. A similar technique exists for the zero-field splitting tensor. The advantage of this method is that it can produce a uniquely defined Zeeman matrix, however nearly degenerate states can result in numerical issues due to the correspondingly small value of ΔE_A.

For light atoms the spin-orbit operator[113,114] can be modelled by ls-coupling. Furthermore the one-electron and two-electron contributions are opposite in sign, so the full operator can be modelled as an effective one-electron operator,[115–117] using a fitted effective nuclear charge, Z_K^{eff}. The resulting one-electron spin-orbit operator can be written as

$$\hat{h}^{SO} = \frac{\alpha^2}{2} \sum_{K}^{nuclei} \frac{Z_K^{\text{eff}}}{r_k^3} \hat{l}_k \cdot \hat{s} \tag{3.44}$$

where α is the fine structure constant ($\alpha = c^{-2} \approx 1/137$), and in general the spin-orbit operator scales in energetic contribution as a α^2 term. This scaling can be used to gauge relative contributions to the energy.

The Zeeman matrix can be split into terms that scale as α^0 and α^2, *i.e.* as powers of the spin-orbit operator. The α^0 component is simply the isotropic interaction of a free electron with a magnetic field, *i.e.* $g_e\mathbf{I}_3$, the remaining α^2 is the Zeeman shift, $\mathbf{\Delta g}$, and is defined as

$$\mathbf{\Delta g} = \mathbf{g} - g_e\mathbf{I}_3 = \Delta g_{\text{iso}}\mathbf{I}_3 + \mathbf{\Delta \tilde{g}} \tag{3.45}$$

And the Zeeman shift can be broken into an isotropic term, $\Delta g_{\text{iso}} = \frac{1}{3}\text{trace}(\mathbf{\Delta g})$ and an anisotropic term, $\mathbf{\Delta \tilde{g}}$. This separation can give insight into the covalent nature of bonding in actinides.[2]

3.7.1 The Zeeman matrix is not a cartesian tensor

A cartesian covariant tensor (of the second rank) is defined as an object with 3^2 components, typically written as a 3×3 matrix, whose components must transform as a vector product (*i.e.* is as $\mathbb{R} \otimes \mathbb{R}$ or $SO(3) \otimes SO(3)$) when the object is subject to Galilean transformations. As an example for a rotation $\mathbf{R}$ of the underlying space such a tensor, $\mathbf{A}$ must satisfy[118]

$$\mathbf{A}^{\text{Transformed}} = \mathbf{RAR}^{-1}. \tag{3.46}$$

Such a tensor reflects physical world coordinates and is the default type of tensor in modern physics. Contravariant tensors transform with the basis of the vector space which is the inverse transformation.

For a $S = 1/2$ hydrogen atom, the second index of the Zeeman matrix $\mathbf{g}$ relates to spin space (SU(2)) not Euclidean space which has different rotational behaviour. The corresponding right-hand-side relates to the set of $(2S+1)\times(2S+1)$ complex true spin matrices $\{\mathbf{S}_x, \mathbf{S}_y, \mathbf{S}_z\}$. Even more problematically, for molecules where SOC is present, then the right hand side of the Zeeman matrix relates to the $(2\tilde{S}+1)\times(2\tilde{S}+1)$ set¶ of pseudospin matrices $\{\widetilde{\mathbf{S}}_x, \widetilde{\mathbf{S}}_y, \widetilde{\mathbf{S}}_z\}$, the PAS system of which is typically rotated relative to the true spin matrices. Hence it is not a true tensor as commonly presented. As a result the object's transformational nature is molecule dependent.

This problem was recognised in Abragam and Bleaney's seminal 1970 work[102] "Electronic Paramagnetic Resonance of Transition Ions" (p.171, 650-652) and the work identifies the difference between the true spin and the fictitious pseudospin as a major source of confusion. Furthermore, the work emphasises that manipulations in the following sections exploit the fact that we have six degrees of freedom to diagonalise $\mathbf{g}$ (and $\mathbf{A}$), not the three degrees of freedom for a true 3×3 tensor. Because of this we will refer to the g-tensor as the Zeeman matrix.

Similar concerns are true for the orbital shielding and hyperfine matrices discussed in the following sections. Both sides of the zero-field splitting (ZFS) tensor relate to the complex pseudospin matrices, so it is a true tensor, but its transformational behaviour is molecule dependent. Because of this it does not have to reflect the symmetry of the molecule. For instance in Chapter 5, we calculate that the orientation of the primary-axis of the ZFS-tensor of the 1,4,7,10-tetrazacyclodecane-1,4,7,10-tetraacetic complex with uranium, U(DOTA), to be along the molecular C_4 axis, but by adding a fluoride ligand along the molecular axis, the primary axis rotates by 90°.

¶Note that in practice $\tilde{S}$ is an empirical number related to the energy levels of the post-SOC wavefunction, and not an eigenfunction of $\hat{\tilde{S}}_z$ or $\hat{\tilde{\boldsymbol{S}}}^2$.

3.7.2 Alternative approaches to calculating the Zeeman matrix

An alternative approach to the using the SOS formulism to form the Zeeman matrix exists. The idea is to form a diagonalisable Zeeman matrix, based on forming the determinant of the matrix elements of the Zeeman Hamiltonian in a Kramers' pair basis.[119] This is based on the observation that the Zeeman Hamiltonian has two definitions.

$$\hat{\mathcal{H}}_{Zeeman} = -\mathbf{B} \cdot \hat{\boldsymbol{\mu}}, \tag{3.47}$$

$$\hat{\mathcal{H}}_{Zeeman} = \mu_B \mathbf{B} \cdot \mathbf{g} \cdot \hat{\tilde{\boldsymbol{S}}}. \tag{3.48}$$

It follows that for a Kramers' pair of states $\{\Phi_{1/2}, \Phi_{-1/2}\}$ the Zeeman splitting energy is given by

$$\Delta E = \left\langle \Phi_{1/2} | -\mathbf{B} \cdot \hat{\boldsymbol{\mu}} | \Phi_{1/2} \right\rangle - \left\langle \Phi_{-1/2} | -\mathbf{B} \cdot \hat{\boldsymbol{\mu}} | \Phi_{-1/2} \right\rangle, \tag{3.49}$$

$$\Delta E = \left\langle \Phi_{1/2} | \mu_B \mathbf{B} \cdot \mathbf{g} \cdot \hat{\tilde{\boldsymbol{S}}} | \Phi_{1/2} \right\rangle - \left\langle \Phi_{-1/2} | \mu_B \mathbf{B} \cdot \mathbf{g} \cdot \hat{\tilde{\boldsymbol{S}}} | \Phi_{-1/2} \right\rangle. \tag{3.50}$$

squaring these expressions and comparing gives

$$(\Delta E)^2 = \sum_{\kappa\upsilon \in \{x,y,z\}} B_\kappa B_\upsilon \sum_{\kappa'\upsilon' \in \{x,y,z\}} \left[\mu_B^2 g_{\kappa\kappa'} g_{\upsilon\upsilon'} \right] = \mu_B^2 \sum_{\kappa_1 \upsilon_2 \in \{x,y,z\}} B_\kappa B_\upsilon G_{\kappa\upsilon}. \tag{3.51}$$

The rightmost term $\mathbf{G} = \mathbf{g}\mathbf{g}^T$ is a true tensor and is called the Abragam-Bleaney tensor.[120] Diagonalising this gives a field-independent tensor form of the square of the $\mathbf{g}$ matrix, which can be diagonalised. The corresponding principal values of the (symmetrised) $\mathbf{g}$ matrix are therefore simply the square roots of eigenvalues of the Abragam-Bleaney tensor, and the principal directions are the eigenvectors. Due to the square root the sign of the principal values is not explicitly determined, but can be infered from the magnetic moment matrices.

Chibotaru[121] recommends building $(\mathbf{g}+\mathbf{g}^T)/2$ and using a rotation matrix to relate the eigenvectors to the original coordinate frame. This relates to $\mathbf{B} \otimes \tilde{\mathbf{S}}$ and does not introduce the sign indeterminacy. Chibotaru also demonstrated that the pseudospin matrices in a basis of $2\tilde{S}+1$ functions, $\{|m_s = -|\tilde{S}\rangle ... |\tilde{S}\rangle\}$, can be related to the true spin matrices by a coordinate rotation, *e.g.* for $\mathbf{S}_z$

$$\widetilde{\mathbf{S}}_z = \mathbf{S}_z + \sum_{\kappa \in \{x,y,z\}} \frac{g_{z\kappa} - g_{\kappa z}}{2g_e} \mathbf{S}_x. \tag{3.52}$$

Hence the PAS of the pseudospin matrices do not 'typically coincide' with the PAS of the true spin matrices,[121] *i.e.* the PAS of $\widetilde{\mathbf{S}}_z$ and $\mathbf{S}_z$ are in rotated coordinate frames. The angle between the principal direction of the true spin of the molecule in a magnetic field, $\mathbf{S}_B$, and the pseudospin, $\widetilde{\mathbf{S}}_B$, $\theta_{\mathbf{S},\widetilde{\mathbf{S}}}$ is dependent on the orientation of the applied magnetic field and is given by (in radians)

$$\theta_{\mathbf{S},\widetilde{\mathbf{S}}} = \frac{1}{2g_e} \sqrt{\sum_{\kappa \upsilon \in \{x,y,x\}} \epsilon_\kappa^2 (g_{\kappa\upsilon} - g_{\upsilon\kappa})^2}, \tag{3.53}$$

where ϵ_κ are the applied field's direction cosines (cosines of the angle of the vector and each coordinate axis).

3.8 The determination of pseudospin

Bulk paramagnetic materials have no net magnetism in the absence of a magnetic field, but will exhibit a magnetic moment when a field is applied.[102] The nature and anisotropy of this moment is mediated by the interplay of spin-orbit coupling (SOC) and electrostatic interactions such as crystal field (CF) effects.[‖] For a system of spin S, in the limit of no spin-orbit-coupling, both interactions can be mapped to a manifold of $2S + 1$ states that correspond both to the eigenfunctions of a spin Hamiltonian and to the full wavefunction[87] However, once spin-orbit coupling is included, spin is no longer a conserved quantity and an effective spin, or pseudospin must be introduced to restore this correspondence. Establishing the correct pseudospin becomes more difficult as the electronic structure becomes more complicated and SOC effects increase. Chibotaru reviewed the use of pseudospin Hamiltonians, describing the theory as "controversial" and established guidelines on their use,[122] considering several common cases and establishing the interplay between SOC and the crystal field. Firstly considering when SOC is small compared to the crystal field, such as in 3d transition metals, *i.e.* $\hat{\mathcal{H}}_{\text{SOC}} << \hat{\mathcal{H}}_{\text{CF}}$, the former can safely be applied as a perturbation on the

---

[‖] The literature refers to these as crystal and ligand field effects interchangably, however since the effect is conceptually treated as electrostatic, this work prefers the former term.

latter; this implies the observed degeneracy adopts the same form as the spin degeneracy, so $\widetilde{\mathbf{S}} = S$. Typically for the lanthanides, the crystal field is much weaker, so the spin-orbit effect dominates, *i.e.* $\hat{\mathcal{H}}_{\mathrm{SOC}} >> \hat{\mathcal{H}}_{\mathrm{CF}}$ so the crystal-field operator can be safely applied as a perturbation. The resulting observed degeneracy is therefore related to the combination of $\hat{\mathcal{L}}$ and $\hat{\mathcal{S}}$ angular momenta and so as a result $\widetilde{\mathbf{S}} = J$. However, if the crystal field is strong enough to isolate the lowest energy state(s) energetically, this is no longer the case, and a traditional spin Hamiltonian formulation would not be appropriate; since only these isolated states influence the paramagnetism of the molecule.

An example is the [$\mathrm{Zn_3Dy(L)(NO_3)(MeOH)_3}$] complex,[121] where L is a hexaimine macrocyclic ligand. Dysprosium has the electronic configuration [Xe] $4f^{10}6s^2$, so an isolated Dy^{3+} ion has nine f electrons. By Hund's rules, maximising the possible multiplicity and orbital angular momentum gives $S = 5/2$ and $L = 5$, and the largest possible total angular momentum, $J = 15/2$, so the corresponding term symbol is $^6\mathrm{H}_{15/2}$ for the ground state, and will therefore form eight Kramers' pairs.

The complex's crystal field splits these doublets so the lowest pair is energetically isolated. A single Kramers' doublet has a pseudospin of 1/2, and Chibotaru showed that the experimental properties could be emulated using only the lowest Kramers' pair to calculate magnetic properties, such as the g-matrix.[122] Such situations are more common in actinide species since the increased size of the 5f orbitals leads to larger crystal fields. Furthermore, SOC effects are even more pronounced leading to greater interaction and mixing of states with different formal spin compared to 4f species. It follows that modelling such systems requires a multi-reference approach and a pseudospin assignment based on the calculated multiplicity of the resulting state energies; there are magnetic subtleties that "will not be adequately described by any crystal field approach."[121]

3.9 The hyperfine coupling matrix

The $\kappa\upsilon^{\mathrm{th}}$ matrix element of the hyperfine coupling matrix is defined by the following partial derivative of the electronic energy, E,

$$\mathbf{A}_{\kappa\upsilon} = \left.\frac{\partial^2 E}{\partial \boldsymbol{\mu}_\kappa \, \partial \boldsymbol{\mu}_\upsilon^K}\right|_{\delta\boldsymbol{\mu},\delta\boldsymbol{\mu}^K=\mathbf{0}} . \tag{3.54}$$

This is typically split into two terms, the Fermi-contact isotropic term, A_{iso}, and the anisotropic spin-dipolar term, $\mathbf{A}^{SD}$, which are summed as (*cf.* Eq. 3.45)

$$\mathbf{A} = A_{iso}\mathbf{I}_3 + \mathbf{A}^{SD}. \tag{3.55}$$

The isotropic term is given by

$$A_{iso} = \frac{4c_{\text{nuc}}}{3\langle\hat{\mathcal{S}}_Z\rangle}\left\langle\Psi\middle|\delta(r_N)\hat{\mathcal{S}}_Z\middle|\Psi\right\rangle, \tag{3.56}$$

where $c_{\text{nuc}} = \mu_B\mu_N g_e g_N$ is a constant defined for brevity and $\delta(r_N)$ is the Dirac delta function ($x = 0 \implies \delta(x) = 1$, otherwise $\delta(x) = 0$). The resulting matrix element is therefore proportional to the spin-density at the nucleus. This is associated with covalency since the effect is transfered through bonding.

The anisotropic term is associated with spin-dipolar interactions and it is given by

$$A^{\text{SD}}_{\kappa\upsilon} = \frac{c_{\text{nuc}}}{\langle\hat{\mathcal{S}}_Z\rangle\, r_N^{-5}}\left\langle\Psi\middle|r_N^2\delta_{\kappa\upsilon} - 3r_{N_\kappa}r_{N_\upsilon}\middle|\Psi\right\rangle. \tag{3.57}$$

This does not include SOC effects, and the scalar-relativistic hyperfine energies scales as α^2. The leading SOC effect is second order, referred to as the paramagnetic spin-orbit (PSO) effect and results from nuclear-spin and electron-orbital interactions. For light atoms this can often be ignored, but is much more significant for heavy atoms or light atoms directly bonded to heavier atoms; the latter is called the heavy-atom light-atom (HALA) effect. This PSO contribution, $\mathbf{A}^{\Delta\text{SO}}_{\kappa\upsilon}$, can be written as[32]

$$\mathbf{A}^{\Delta\text{SO}}_{\kappa\upsilon} = -\frac{c_{\text{nuc}}}{2S}\sum_{kl}^{\textit{orbitals}}\frac{\partial P_{kl}}{\partial I_\upsilon}\left\langle\psi_\upsilon|\hat{h}^{so}_\kappa|\psi_l\right\rangle \tag{3.58}$$

where $\mathbf{P} = \mathbf{C}^T\mathbf{C}$ is the molecular orbital density matrix formed from the molecular orbital coefficients $\mathbf{C}$. In principle the corresponding shift in energy scales as α^4, However the magnitude of this effect is not always intuitive, and PSO corrections are needed to ameliorate any doubts.

As an example, the experimentally obtained negative sign of A_{iso} for the protons in the η-bonded bis(cycloheptatrienyl)uranium complex, $\text{U(C}_7\text{H}_7)_2^-$ appears to be largely due to a spin-orbit induced PSO mechanism.[123,124] The uranium atom in this complex has a formal assignment of U^{V}, *i.e.* a f^1 configuration, but the strong covalency of the metal-ligand η bond can imply that the compound has significant U^{III}, *i.e.* f^3 character.[124]

As with the Zeeman matrix, the hyperfine matrix is not necessarily symmetrical. The principal values for this matrix can be calculated by defining an auxiliary set of three cartesian generalised hyperfine operators $\hat{\boldsymbol{\mathcal{F}}}^I = \hat{\mathcal{A}} \cdot \hat{\mathcal{I}} = \{\hat{\mathcal{F}}^I_x, \hat{\mathcal{F}}^I_y, \hat{\mathcal{F}}^I_z\}$ which represents the part of the magnetic dipole operator of the nucleus that is fully independent of the applied magnetic field. Considering the following two Hamiltonians over an electronic and protonic Kramers' pair $\{\Phi^I_{1/2}, \Phi^I_{-1/2}\}$, then the energy is given by

$$\Delta E = \langle \Phi_{1/2}\Phi^I_{1/2}|\hat{\mathcal{S}} \cdot \hat{\boldsymbol{\mathcal{F}}}^I|\Phi_{1/2}\Phi^I_{1/2}\rangle - \langle \Phi_{-1/2}\Phi^I_{-1/2}|\hat{\mathcal{S}} \cdot \hat{\boldsymbol{\mathcal{F}}}^I|\Phi_{-1/2}\Phi^I_{-1/2}\rangle, \tag{3.59}$$

$$\Delta E = \langle \Phi_{1/2}\Phi^I_{1/2}|\hat{\mathcal{S}} \cdot \mathbf{A} \cdot \hat{\mathcal{I}}|\Phi_{1/2}\Phi^I_{1/2}\rangle - \langle \Phi_{-1/2}\Phi^I_{-1/2}|\hat{\mathcal{S}} \cdot \mathbf{A} \cdot \hat{\mathcal{I}}|\Phi_{-1/2}\Phi^I_{-1/2}\rangle. \tag{3.60}$$

The matrix representation of the $\hat{\boldsymbol{\mathcal{F}}}^I$ operators in a $\{|m_I = -I\rangle ... |m_I = I\rangle\}$ basis is squared via $\mathbf{F} = \mathbf{A}'^T\mathbf{A}'$ to form a true tensor,. The principal values of the hyperfine matrix are the square root of the eigenvalues of $\mathbf{A}'^T\mathbf{A}'$.

3.10 Modelling zero-field splitting

Ramsey[125–127] posited that because nuclear motion is much slower than electronic motion, the nuclear magnetic moment $\boldsymbol{\mu}_{\mathrm{nuc}}$ changes much more slowly than the electronic magnetic moment $\boldsymbol{\mu}$, and can be treated as time-independent, effectively as a parameter. Assuming equilibrium is reached within experimental time scales, the observed NMR shielding tensor can be shown[128] to be given by the second derivative of the electronic energy with respect to the components of the magnetic field and the nuclear magnetic moment at the limit of zero field and magnetic moment

$$\sigma_{\kappa \upsilon} = \left. \frac{\partial^2 E}{\partial B_\kappa \, \partial \mu_{\mathrm{nuc},\nu}} \right|_{\substack{\mathbf{B}\to\mathbf{0} \\ \boldsymbol{\mu}_{\mathrm{nuc}}\to\mathbf{0}}}. \tag{3.61}$$

The resulting energy levels are often close enough to have significant occupation above the ground state, so Boltzmann averaging of observables is required. The Boltzmann average $\langle A \rangle_0$ of a set of observables $\{A_n\}$ with n energy levels, $\{W_n\}$ is given by:

$$\langle A \rangle_0 = \frac{\sum_n A_n e^{-W_n/k_B T}}{\sum_n e^{-W_n/k_B T}}. \tag{3.62}$$

Following Moon and Patchkovskii's summary[128] the approach we use is based on Kurland and McGarvey's work,[129] which allows the pNMR Hamiltonian to be split into

Zeeman and hyperfine terms. The field-independent form of the shielding tensor[128] can be decomposed into diamagnetic and paramagnetic shielding tensors, $\boldsymbol{\sigma}^{\text{orb}}$ and $\boldsymbol{\sigma}^{\text{p}}$ respectively

$$\sigma^{\text{orb}}_{\kappa\upsilon} = \left\langle \frac{\partial^2 E}{\partial B_\kappa \, \partial \mu_{\text{nuc},\nu}} \right\rangle_0 \qquad \sigma^{\text{p}}_{\kappa\upsilon} = -\frac{1}{k_B T} \left\langle \frac{\partial E}{\partial B_\kappa} \cdot \frac{\partial E}{\partial \mu_{\text{nuc},\upsilon}} \right\rangle_0 .$$

Taking $\mathbf{g}$ and $\mathbf{A}$ as the following partial derivatives

$$g_{\kappa\upsilon} = \left. \frac{\partial^2 E}{\partial B_\kappa \, \partial S_\nu} \right|_{\mathbf{B}\to\mathbf{0}} \qquad A_{\kappa\upsilon} = \gamma_{\text{nuc}} \left. \frac{\partial^2 E}{\partial S_\kappa \, \partial \mu_{\text{nuc},\nu}} \right|_{\boldsymbol{\mu}_{\text{nuc}}\to\mathbf{0}} \tag{3.63}$$

it can be shown that, in the low spin-orbit coupling limit[130–132]

$$\begin{aligned} \sigma^{\text{p}}_{ab} &= -\frac{1}{k_B T} \left\langle \frac{\partial E}{\partial B_a} \cdot \frac{\partial E}{\partial \boldsymbol{\mu}_{\text{nuc,b}}} \right\rangle_0 && (3.64) \\ &= -\frac{1}{\gamma_{\text{nuc}} k_B T} \langle (\mathbf{g} \cdot \mathbf{S})_a (\mathbf{S} \cdot \mathbf{A})_b \rangle_0 && (3.65) \\ &= -\frac{1}{\gamma_{\text{nuc}} k_B T} \mathbf{g} \cdot \mathbf{Z} \cdot \mathbf{A} = -\frac{1}{\gamma_{\text{nuc}} k_B T} \sum_{\kappa\upsilon}^{\{x,y,z\}} g_{a\kappa} Z_{\kappa\upsilon} A_{\upsilon b} \,, && (3.66) \end{aligned}$$

where $\mathbf{Z}$ is a 3×3 coupling matrix, the $\kappa\upsilon^{\text{th}}$ element of which can be thought of as the expectation value of a Boltzmann averaged combination of transformed $\hat{\mathcal{S}}_\kappa$ and $\hat{\mathcal{S}}_\upsilon$ operators, *i.e.* a spin-spin interaction;[130]

$$Z_{\kappa\upsilon} = \left\langle \int_0^{1/(k_B T)} \mathrm{d}\beta \; e^{\beta \hat{\mathcal{H}}_0} \hat{\mathcal{S}}_\kappa \; e^{-\beta \hat{\mathcal{H}}_0} \hat{\mathcal{S}}_\upsilon \right\rangle_0 \tag{3.67}$$

In the absence of zero-field splitting, $Z_{\kappa\upsilon} = \frac{1}{3} S(S+1) \delta_{\kappa\upsilon}$, where $\delta_{\kappa\upsilon}$ is the Kronecker delta and the resulting matrix is diagonal.

Pennanen and Vaara[133] formulated a practical approach to modelling ZFS in the context of modern quantum chemistry, the "no coupling approximation." This requires the formation of the $(2S+1) \times (2S+1)$ matrix, $\mathbf{S}^T \cdot \mathbf{D} \cdot \mathbf{S}$, which is then diagonalised to obtain eigenvalues E_n and eigenstates $|n\rangle$, the latter being linear combinations of pure spin states $|S m_S\rangle$. Soncini and van den Heuvel[130] presented a fully coupled approach, which can be expressed as

$$Z_{\kappa\upsilon} = \omega^{-1} \sum_{nm}^{\text{eigenstates}} q_{nm} \langle n | \hat{\mathcal{S}}_\kappa | m \rangle \langle m | \hat{\mathcal{S}}_\upsilon | n \rangle \qquad \text{where} \qquad \omega = \sum_n e^{-E_n / k_B T}, \tag{3.68}$$

with q_{nm} being a Boltzmann weighting term

$$q_{nm} = \begin{cases} e^{-E_n / k_B T} & E_m = E_n \\ -\frac{k_B T}{E_n - E_m} \left(e^{-E_n / k_B T} - e^{-E_m / k_B T} \right) & \text{otherwise.} \end{cases} \tag{3.69}$$

3.10.1 Extending the approach to states with arbitrary degeneracy

In 2012 Van den Heuvel and Soncini[1] presented an extended approach to handle cases with arbitrary degeneracy. It is based, in part, on the observation that the set of spin tensors $\{S_q^{(k)} : k \leqslant 2\tilde{S}\}$ form a complete basis for the set of all complex square matrices of dimension $2\tilde{S}+1$. For instance, the z component of the magnetic moment $\boldsymbol{\mu}$ can be decomposed via

$$\boldsymbol{\mu}_z = \sum_{k \text{ odd}}^{k\leqslant 2\tilde{S}} \sum_{k}^{q=-k} (-1)^q g_{qz}^{(k)} \mathbf{S}_{-q}^k, \qquad \text{where } g_{qz}^{(k)} = \frac{2k+1}{\langle S||S^{(k)}||S\rangle} Tr\left(\mathbf{S}_q^{(k)} \boldsymbol{\mu}_z\right), \tag{3.70}$$

and the coefficient $g_{qz}^{(k)}$ is referred to as a generalised Zeeman "tensor". In the absence of ZFS, the pNMR contribution to the shift is given by

$$\sigma_{\kappa\upsilon} = -\frac{\mu_B}{g_n k_B T} \cdot \frac{1}{S+1} \sum_{k=1}^{2S} \sum_{q=-k}^{k} g_{q\kappa}^{(k)} (a_{q\upsilon}^{(k)})^* \frac{\langle S||S^k||S\rangle^2}{2K+1}. \tag{3.71}$$

ZFS is accounted for via a spin projection $\mathbf{P}_0$ of the ZFS Hamiltonian

$$\hat{\mathcal{P}}_0 \hat{\mathcal{H}}_{ZFS} \hat{\mathcal{P}}_0 = \sum_{k \text{ even}}^{K\leq 2\tilde{S}} \sum_{k}^{q=-k} D_q^{2k} S_{-q}^{2k}, \qquad \text{where } \hat{\mathcal{P}}_0 = \sum_{q=|S,-S\rangle \ldots |S,S\rangle} |q\rangle\langle q| \tag{3.72}$$

Forming the $\hat{\mathcal{P}}_0 \hat{\mathcal{H}}_{ZFS} \hat{\mathcal{P}}_0$ matrix in the $\{|m_{\tilde{S}} = |-\tilde{S}\rangle \ldots |m_{\tilde{S}} = -\tilde{S}\rangle\}$ basis and diagonalising it gives $(2\tilde{S}+1)$ eigenfunctions $|\lambda\rangle$. which can be used to build the spin projector and from these it can be shown that

$$\sigma_{\kappa\upsilon} = \sigma_{\kappa\upsilon}^{\text{orb}} - \frac{\mu_B}{\mu_N} . \frac{1}{g_N} \sum_{k,k'=1}^{2\tilde{S}} \sum_{q=-k}^{k} \sum_{q'=-k'}^{k'} g_{q\kappa}^{(k)} \, Q_{k'q'}^{kq} \, a_{q'\upsilon}^{(k')}, \text{where}$$

$$Q_{k'q'}^{kq}(\lambda, \lambda') = \sum_{\{\lambda\},\{\lambda'\}}^{deg.St.} \cdot \begin{cases} \frac{e^{-E_\lambda/k_B T}}{\omega k_B T} \sum_{\lambda}^{\{\lambda\}} \langle\lambda|S_q^k|\lambda\rangle\langle\lambda|S_q^k|\lambda\rangle & E_\lambda = E_{\lambda'} \\ \frac{-2e^{-E_\lambda/k_B T}}{\omega(E_\lambda - E_{\lambda'})} \Re\left[\sum_{\lambda}^{\{\lambda\},\{\lambda\}} \lambda|S_q^k|\lambda'\rangle\langle\lambda'|S_q^k|\lambda\rangle\right] & \text{otherwise,} \end{cases}$$

and ω is the sum of Boltzmann weights, a are the hyperfine coefficients.

3.10.2 Practical implementation

We have produced three programs that form the paramagnetic contribution to the NMR shift.

Non ITO-based approach

The first was a C++ program using the formulation in Section 3.10, *i.e.* Eqs. 3.68–3.69, which was then used for all calculations in Chapter 4. This agreed with, and was superseded by a faster program made available by Autschbach's group, PNMR-Shift.[131,134,135]

Main ITO-based approach

The second is a family of Matlab scripts** that use the full ITO approach for a system with axial symmetry. That is they implement Eqs. 3.70–3.71. They take the ORCA output of the spin and orbital ar momentum matrices of the spin-orbit-free (SOF) states calculated at NEVPT2 level. Then the program forms the electronic magnetic dipole moments, $\{\boldsymbol{\mu}_x, \boldsymbol{\mu}_y, \boldsymbol{\mu}_z\}$ in the SOF basis and parses the QDPT-SOC state description to transform each of these into the SOC basis. These are then truncated to $(2\tilde{S}+1) \times (2\tilde{S}+1)$ submatrices which are used to form the corresponding coefficients, $\mathbf{g}_{\kappa 0}^{(k)} : k = 1, 3, 5, ..., \kappa \in \{x, y, z\}$, from the $S_0^{(k)}$ ITO. The remaining Zeeman coefficients can be formed similarly, using Wigner-Eckart theory to build the ITOs.[136]

The ZFS operator is time even, so its decomposition only includes even terms, and the zeroth term only shifts the energy (and can therefore be ignored). The λ eigenvectors and energies can be inferred by diagonalising the NEVPT2 $\widetilde{\mathbf{S}}^T \cdot \mathbf{D} \cdot \widetilde{\mathbf{S}}$ matrix. This introduces no new approximations over the standard approach provided that $\tilde{S} \leqslant 3/2$. The pseudospin matrices $\widetilde{\mathbf{S}}_x, \widetilde{\mathbf{S}}_y, \widetilde{\mathbf{S}}_z$ are built from the Zeeman matrix via Eq. 3.52.

** and a parallel C++ program

This leaves the hyperfine ITO coefficients, *e.g.* $a_{0z}^{(1)}$. It can be shown[1] that the paramagnetic shielding matrix, $\sigma_{\kappa\upsilon}^{I}$, for a system with a ω-fold degenerate state is given by

$$\sigma_{\kappa\upsilon}^{p} = -\frac{1}{\omega k_B T} Tr(\mathbf{P_0}\boldsymbol{\mu}_\kappa \mathbf{P_0}\hat{\boldsymbol{\mathcal{F}}}_{\upsilon}^{I}\mathbf{P_0}), \tag{3.73}$$

where $\hat{\mathcal{F}}_{\upsilon}^{I}$ represents the contact, pseudocontact and paramagnetic-spin-orbit components of the hyperfine interaction in the υ^{th} direction, conceptually this is the applied field-independent part of the magnetic response of the nucleus (*i.e.* $\mathbf{f}^I$ in Eq. 3.50). It is this matrix that, when decomposed via Eq. 3.52, gives the hyperfine ITO coefficients. For $S = 1$, the $a_{i\kappa}^{(1)} : i = -1, 0, 1, \kappa = \{x, y, z\}$ terms are an ITO representation of the standard hyperfine matrix.[1]

For an axial system, only the $\mathbf{S}_z D_{zz} \mathbf{S}_z$ term survives and only $\{a_{iz}^{(1)}\}$ is non-zero. Provided that $\widetilde{\mathbf{S}}_z \approx \mathbf{S}_z$ (*i.e.* from Eq. 3.35, $g_{xz} \approx g_{zx}$ and $g_{yz} \approx g_{zy}$) then it follows that the decomposition of $\hat{\mathcal{F}}_{z}^{I}$ by the ITOs $\mathbf{S}_0^{(1)}$ approximates to a decomposition by $\widetilde{\mathbf{S}}_z$. Therefore $a_{0z}^{(1)}$ is approximately the square root of the $\mathbf{A}^T\mathbf{A}$ tensor.[††] This introduces a sign indetermancy for $a_{0z}^{(1)}$, but due to the restriction on the off-diagonal elements, in most cases, the sign of $a_{0z}^{(1)}$ is the same as that of the zz-component of the normal hyperfine matrix. For this simple case, a calculation using the methods of Section 3.9 should give the direction of the paramagnetic component and by extension the sign of $a_{0z}^{(1)}$.

Since μ_κ and $\hat{\mathcal{F}}_{\upsilon}^{I}$ are time-odd operators their decomposition only involves odd terms. This means that for $\tilde{S} = 1$ only first order terms appear. For $S = 3/2$, third order terms are present. While $g_{ik}^{(3)}$ is built from $\boldsymbol{\mu}$, there is no ITO approach to build $a_{0z}^{(3)}$ from $a_{0z}^{(1)}$. For an axial system, the ratio $a_{0z}^{(3)}/a_{0z}^{(1)}$ is approximately[1] the same as $g_{0z}^{(3)}/g_{0z}^{(1)}$, so the approach can be approximated by such scaling,

For $\tilde{S} = 2$, the decompostion of $\hat{\mathcal{H}}_{ZFS}$ has fourth-order terms that are not included in the $\mathbf{S}^T \cdot \mathbf{D} \cdot \mathbf{S}$ approximation. For $\tilde{S} > 2$, additional scaling approximations are needed, *e.g.* for $a_{0z}^{(5)}$. Hence the quality of the approximation rapidly degrades as $\tilde{S}$ increases.

[††] The pseudospin for **A** is the same as that of **g**, but ideally **A** and **g** should be in the same frame. For an axial system, the diagonalisation is equivalent to a rotation of the coordinate system about the z-axis, and for $a_{0x}^{(1)}$ and $a_{0y}^{(1)}$, this needs to be accounted for.

For an axially symmetric system, there are often atoms that are chemically equivalent but the imposition of a coordinate system creates atoms that are computationally different. This is usually handled by taking the average hyperfine matrix for each set of chemically equivalent atoms. This averaged hyperfine matrix is typically more symmetric, and as a result the $\mathbf{F}^I$ tensor is typically a better approximation for the hyperfine interaction.

Experimental ITO-based approach

The third, most recent Matlab development is an experimental fork of the second and uses the full ITO approach for systems with $\tilde{S} = 1$. This follows the above formulation, but constructs the hyperfine interaction $\hat{\boldsymbol{\mathcal{F}}}^{\boldsymbol{I}}_{\boldsymbol{\kappa}}$ from $\widetilde{\mathbf{S}}_{\kappa}\mathbf{A}^T\mathbf{A}$ to account for a general pseudospin rotation, and decomposes this by the ITOs (as for $\boldsymbol{\mu_x}$). This approach is only valid for $\tilde{S} = 1$ since for other pseudospins, the resulting complex matrix is not square. Due to time constraints we used the NEVPT2-SOC Zeeman matrix, but since the hyperfine matrices in this work are calculated at the DFT level, the pseudospin matrices should be constructed from DFT Zeeman matrices.

Chapter 4

Modelling the effect of zero-field splitting on the chemical shifts of lanthanide and actinide compounds.

This chapter presents a slightly improved version of the a paper published in magnetochemistry,[2] references have been merged with those in this thesis.

The project started from the work of Helen Moylan as presented in her PhD thesis, "Computational Prediction of Paramagnetic NMR Chemical Shifts in f-Element Complexes"[137] which established the in-house atomic ZORA (aZORA) gaussian link which was used for all geometry optimisations in this thesis. Moylan's thesis examined pNMR spectra for 14 lanthanide and actinide species, which were f^1 and f^3 species.[28] For the former group a correlation coefficient between experiment and theory of $R^2 = 0.89$ was obtained showing strong correlation. However, for the f^3 species, "the consistency and reliability of the results wavers in comparison with those obtained for f_1."[28] The thesis identifies three opportunities to improve our process.

- Zero-field field splitting (ZFS) was not modelled.
- Paramagnetic spin-orbit corrections to the hyperfine matrices were not added.
- The Zeeman matrix was calculated at CASSCF level, ignoring dynamic correlation.

This paper focuses on modelling ZFS, with a view to establishing its relative importance and in the hope of approaching quantitative results. Using ZFS it successfully qualitatively assigns the ^{1}H, ^{13}C and ^{29}Si shifts of the six f^3 compounds shown in Figure 4.1 and shows that the correlation between calculated and experimental results where ZFS is applied across the five compounds where the experimental shifts have been assigned improves from $R^2 = 0.86$ to $R^2 = 0.90$. Of particular note is that the change due to ZFS for ^{1}H spectra is of the order of ppm and can therefore be very important in correctly assigning closely spaced spectra (see Section 4.5.7).

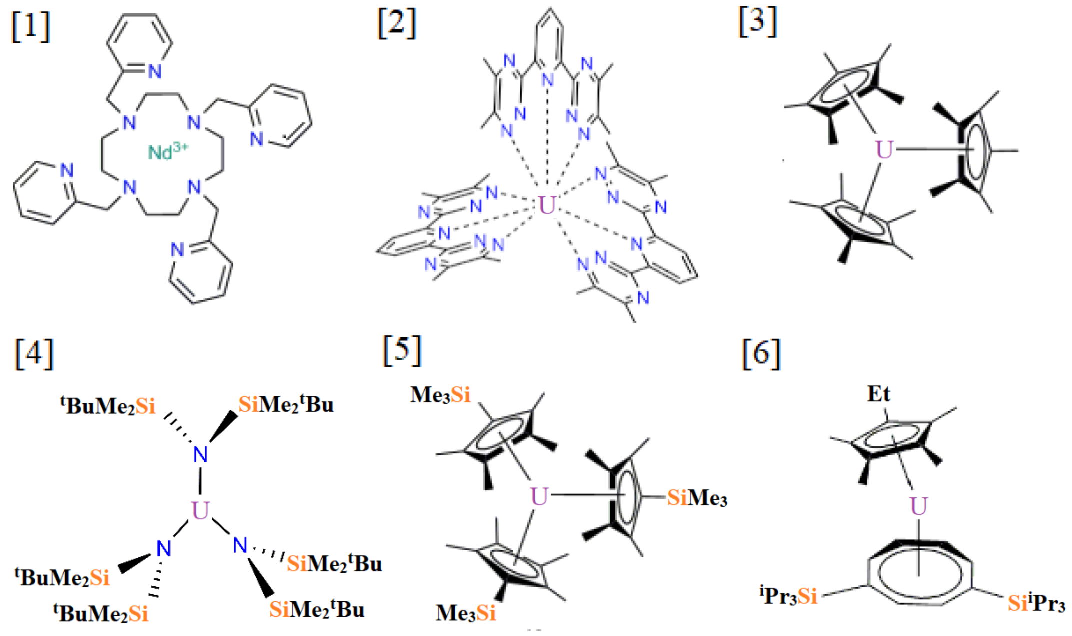

Figure 4.1: The molecules studied in this work, numbered in order of appearance in the main text.

,

In compounds where heavy-atom-light-atom (HALA) effects are important, such as tris(pentamethylcyclopentadienyl)uranium (III), U(C_5Me_5)$_3$, the hyperfine coupling coefficient matrices were also calculated. These were shown to have profound effects on the ^{13}C pNMR shifts of the U(C_5Me_5)$_3$ molecule, with the shift for the ring carbons improving from 182.59 ppm to 341.23 ppm. (Experimental value 324.80 ppm)

Establishing the optimum state averaging

The paper does not give full details of the approach used to establish the optimal state averaging, a topic that is discussed more fully in the following chapter. As an example of this, we consider the procedure used for the second molecule in the study, further discussed in Section 4.5, $\mathrm{U^{III}(MeBTP)_3^{3+}}$, where MeBTP is the 2,6-bis(5,6-dialkyl-1,2,4-triazin-3-yl)pyridine ligand. Figure 4.2 shows the behaviour of the predicted ^{1}H shielding (without ZFS) against the number of quartet states used in the state-averaging for the calculation of the Zeeman matrix, using the state averaging data from reference 137. As can be seen from the figure, after adding 14 quartet states to the SA-CASSCF calculation, the variation in the predicted shift after adding additional quartet states is small. Hence the optimal number of roots was predicted to be 14. A similar process was used to reach the optimal state averaging of 14 quartets and 25 doublets for this molecule, and for all the molecules in this chapter.

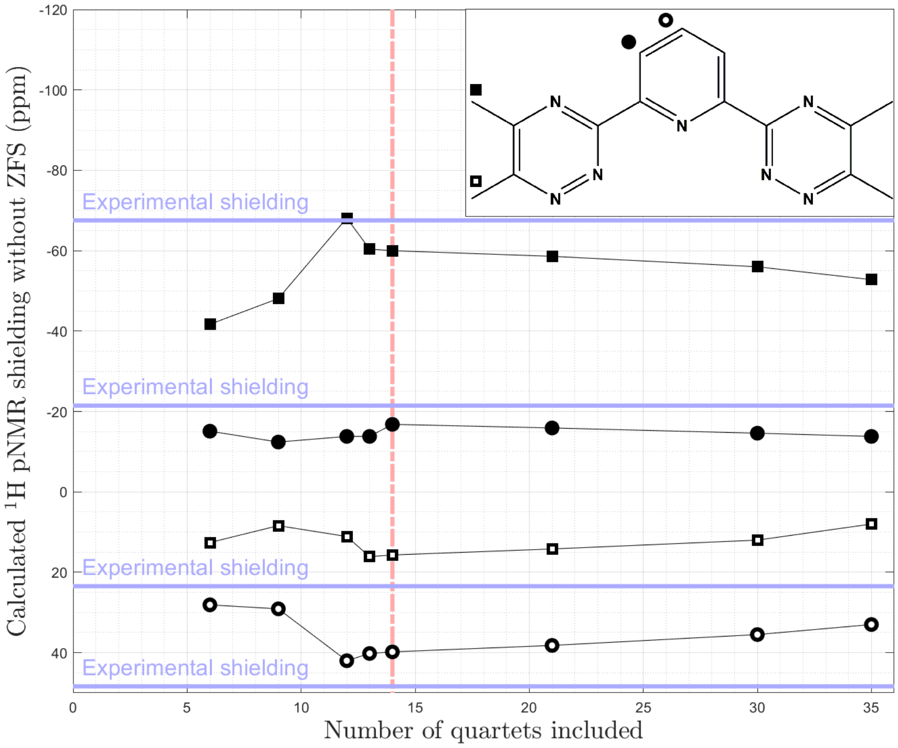

Figure 4.2: ^{1}H Chemical shielding of tris(2,6-bis(5,6-dialkyl-1,2,4-triazin-3-yl)pyridine) uranium(III) against number of quartet states included in the state-averaging for the Zeeman matrix. The MeBTP ligand is shown and the markers for the four chemically equivalent types of hydrogen atom are included. The blue lines show the experimental shielding ($\delta - \sigma_{\text{ref}}$)). for each equivalence group. The dotted red line shows the number of states that were chosen to be included in the final state averaging. Figure based on data from reference 137.

Modelling the effect of zero-field splitting on the ^{1}H, ^{13}C and ^{29}Si chemical shifts of lanthanide and actinide compounds.

Authors:

A. W. Lloyd, H. M. Moylan, J. J. W. McDouall,

Affiliation:

Department of Chemistry, The University of Manchester,
Oxford Road, Manchester, UK

Author contributions:

Original draft preparation AWL, reviewing and editing AWL and JJWM, geometry optimisation HMM, orbital and Zeeman matrix calibration and calculation HMM, application of ZFS AWL, spin-orbit corrected hyperfine calculations JJWM and AWL.

4.1 Abstract

The prediction of paramagnetic NMR (pNMR) chemical shifts in molecules containing heavy atoms presents a significant challenge to computational quantum chemistry. The importance of meeting this challenge lies in the central role that NMR plays in the structural characterisation of chemical systems. Hence there is a need for reliable assignment and prediction of chemical shifts. In a previous study[28] we looked at the computation of pNMR chemical shifts in lanthanide and actinide complexes using a spin Hamiltonian approach. In that study we were principally concerned with molecules with S=1/2 ground states. In the present work we extend that study by looking at the effect of zero-field splitting (ZFS) for six complexes with S=3/2 ground states. It is shown that the inclusion of ZFS can produce substantial shifts in the predicted chemical shifts. The computations presented are typically sufficient to enable assignment of experimental spectra. However for one case, in which the peaks are closely clustered, the inclusion of ZFS re-orders the chemical shifts making assignment quite difficult. We also observe, and echo, the previously reported importance of including the paramagnetic spin-orbit hyperfine interaction for ^{13}C and ^{29}Si atoms,

when these are directly bound to a heavy element and thus subject to heavy-atom-light-atom effects. The necessary computations are very demanding, and more work is needed to find theoretical and computational approaches that simplify the evaluation of this term. We discuss the computation of each term required in the spin Hamiltonian. The systems we study in this work are restricted to a single heavy atom ion (one Nd(III) and five U(III) complexes), but typify some of the computational complexity encountered in lanthanide and actinide containing molecules.

4.2 Introduction

Interest in lanthanide and actinide chemistry continues to expand as new applications are found and existing areas of research are developed. Examples include novel synthetic techniques, such as the development of reusable reagents in the synthesis of cyclic oxycarbon compounds,[138] and the investigation into the nature of actinide containing single molecule magnets.[139]

Radioactivity is the most exploited property of the actinides, as they potentially offer an efficient and low carbon alternative to fossil fuels for large scale energy generation. At the opposite end of the scale, nuclear powered batteries are used for powering small devices such as heart pacemakers.[140] Because of their industrial use, the reprocessing of nuclear waste to extract fissile material and reduce waste volumes is of paramount importance. This leads directly to a demand for better extractants, which in turn needs a better understanding of metal-ligand selectivity for actinide over lanthanide ions.[141] This is an area that benefits from improved and reliable computational modelling techniques.

Nuclear magnetic resonance spectroscopy (NMR) is a well-established and much used analytical tool for characterising molecules and providing insight into their constituent chemical bonds. Many experimental techniques exist for obtaining NMR spectra in diverse chemical and physical situations. The analysis and interpretation of complex spectra for most diamagnetic molecules, that lack heavy nuclei, are routine. Complementary to this experimental work, the development of computational tools for predicting NMR chemical shifts has also become common.[142]

NMR studies of actinide species provide significant challenges to computational techniques. Firstly, for light atoms the effects of relativity are small, and the representation of electron correlation is significantly more important. However the relativistic correction to the energy of an atomic system approximately scales as $(Zc^{-1})^2$.[77] For heavy elements relativistic effects have a profound influence on the ordering of energy levels within their atoms and molecules, and a concomitant effect on the molecular properties of such systems. The computational treatment of relativistic effects begins with scalar relativistic corrections and these are often sufficient for the prediction of molecular geometries. For paramagnetic molecules the presence of the unpaired electronic spin requires that the coupling between orbital and spin angular momenta are treated reliably. This can also have a significant effect on the splitting of electronic energy levels. Equally, spin-dependent properties such as the Zeeman interaction, the hyperfine interaction and the spin-spin interaction will depend on the theoretical method used for their evaluation and require calibration against reliable experimental data. These considerations provide significant challenges for the theoretical formulation of paramagnetic NMR (pNMR) chemical shifts, as well as for their computational realisation. Calculating pNMR shifts of paramagnetic molecules remains a challenging problem that is still under much investigation.[143,144]

Experimental spectra are normally reported as δ shifts. The δ shift is obtained with respect to a reference chemical shift, σ_{ref}. It is conventional to separate the experimental paramagnetic chemical shift σ_{exp} into three terms: the orbital contribution σ_{orb}, which is approximated as the shift that would be observed if the species was diamagnetic, and the contact σ_{c} and pseudocontact σ_{pc} shifts arising from the unpaired electronic spin:

$$\delta = \sigma_{\mathrm{ref}} - \sigma_{\mathrm{exp}} \tag{4.1}$$

$$\sigma_{\mathrm{exp}} = \sigma_{\mathrm{orb}} + \sigma_{\mathrm{c}} + \sigma_{\mathrm{pc}}. \tag{4.2}$$

For simple systems, the contact term relates to the interaction of the unpaired electron spin density and the nuclear magnetic moment at the nucleus. The contact interaction is isotropic. The pseudocontact shift is the residual long range interaction of the spin-dipoles and is anisotropic.[145] Qualitatively the contact shift is traditionally interpreted as arising from the transfer of spin density through bonds and may be associated with covalent interactions. The pseudocontact shift is interpreted as acting through space and is a dipole-dipole type interaction.[131] The theoretical justification for the decomposition into these terms weakens when relativistic treatments are included.[132]

The theoretical framework of pNMR shifts can be formulated in a number of ways. The full pNMR shielding expression in a sum over states (SOS) formalism was derived in references 127 and 130. In reference 146, multireference wavefunction calculations of pNMR shifts were performed, for the first time, directly employing the SOS formalism without reference to the spin Hamiltonian formalism. This study was extended to carbonate complexes of U, Np and Pu.[147] In references[146,147] the wavefunction code used was implemented as part of the OpenMolcas code but has not yet been released. Accordingly, in this work we shall adopt the spin Hamiltonian approach, which represents each of the three paramagnetic operators with a coupling matrix and is detailed in the next section. This approach has the advantage that the necessary components are readily available in many quantum chemistry packages, however the main disadvantage is that the computational framework that is used to calculate each component has a significant effect on the results obtained. To achieve reliable results it is necessary to assess each component, and calibrate the most effective approach against an often limited set of experimental values for similar chemical species. Detailed overviews of the evaluation of spin Hamiltonian parameters in the context of modern computational chemistry are available from Vaara,[148] Bolvin[149] and Autschbach.[150] We shall mostly be concerned with studying the effect of zero-field splitting (ZFS) on the predicted ^{1}H, ^{13}C, ^{29}Si shifts of six compounds. We will illustrate situations where the inclusion of ZFS causes a reordering in the predicted ^{1}H shifts, and where the inclusion of spin-orbit effects on the hyperfine term for the ^{13}C shifts of nuclei involved in a η-coordinated C-U bond dominate the hyperfine interaction. With the exception of the first example, our results are accurate enough to enable qualitative assignment of observed shifts.

4.3 The spin Hamiltonian approach to paramagnetic NMR

Applying a magnetic field $\mathbf{B}$ to an isolated atom with nuclear spin I_{nuc} results in each energy level splitting by $2\gamma_{\text{nuc}}|\mathbf{B}|$, where γ_{nuc} is the magnetogyric ratio of the nucleus under investigation. In any electronic system, the circulation of electrons induced by the applied magnetic field generates an opposing magnetic field. This effect is represented by $\boldsymbol{\sigma}_{\text{orb}}$, the chemical shift or orbital shielding tensor. For a diamagnetic molecule, the Hamiltonian corresponding to the energy shift, in atomic units, is given by

$$\hat{\mathcal{H}}_{\text{NMR}} = -\gamma_{\text{nuc}}\mathbf{B} \cdot (\mathbf{I}_3 - \boldsymbol{\sigma}_{\text{orb}}) \cdot \hat{\mathcal{I}}_{nuc}, \tag{4.3}$$

However for a system with unpaired electrons, there is a permanent magnetic moment associated with the electronic spin. It is energetically favourable for this to align with an applied magnetic field and the resulting (thermally averaged) dipole must be accounted for. The corresponding paramagnetic NMR Hamiltonian is given by:[108–110,133]

$$\hat{\mathcal{H}}_{\text{pNMR}} = -\gamma_{\text{nuc}}\mathbf{B} \cdot (\mathbf{I}_3 - \boldsymbol{\sigma}_{\text{orb}}) \cdot \hat{\mathcal{I}}_{nuc} + \mu_B \, \mathbf{B} \cdot \, \mathbf{g} \cdot \hat{\tilde{\mathbf{S}}} + \hat{\tilde{\mathbf{S}}} \cdot \mathbf{D} \cdot \hat{\tilde{\mathbf{S}}} + \hat{\tilde{\mathbf{S}}} \cdot \mathbf{A} \cdot \hat{\mathcal{I}}_{nuc}. \tag{4.4}$$

The Zeeman coupling matrix, $\mathbf{g}$, represents the interaction of the electronic spin-dipole with the applied magnetic field. An effective parameter, referred to as the pseudospin $\tilde{\mathbf{S}}$, is introduced. In the absence of spin-orbit coupling $\tilde{\mathbf{S}} = \mathbf{S}$, which is an often used approximation. For molecules where the spin-orbit interaction is strong, the effective degeneracy of the molecule is reduced so a smaller effective spin $\tilde{\mathbf{S}}$ is chosen based on the splitting pattern of the electronic states.[149] The interaction between the nuclear and electronic spin-dipoles is represented by the hyperfine coupling matrix, $\mathbf{A}$. In a system with more than one unpaired electron, the interaction of the electron spin-dipoles is represented by the ZFS or $\mathbf{D}$ tensor.

4.3.1 The orbital shielding tensor, $\boldsymbol{\sigma}_{\mathbf{orb}}$

For a diamagnetic molecule the orbital, or Ramsey, shielding matrix[126] is the only contribution to the observed chemical shift and as such, its isotropic value is readily extractable from NMR spectra. For a paramagnetic molecule it is not possible to directly extract this term and as a result, the reliability of any computational method must be assessed on diamagnetic analogues of the species under investigation. Because magnetic fields are defined by the action of an infinitesimal rotation of a vector potential and this operation is independent of the origin of the co-ordinate system used, the calculation of magnetic properties has an artificial dependence on the choice of origin, known as gauge dependence. The gauge dependence vanishes in the limit of the exact wavefunction. It has been demonstrated that for calculations targeting a single nucleus, the dependence is minimised by setting the origin at the nucleus. For molecules in general, choosing the centre of electronic charge as the origin minimises gauge dependence,[105] but the most reliable approach is to employ gauge-including atomic orbitals (GIAO),[151,152] which remove the gauge dependence.

For actinide compounds, modelling relativistic effects is essential and many frameworks can be used. The relativistic Dirac equation can be satisfied by a four component wavefunction, partitioned into pairs of electronic and positronic spinors. The presence of the positronic solution hinders a variational approach, since simply minimising the energy is no longer possible due to an unbounded and infinite set of negative positronic states. For four component methods, this issue must be addressed, *e.g.* by kinetic balance.[39] However, since the positronic component is much smaller, efficient two component techniques have been developed to eliminate it. These techniques produce a spin-free (scalar) and a spin-dependent component. Observables in the Dirac framework are implicitly dependent on all four components, and the corresponding two component operator erroneously does not involve the full solution. This effect is called the picture change error[150] and can be addressed using a transformation of the operator equivalent to that used to transform the four component wavefunction to a two component wavefunction.

Scalar relativistic approaches such as the zero-order regular approximation (ZORA),[153] and the Douglas-Kroll Hamiltonian (DKH)[154] are implemented in a number of quantum chemistry packages. In principle, the non-linear dependence of the ZORA electrostatic potential that is used as a perturbation is inherently gauge dependent,[153] and this is not resolved by using GIAOs, although in practice the error introduced is small for large basis sets.[135,155]

4.3.2 The Zeeman coupling matrix, g

The Zeeman coupling matrix, **g**, more commonly referred to as the "g tensor",[*] represents the effect of the magnetic field on the average electronic spin-dipole. With the addition of spin-orbit coupling, the electronic spin of a molecule is no longer well defined and the pseudospin parameter is introduced to describe the observed splitting of spin multiplets.[108] The theory and computation of spin-orbit coupling has a detailed review by Marian.[87] Because spin-orbit coupling has such a large effect on the effective spin-dipole, the reliable evaluation of the **g** tensor is directly dependent on how well this effect is modelled.

For cases of a weak spin-orbit interaction, density functional theory (DFT) and linear response theory (DFT-LRT) can successfully be used.[156] However DFT-LRT is unable to produce reliable results where degeneracies or low-lying excited states exist, or where the ground state is multiconfigurational in nature. Instead we have used a multiconfigurational approach that can describe the ground and excited states equally well, *i.e.* state-averaged complete active-space self-consistent field theory (SA-CASSCF). It is possible to include spin-orbit effects at a variational level. This type of approach is available in the SPOCK-CI program,[157] which is a spin-orbit configuration interaction (CI) package. While this would be the preferred approach it is demanding and perturbation techniques can be used to represent the interaction more efficiently.

One multiconfigurational approach is to use double perturbation theory and a sum over states (SOS) formalism to generate the **g** tensor directly. The double perturbation theory approach can be modified for degenerate systems, but for nearly degenerate systems, individual contributions to the SOS depend inversely on the energy difference

---

[*] Since it relates two quantities defined in space and spin coordinate frames respectively it is not a true tensor.

between states, if this energy difference is small the resulting perturbation theory can be divergent. The spin-orbit term can also be applied using a quasi-degenerate perturbation theory (QDPT) approach which constructs a matrix over the manifold of spin states. The diagonal elements are taken as the energies of the spin pure states (*e.g.* from a SA-CASSCF calculation), and the off-diagonal elements couple the spin free states under the action of the spin-orbit operator. Diagonalisation gives the spin-orbit energy levels and wavefunctions.

In the case of a molecule with spin $S = \frac{1}{2}$, the lowest energy pair of spin-orbit wavefunctions must be degenerate in the absence of an applied magnetic field due to Kramers theorem,[158] which states that the degeneracy of a state with half-integer spin must be at least two in the absence of a magnetic field. The energy splitting ΔE_{Zeeman} upon application of a magnetic field is given by the difference in expectation values of the Kramers pair, represented by $|\Phi_{\pm 1/2}\rangle$, the subscript indicating the sign of the associated pseudospin, that is,

$$\begin{aligned}\Delta E_{\text{Zeeman}} &= \mu_B \left\langle \Phi_{1/2} \right| - \mathbf{B} \cdot \hat{\boldsymbol{\mu}} \left| \Phi_{1/2} \right\rangle - \mu_B \left\langle \Phi_{-1/2} \right| - \mathbf{B} \cdot \hat{\boldsymbol{\mu}} \left| \Phi_{-1/2} \right\rangle . && (4.5)\\ &= \mu_B \left\langle \Phi_{1/2} \middle| \mathbf{B} \cdot \mathbf{g} \cdot \hat{\hat{\mathbf{S}}} \middle| \Phi_{1/2} \right\rangle - \mu_B \left\langle \Phi_{-1/2} \middle| \mathbf{B} \cdot \mathbf{g} \cdot \hat{\hat{\mathbf{S}}} \middle| \Phi_{-1/2} \right\rangle . && (4.6)\end{aligned}$$

In the above equation, the magnetic moment operator $\hat{\boldsymbol{\mu}}$ is related to the magnetogyric ratio for the electron, $g_e = 2.0023193$ and the spin, $\hat{\mathcal{S}}$, and angular momentum, $\hat{\mathcal{L}}$, operators by $\hat{\boldsymbol{\mu}} = -\mu_B(\hat{\mathcal{L}} + g_e \hat{\mathcal{S}})$. Squaring Eqs. 4.5 and 4.6 gives a relationship between the related tensor $\mathbf{G} = \mathbf{g} \cdot \mathbf{g}^T$, called the Abragam-Bleaney tensor,[120] and the matrix elements of $\boldsymbol{\mu}$ in the Kramers pair basis. The principal values of the Zeeman matrix are the square roots of the eigenvalues of the Abragam-Bleaney tensor.[159] While this relationship is only valid for $S = \frac{1}{2}$, similar ones have been derived for $S > \frac{1}{2}$.[122] This process has two drawbacks, the resulting $\mathbf{g}$ matrix is necessarily symmetric, and because of the use of a square root precursor matrix, there is a sign indeterminacy for the principal values of $\mathbf{g}$. For weak spin coupling, the principal values must be close to the free electron value, and therefore positive. Otherwise, the signs can be inferred by exploiting relationships between the sign of combinations of the principal values and the sign of combinations of the eigenvalues of the $\boldsymbol{\mu}_\kappa$ matrices (where κ represents a cartesian direction).[122]

The final consideration is the treatment of the spin-orbit operator. It is possible to use the full two electron form of the operator, but as with two-electron repulsion integrals, this results in a considerable computational cost. It is often preferable to use a one-electron operator. Three operators are in common use, the first an empirical operator based on an effective nuclear charge calibrated against calculations on small molecules as developed by Kosekii.[115–117] The second is the spin-orbit mean field (SOMF) operator which forms an effective one-electron operator, similar to the Fock operator in Hartree-Fock theory. Finally the atomic mean-field approximation (AMFI) to the spin–orbit operator forms a similar one-electron operator, but discards the multicentre two-electron spin-orbit integrals, exploiting the short range of the two-electron spin-orbit operator while retaining the simpler one-centre, two-electron integrals.[114,160]

4.3.3 The zero-field splitting (ZFS) tensor, D

The ZFS interaction primarily represents the interelectronic dipolar interaction, and can be split into a first order term, directly corresponding to spin-spin interaction and a second order term representing corrections due to spin-orbit coupling.[161] When represented over a manifold of spin states S, M_S, the first order term is diagonal. It is evaluated over the ground state eigenfunction. The second order term includes off-diagonal elements with selection rule $-1 \leqslant \Delta S, \Delta M_S \leqslant 1$. This term must be evaluated over ground and excited states. Available computational approaches are similar to those used for the Zeeman matrix. Single reference wavefunction methods include a modified DFT coupled-perturbed approach to handle the spin-orbit perturbation.[162] In multireference approaches, the spin-spin contribution can be obtained from first-order perturbation theory, while the spin-orbit contribution requires second-order perturbation theory. However, as for the Zeeman matrix, near degeneracy often produces spurious results. A QDPT effective Hamiltonian approach gives more reliable ZFS tensors in such cases,[32] and it is the latter approach that we have adopted. We shall outline below for each molecule the choice of active space used and states averaged in producing the ZFS tensor.

4.3.4 The hyperfine coupling (HFCC) matrix, A

A set of generalised hyperfine operators for a nucleus, K, $\hat{\boldsymbol{\mathcal{F}}}^{\mathbf{S}}_{\kappa}$ (where κ represents a cartesian direction), can be defined by its relation to the Hamiltonian for the hyperfine interaction, $\hat{\mathcal{H}}^{\mathrm{HFC}}_{K}$, and the nuclear magnetic moment operator, $\hat{\boldsymbol{\mu}}_K$ via

$$\hat{\mathcal{H}}^{\mathrm{HFC}}_{K} = \hat{\boldsymbol{\mathcal{F}}}^{\mathbf{S}}_{K} \cdot \hat{\boldsymbol{\mu}}_K = g_K \mu_B \hat{\boldsymbol{\mathcal{F}}}^{\mathbf{S}}_{K} \cdot \hat{\mathcal{I}}_K, \tag{4.7}$$

where g_K is the g-factor for the target nucleus. Like the Abragam-Bleaney tensor, this is a real tensor.

The more commonly reported hyperfine coupling constant (HFCC) matrix, $\mathbf{A}_K$, represents the interaction between the nuclear and the electronic spin-dipoles. Like the Zeeman matrix, the HFCC matrix can be recovered by forming the $\mathbf{A}^T \cdot \mathbf{A}$ product. *e.g.* For an electronic Kramers' doublet, the HFCC matrix is given by[149]

$$\left[\mathbf{A}^T_K \mathbf{A}_K\right]_{\kappa \upsilon} = g_K^2 \mu_B^2 \sum_{S=\pm 1/2} \sum_{S'=\pm 1/2} \left\langle \Phi_S | \hat{\boldsymbol{\mathcal{F}}}^{\mathbf{S}}_{K,\kappa} | \Phi_{S'} \right\rangle \left\langle \Phi_{S'} | \hat{\boldsymbol{\mathcal{F}}}^{\mathbf{S}}_{K,\upsilon} | \Phi_S \right\rangle \tag{4.8}$$

A wide range of approaches are available, such as DFT linear response and SOS double perturbation methods. However, the hyperfine interaction has strong inverse dependence on electron-nucleus separation and is strongly influenced by relativistic effects.[77] Relativistic corrections cannot be ignored, at least scalar relativistic treatments are needed for a reliable approach.[135] However additional corrections for spin-orbit coupling are computationally demanding, since three sets of coupled-perturbed equations must be solved for each nucleus. In principle, it is possible to avoid the solution of the CP-SCF equations by adopting a 4-component approach,[163,164] although this has an associated computational overhead in performing the 4-component calculation. For a light target nucleus the corrections are small and often can be safely ignored, except when the target nucleus is bonded to a heavy nucleus; the latter can have a substantial effect on the electronic structure of its neighbour, a phenomenon referred to as the "heavy atom-light atom" (HALA) effect,[165] and the spin-orbit correction to the hyperfine interaction must be included for reliable results.

A remaining issue in predicting isotropic chemical shifts is due to our calculations being based on a single geometry, ignoring vibrational and rotational motion. This is a valid approach for electronic transitions which operate on a much faster timescale than significant nuclear motion, but nuclear transitions are slow enough for the motion to be significant. The pNMR measurement is an average over nuclear motion. It is necessary to calculate the orbital shielding and hyperfine matrices for all nuclei and then group them by chemically equivalent nuclei, and generate the averaged hyperfine matrices over these groups.

4.3.5 Zero-field splitting — theory[†]

Ramsey[125–127] posited that because nuclear motion is much slower than electronic motion, the nuclear magnetic moment $\boldsymbol{\mu}_{\text{nuc}}$ changes much more slowly than the electronic magnetic moment $\boldsymbol{\mu}$, and can be treated as time-independent, effectively as a parameter. Assuming equilibrium is reached within experimental time scales, the observed NMR shielding tensor can be shown[128] to be given by the second derivative of the electronic energy with respect to the components of the magnetic field and the nuclear magnetic moment at the limit of zero field and magnetic moment

$$\sigma_{\kappa\upsilon} = \left.\frac{\partial^2 E}{\partial B_\kappa \, \partial \mu_{\text{nuc},\nu}}\right|_{\substack{\mathbf{B}\to\mathbf{0} \\ \boldsymbol{\mu}_{\text{nuc}}\to\mathbf{0}}} . \tag{4.9}$$

The resulting energy levels are often close enough to have significant occupation above the ground state, so Boltzmann averaging of observables is required. The Boltzmann average $\langle A \rangle_0$ of a set of observables $\{A_n\}$ with n energy levels, $\{W_n\}$ is given by:

$$\langle A \rangle_0 = \frac{\sum_n A_n e^{-W_n/k_B T}}{\sum_n e^{-W_n/k_B T}} . \tag{4.10}$$

Following Moon and Patchkovskii's summary[128] the approach we use is based on Kurland and McGarvey's work,[129] which allows the pNMR Hamiltonian to be split into Zeeman and hyperfine terms. The field-independent form of the shielding tensor[128] can be decomposed into diamagnetic and paramagnetic shielding tensors, $\boldsymbol{\sigma}^{\text{orb}}$ and $\boldsymbol{\sigma}^{\text{p}}$ respectively

$$\sigma^{\text{orb}}_{\kappa\upsilon} = \left\langle \frac{\partial^2 E}{\partial B_\kappa \, \partial \mu_{\text{nuc},\nu}} \right\rangle_0 \qquad \sigma^{\text{p}}_{\kappa\upsilon} = -\frac{1}{k_B T} \left\langle \frac{\partial E}{\partial B_\kappa} \cdot \frac{\partial E}{\partial \mu_{\text{nuc},\upsilon}} \right\rangle_0 .$$

Taking $\mathbf{g}$ and $\mathbf{A}$ as the following partial derivatives

$$g_{\kappa\upsilon} = \left.\frac{\partial^2 E}{\partial B_\kappa \, \partial S_\nu}\right|_{\mathbf{B}\to\mathbf{0}} \qquad A_{\kappa\upsilon} = \gamma_{\text{nuc}} \left.\frac{\partial^2 E}{\partial S_\kappa \, \partial \mu_{\text{nuc},\nu}}\right|_{\boldsymbol{\mu}_{\text{nuc}}\to\mathbf{0}} \tag{4.11}$$

[†] This subsection (up to Eq 4.15) is a repeat of Section 3.10 and is included for completeness.

it can be shown that, in the low spin-orbit coupling limit[130–132]

$$\sigma^{\mathrm{p}}_{ab} = -\frac{1}{k_B T}\left\langle \frac{\partial E}{\partial B_a}\cdot\frac{\partial E}{\partial \boldsymbol{\mu}_{\mathrm{nuc,b}}}\right\rangle_0 \tag{4.12}$$

$$= -\frac{1}{\gamma_{\mathrm{nuc}} k_B T}\left\langle (\mathbf{g}\cdot\mathbf{S})_a(\mathbf{S}\cdot\mathbf{A})_b\right\rangle_0 \tag{4.13}$$

$$= -\frac{1}{\gamma_{\mathrm{nuc}} k_B T}\mathbf{g}\cdot\mathbf{Z}\cdot\mathbf{A} = -\frac{1}{\gamma_{\mathrm{nuc}} k_B T}\sum_{\kappa\upsilon}^{\{x,y,z\}} g_{a\kappa}Z_{\kappa\upsilon}A_{\upsilon b}\ , \tag{4.14}$$

where $\mathbf{Z}$ is a 3×3 coupling matrix, the $\kappa\upsilon^{\mathrm{th}}$ element of which can be thought of as the expectation value of a Boltzmann averaged combination of transformed $\hat{\mathcal{S}}_\kappa$ and $\hat{\mathcal{S}}_\upsilon$ operators, *i.e.* a spin-spin interaction;[130]

$$Z_{\kappa\upsilon} = \left\langle \int_0^{1/(k_B T)} \mathrm{d}\beta\ e^{\beta\hat{\mathcal{H}}_0}\hat{\mathcal{S}}_\kappa\ e^{-\beta\hat{\mathcal{H}}_0}\hat{\mathcal{S}}_\upsilon\right\rangle_0 \tag{4.15}$$

In the absence of zero-field splitting, $Z_{\kappa\upsilon} = \frac{1}{3}S(S+1)\delta_{\kappa\upsilon}$, where $\delta_{\kappa\upsilon}$ is the Kronecker delta and the resulting matrix is diagonal.

Pennanen and Vaara[133] formulated a practical approach to modelling ZFS in the context of modern quantum chemistry, the "no coupling approximation." This requires the formation of the $(2S+1)\times(2S+1)$ matrix, $\mathbf{S}^T\cdot\mathbf{D}\cdot\mathbf{S}$, which is then diagonalised to obtain eigenvalues E_n and eigenstates $|n\rangle$, the latter being linear combinations of pure spin states $|Sm_S\rangle$. Soncini and van den Heuvel[130] presented a fully coupled approach, which can be expressed as

$$Z_{\kappa\upsilon} = \omega^{-1}\sum_{nm}^{\text{eigenstates}} q_{nm}\langle n|\hat{\mathcal{S}}_\kappa|m\rangle\langle m|\hat{\mathcal{S}}_\upsilon|n\rangle \qquad \text{where} \qquad \omega = \sum_n e^{-E_n/k_B T}, \tag{4.16}$$

with q_{nm} being a Boltzmann weighting term

$$q_{nm} = \begin{cases} e^{-E_n/k_B T} & E_m = E_n \\ -\frac{k_B T}{E_n - E_m}\left(e^{-E_n/k_B T} - e^{-E_m/k_B T}\right) & \text{otherwise.} \end{cases} \tag{4.17}$$

Pierre Curie observed that the magnetisation of a paramagnetic material is approximately inversely proportional to the temperature. If the occupation of the ground state (*i.e.* its Boltzmann weight) is nearly one, this is observed for a doublet and in the no coupling approximation. In the coupling described in Eqs. 4.16 and 4.17, the collection of terms corresponding to $E_m = E_n$ have approximate $1/T$ dependence and the combined contribution is referred to as the Curie term. The remaining terms have an approximate $1/T^2$ dependence.

The derivation used for both approaches assumes weak spin-orbit coupling. Van den Heuvel and Soncini presented an extended approach[1] which is valid for strong spin-orbit coupling. Because of its potential as an improved treatment, an outline of the approach is presented in appendix A. The approach depends on using Eq. 3.70 to form irreducible tensor operator (ITO) representations of the $\boldsymbol{\mu}$ and $\mathbf{F}_K$ matrices introduced in sections 3.10.1[‡] respectively.

4.3.6 Contact and pseudocontact shifts

The separation of the paramagnetic chemical shift into contact and pseudocontact shifts provides insight into the chemical environment of the target nucleus, however as additional effects are included in the model, the separation becomes increasingly difficult and debatable. The simplest approach is to decompose the Zeeman and hyperfine coupling matrices into isotropic and anisotropic components, and evaluate their nature and relative sizes in terms of their scaling with respect to the fine structure constant α.[133,166]

The spin-orbit operator is multiplied by α^2, where $\alpha = 1/137\,\text{a.u.}$ is the fine structure constant, (*i.e.* the reciprocal of the speed of light). The typical relative energetic contribution of the terms in the decomposition of the Zeeman matrix can be assessed by ordering them in terms of their dependence on α^2. The only zeroth-order term corresponds to the magnetogyric ratio of the free electron, the remaining terms relate the g-shift, $\mathbf{\Delta g} = \mathbf{g} - g_e\mathbf{I}_3$ which is decomposed into an isotropic scalar g-shift, $\Delta g_{\text{iso}} = \frac{1}{3}\text{trace}\left(\mathbf{\Delta g}\right)$, and the remaining anisotropic matrix, $\mathbf{\Delta\tilde{g}} = \mathbf{\Delta g} - \Delta g_{\text{iso}}\mathbf{I}_3$.

[‡] This was published as an appendix that was an earlier version of 3.10.1.

The hyperfine matrix has no first order terms, but is entirely second order in the absence of relativistic corrections and we will denote the scalar relativistic[§] matrix as $\mathbf{A}^{\mathrm{SR}}$. This is decomposed into its isotropic scalar $A_{\mathrm{iso}} = \frac{1}{3}\mathrm{trace}\left(\mathbf{A}^{\mathrm{SR}}\right)$ and an anisotropic spin-dipolar matrix $\mathbf{A}^{\mathrm{SD}} = \mathbf{A}^{\mathrm{SR}} - A_{\mathrm{iso}}\mathbf{I}_3$, which is symmetric. The relativistic corrections are entirely fourth order, and are separated into an isotropic scalar $A_{\mathrm{iso}}^{\Delta\mathrm{SO}}$ and an anisotropic $\mathbf{A}_{\mathrm{aniso}}^{\Delta\mathrm{SO}}$ matrix. The anisotropic component is further split into a symmetric matrix $\mathbf{A}^{\Delta\mathrm{SO,SYM}} = \frac{1}{2}\left(\mathbf{A}_{\mathrm{aniso}}^{\Delta\mathrm{SO}} + \left(\mathbf{A}_{\mathrm{aniso}}^{\Delta\mathrm{SO}}\right)^{\mathrm{T}}\right)$ and an asymmetric matrix $\mathbf{A}^{\Delta\mathrm{SO,AS}} = \mathbf{A}_{\mathrm{aniso}}^{\Delta\mathrm{SO}} - \mathbf{A}^{\Delta\mathrm{SO,SYM}}$. These decompositions are outlined in Table 4.1.

Table 4.1: Decomposition of the components of the Zeeman and hyperfine coupling matrices by isotropic and anisotropic components, $\mathbf{I}_3$ indicates a 3×3 identity matrix.

Matrix	O(1) component	O(α^2) components	O(α^4) components
$\mathbf{g}$	$g_e\mathbf{I}_3$	$\Delta g_{\mathrm{iso}}\mathbf{I}_3,\ \boldsymbol{\Delta}\tilde{\mathbf{g}}$	
$\mathbf{A}$		$A_{\mathrm{iso}}\mathbf{I}_3,\ \mathbf{A}^{\mathrm{SD}}$	$A_{\mathrm{iso}}^{\Delta\mathrm{SO}}\mathbf{I}_3,\ \mathbf{A}^{\Delta\mathrm{SO,SYM}},\ \mathbf{A}^{\Delta\mathrm{SO,AS}}$

In the absence of ZFS, $\boldsymbol{\sigma}^{\mathrm{p}}$ is directly proportional to $\mathbf{g} \cdot \mathbf{A}$, and the decomposition of product of the matrices, $\mathbf{g} \cdot \mathbf{A}$ provides useful insight into the covalency of the metal-ligand bond. This decomposition has fifteen terms, six of which are sixth order in α. In this work we use two methods to qualitatively divide the paramagnetic chemical shift into contact and pseudocontact contributions.[128] The first method is to relate the terms derived from isotropic scalars of the hyperfine matrix to the contact shift and those from the anisotropic matrices to the pseudocontact shift.[131,135] The second is to truncate the expansion to fourth order, resulting in nine remaining terms. The remaining difference is that all contributions with an anisotropic component, most notably the term $A_{\mathrm{iso}}\boldsymbol{\Delta}\tilde{\mathbf{g}}$ (a contact term in scheme 1) are considered to relate to the pseudospin.[132,167,168] We will refer to these decompositions as methods 1 and 2 respectively, as outlined in Table 4.2.

Method 2 is elaborated on by Kaupp,[143] who presents a separation of terms for a doublet. In EPR terminology, $A_{\mathrm{iso}}^{\Delta\mathrm{SO}}$ is sometimes referred to as the pseudocontact term.

[§] Strictly the scalar relativistic corrections implicitly include $O(\alpha^4)$ terms, but to simplify the analysis we will consider $\mathbf{A}^{\mathrm{SR}}$ to be a $O(\alpha^2)$ term.

Table 4.2: Classification of components of the $\mathbf{g} \cdot \mathbf{A}$ matrix.

				Order	Decomposition	
Hyperfine		Zeeman		in α	Method 1	Method 2
Isotropic	A_{iso}	Free electron	g_e	2nd	Contact	Contact[1]
Scalar		Iso. g-shift	Δg_{iso}	4th	Contact	Contact[1]
Relativistic		Aniso. g-shift	$\boldsymbol{\Delta}\tilde{\mathbf{g}}$	4th	Contact	Pseudocontact[2]
Isotropic	$A_{\text{iso}}^{\Delta\text{SO}}$	Free electron	g_e	4th	Contact	Contact[1]
SO Correction		Iso. g-shift	Δg_{iso}	6th	Contact	—
		Aniso. g-shift	$\boldsymbol{\Delta}\tilde{\mathbf{g}}$	6th	Contact	—
Anisotropic	$\mathbf{A}^{\text{SD}}$	Free electron	g_e	2nd	Pseudocontact	Pseudocontact[2]
Scalar		Iso. g-shift	Δg_{iso}	4th	Pseudocontact	Pseudocontact[2]
Relativistic		Aniso. g-shift	$\boldsymbol{\Delta}\tilde{\mathbf{g}}$	4th	Pseudocontact	Pseudocontact[3]
Symmetric	$\mathbf{A}^{\Delta\text{SO,SYM}}$	Free electron	g_e	4th	Pseudocontact	Pseudocontact[2]
Anisotropic		Iso. g-shift	Δg_{iso}	6th	Pseudocontact	—
SO Correction		Aniso. g-shift	$\boldsymbol{\Delta}\tilde{\mathbf{g}}$	6th	Pseudocontact	—
Asymmetric	$\mathbf{A}^{\Delta\text{SO,AS}}$	Free electron	g_e	4th	Pseudocontact	Pseudocontact
Anisotropic		Iso. g-shift	Δg_{iso}	6th	Pseudocontact	—
SO Correction		Aniso. g-shift	$\boldsymbol{\Delta}\tilde{\mathbf{g}}$	6th	Pseudocontact	—

[1] For a doublet is a pure contact term, relates isotropic spin density at the atom.[143]

[2] For a doublet is a pure spin-dipolar term.

[3] For a doublet relates to spin density in p orbitals.

The anisotropic matrices are traceless, so without ZFS, $\mathbf{Z}$ is diagonal, so only the isotropic hyperfine/isotropic Zeeman and the anisotropic hyperfine/anisotropic Zeeman terms produce an interaction with a non-zero trace. In the absence of spin-orbit coupling these interactions can unambiguously be related to the contact and pseudocontact terms, respectively. However the nature of the fourth order spin-orbit corrections to the hyperfine is unclear and the application of zero-field splitting results in non-diagonal elements in $\mathbf{Z}$ which couple isotropic and anisotropic terms. As a result, the separation of magnetic chemical shifts into contact, bond mediated, effects and pseudocontact, dipolar-interaction, effects is not strictly consistent. With this in mind, we will use both methods to analyse our results.

The truncation to fourth order terms used in the second method is based on the assumption that the order in α determines the size of the contributions. This implies that the spin-orbit corrections to the hyperfine are small compared to the scalar relativistic hyperfine. If these, computationally demanding, corrections are not included, no sixth-order terms are present, so the final shift is the same for both decompositions. However in cases of hyperfine calculations on heavy nuclei or on nuclei that are bonded to heavy nuclei, this assumption is not valid: spin-orbit corrections typically scale in terms of the atomic number to the fourth power (Z^4) making the spin-orbit correction considerably larger. In such cases, the isotropic spin-orbit correction may be larger than the isotropic value of the uncorrected hyperfine matrix.[149]

4.3.7 An example of a spin-orbit description of a molecular ground state

Our calculations allow for mixing of electronic states under the action of the spin-orbit operator. The number of electronic states included in each calculation was motivated by the quality of the Zeeman matrix produced, as discussed in our previous paper.[28] As an example, for our first actinide molecule (section 4.5.1) we performed state-averaged CASSCF calculations over 14 quartet and 25 doublet states[¶] to generate the Zeeman and ZFS matrices. The resulting ground state wavefunction, corrected for spin-orbit coupling is detailed in Table 4.3.

Chibotaru states that the spin Hamiltonian approach is applicable when a QDPT-SOC calculation is convergent for a manifold of spin states,[122] and later he discusses the differences between the fictitious pseudospin and the spin. In the limiting cases of weak SOC the pseudospin can be set equal to the spin. In the limiting case of strong SOC, the degeneracy of the states is broken in low symmetry molecules, and the pseudospin mirrors a doublet, $\tilde{\mathbf{S}} = 1/2$.[149] Chibotaru considers actinide ionic complexes to fall in the intermediate range,[122] where the model Hamiltonian cannot be defined by the total angular momentum because of the mixture of states that we describe above, however he does still associate the pseudospin with a manifold of electronic states, and so this is the approach we employ. Furthermore, in systems for which $S \geqslant 3/2$ the calculation

---

[¶] *i.e.* being a subset of the 35 quartet and 112 doublet states implicitly included in the CASSCF(7,3) configuration state function (CSF) expansion.

ideally should include third order tensorial spin, Zeeman and Hyperfine matrices,[1] as we summarise in the appendix. However, it must be noted that to implement this scheme would require generalised hyperfine tensors that are not currently generally available. We are not aware of the use of the generalised hyperfine operators by any other researchers.

In Table 4.3 we list the relative energies of the first five Kramers pairs for all molecules studied in this work.

Table 4.3: One of the Kramers' pair wavefunctions of $U(MeBTP)_3^{3+}$, spin-orbit corrected, SA-CASSCF(3,7) wavefunction, with 14 quartet and 25 doublet states. The second state can be inferred, via Kramers degeneracy, exchanging the weights of each $+M_S$ state with that of the corresponding $-M_S$ state. States with weight less than 0.01 are omitted.

Quartet(a)								Doublet(b)			
$\lvert\frac{3}{2},\frac{3}{2}\rangle$		$\lvert\frac{3}{2},\frac{1}{2}\rangle$		$\lvert\frac{3}{2},-\frac{1}{2}\rangle$		$\lvert\frac{3}{2},-\frac{3}{2}\rangle$		$\lvert\frac{1}{2},\frac{1}{2}\rangle$		$\lvert\frac{1}{2},-\frac{1}{2}\rangle$	
Weight	Root	Weight	Root	Weight	Root	Weight	Root	Weight	Root	Weight	Root
0.076	1	0.068	2	0.021	1	0.048	1	0.012	5	0.011	3
0.048	2	0.020	3	0.024	2	0.089	3	0.017	7	0.019	6
0.064	3	0.042	4	0.019	3	0.021	4	0.030	10	0.012	9
0.018	5	0.014	9	0.051	5					0.017	10
0.017	6	0.012	12	0.011	11						

(a) Energies of first 12 quartet spin-free SA-CASSCF states, measured from lowest root are (1) 0 cm^{-1}, (2) 447 cm^{-1}, (3) 448.1 cm^{-1}, (4) 671.4 cm^{-1}, (5) 684.7 cm^{-1}, (6) 773.7 cm^{-1}, (7) 1457.9 cm^{-1}, (8) 1712.7 cm^{-1}, (9) 1784.5 cm^{-1}, (10) 1985.8 cm^{-1}, (11) 2121.2 cm^{-1}, (12) 2164.9 cm^{-1}.

(b) Energies of first 10 doublet states, measured from lowest root in (a) are (1) 2971.7 cm^{-1}, (2) 3022.4 cm^{-1}, (3) 3079.2 cm^{-1}, (4) 3124.8 cm^{-1}, (5) 3766.2 cm^{-1}, (6) 3788.9 cm^{-1}, (7) 4100.9 cm^{-1}, (8) 4174.8 cm^{-1}, (9) 4421.0 cm^{-1}, (10) 4439.1 cm^{-1},

Table 4.4: Relative energies (cm^{-1}) for the 10 lowest spin-orbit states of the six compounds studied here, showing the increased gap between first and second excited pairs compared to that of the first pair and the ground state pair.

	1–2	3–4	5–6	7–8	9–10
$[\,\mathrm{Nd\,L^{py}}\,]^{3+}$	0	41	139	218	265
$U(MeBTP)_3^{3+}$	0	44	260	387	464
$U(C_5Me_5)_3$	0	580	1365	2495	2552
$U(N(SiMe^tBu_2)_2)_3$	0	190	432	1101	1269
$U(C_5Me_4SiMe_3)_3$	0	61	144	1034	1183
$U(\eta\text{-}C_5Me_4Et)(\eta\text{-}(1,4\text{-}C_8H_6(Si^iPr_3)_2)$	0	374	841	1190	1255

4.4 Previous work and the ZFS tensor

In a recent study we looked at the pNMR shifts of 14 f-element compounds.[28] The present work studies the effects of zero-field splitting on the six f^3 compounds from that study. One compound contains neodymium as a sample lanthanide, detailed in section 4.5.1 and shown in Figure 4.3. The remaining five are uranium compounds detailed in sections 4.5.2–4.5.6. Equation 4.4 shows that the pNMR shift depends explicitly on the four magnetic interactions ($\boldsymbol{\sigma}^{\text{orb}}, \mathbf{g}, \mathbf{D}$ and $\mathbf{A}$) and implicitly on the geometry at which the various terms are evaluated. We summarise the findings of our previous study in justifying the approach we have adopted in evaluating each of the necessary terms. More details can be found in the aforementioned paper.

4.4.1 Geometry optimisation

Geometry optimisation was performed using GAUSSIAN 09.[169] Since geometries largely depend on the ground state electronic structure, it was considered reasonable to use DFT with the PBE0[55] functional. Due to the presence of uranium, relativistic effects are important, but it is sufficient to only consider scalar relativistic effects. We prefer an all-electron approach and previously created a program in which implements the zeroth order regular approach (ZORA),[27,39] and applies the correction to the one-electron Hamiltonian in atomic blocks, removing the gauge dependence issue. This program was interfaced to the GAUSSIAN programs and used in all geometry optimisations. We used the segmented all-electron relativistically corrected (SARC) basis set[30,31] for the heavy atoms[†] with Def2-SVP[23] for the remaining atoms. This approach showed reliable agreement against a test set of crystal structure data for a set of 11 molecules, producing correlation coefficients of $R^2 = 1.00$ for bond length and $R^2 = 0.99$ for bond angles.[28]

[†] TVZP quality with $29s20p16d12f1g/21s13p10d7f1g$ uncontracted/contracted gaussian functions for a uranium atom and $23s16p12d6f1g/18s12p9d3f1g$ uncontracted/contracted gaussian functions for a neodymium atom.

4.4.2 Orbital shielding, $\boldsymbol{\sigma}^{\mathbf{orb}}$

The orbital component of the chemical shifts were obtained using GAUSSIAN 09, DFT linear response theory (PBE0), the ZORA relativistic treatment outlined above, and gauge- including atomic orbitals (GIAO).[151,170] A Def2-TZVP basis was used for ^{1}H chemical shifts, and an uncontracted Def2-SVP basis for the ^{13}C, otherwise the basis used was as in the previous section. This approach was calibrated against 20 ^{1}H and 32 ^{13}C chemical shifts of four diamagnetic molecules, producing correlation coefficients for ^{1}H and ^{13}C of $R^2 = 0.99$ and $R^2 = 0.98$ respectively.[28] Deviations were noted when a light atom under investigation was directly bonded to a heavy atom. These cases are subject to the HALA effect working through the chemical bond and as such, need a more elaborate relativistic treatment.[165]

4.4.3 Hyperfine coupling matrix, A

The reported A tensors were calculated using the ORCA 3.0.3 program[171] , DFT (PBE0), the Douglas-Kroll-Hess transformation to second-order (DKH2).[172,173] Analysis of the effect that picture change has on these hyperfine coupling coefficients (without spin-orbit correction) was performed in our previous paper,[28] and except for ^{1}H calculations, picture change effects were found to be significant. Therefore they were included as implemented in ORCA and documented by Sandhoefer *et al.*[174] The second order DKH transformation is applied to the Fermi contact, spin-dipole and Zeeman operators. The transformation of the paramagnetic spin-orbit term was treated to first order only. Relevant experimental results are extremely scarce, but the approach has been calibrated against $[\mathrm{U}(\mathrm{C}_7\mathrm{H}_7)_2]^-$ for increasing sizes of basis set, and density functional, and the most accurate functional (PBE0) was employed as used below.[137]

For the nuclei of interest, a Def2-TZVP basis was used with three additional uncontracted s orbitals with large exponents added to allow improved description of the electronic environment close to the nucleus, otherwise the basis used was as in the previous section. The exponents were derived using a geometric progression starting from the largest s function exponents of the existing basis, following the requirements of basis set design for hyperfine coupling calculations outlined by Chipman.[175] Because of the high computational cost, the calculation generally did not include spin-orbit corrections to the hyperfine calculation. We indicate in the text the two molecules for which this term was evaluated. In these cases the calculation used the same methods as detailed above for the other hyperfine terms but included solution of the relevant coupled perturbed Kohn-Sham equations to obtain the derivative of the spin density, followed by contraction with the nuclear (spin) - electron (orbit) integrals.

4.4.4 Zeeman coupling matrix, g

It is possible to calculate **g** tensors with DFT and use linear response theory to include spin-orbit coupling as a first-order perturbation,[149,176] however this approach is only effective for weak spin-orbit coupling and in the absence of low-lying excited states. For the molecules under investigation here neither condition is true, and the ground states are all clearly degenerate. As a result a multiconfigurational approach is necessary. ORCA 3.0.3 was used to perform a series of State-Averaged Complete Active Space Self Consistent Field (SA-CASSCF) calculations, using an active space of three electrons and seven orbitals, *i.e.* the f electrons of the heavy element distributed in the relevant manifold of f orbitals. Relativistic effects were added using DKH2. Spin-orbit coupling was included by utilising the SOMF operator,[177] using the centre of electronic charge as the origin of the molecule to minimise gauge dependence.[178] A SARC basis set was used for uranium, with a Def2-SVP for hydrogen and the remainder using a Def2-TZVP. The **g** tensor was evaluated within the effective Hamiltonian approach. The number of states included in the SA-CASSCF-SOC calculations were explored empirically, by increasing the number of states, until adding additional states did not significantly change the principal values of the **g** tensor.[27,149]

4.4.5 The ZFS tensor, D

For efficiency, the **D** tensor was calculated at the same level of theory as detailed in the previous section to obtain **g**.

We have written a MATLAB script that uses the approaches detailed in section 4.3.5 to model the effect of zero-field splitting on pNMR shifts. We have separated the results into contact and pseudocontact components as outlined in section 4.3.6. This script was validated with test data[†] and a generally available program[‡] provided by Autschbach.[131,135]

4.5 Results

4.5.1 ^{1}H pNMR shifts of a neodymium tetrapyridyl appended cyclen

The first molecule under investigation is a neodymium 1,4,7,10-tetrakis(2-pyridylmethyl)-1,4,7,10-tetraazacyclododecane complex $[\ \mathrm{Nd\,L^{py}}\ ]^{3+}$ with a triflate $CF_3SO_3^-$ counterion. This was synthesised and studied by Natrajan *et al.*,[179] who produced 500Mz ^{1}H NMR spectra of the species in a D_2O solvent at room temperature. The molecule is shown in Figure 4.3. The observed shifts were −0.2, 2.4, 4.6, 5.2, 6, 8, 8.3, 8.4, 10.8 and 12.4 ppm and were not assigned in the paper. In our previous work,[28] we found that inclusion of the triflate counterion produced a significant change in the geometry of the complex and so needs to be included in modelling this structure.

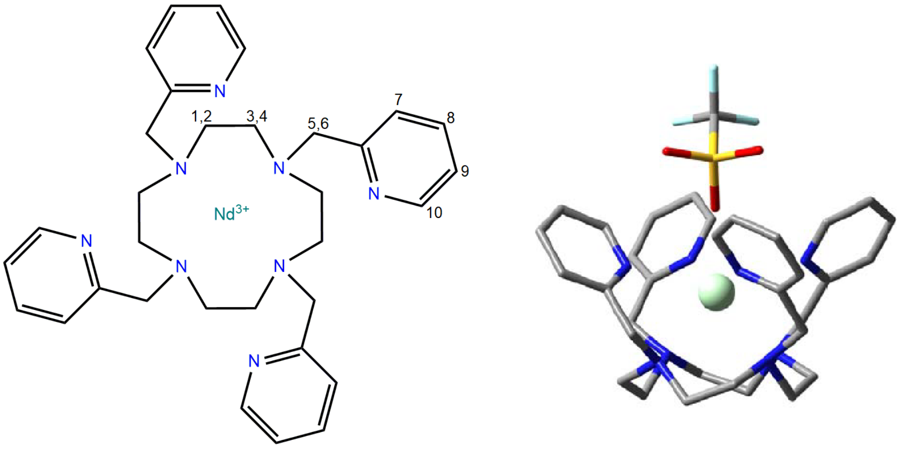

Figure 4.3: Structure of the cyclen complex $[\ \mathrm{Nd\,L^{py}}\ ]^{3+}$. Labels refer to the 10 chemically distinct H atoms, with 1,3,5 representing equatorial CH_2 protons and 2,4,6 representing axial protons.

[†] http://www.ens-lyon.fr/crmn/pnmr/wp-content/uploads/2013/12/2014-02-Mariapfarr-presentation-Juha-Vaara.pdf

[‡] http://ja01.chem.buffalo.edu/ jochena/downloads/downloads.html

The calculation of the **g** and **D** matrices used 21 quartet and 40 doublet states from a SA-CASSCF-SOC(3,7) calculation. The matrices are listed in Table A1 of the appendix. The resulting isotropic g value is negative, a phenomenon observed for states with significant spin-orbit coupling as discussed in references 180 and 122.

We find in the absence of ZFS corrections from our calculations a range of shifts spanning $-2.56 - 16.51$ ppm. Inclusion of ZFS produces a wider spread of values which are compared in Figure 4.4. Table 4.5 outlines the details of the components.[‖]

It is noticeable that adding ZFS has very little effect on the contact part of the shielding, but the size (and composition) of the pseudocontact term significantly changes. Examining the pseudocontact components, the term derived from the isotropic hyperfine changes only slightly and the interaction between the anisotropic Zeeman and the spin-dipole hyperfine term is negligible. The change derives from the interaction of the spin-dipole part of the hyperfine and the isotropic g term (decomposed into the free electron part and the shift). While the predicted chemical shift changes by only a few ppm, it is sufficient to shift the predicted order of the peaks and as a result assignment of all ten ^{1}H shifts is not possible. We have omitted the spin-orbit correction to the hyperfine coupling matrix as the calculations are extremely demanding. However it is unlikely that these ^{1}H shifts will be strongly influenced by this omission since the protons are well removed from the heavy atom.

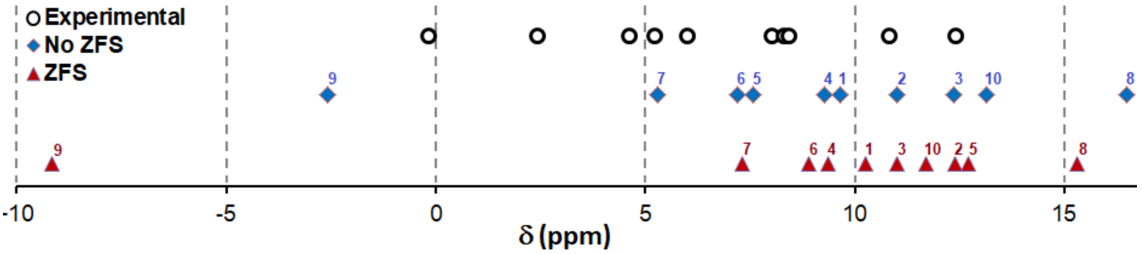

Figure 4.4: Experimental and computed pNMR spectra for [Nd L^{py}]$^{3+}$ with and without ZFS at 298.15 K. For numbering of protons see Figure 4.3.

[‖] In the following tables, the results are given to 2.dp. so that the variation in smaller components is visible, this should not be taken as a measure of accuracy of the method.

Table 4.5: Calculated ^{1}H pNMR shifts of [Nd L^{py}]$^{3+}$ organised in increasing δ. For numbering of protons see Figure 4.3. The reference chemical shift is 31.58 ppm (TMS) and the temperature is 298.15 K.

Component			**H$^{(9)}$**		**H$^{(7)}$**		**H$^{(6)}$**		**H$^{(4)}$**		**H$^{(1)}$**	
A	**g**	**Order**	**No ZFS(a)**	**ZFS(b)**	**No ZFS**	**ZFS**	**No ZFS**	**ZFS**	**No ZFS**	**ZFS**	**No ZFS**	**ZFS**
A_{iso}	g_e	2	−0.07	−0.07	0.44	0.44	3.63	3.62	2.51	2.51	1.04	1.04
	Δg_{iso}	4	0.12	0.12	−0.70	−0.70	−5.77	−5.76	−3.99	−3.99	−1.66	−1.66
	$\boldsymbol{\Delta\tilde{g}}$	4	0.00	0.00	0.00	0.00	0.00	−0.01	0.00	-0.01	0.00	0.00
$\mathbf{A}^{\text{SD}}$	g_e	2	0.00	−10.86	0.00	3.33	0.00	2.78	0.00	0.10	0.00	0.97
	Δg_{iso}	4	0.00	17.27	0.00	−5.30	0.00	−4.42	0.00	−0.17	0.00	−1.54
	$\boldsymbol{\Delta\tilde{g}}$	4	6.41	6.60	−1.95	−2.01	−1.68	-1.72	0.01	0.00	−0.56	−0.57
Orbital Contribution		σ_{orb}	27.59		28.40		28.11		23.66		23.00	
Contact	**Method 1(c)**	σ_{c}	0.04	0.04	−0.26	−0.26	−2.14	−2.15	−1.48	−1.49	−0.62	−0.61
	Method 2		0.04	0.04	−0.26	−0.26	−2.14	−2.15	−1.48	−1.48	−0.62	−0.61
Pseudocontact	**Method 1**	σ_{pc}	6.41	13.01	−1.95	−3.98	−1.68	−3.37	0.01	−0.07	−0.56	−1.14
	Method 2		6.41	13.00	−1.95	−3.98	−1.68	−3.37	0.01	−0.08	−0.56	−1.14
Total isotropic shielding		$\sigma_{\text{iso}} = \sigma_{\text{orb}} + \sigma_{\text{c}} + \sigma_{\text{pc}}$	34.05	40.64	26.18	24.16	24.29	22.59	22.19	22.12	21.82	21.24
Delta		$\sigma_{\text{ref}} - \sigma_{\text{iso}}$	−2.46	−9.06	5.40	7.42	7.29	8.99	9.39	9.46	9.76	10.35
Component			**H$^{(3)}$**		**H$^{(10)}$**		**H$^{(2)}$**		**H$^{(5)}$**		**H$^{(8)}$**	
A	**g**	Order	**No ZFS**	**ZFS**	**No ZFS**	**ZFS**	**No ZFS**	**ZFS**	**No ZFS**	**ZFS**	**No ZFS**	**ZFS**
A_{iso}	g_e	2	9.86	9.84	20.51	20.49	3.28	3.28	−2.90	−2.89	25.96	25.93
	Δg_{iso}	4	−15.67	−15.65	−32.62	−32.58	−5.22	−5.21	4.61	4.60	−41.29	−41.24
	$\boldsymbol{\Delta\tilde{g}}$	4	0.00	−0.02	0.00	−0.05	0.00	−0.01	0.00	0.01	0.00	−0.06
$\mathbf{A}^{\text{SD}}$	g_e	2	0.00	−2.27	0.00	−2.41	0.00	2.26	0.00	8.47	0.00	−2.02
	Δg_{iso}	4	0 0.00	3.61	0.00	3.83	0.00	−3.60	0.00	−13.47	0.00	3.22
	$\boldsymbol{\Delta\tilde{g}}$	4	1.81	1.83	1.42	1.46	−1.36	−1.39	−5.16	−5.30	1.20	1.24
Orbital Contribution		σ_{orb}	23.14		29.04		23.77		27.35		29.11	
Contact	**Method 1**	σ_{c}	−5.81	−5.83	−12.11	−12.14	−1.94	−1.94	1.71	1.72	−15.33	−15.38
	Method 2		−5.81	−5.81	−12.11	−12.09	−1.94	−1.93	1.71	1.71	−15.33	−15.31
Pseudocontact	**Method 1**	σ_{pc}	1.81	3.17	1.42	2.88	−1.36	−2.74	−5.16	−10.30	1.20	2.41
	Method 2		1.81	3.15	1.42	2.83	−1.36	−2.74	−5.16	−10.29	1.20	2.38
Total isotropic shielding		$\sigma_{\text{iso}} = \sigma_{\text{orb}} + \sigma_{\text{c}} + \sigma_{\text{pc}}$	19.13	20.48	18.35	19.78	20.48	19.10	23.90	18.77	14.98	16.18
Delta		$\sigma_{\text{ref}} - \sigma_{\text{iso}}$	12.45	11.10	13.23	11.80	11.10	12.48	7.68	12.81	16.60	15.41

(a) The No ZFS approach uses Eq. 4.14 with $\mathbf{Z} = \frac{1}{3}S(S+1)\mathbf{I}$, (b) The full coupling approach uses Eq. 4.14 with $\mathbf{Z}$ defined in Eqs. 4.16 and 4.17

(c) Methods 1 and 2 are outlined in Table 4.2, (d) The observed shifts were −0.2, 2.4, 4.6, 5.2, 6, 8, 8.3, 8.4, 10.8 and 12.4 ppm and were not assigned in the paper.

4.5.2 ^{1}H pNMR shifts of tris(2,6-bis(5,6-dialkyl-1,2,4-triazin-3-yl)pyridine) uranium(III), $U(MeBTP)_3^{3+}$

2,6-Bis(5,6-dialkyl-1,2,4-triazin-3-yl)pyridine (BTP) is an effective chelating agent and has been investigated as a reagent for processing waste containing uranium (III) species,[141,181] with the family of ligands showing preference for coordinating selectively with trivalent actinides over trivalent lanthanides due to the "much softer character of the N atoms in this weakly basic ligand".[141] It is thought that actinide/lanthanide selectivity results from the difference in the nature of the f orbitals, the lanthanide $4f$ orbitals displaying "core-like" behaviour and participating weakly in bonding, whereas the more extended $5f$ orbitals of actinide species participate more in covalent bonding.[182] As such there is much interest in better understanding the nature of this U-N bond. The experimental results that we are using for comparision are 200 MHz ^{1}H NMR spectra taken at 30°C in deuterated pyridine.[141] The molecule has four chemically equivalent types of hydrogen atoms. The numbering used to refer to these sets of protons is shown in Figure 4.5 and the stereochemistry in Figure 4.6. All hydrogen atoms are relatively distant from the U-N bond, and as such we expect that spin-orbit component of the hyperfine interaction is not significant, hence they have not been included here.

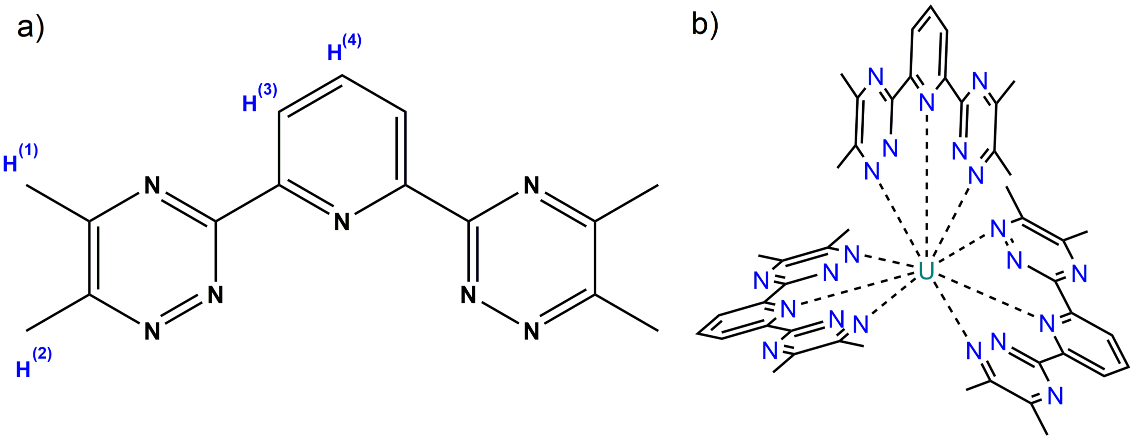

Figure 4.5: a) The MeBTP ligand, labels identify the four types of chemically equivalent ^{1}H, b) The full structure of tris(2,6-bis(5,6-dialkyl-1,2,4-triazin-3-yl)pyridine) uranium(III).

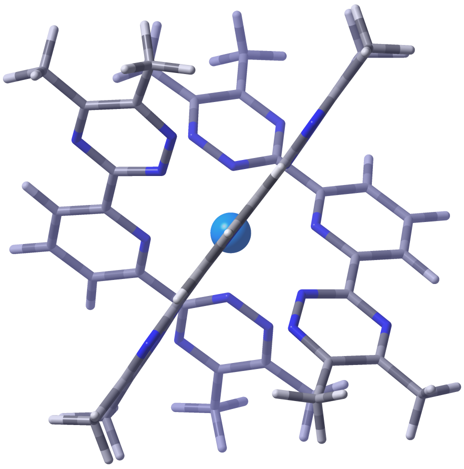

Figure 4.6: Stereochemistry of $U(MeBTP)_3^{3+}$, showing the three planar ligands, staggered with approximate 3-fold rotational symmetry.

The SA-CASSCF-SOC(3,7) calculation of the **g** and **D** matrices used 14 quartet and 25 doublet states. The matrices are listed in the Supporting Information (Table A2). Our results are shown in Tables 4.6 and 4.7. For each distinct type of hydrogen we show the effect of the ZFS correction. We list the contribution to the paramagnetic shift from each component of $\mathbf{g} \cdot \mathbf{Z} \cdot \mathbf{A}$ and a qualitative partition of contact and pseudocontact terms. Overall the paramagnetic shift is calculated to be slightly larger than the orbital contribution, except for the $H^{(2)}$ atoms. In the absence of the ZFS correction $H^{(1)}$ and $H^{(3)}$ proton chemical shifts are predicted to be larger in magnitude that the observed shifts, although the signs of the shifts are predicted correctly. The ZFS correction reduces the magnitudes in the direction of the experimental values. In this system including the ZFS produces shifts that are closer to the observed values but are still too large in magnitude. The experimental shifts span a range of about 52 ppm, while the neglect of ZFS altogether gives a span of calculated values of 117 ppm. The ZFS correction reduces the range to 90 ppm. This is shown in Figure 4.7. The contact and pseudocontact terms vary according to the method of partitioning them, but the contact shift is consistently predicted to be larger than the pseudocontact shift in all cases. However for $H^{(2)}$ and $H^{(3)}$ the values are much closer in magnitude.

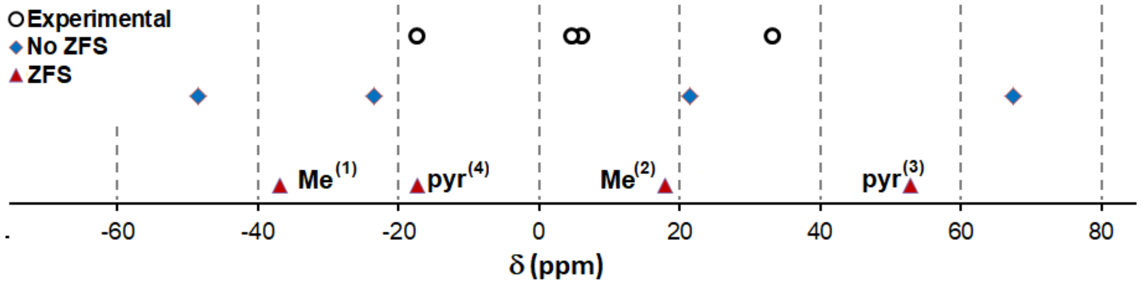

Figure 4.7: Experimental and predicted pNMR shifts of U(MeBTP)$_3^{3+}$ with and without ZFS at 303 K. For numbering of protons see Figure 4.5. The order is consistent in all cases.

Table 4.6: Calculated ^{1}H pNMR shifts for the methyl H atoms of U(MeBTP)$_3^{3+}$ in ppm at 303K. For numbering of protons see Figure 4.3.

Component			**methyl H$^{(1)}$**		**methyl H$^{(2)}$**	
A	**g**	Order	**No ZFS**	**ZFS**	**No ZFS**	**ZFS**
A_{iso}	g_e	2	−113.43	−69.47	28.79	17.63
	Δg_{iso}	4	166.55	102.00	−42.28	−25.89
	$\mathbf{\Delta\tilde{g}}$	4	−0.00	8.85	0.00	−2.25
$\mathbf{A}^{\text{SD}}$	g_e	2	0.00	2.26	0.00	6.82
	Δg_{iso}	4	0.00	−3.32	−0.00	−10.01
	$\mathbf{\Delta\tilde{g}}$	4	−2.12	−0.85	−6.27	−2.54
Ave. Calc. **U-H** distance, Angstrom			7.16		6.15	
Orbital Contribution			28.96		29.88	
Reference shift			31.58		31.58	
Contact		Method 1	53.12	41.38	−13.48	−10.51
		Method 2	53.12	32.53	−13.48	−8.26
Pseudocontact		Method 1	−2.12	−1.91	−6.27	−5.73
		Method 2	−2.12	6.94	−6.27	−7.98
Total isotropic shielding			79.96	68.43	10.13	13.65
Delta			−48.38	−36.85	21.45	17.93
Experimental δ shift[141]			−18.04		4.59	

Table 4.7: Calculated ^{1}H pNMR shifts for the ring H atoms of U(MeBTP)$_3$ in ppm at 303 K. For numbering see Figure 4.5.

Component			**ortho-pyridine H$^{(3)}$**		**para-pyridine H$^{(4)}$**	
A	**g**	Order	**No ZFS**	**ZFS**	**No ZFS**	**ZFS**
A_{iso}	g_e	2	−49.74	−30.46	155.85	95.45
	Δg_{iso}	4	73.03	44.72	−228.84	−140.15
	$\boldsymbol{\Delta\tilde{g}}$	4	−0.00	3.88	0.00	−12.16
$\mathbf{A}^{\mathrm{SD}}$	g_e	2	0.00	−10.72	0.00	−15.21
	Δg_{iso}	4	0.00	15.73	0.00	22.34
	$\boldsymbol{\Delta\tilde{g}}$	4	10.01	4.03	14.48	5.83
Calculated **U-H** distance, Å			5.52		6.38	
Orbital Contribution			21.75		22.56	
Reference shift			31.58		31.58	
Contact		Method 1	23.29	18.14	−72.99	−56.86
		Method 2	23.29	14.26	−72.99	−44.70
Pseudocontact		Method 1	10.01	9.04	14.48	12.96
		Method 2	10.01	12.92	14.48	0.80
Total isotropic shielding			55.05	48.94	−35.95	−21.35
Delta			−23.47	−17.36	67.53	52.92
Experimental δ shift[141]			5.64		33.95	

4.5.3 ^{1}H and ^{13}C pNMR shifts of tris(pentamethylcyclopentadienyl) uranium (III), $U(C_5Me_5)_3$

It was originally thought impossible to synthesise an organometallic complex consisting of a single atom and three η^5-bonded pentamethylcyclopentadienyl rings due to the steric hindrance presented by the methyl groups. However a samarium complex was synthesised in 1991 followed by a uranium complex shortly after. The optimised geometry of the complex is shown in Figure 4.8, with the methyl carbons residing above the plane of the ring due to steric effects. The paper reporting the synthesis[183] also reported the chemical shifts observed in ^{1}H and ^{13}C spectra taken at 500 MHz, 25°C in a deuterated benzene solvent and these act as our baseline for comparision.

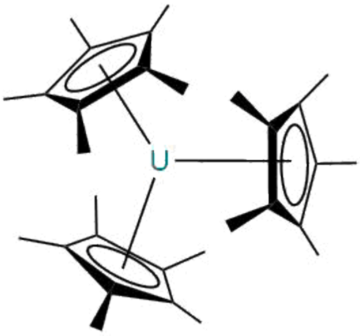

Figure 4.8: The structure and stereochemistry of $U(C_5Me_5)_3$.

The SA-CASSCF-SOC(3,7) calculation of the **g** and **D** matrices used 28 quartet and 55 doublet states. The matrices are listed in the Supporting Information (Table A3). Our results for the methyl hydrogen atoms are shown in Tables 4.8, again reflecting the treatment of ZFS, the individual contributions to the paramagnetic shift and the qualitative partition of contact and pseudocontact terms. Overall the paramagnetic shift is calculated to be significantly smaller (14-17%) than the orbital contribution.

Table 4.8: Calculated ^{1}H pNMR shifts for $U(C_5Me_5)_3$ in ppm at 298 K.

A	**g**	Order	**No ZFS**	**ZFS**
A_{iso}	g_e	2	−6.02	−5.13
	Δg_{iso}	4	7.83	6.68
	$\boldsymbol{\Delta\tilde{g}}$	4	−0.00	1.12
$\mathbf{A}^{\text{SD}}$	g_e	2	−0.00	−2.36
	Δg_{iso}	4	0.00	3.07
	$\boldsymbol{\Delta\tilde{g}}$	4	2.83	1.61
Orbital Contribution			29.95	
Contact		Method 1	1.82	2.67
		Method 2	1.82	1.55
Pseudocontact		Method 1	2.83	2.32
		Method 2	2.83	3.44
Total isotropic shielding			34.60	34.94
Reference shift, 31.58 ppm (TMS)				
Delta			−3.02	−3.36
Experimental δ shift[183]			−0.90	

In the absence of the ZFS correction, the predicted chemical shift was −3.02 ppm, with the correction the predicted chemical shift was −3.36 ppm, hence the full ZFS correction only contributes −0.34 ppm to the final computed shift. This is unlikely to be significant compared to the errors associated with the approximations used to generate the pNMR matrices, and this result remains a good match for the experimental value. Both the contact and pseudocontact shielding terms are positive, although the two decompositions used disagree with respect to the relative magnitudes of the contact and pseudocontact shifts. It must be noted that the hyperfine couplings have been evaluated using a DFT method. The choice of exchange-correlation functional can introduce a variation in the predicted hyperfine matrices. It is difficult currently to deal with this property using purely wavefunctional techniques, which would in principle would allow a degree of systematic refinement. Given the size and complexity of the systems studied here, the approach is a suitable starting point. However, as wavefunction methods become more available for these operators further refinements of the computations can and should be sought[59]

Table 4.9 presents the shifts for ^{13}C pNMR shifts for the ring and methyl carbon atoms. Due to the computational expense of calculating the spin-orbit corrections to the hyperfine coupling matrix and the fact that ^{13}C is a light atom, we initially did not apply this correction to our calculations. However this complex contains a set of η-coordinated carbon–uranium bonds, and the HALA effects alluded to earlier are likely to be in operation. Additionally, in the work of Autschbach *et al.* on actinide carbonate molecules,[146,147] it was noted that the spin-orbit correction dominated the hyperfine interaction. Accordingly, we computed the spin-orbit correction to the hyperfine tensor using the methodology detailed in Section 4.4.3, and report our findings in Table 4.10.

Table 4.9: Calculated ^{13}C pNMR shifts for $U(C_5Me_5)_3$ in ppm with no spin-orbit corrections to the hyperfine term at 298 K.

Component			**Cyclopentadienyl**		**Methyl**	
A	**g**	Order	**No ZFS**	**ZFS**	**No ZFS**	**ZFS**
A_{iso}	g_e	2	256.34	218.66	−343.69	−293.18
	Δg_{iso}	4	−333.83	−284.76	447.59	381.80
	$\boldsymbol{\Delta\tilde{g}}$	4	−0.00	−47.79	0.00	64.07
$\mathbf{A}^{\mathrm{SD}}$	g_e	2	−0.01	−64.23	−0.01	−11.63
	Δg_{iso}	4	0.01	83.65	0.01	15.14
	$\boldsymbol{\Delta\tilde{g}}$	4	77.50	43.90	13.76	7.88
Orbital Contribution			57.01		173.62	
Reference shift			189.03		189.03	
Contact		Method 1	−77.49	−113.89	103.89	152.69
		Method 2	−77.49	−66.10	103.89	88.62
Pseudocontact		Method 1	77.51	63.31	13.76	11.39
		Method 2	77.51	15.53	13.76	75.46
Total isotropic shielding			57.02	6.44	291.27	337.70
Delta			132.00	182.59	−102.25	−148.68
Experimental δ shift[183]			324.80		−86.70	

The format of this table is similar to the previous ones, but the individual contributions have been expanded. The table includes a comparison with the values before the spin-orbit correction to the hyperfine matrix was added and the bottom section highlights the two decomposition methods. Table 4.10 shows that the predicted isotropic chemical shielding (and chemical shift) of the two decomposition methods is different. This is due to the neglect of the $O(\alpha^6)$ terms that method 2 uses, which is not valid when spin-orbit effects are significant. With reference to the method 1 decomposition, we note that the effect of the inclusion of the spin-orbit hyperfine term is less marked on the methyl carbon atoms than for the ring carbons. There is now qualitative agreement with experiment for the latter. For the methyl carbons, the effect is smaller, perhaps due to their being further removed from the heavy nucleus.

Table 4.10: Calculated ^{13}C pNMR shifts for $U(C_5Me_5)_3$ in ppm with spin-orbit corrections to the hyperfine term at 298 K.

Component			**Cyclopentadienyl**		**Methyl**	
A	**g**	**Order**	**No ZFS**	**ZFS**	**No ZFS**	**ZFS**
Isotropic Hyperfine Contribution						
A_{iso}	g_e	2	256.34	218.66	−343.69	−293.18
	Δg_{iso}	4	−333.83	−284.76	447.59	381.80
	$\boldsymbol{\Delta\tilde{g}}$	4	−0.00	−47.79	0.00	64.07
$A_{\text{iso}}^{\Delta\text{SO}}$	g_e	4	74.44	63.50	−5.38	−4.59
	Δg_{iso}	6	−96.94	−82.69	7.00	5.97
	$\boldsymbol{\Delta\tilde{g}}$	6	−0.00	−13.88	0.00	1.00
Anisotropic Hyperfine Contribution						
$\mathbf{A}^{\text{SD}}$	g_e	2	−0.01	−64.23	−0.01	−11.63
	Δg_{iso}	4	0.01	83.65	0.01	15.14
	$\boldsymbol{\Delta\tilde{g}}$	4	77.50	43.90	13.76	7.88
$\mathbf{A}^{\Delta\text{SO,SYM}}$	g_e	4	0.00	127.76	0.00	10.78
	Δg_{iso}	6	−0.00	−166.38	−0.00	−14.04
	$\boldsymbol{\Delta\tilde{g}}$	6	−152.63	−86.94	−12.76	−7.31
$\mathbf{A}^{\Delta\text{SO,AS}}$	g_e	4	−0.00	0.00	−0.00	−0.00
	Δg_{iso}	6	−0.00	−0.00	−0.00	0.00
	$\boldsymbol{\Delta\tilde{g}}$	6	−0.00	−0.01	0.00	0.00
Orbital Contribution			**57.01**		**73.62**	
Reference shift			**189.03**		**189.03**	
Method 1						
Contact*		**A** − no PSO	−77.49	−113.89	103.89	152.69
		A + PSO	99.99	−146.96	105.52	155.08
Pseudocontact		**A** − no PSO	77.51	63.31	13.76	11.39
		A + PSO	−75.13	−62.25	1.00	0.82
Isotropic shielding		**A** − no PSO	57.02	6.44	291.27	337.70
		A + PSO	−118.11	−133.18	280.14	329.52
Delta		**A** − no PSO	132.00	182.59	−102.25	−148.68
		A + PSO	307.14	341.23	−91.11	−140.50

Table 4.10 — *cont.*

Component		**Cyclopentadienyl**		**Methyl**	
		No ZFS	**ZFS**	**No ZFS**	**ZFS**
Method 2					
Contact	**A** – no PSO	−77.49	−66.10	103.89	88.62
	A + PSO	−3.05	−2.61	137.46	84.04
Pseudocontact	**A** – no PSO	77.51	15.53	13.76	75.46
	A + PSO	77.51	143.29	13.76	86.24
Isotropic shielding	**A** – no PSO	57.02	6.44	291.27	337.70
	A + PSO	131.47	197.69	324.84	343.90
Delta	**A** – no PSO	132.00	182.59	−102.25	−148.68
	A + PSO	57.57	−8.66	−135.81	−154.87
Experimental δ shift.[183]		**324.80**		**−86.70**	

* Rows marked "A — no PSO" refer to the results before the hyperfine matrix has been corrected with spin-orbit effects, "A + PSO" are results including this correction.

Figure 4.9 shows the deviation from the averaged value for the isotropic paramagnetic shielding of the ring and methyl ^{13}C nuclei. Overall the ring ^{13}C range from −63 to 92 ppm and the methyl ^{13}C range from −74 to 94 ppm. Note that the experimental values of the shifts lies within both ranges.

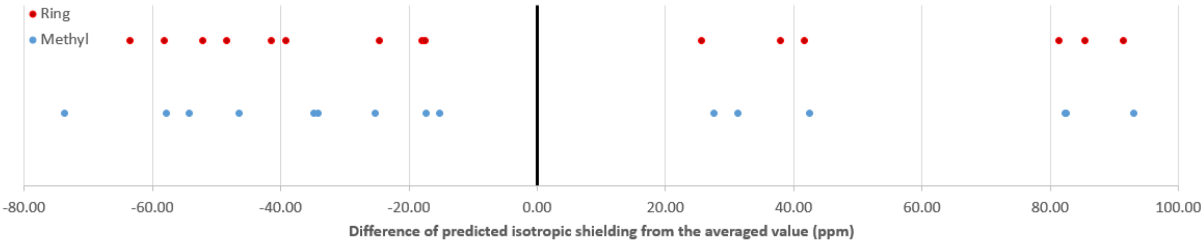

Figure 4.9: Difference of the predicted isotropic shielding of individual ^{13}C nuclei from the averaged value at 298 K.

4.5.4 ^{29}Si pNMR shifts of the Uranium(III) compound, U(N(SiMe^{t}Bu$_2$)$_2$)$_3$

Our next molecule is a single molecule magnet which, unusually, has a trigonal planar coordination around the uranium atom when in the solid state, instead of the more common trigonal pyramidal geometry that is seen in other three-coordinate actinide compounds. This is due to the large steric hindrance introduced by the t-butyl groups. Steric hindrance is a commonly used tool to prevent the molecules oligomerising, and there is much interest in understanding how the magnetic properties of the molecule are affected by the ligand. For comparison with experiment, we use the 73 Hz ^{29}Si chemical shift of −296.04 ppm taken at 25°C in a solution with deuterated benzene.[139] Our calculation refers to an optimised gas phase structure,[28] and is shown in Figure 4.10.

The SA-CASSCF-SOC(3,7) calculation of the **g** and **D** matrices used 21 quartet and 39 doublet states. The matrices are listed in the supporting information (Table A4). Table 4.11 shows the resulting ZFS calculations. The orbital and paramagnetic contributions are predicted to have a similar size, and the contact interaction is positive and much larger than the pseudocontact, so the paramagnetic shift is largely due to increased spin-density at the nucleus. Without applying ZFS, the chemical shift predicted was 18.54 ppm less than the experimental value. Using the full coupling method, the predicted chemical shift reduced by 46.19 ppm, which is further from the experimental value. Given our findings for the ^{13}C shifts in U(C$_5$Me$_5$)$_3$, the spin-orbit correction to the hyperfine tensor cannot be neglected. Due to computational cost we have only obtained the corrected tensors for two silicon nuclei. The hyperfine matrices of the two silicon atoms considered result in very different isotropic shielding, specifically 559 and 371 ppm. We note that in our optimised structure, the uranium-silicon distance of two atoms we applied PSO corrections was 3.31 and 3.66 Å (see Figure 4.10). The asymmetry of the optimised molecule is unusual, but mirrors previous calculations by Goodwin *et al.*, who believe that the experimentally determined solid-state trigonal planar structure is enforced by the lattice; in the gas phase, partial relief of the very large steric hinderance in the molecule leads to an asymmetric equilibrium geometry.

The magnitude of the change in the isotropic shielding for the silicon atoms that we have computed clearly indicates that it is essential to carry out the average over the full set of silicon atoms to obtain a reliable estimate of the shifts. This remains to be done and we are exploring more computationally efficient ways to obtain the spin-orbit hyperfine interaction.

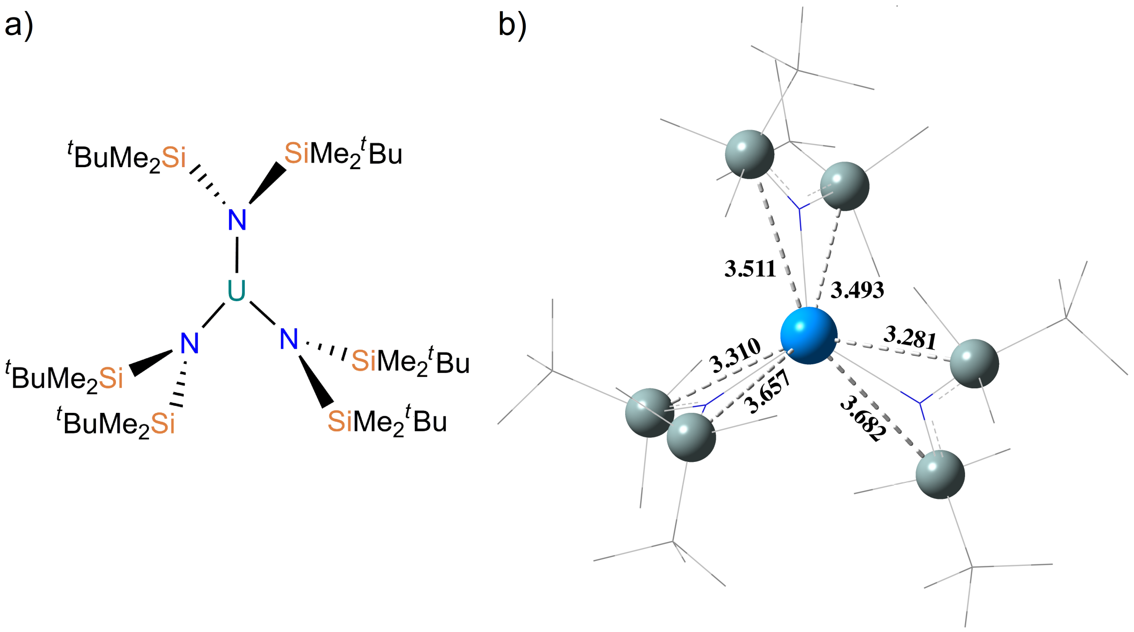

Figure 4.10: Geometry of U(N(SiMe^{t}Bu$_2$)$_2$)$_3$: a) Chemical structure, b) Stereochemistry with uranium and silicon nuclei shown as spheres and the remaining non-hydrogen nuclei in wireframe. Stated distances are in Angstroms.

Table 4.11: Calculated ^{29}Si pNMR shifts of $U(N(SiMe^tBu_2)_2)_3$ in ppm at 298 K.

A	**g**	Order	**No ZFS**	**ZFS**
A_{iso}	g_e	2	-624.79	-608.68
	Δg_{iso}	4	889.64	866.71
	$\boldsymbol{\Delta\tilde{g}}$	4	-0.00	48.19
$\mathbf{A}^{\text{SD}}$	g_e	2	-0.00	-6.14
	Δg_{iso}	4	-0.00	8.74
	$\boldsymbol{\Delta\tilde{g}}$	4	37.26	39.49
Contact		Method 1	264.85	306.22
		Method 2	264.85	258.03
Pseudocontact		Method 1	37.26	42.09
		Method 2	37.26	90.28
Orbital Contribution			344.04	
Reference shift			331.60	
Total isotropic shielding			646.15	692.34
Delta			-314.54	-360.74
Experimental δ shift[139]			-296.00	

4.5.5 ^{29}Si pNMR shifts of tris(trimethylsilyltetramethylcyclopentadienyl)uranium(lll), U($C_5Me_4SiMe_3$)$_3$.

Tris(trimethylsilyltetramethylcyclopentadienyl)uranium(lll) demonstrates even more steric crowding than the pentamethylcyclopentadienyl ring studied in section 4.5.3, and was part of a systematic study of ^{29}Si shifts of similar compounds, focused on discovering trends[184] in the chemical shifts of uranium-silicon compounds. The SI for reference 184 includes a graph that may indicate very weak correlation ($R^2 = 0.678$) between U^{III}-Si distance and ^{29}Si pNMR chemical shift, but cautions against treating their results as definitive, citing the complexity involved when studying paramagnetic species and effects that are in opposition. That study reported an experimental value of -155 ppm (99.2 MHz spectra, taken at 298 K in deuterated benzene with an iodide counter anion). The SA-CASSCF-SOC(3,7) calculation of the **g** and **D** matrices used 21 quartet and 39 doublet states. The matrices are listed in the supporting information (Table A5). Our calculated value before splitting was +18.92 ppm from the observed value, applying ZFS using the full coupling approach resulted in a small correction of +1.73 ppm, so in this case ZFS has very little effect on the total shift. For silicon nuclei, the implication of our results presented in Section 4.5.3 is that spin-orbit effects must also be important here. Further investigation by including spin-orbit corrections to the hyperfine matrices is needed to clarify if this is the case. Although the situation is slightly different in that the silicon atoms are not directly bound to the heavy atom and this may ameliorate the relative importance of including the spin-orbit part of the hyperfine interaction.

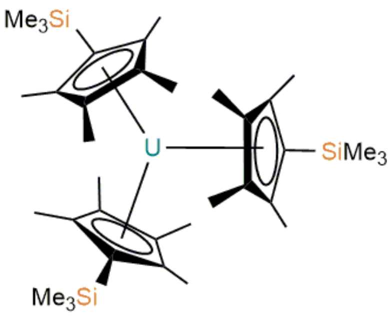

Figure 4.11: Structure of tris(trimethylsilylcyclopentadienyl)uranium(lll) , U($C_5Me_4SiMe_3$)$_3$.

Table 4.12: Calculated ^{29}Si pNMR shifts of U($C_5Me_4SiMe_3$)$_3$ in ppm at 298 K.

A	**g**	Order	**No ZFS**	**ZFS**
A_{iso}	g_e	2	−389.29	−376.21
	Δg_{iso}	4	532.93	515.02
	$\boldsymbol{\Delta\tilde{g}}$	4	0.00	4.55
$\mathbf{A}^{\mathrm{SD}}$	g_e	2	0.00	0.99
	Δg_{iso}	4	0.00	−1.36
	$\boldsymbol{\Delta\tilde{g}}$	4	−19.09	−20.19
Ave. Calc. **U-H** distance, Angstrom			4.16	
Contact		Method 1	143.64	143.36
		Method 2	143.64	138.81
Pseudocontact		Method 1	−19.09	−20.56
		Method 2	−19.09	−16.01
Orbital Contribution			358.12	
Reference shift			346.58	
Total isotropic shielding			482.66	480.93
Delta			−136.08	−134.35
Experimental δ shift[184,185]			−155.00	

4.5.6 ^{29}Si pNMR shifts of the mixed-sandwich uranium(III) compound, U(η-C_5Me_4Et)(η-(1,4-$C_8H_6(Si^iPr_3)_2$)

Mixed-sandwich organo-uranium complexes have been used for more environmentally friendly synthesis of oxocarbo rings from carbon dioxide and carbon monoxide with the ability to reform the complex after use. Similar uses for olefin processing exist, and there is interest in understanding this process better.[138] That study reported an experimental value of −136.70 ppm (99.2 MHz spectra, taken at 298 K in deuterated benzene with an iodide counter anion).

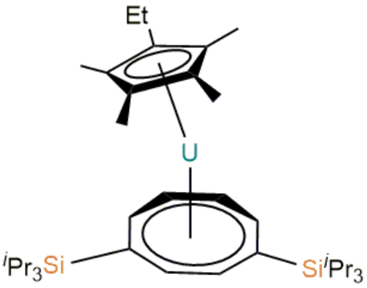

Figure 4.12: Structure of the asymmetric[186] mixed-sandwich uranium(III) compound, U(η-C_5Me_4Et)(η-(1,4-$C_8H_6(Si^iPr_3)_2$)

The SA-CASSCF-SOC(3,7) calculation of the **g** and **D** matrices used 13 quartet and 32 doublet states. The matrices are listed in Table A6 of the appendix. Inspection of our results in Table 4.13 shows that the contact term is substantially larger than the pseudocontact, and as for the example in Section 4.5, we interpret this as implying a strong interaction through the C–Si bond.

Table 4.13: Calculated ^{29}Si pNMR shifts of U(C$_5$Me$_5$Et)(1,4-C$_8$H$_6$(Si$^{\mathrm{i}}$Pr) in ppm at 298 K.

A	**g**	Order	**No ZFS**	**ZFS**
A_{iso}	g_e	2	−324.51	−298.57
	Δg_{iso}	4	512.84	471.85
	$\boldsymbol{\Delta\tilde{g}}$	4	0.00	30.66
$\mathbf{A}^{\mathrm{SD}}$	g_e	2	0.00	−6.60
	Δg_{iso}	4	−0.00	10.43
	$\boldsymbol{\Delta\tilde{g}}$	4	5.66	6.25
Contact		Method 1	188.33	203.95
		Method 2	188.33	173.28
Pseudocontact		Method 1	5.66	10.08
		Method 2	5.66	40.74
Orbital Contribution			326.64	
Reference shift			346.34	
Total isotropic shielding			520.64	540.66
Delta			−174.29	−194.32
Experimental δ shift[138]			−136.70	

4.5.7 Summary

Considering our six examples as a whole, Figure 4.13 shows the calculated values of pNMR shifts of the five uranium molecules plotted against the experimental values. Since this is a small sample, firm conclusions are not possible but, perhaps not surprisingly, the correlation coefficients improve as the treatment of ZFS improves; from $R^2 = 0.86$ for the treatment without ZFS to $R^2 = 0.90$ with of ZFS.

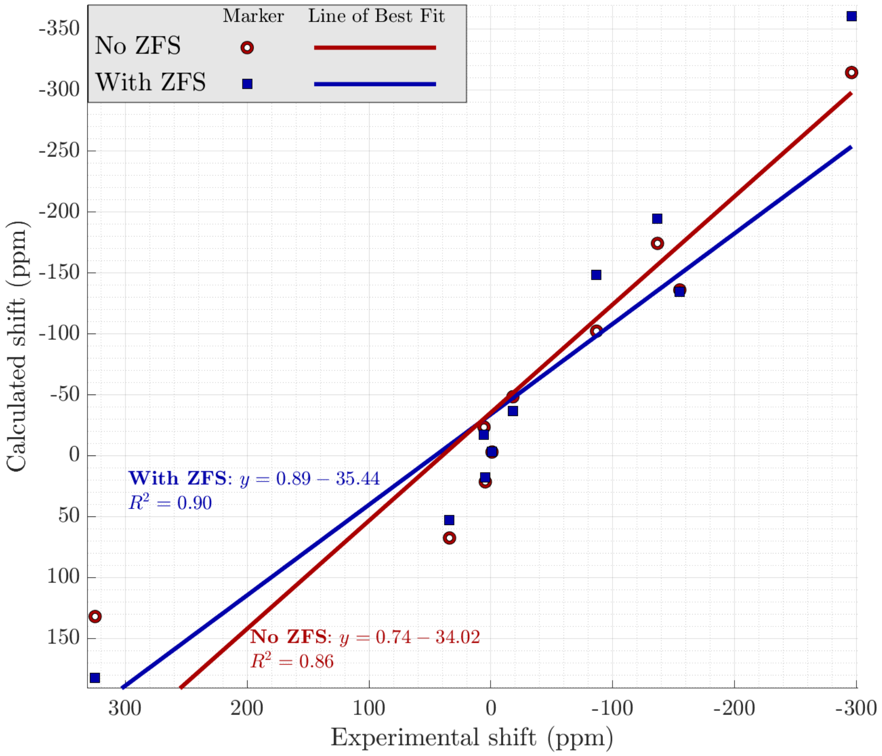

Figure 4.13: Calculated results against experimental results.

4.6 Conclusions

In this paper we have demonstrated the importance of including ZFS for assigning and predicting the pNMR chemical shifts of the lanthanide and actinide f^3 species. With the exception of the first example, our results are accurate enough to assign the observed shifts, and the first example demonstrates that applying ZFS can reorder shifts that are tightly grouped. However we have also demonstrated the importance of including spin-orbit coupling corrections to the hyperfine coupling matrix, especially when studying the chemical shifts of nuclei directly bonded to heavy nuclei. These necessary corrections are computationally demanding, and more work is needed to find theoretical and computational approaches that simplify applying this correction without sacrificing accuracy. The systems we have used as examples in this work typify the complexity of lanthanide and actinide containing molecules and the difficulties they pose for the computational predictions of their magnetic spectra. The modelling remains challenging and incomplete and requires further refinement as theoretical and computational progress is made.

4.7 Afterword

Some time for reflection has passed since this paper was published, and while it achieved its principal objective of qualitatively assigning the pNMR shifts for the actinide complexes, and showed that unambiguous assignment of experimental shifts is possible provided the separation between shifts is sufficient (*e.g.* larger than a couple of ppm for ^{1}H pNMR).

There follow further opportunities to improve both the methodology, and the model, and thereby potentially expand the qualitative power of the approach, with aim, albeit in the longer term, to progress towards quantitative results.

Improving the wavefunction

The most obvious improvement is to to add dynamic correlation to the SA-CASSCF wavefunction, *e.g.* via NEVPT2, as is the case in the remainder of the thesis. A further refinement is possible by noting that while in this study the number of states used to calculate the Zeeman matrix and ZFS tensor is the same as those used the state-averaging step, as discussed in the next chapter, it is possible to use the orbitals from a state-averaged calculation to perform an additional CASCI-SOC calculation (or a CASCI/NEVPT2-SOC calculation), and thereby represent small higher energy state contributions to the Zeeman matrix and ZFS tensor without unduly changing the one-electron description. This allows for the possibility of the establishment of a more robust cut-off, *e.g.* by both NEVPT2 energy and Zeeman-matrix contribution.

Modelling the pseudospin

This paper was written with the expectation that the pseudospin could be empirically modelled by $\tilde{S} = 3/2$. This was a very useful approximation for demonstrating the importance of the inclusion of ZFS, and of empathising the importance of PSO corrections to hyperfine matrices, especially where HALA effects are present.

However, while the paper met its stated aim, it could be improved, and one avenue of improvement becomes clear when examining the following energy level diagram (Figure 4.14) for the six molecules in this study, following the order set out in Figure 4.1. From the Boltzmann coefficients in the rightmost plot, it can be seen that for the first molecule, $\mathrm{Nd[\,L^{py}\,]^{3+}}$, the first four states will dominate, but higher order states are thermally accessible (at 300 K). By Hund's rules the lowest energy term symbol for $\mathrm{Nd^{III}}$ is $^4I_{9/2}$ (assuming that $J = |L - S|$) and the observed splitting may be more appropriately considered to correspond to a pseudospin of $\tilde{S} = J = 9/2$. A similar issue can be seen with the fifth molecule, $\mathrm{U(C_5Me_4SiMe_3)_3}$, where in retrospect an exploration of an empirical pseudospin of $\tilde{S} = 5/2$ may have been fruitful.

For the second and fourth molecule, $\mathrm{U(MeBTP)_3^{3+}}$ and $\mathrm{U(N(SiMe^tBu_2)_2)_3}$ respectively, the assigned pseudospin, $\tilde{S} = 3/2$, seems somewhat more reasonable as the CASSSF-SOC states are less thermally available, although a more robust treatment of pseudospin may well improve the result. Finally the third and sixth molecules, $\mathrm{U(C_5Me_5)_3}$ and $\mathrm{U(\eta\text{-}C_5Me_4Et)(\eta\text{-}(1,4\text{-}C_8H_6(Si^iPr_3)_2)}$, show only two accessible Kramers' doublet, so assigning a pseudospin of 3/2 seems more reasonable.

This implies that using $S = 3/2$ as an empirical pseudospin improves the correlation between the calculated and experimental shifts, but it is not the best possible approach. The following chapter presents a more refined study.

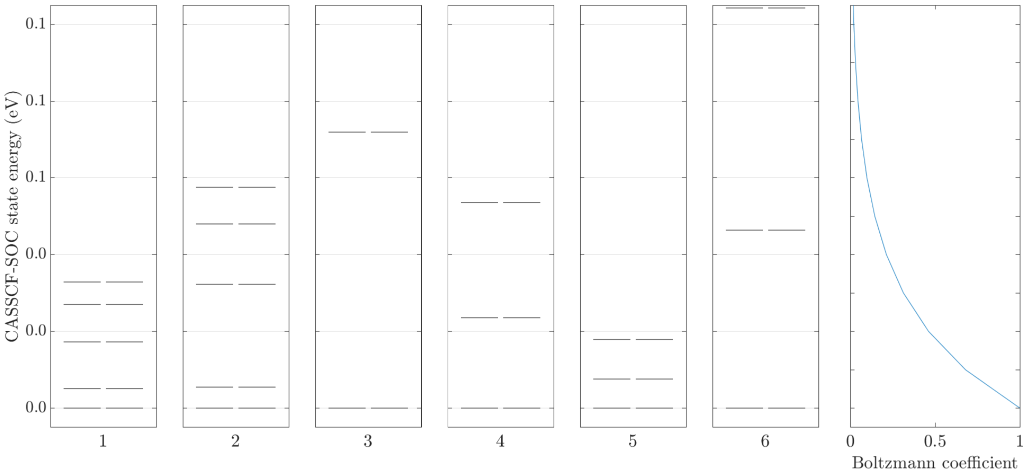

Figure 4.14: Left: CASSCF-SOC state energies for the six molecules in this chapter, measured from the lowest SOC state in each case. Numbering is as in Figure 4.1. Right: The Boltzmann coefficient at 300 K (x-axis) for corresponding energy separation for the previous four energy level diagrams (y-axis).

Chapter 5

Computational study of the magnetic properties of U(DOTA)

This chapter presents the text from a paper in preparation. References have been merged with those in this thesis. The corresponding supplementary information is presented in appendix B, and references to the tables contained therein reflect this.

The paper is concerned with U(DOTA), where DOTA is the ligand 1,4,7,10-tetraazacyclododecane-1,4,7,10-tetraacetate. As discussed in the Section 5.2, the complex exists in two conformers, described by the arrangement of the eight donor atoms of the DOTA ligand, the main conformer has a square antiprism (SAP) arrangement and the minor conformer has a twisted square antiprism (TSA), differentiated by the twist angle between two parallel squares. We performed partial geometry optimisations for a range of twist angles, but NEVPT2 calculations for the ground state of the TSA conformer implied that the minor conformer was largely absent at 300 K, so the minor conformer and intermediate geometries were deprioritised. However, SOC effects have an important role in stabilising U(DOTA), and the full SA-NEVPT2-SOC calculations implied there was an energy difference of 0.0018 hartree between the conformers, and a Boltzmann population of 15% for the TSA conformer. Further calculations on these intermediate geometries should allow for closer results to be calculated for the equatorial hydrogen atoms of the cyclen ring.

This chapter also presents a series of values for the Zeeman matrix and the ZFS tensor. Because the former matrix is not symmetrical, it is often symmetrised before analysis and diagonalised to obtain the principle coefficients, *i.e.* the g-factors, and the corresponding eigenvectors define the principal axis system (PAS) for the calculated quantity. It should be noted that doing so looses information and should be considered carefully as an approximated model.

There are two methods of symmetrising the Zeeman matrix.

1. Average the Zeeman-matrix and its transpose. This has the virtue of preserving the matrix's physical meaning, *i.e.* the matrix representation of the interaction of the magnetic field and the (pseudo)spin of the molecule, but it is not a tensor.

2. Multiply the Zeeman-matrix and its transpose, *i.e.* form the Abragam-Bleaney tensor. Then decompose the resulting 3×3 matrix into a set of eigenvalues and eigenvectors, the latter can then be used to define the PAS, the former are the square of the g-factors. This has the virtue of producing a true tensor, and because of this it is the preferred method for ORCA,[32] but it introduces a sign indeterminacy for the g-values.

The following four figures present the PAS for the Zeeman matrix and the ZFS tensor for the four molecules. The anionic species show the PAS of the Zeeman matrix assigned via the averaged matrix is rotated relative to those of the Abragam-Bleaney tensor system (The U(DOTA) eigenvectors only differ by sign). They are included to highlight that the symmetrisation, while conceptually valuable, becomes in the author's opinion, increasingly difficult to justify for molecules with large spin-orbit coupling due to the large asymmetry of the parent matrix. This is why this work prefers the irreducible tensor operator (ITO) approach.

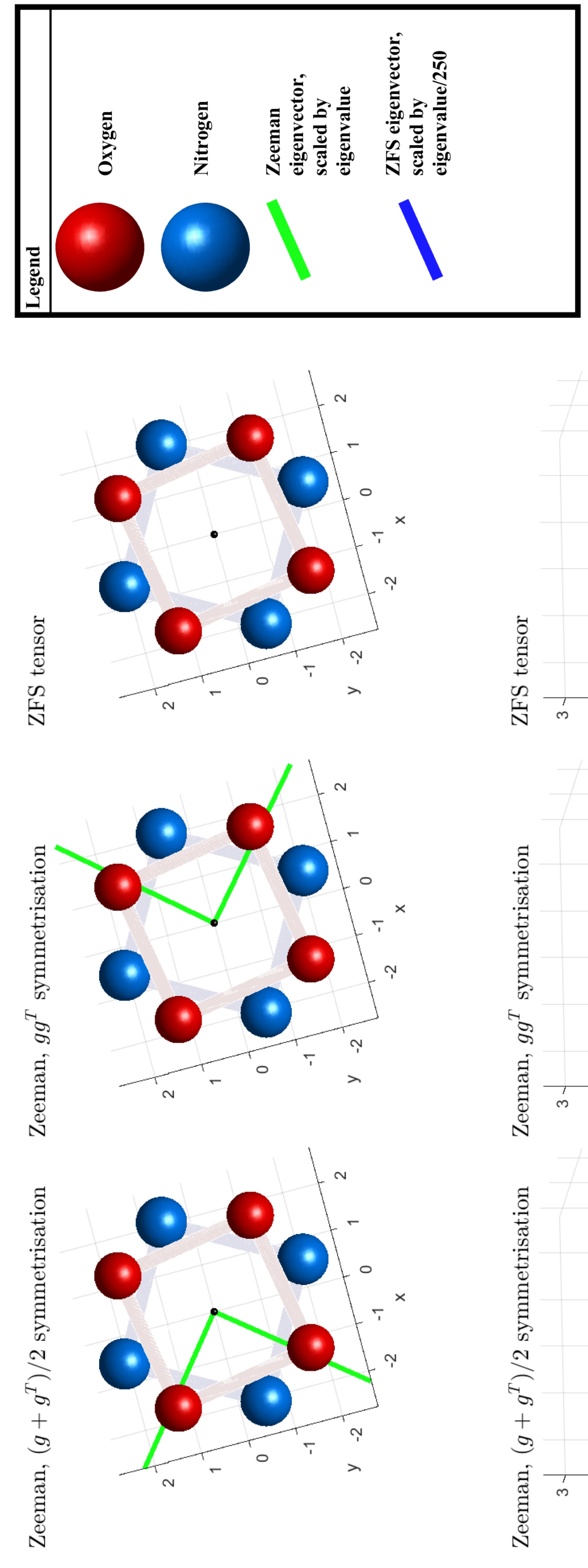

Figure 5.1: U(DOTA) Zeeman and ZFS eigenvectors defining a PAS: Eigenvectors are scaled by their corresponding eigenvalues. Carbon and hydrogen atoms are not shown for clarity. Axes are in Angstrom.

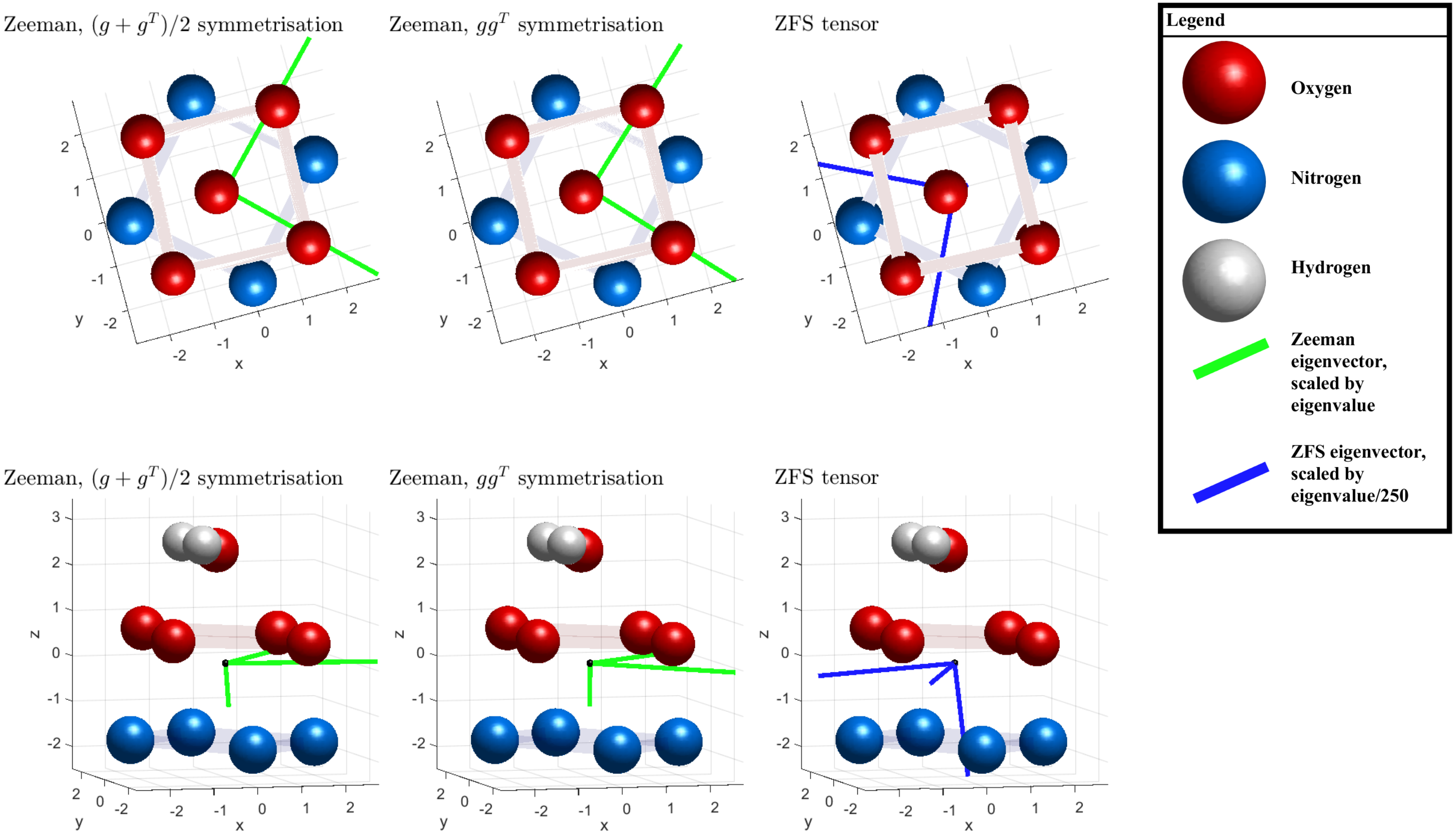

Figure 5.2: [U(DOTA)H_2O] Zeeman and ZFS eigenvectors defining a PAS: Eigenvectors are scaled by their corresponding eigenvalues. Cyclen carbon and hydrogen atoms and the top view water hydrogen atoms are not shown for clarity. Axes are in Angstrom.

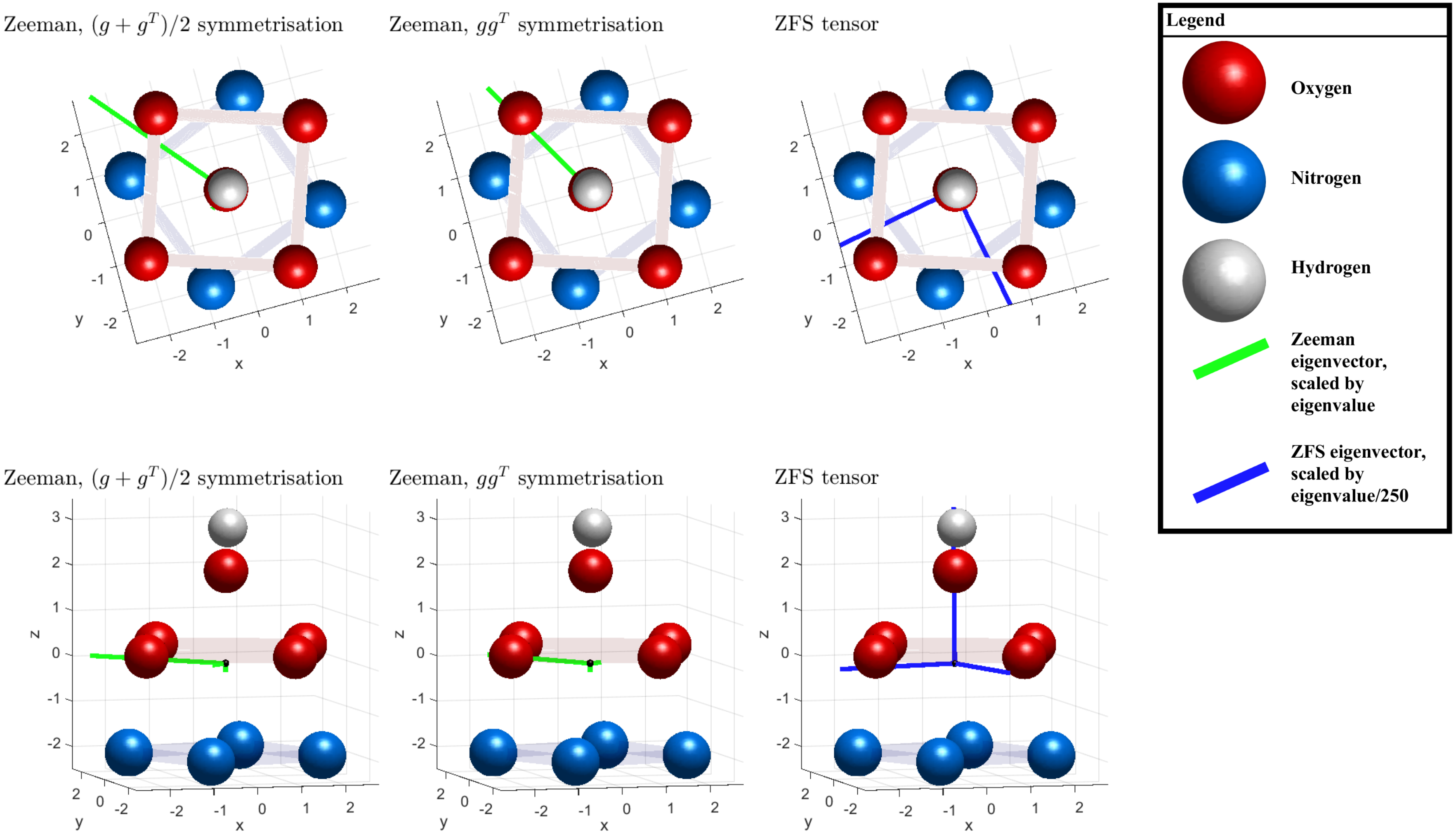

Figure 5.3: $[\mathrm{U(DOTA)OH}]^-$ Zeeman and ZFS eigenvectors defining a PAS: Eigenvectors are scaled by their corresponding eigenvalues. Cyclen carbon and hydrogen atoms are not shown for clarity. Axes are in Angstrom.

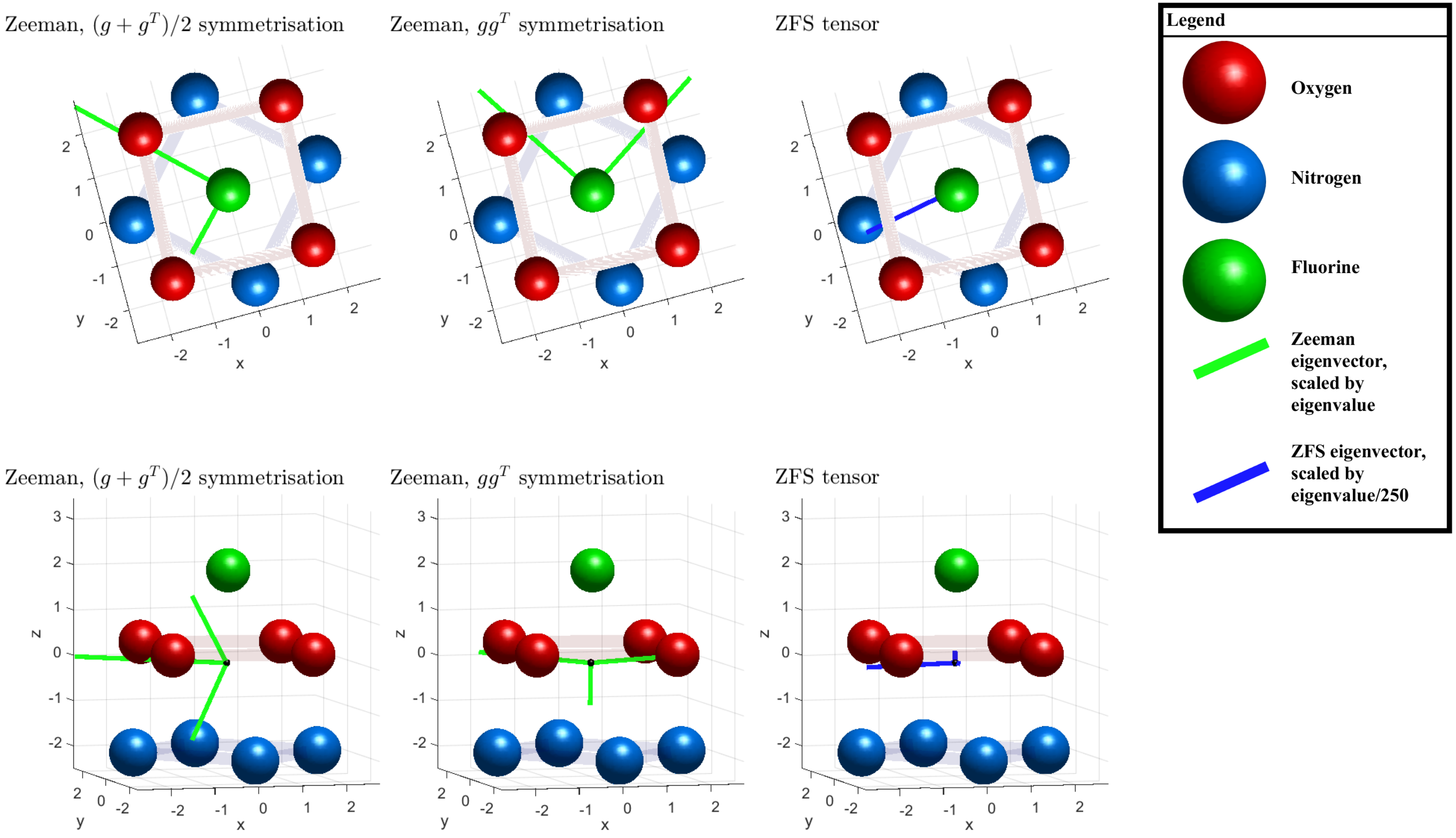

Figure 5.4: $[\mathrm{U(DOTA)F}]^-$ Zeeman and ZFS eigenvectors defining a PAS: Eigenvectors are scaled by their corresponding eigenvalues. Cyclen carbon and hydrogen atoms are not shown for clarity. Axes are in Angstrom.

Computational study of the magnetic properties of U(DOTA), with a focus on pNMR spectra and the effects of axial substitution.

Authors:

A. W. Lloyd, J. J. W. McDouall, D. Collison, V. Timmerman, L. S. Natrajan

Affiliation:

Department of Chemistry, The University of Manchester,

Oxford Road, Manchester, UK

Author contributions:

Draft preparation AWL, reviewing and editing AWL, JJWM, DC, LN,

pNMR experiments VT, Computational experiments AWL.

5.1 Abstract

This work studies the magnetic properties of U(DOTA) and three axially substituted variants, [U(DOTA)H_2O], [U(DOTA)OH]$^-$ and [U(DOTA)F]$^-$. This is achieved by calculating the main magnetic matrices and paramagnetic NMR (pNMR) spectra. U(DOTA) has two suggested assignments for its ^{1}H spectra,[3,4] and our calculations allow a definitive assignment. The complications due to large spin-orbit coupling (SOC) and the interchange between the square antiprism (SAP) and twisted square antiprism (TSA) conformers are discussed. The axial symmetry of the molecule allows a tensor decomposition technique to be used to model the Zeeman contribution, and this results in strong correlation between calculated and experimental results. Experimental assignments for the axially substituted variants do not distinguish between protons attached to the same carbon atom,[5] and we are able to separate these. The binding of a water ligand has little effect on the calculated spectra, but binding an anionic ligand results in a compression of the spectral range which our results duplicate. Binding an anionic ligand also causes the anisotropy axis to rotate by 90°. These effects are examined with reference to spin density. Finally ^{13}C spectra are predicted for future experimental verification.

5.2 Introduction.

Paramagnetic NMR (pNMR) is a useful probe into the nature and bonding of paramagnetic compounds, however actinide compounds challenge experimental pNMR techniques and computational models. Experimentally, radioactive nuclides require precautions to protect personnel and equipment; these become more significant for more radioactive nuclei, and decay processes also produce heat that interferes with experiments. Heat production can be slowed by reducing concentrations, but multidimensional approaches often need larger concentrations. Peak broadening and bleaching by paramagnetic relaxation enhancement (PRE) are also common.[187] Finally, nuclear decay processes can create other nuclei. As a result of these difficulties, paramagnetic spectra of actinides are uncommon and often unassigned.[3]

Computationally, actinide species require demanding calculations due to their open-shell, typically multiconfigurational nature along with the necessity of including scalar and spin-orbit relativistic effects and dynamic electron correlation[2,27,28,39] Furthermore, while the contracted nature of the lanthanide $4f$ orbitals implies that the unpaired electrons of lanthanide nuclei are not involved in bonding and the crystal field interaction energy is small, this is not true for the larger $5f$ orbitals. Actinide nuclei can form complexes with significant covalent nature.[188] This prevents the use of parameterised methods such as those discussed in the next section.

This paper studies the pNMR spectra of the uranium(IV) compound U(DOTA), [DOTA=1,4,7,10-tetraazacyclododecane-1,4,7,10-tetraacetate, Figure 5.5], and three axially substituted variants (F^-, OH^-, H_2O). DOTA is a modified cyclen, with the number of binding sites used dependent on the metal. Typically, it forms an octadentate structure with actinides, as in U(DOTA), with a C_4 symmetry axis. The oxygen and nitrogen atoms lie on separate parallel planes and form squares. This allows a twist angle to be defined (Figure 5.6). The dominant conformer has a twist angle of 39° and forms an approximate square antiprism (SAP) geometry,[5,179] the remaining significant conformer (twisted square antiprism, TSA) has a twist angle of 24° (geometry optimisations for this paper). Calculated geometries are presented in the Supplementary Information (SI), Table B1. An axial ligand can bind on the oxygen side of the molecule, but the nitrogen side is sterically blocked. Finally, U(IV) has an

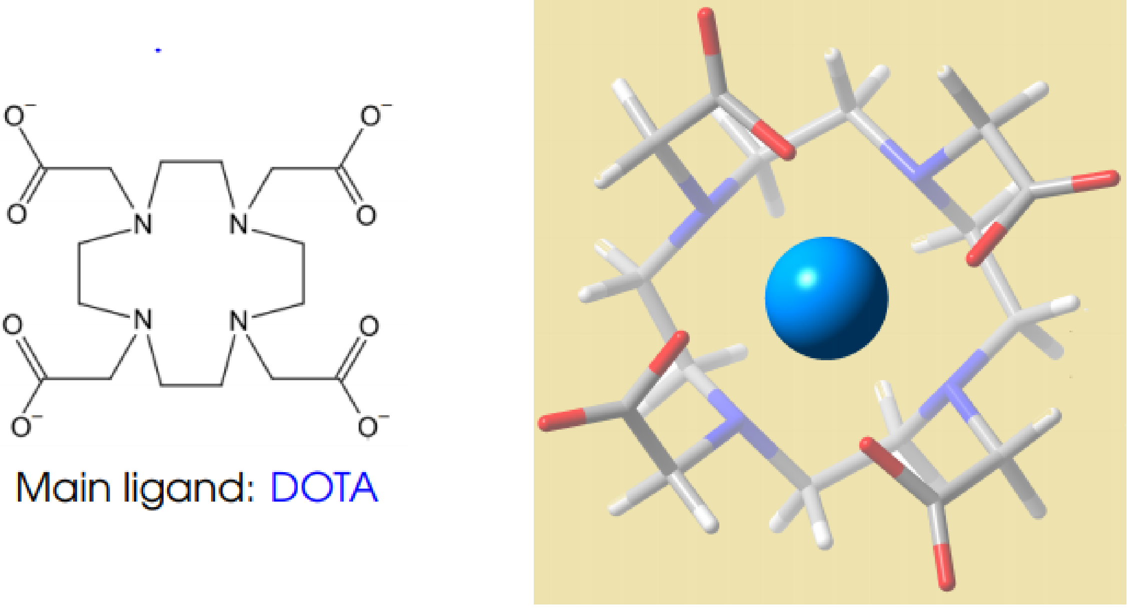

Figure 5.5: 1,4,7,10-Tetraazacyclododecane-1,4,7,10-tetraacetate (DOTA) and U(DOTA). Uranium is represented by the blue sphere, oxygen atoms are in red, nitrogen in blue, carbon in grey, hydrogen in white. Viewed from the oxygen side.

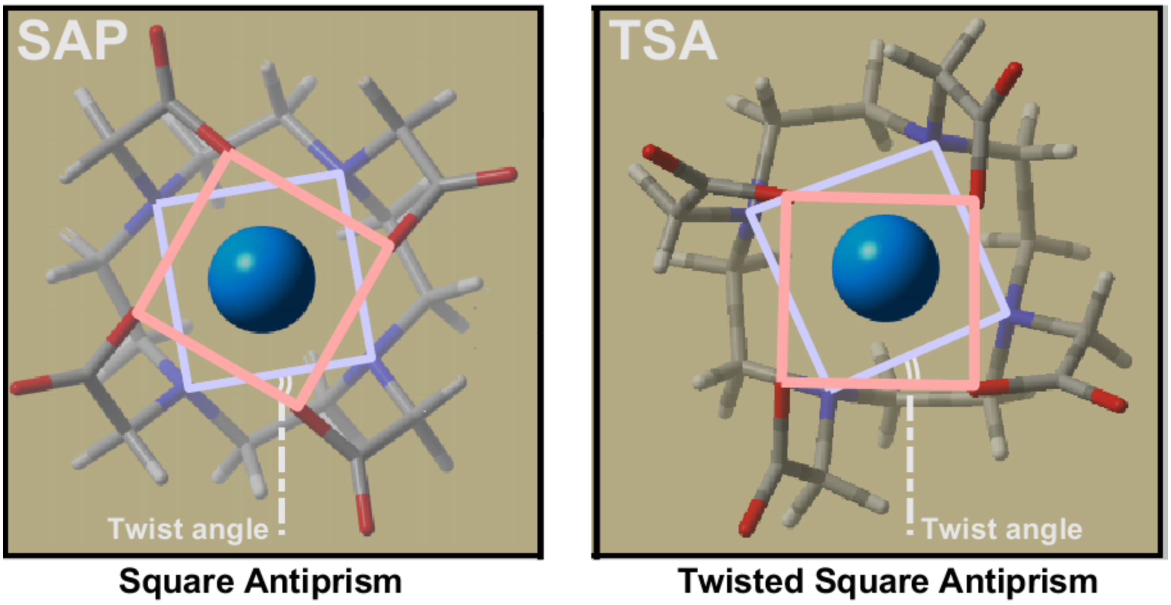

Figure 5.6: Conformers of U(DOTA). Colouring scheme as above. Viewed from the oxygen side.

f^2 electronic configuration and therefore has spin $S = 1$, so zero-field-splitting (ZFS) is a further complication that needs to be considered when assigning pNMR spectra.

Industrially the separation of nuclear waste products and recovery of fissile material is dependent on extractants exploiting differences in ligand binding.[189] Improving our understanding of this could lead to more efficient and effective separation allowing more tailored storage. Modified DOTA complexes are used extensively in magnetic resonance imaging (MRI) and radiological medical imaging due to their "high thermodynamic stability and kinetic inertness"[190] leading to high *in vivo* stability.[191] Further developments in chemotherapy are also being investigated.[192]

5.3 Theoretical approach

Experimental NMR signals, δ_{exp}, are reported as a shift from a reference signal, σ_{ref}, *i.e.*

$$\delta_{\text{exp}} = \sigma_{\text{ref}} - \sigma_{\text{exp}}. \tag{5.1}$$

where σ_{ref} and σ_{exp} are the isotropic chemical shielding of the reference molecule and the target molecule. These shifts are proportional to the spectrometer frequency and are reported in parts per million (ppm) of that frequency.

For a diamagnetic molecule, the orbital or Ramsey shielding, σ_{orb}[126] present in δ_{exp}, is split into two terms; the first term being a response purely from the ground state of the system labelled as the "diamagnetic" component, while the second term arises due to interactions between ground and excited states and is labelled as the "paramagnetic" component. Both terms exist in all molecules and the labels used for the orbital shielding do not relate to the presence or absence of unpaired electrons.[193]

For a paramagnetic molecule two additional terms must be considered and the total chemical shielding is given by

$$\sigma_{\text{exp}} = \sigma_{\text{orb}} + \sigma_{\text{c}} + \sigma_{\text{pc}}. \tag{5.2}$$

The contact term, σ_{c}, is caused by non-zero spin-density at the atomic nucleus. This is only possible in the presence of *s* orbitals and is interpreted as an interaction through bonds; the size of the contact shift acts as a qualitative measure of covalency. It relates to the isotropic part of the hyperfine matrix. The pseudocontact term, σ_{pc}, represents the effect of spin-dipole interactions between the nuclear and electronic spins that are mediated through space. A common approach to calculating pNMR shifts for lanthanide complexes is based on the assumption that the ligand interaction is primarily electrostatic, and the contact term is small. Ligand field effects on the unpaired f electrons are typically small and considerably less than electronic correlation and spin-orbit coupling (SOC); this implies that the nature of transitions between electronic energy levels are similar for a range of ligands, so the ligand interaction can be modelled perturbationally, with crystal field theory applied to split a $(2J+1)$ manifold of m_j states of fixed $J = L + S$. This typically exploits a tensorial decomposition to give a model Hamiltonian,[194]

$$\hat{H}_{\text{Ligand Field}} = \sum_{k=2,4,6} \theta_k \sum_{q=-k}^{k} B_q^k \hat{O}_k^q, \tag{5.3}$$

where B_q^k are crystal field parameters which can be tabulated for lanthanide systems, $\hat{O}_k^q$ are the Stevens' operators[195] and θ_k are operator equivalent coefficients. Bleaney's theory of magnetic anisotropy[196] gives an approach to predicting lanthanide pNMR shifts based on the magnetic susceptibility tensor, χ, and its eigenvalues $\{\chi_x, \chi_y, \chi_z\}$. This approach assumes that the spin interaction is largely mediated through space (pseudocontact or spin-dipolar interaction) and not through bonds (contact, implying spin density at the nucleus). The paramagnetic shift in spherical coordinates (r, θ, ϕ), with the paramagnetic centre at the origin is given by[194,197]

$$\delta_p(r,\theta,\phi) = \frac{1}{12\pi r^3}\left[\chi_{\text{ax}}\left(3\cos^2\theta - 1\right) + 3\chi_{\text{rh}}\sin^2\theta\cos 2\phi\right]. \tag{5.4}$$

The axial and rhombic components of the susceptibility tensor are defined as $\chi_{\text{ax}} = \frac{3}{2}\chi_{\text{z}}$ and $\chi_{\text{rh}} = \frac{1}{2}(\chi_{\text{x}} - \chi_{\text{y}})$ respectively. These are related to the crystal field parameters by

$$\chi_{\text{ax}} = -\frac{\mu_0\mu_B^2}{10(k_BT)^2}C_JB_2^0, \qquad \chi_{\text{rh}} = -\frac{\mu_0\mu_B^2}{30(k_BT)^2}C_JB_2^2, \tag{5.5}$$

where μ_0 is the magnetic permeability of a vacuum, μ_B is the Bohr magneton, k_B is the Boltzmann constant, T is the temperature, and C_J is Bleaney's constant. This approach allows the parametrisation of B_0^2 and B_2^2 for many lanthanide systems. Furthermore, for a molecule with a n-fold ($n > 2$) symmetry axis, then $\chi_{\text{x}} = \chi_{\text{y}}$, so only the χ_{ax} term survives. Hence the predicted Bleaney pseudocontact shift, $\delta_p(r,\theta,\phi)$, has a similar shape to a d_{z^2} orbital, with areas of paramagnetic shielding and deshielding, split by a magic angle of $\cos^{-1}(\pm\sqrt{1/3}) = \{70.5°, 109.5°\}$. Unfortunately, this theory makes several assumptions that make it unsuitable for predicting actinide paramagnetic shifts, and these are listed below.

- The crystal field splitting is much less than the thermal energy, k_BT,[197] so the J manifold energy levels are equally populated.
- Most of the crystal field parameters can be neglected.[198]
- The electron is a point charge, and it relaxes from an excited state instantly.
- The susceptibility tensor aligns with the principal symmetry axis
- J is a good quantum number; in cases where this is not true the concept of "J-mixing" is used,[199] for example in some lanthanide(III) species.

We prefer a more direct approach. Consider a diamagnetic atom with nuclear spin $\mathbf{I}_{\text{nuc}}$ within a magnetic field $\mathbf{B}$. If there were no electrons, the atomic energy levels would be symmetrically split by $2\gamma_{\text{nuc}}|\mathbf{B}|$, where γ_{nuc} is the magnetogyric ratio of the nucleus. However, the field induces an electronic current reducing the field experienced by the nucleus. This effect is modelled by the chemical shift matrix, $\boldsymbol{\sigma}_{\text{orb}}$. The resulting Hamiltonian in atomic units is given by $\hat{\mathcal{H}}_{\text{NMR}} = -\gamma_{\text{nuc}}\mathbf{B}\cdot(\mathbf{I}_3 - \boldsymbol{\sigma}_{\text{orb}})\cdot\mathbf{I}_{\text{nuc}}$, where $\mathbf{I}_3$ is a 3×3 identity matrix. If, however, the atom is paramagnetic, the magnetic moment aligns with the field. The three dominant interactions are the Zeeman interaction between the field and the electronic spin-dipole, the hyperfine interaction between the nuclear and electronic spin-dipoles, and, if there are two or more unpaired electrons present, the interaction between electronic spin-dipoles, resulting in a further splitting between different m_s states (zero field splitting, ZFS). These are represented by the Zeeman coupling matrix, $\mathbf{g}$, the hyperfine coupling matrix, $\mathbf{A}$ and the ZFS tensor $\mathbf{D}$ respectively. The corresponding pNMR Hamiltonian is given by,[108–110,133]

$$\hat{\mathcal{H}}_{\text{NMR}} = -\gamma_{\text{nuc}}\mathbf{B}\cdot(\mathbf{I}_3 - \boldsymbol{\sigma}_{\text{orb}})_{\text{nuc}} + \mu_B\mathbf{B}\cdot\mathbf{g}\cdot\widetilde{\mathbf{S}} + \widetilde{\mathbf{S}}\cdot\mathbf{D}\cdot\widetilde{\mathbf{S}}, \tag{5.6}$$

where $\widetilde{\mathbf{S}}$ is an effective parameter referred to as the pseudospin.[122,149] In the absence of SOC the pseudospin is simply the electronic spin. The corresponding paramagnetic shielding matrix σ_{p} at temperature T, can be written as[127,130–133]

$$\sigma_{\text{p}} = -\frac{1}{\gamma_{\text{nuc}}k_BT}\mathbf{g}\cdot\mathbf{Z}\cdot\mathbf{A}, \tag{5.7}$$

where $\mathbf{Z}$ is a 3×3 coupling matrix with trace always equal to $S(S+1)$. In the absence of ZFS this matrix is diagonal with equal elements. When modelling ZFS, a second order approximation can be made by forming and diagonalising the $\mathbf{S}\cdot\mathbf{D}\cdot\mathbf{S}$ matrix.[130,133] The resulting eigenstates $|n\rangle$ are linear combinations of pure spin states, and we label the eigenvalues E_n. The coupling matrix is then formed via

$$Z_{\mathrm{xy}} = \frac{1}{\omega}\left[\sum_{nm}^{\text{eigenstates}} q_{nm}\,\langle n|\mathbf{S}_{\mathrm{x}}|m\rangle\,\langle m|\mathbf{S}_{\mathrm{y}}|n\rangle\right], \tag{5.8}$$

$$\text{where}\quad q_{nm} = \begin{cases} e^{\frac{E_n}{k_BT}} & E_n = E_m \\ -\frac{k_BT}{E_n-E_m}(q_{nn}-q_{mm}) & E_n \neq E_m, \end{cases} \tag{5.9}$$

and ω is the sum of the Boltzmann coefficients, q_n. Higher order methods are reliant on matrices that are not currently available,[1] however for an axially symmetric system an irreducible tensor operator (ITO) approach is possible. This method improves the description of the Zeeman component, but because the corresponding hyperfine matrix is unavailable, approximates the hyperfine component by diagonalising $\mathbf{A}\mathbf{A}^T$. This is suitable for U(DOTA), but because of the reduced symmetry of [U(DOTA)H_2O] and the non-axial behaviour of the magnetic anisotropy axis for [U(DOTA)OH]$^-$ and [U(DOTA)F]$^-$, this hyperfine approximation is not appropriate.

5.3.1 The ITO approach[*]

In 2012 Van den Heuvel and Soncini[1] presented an extended approach to handle cases with arbitrary degeneracy. It is based, in part, on the observation that the set of spin tensors $\{S_q^{(k)} : k \leqslant 2\tilde{S}\}$ form a complete basis for the set of all complex square matrices of dimension $2\tilde{S}+1$. For instance, the z component of the magnetic moment $\boldsymbol{\mu}$ can be decomposed via

$$\boldsymbol{\mu}_z = \sum_{k\text{ odd}}^{k\leqslant 2\tilde{S}}\ \sum_{k}^{q=-k} (-1)^q g_{qz}^{(k)} \mathbf{S}_{-q}^{k}, \qquad \text{where}\ \ g_{qz}^{(k)} = \frac{2k+1}{\langle S||S^{(k)}||S\rangle} Tr\left(\mathbf{S}_q^{(k)}\boldsymbol{\mu}_z\right), \tag{5.10}$$

and the coefficient $g_{qz}^{(k)}$ is referred to as a generalised Zeeman “tensor”. In the absence of ZFS, the pNMR contribution to the shift is given by

$$\sigma_{\kappa v} = -\frac{\mu_B}{g_n k_B T}\cdot\frac{1}{S+1}\sum_{k=1}^{2S}\sum_{q=-k}^{k} g_{q\kappa}^{(k)}(a_{qv}^{(k)})^*\frac{\langle S||S^{(k)}||S\rangle^2}{2K+1}. \tag{5.11}$$

---

[*] This subsection is a repeat of Section 3.10.1 and included for completeness.

where $\langle S||S^{(k)}||S\rangle$ is the reduced matrix element of the tensor operator $\hat{\mathcal{S}}^{(k)}$ in a basis of $2S+1$ spin states, *i.e.* $\{|S,-S\rangle...|S,S\rangle\}$, being derived via Wigner-Eckhart theory

ZFS is accounted for via a spin projection $\hat{\mathbf{P}}_0$ of the ZFS Hamiltonian

$$\hat{\mathcal{P}}_0\,\hat{\mathcal{H}}_{ZFS}\,\hat{\mathcal{P}}_0 = \sum_{k\text{ even}}^{K\leqslant 2\tilde{S}}\;\sum_{k}^{q=-k} D_q^{2k} S_{-q}^{2k}, \qquad \text{where } \hat{\mathcal{P}}_0 = \sum_{q=|S,-S\rangle...|S,S\rangle} |q\rangle\langle q| \tag{5.12}$$

Forming the $\hat{\mathcal{P}}_0\hat{\mathcal{H}}_{ZFS}\hat{\mathcal{P}}_0$ matrix in the $\{|m_{\tilde{S}} = |-\tilde{S}\rangle...|m_{\tilde{S}} = -\tilde{S}\rangle\}$ basis and diagonalising it gives $(2\tilde{S}+1)$ eigenfunctions $|\lambda\rangle$ which can be used to build the spin projector and from these it can be shown that

$$\sigma_{\kappa\upsilon} = \sigma_{\kappa\upsilon}^{\text{orb}} - \frac{\mu_B}{\mu_N}.\frac{1}{g_N}\sum_{k,k'=1}^{2\tilde{S}}\;\sum_{q=-k}^{k}\;\sum_{q'=-k'}^{k'} g_{q\kappa}^{(k)}\; Q_{k'q'}^{kq}\; a_{q'\upsilon}^{(k')}\text{, where}$$

$$Q_{k'q'}^{kq}(\lambda,\lambda') = \sum_{\{\lambda\},\{\lambda'\}}^{deg.St.} \cdot \begin{cases} \frac{e^{-E_\lambda/k_BT}}{\omega k_BT}\sum_{\lambda}^{\{\lambda\}}\langle\lambda|S_q^k|\lambda\rangle\langle\lambda|S_q^k|\lambda\rangle & E_\lambda = E_{\lambda'} \\ \frac{-2e^{-E_\lambda/k_BT}}{\omega(E_\lambda - E_{\lambda'})}\Re\left[\sum_{\lambda}^{\{\lambda\},\{\lambda\}} \lambda|S_q^k|\lambda'\rangle\langle\lambda'|S_q^k|\lambda\rangle\right] & \text{otherwise,} \end{cases}$$

and ω is the sum of Boltzmann weights, a are the hyperfine coefficients.

5.4 Methodology

Figure 5.7 outlines the basic methodology, which is similar to our previous work.[2] Unless stated all calculations were performed using ORCA 4.2.1 and a SARC basis set with a g polarisation function† on the uranium atom[30] and a def2-TZVP basis set on the lighter atoms. Geometries were generated using Gaussian09[169] at the DFT level with the PBE0[55] functional. An in-house atomic ZORA procedure was used to represent scalar relativistic effects.[27,28] This procedure ensures gauge independence. Orbital shielding and hyperfine matrices were obtained using DFT and the Douglas-Kroll Hamiltonian (DKH)[154] to represent scalar relativistic effects. Additional tight s functions on the active nuclei were added for hyperfine calculations; these better represent the nuclear cusp. The nuclear spin – electron orbit contributions were also included in the hyperfine calculation. The latter is the most computationally expensive part of the process.

The starting orbitals for the CASSCF(2,7) calculation were the f manifold from a DFT/LDA calculation, obtained using a smaller basis set (def2-SVP) on the light

---

†TVZP quality with $29s20p16d12f1g/21s13p10d7f1g$ uncontracted/contracted gaussian functions for a uranium atom.

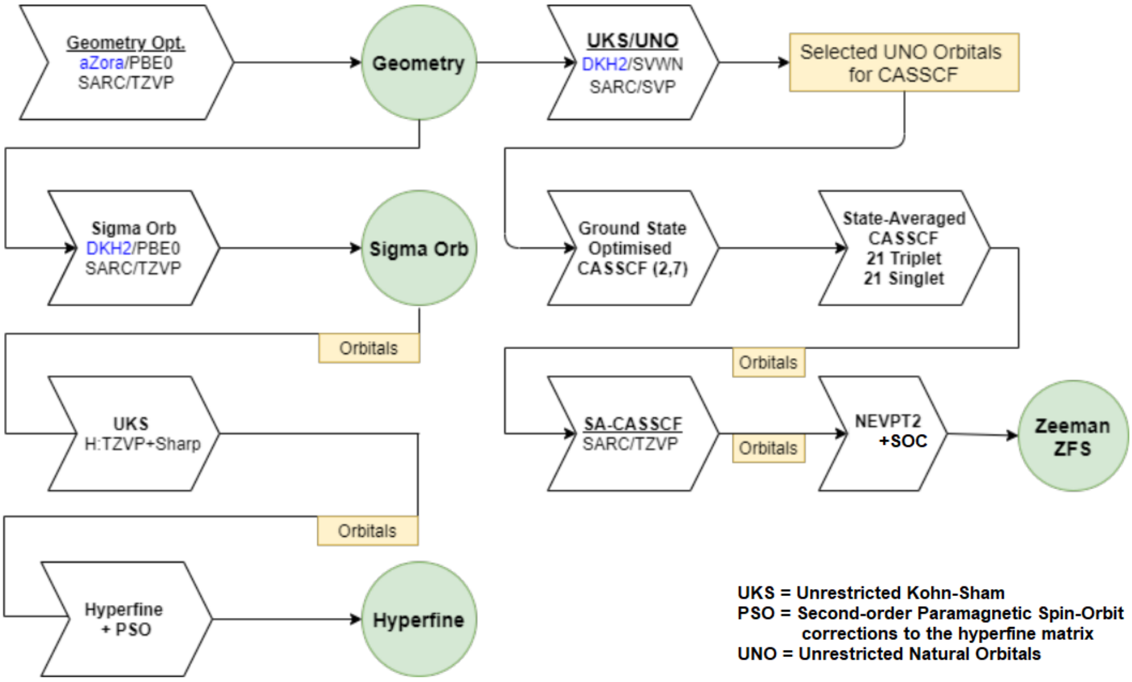

Figure 5.7: Computational methodology. See text for details of individual steps / terms.

atoms and optimised over the ground state. The resulting orbitals were used to establish the optimal state-averaging (SA) as discussed below, and reoptimised with a SA-CASSCF calculation with the default basis. These optimised orbitals were used to generate the Zeeman and ZFS matrices via CASCI/NEVPT2-SOC over all available states.

The use of CASSCF requires the selection of an active space of orbitals.[63] One approach is to consider the occupation numbers from the natural orbitals formed from a unrestricted DFT calculation and select orbitals within a range of orbital occupancies (*e.g.* 0.02–1.98). This is necessarily flawed as they are derived from a single Kohn-Sham configuration. We exploited a more representative multiconfigurational approach, the iterative configuration expansion (ICE)[200] method to assess the active space. The ICE method uses a truncated expansion of the CI wavefunction and perturbationally selects the most important components and improves them iteratively. Figure 5.8 shows the orbital occupations that result from a CASCI-ICE(22,60), with the f-orbitals (151-157) indicated. From this we conclude that the f-shell provides good coverage of the multiconfigurational states since the other orbitals have occupation numbers that differ from fully occupied (*i.e.* 2) or unoccupied (*i.e.* 0) by less than 0.02. Figure 5.9 shows the active space orbitals and their energies from the final SA-NEVPT2 calculation.

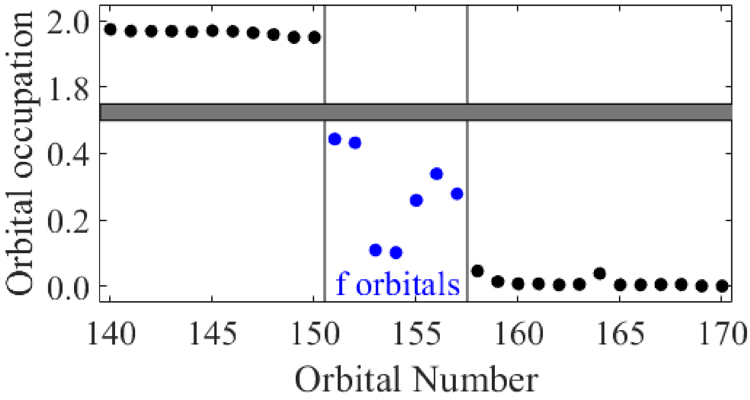

Figure 5.8: Orbital occupation numbers from a CASCI-ICE(22,60) calculation on U(DOTA), using the unrestricted natural orbitals from a DFT/LDA calculation (basis as in text).

.

The state-averaged CASSCF process optimises the one-electron molecular orbitals and the CI expansion coefficients for the ground and excited electronic states; the Zeeman and ZFS matrices depend on the interaction between these states. Ideally the MOs should be individually optimised for each state, but this produces sets of non-orthogonal orbitals which are computationally challenging to use and are not implemented for magnetic property calculations. Instead a single set of MOs is used for all electronic states. This implies that the MOs need to be optimised over a set of states, a technique known as state averaging. This creates a trade-off: as more states are added to the state-averaging process, the one-electron representation of a given state becomes less accurate.

The D parameter of the ZFS tensor is sensitive to changes in state-averaging and can be used to establish the most appropriate states to be include in the process. Figure 5.10 shows the D parameter obtained from a CASSCF(2,7) calculation on U(DOTA) with all 21 triplet and singlet states included in the calculation, but with the number of states included in the averaging process being systematically increased (states 19 and 20 are degenerate and the calculation will not converge if only state 19 is included).

The flattening of this graph implies that state-averaging over 18 triplet states results in suitable orbitals for calculating the triplet contributions to D. Continuing this

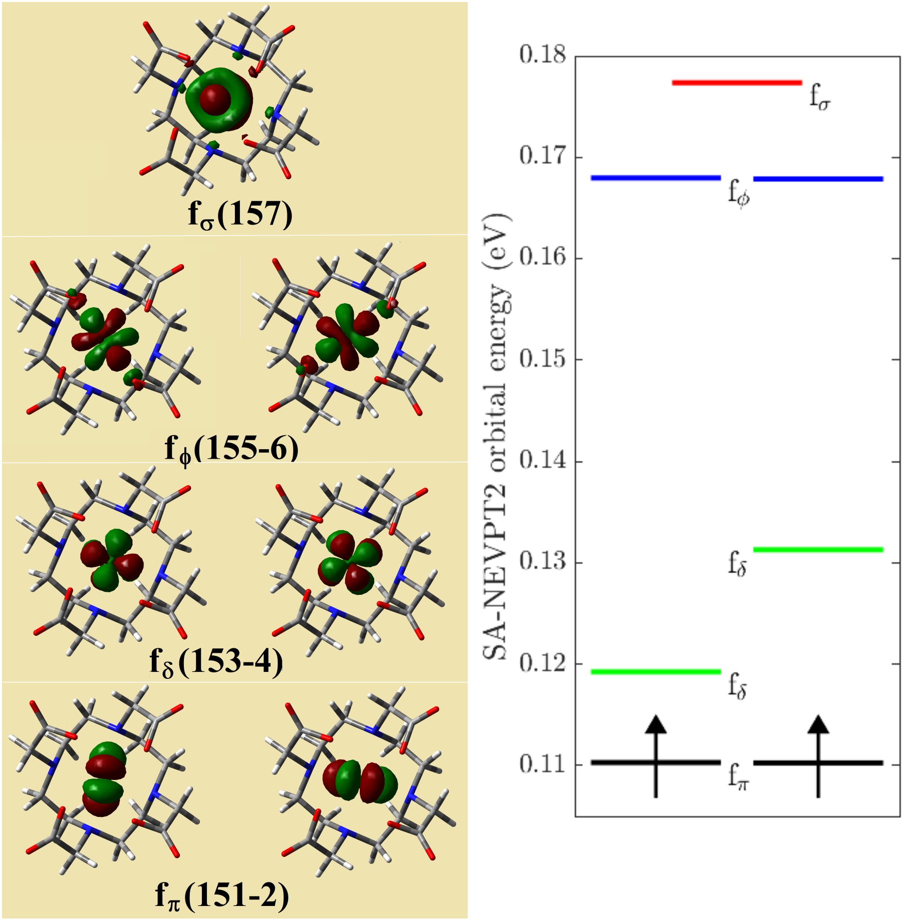

Figure 5.9: U(DOTA) active space orbitals (left) and qualitative SA-CASSCF natural orbital energies (right). Colouring as in Figure 5.12, viewed from the oxygen side.

approach by including singlet states indicates that only the first 4 singlet states should be included. Figure 5.11 shows that NEVPT2 state energies from the resulting state-averaged calculation, and implies that this approach is consistent with introducing a 1 eV cut-off for the state energies. The figure also shows the contribution of each state to the D parameter of the ZFS tensor confirming that the states with the largest contributions are included in the state averaging process. This cut-off was adopted for the substituted species based on their fully state-averaged energies. Similar plots for the substituted species, U(DOTA)OH$_2$, [U(DOTA)OH]$^-$ and [U(DOTA)F]$^-$ are shown in the supplementary information (SI: Figures B.1–B.3) and indicate the state-averaging used.

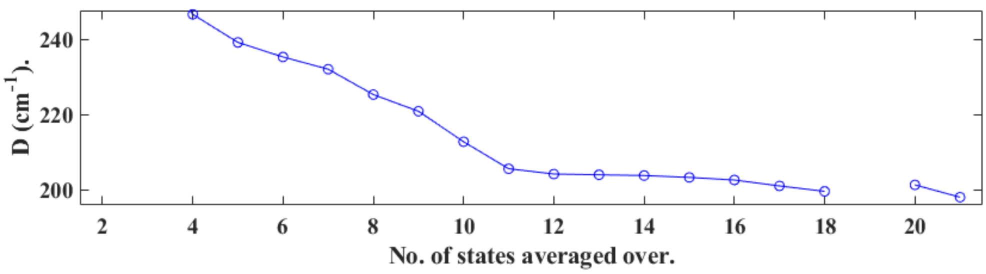

Figure 5.10: Variation of ZFS parameter D for U(DOTA) as state-averaging increases. ZFS matrix is formed over 21 triplet and singlet states, the indicated number of triplet states are included in the averaging.

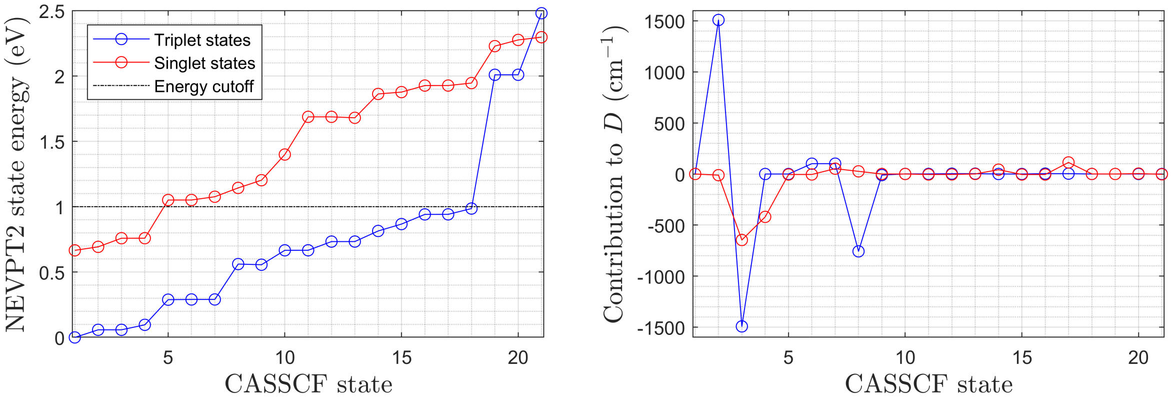

Figure 5.11: 18 triplet, 4 singlet SA-NEVPT2 individual state energies (eV from lowest state) for U(DOTA) and their contributions to the D tensor (SARC/def-TZVP basis).

.

5.5 U(DOTA)

Figure 5.12 shows the labelling scheme for the chemically distinct hydrogen and carbon atoms. The scheme defines the oxygen plane to be above the nitrogen plane and labels the staggered carbon atoms in the cyclen ring closer to the oxygen plane as $C_{\uparrow}$; $C_{\downarrow}$ is defined as further away. The cyclen protons inherit the attached carbon arrow label and are labelled A and E for axial and equatorial respectively. The acetate carbon atoms are labelled C_{arm} (methylene) and C_{carboxyl}, and the pendent protons on C_{arm} are labelled $H_{\uparrow}$ and $H_{\downarrow}$. The averaged uranium-atom distances for U(DOTA) are shown in Table 5.1, the pendent carbon-uranium distances are shorter than for all distances to cyclen carbon atoms, and both axial protons are closer to the metal than the equatorial ones. The optimised geometries of all species are given in the SI (Tables B.1 to B.4).

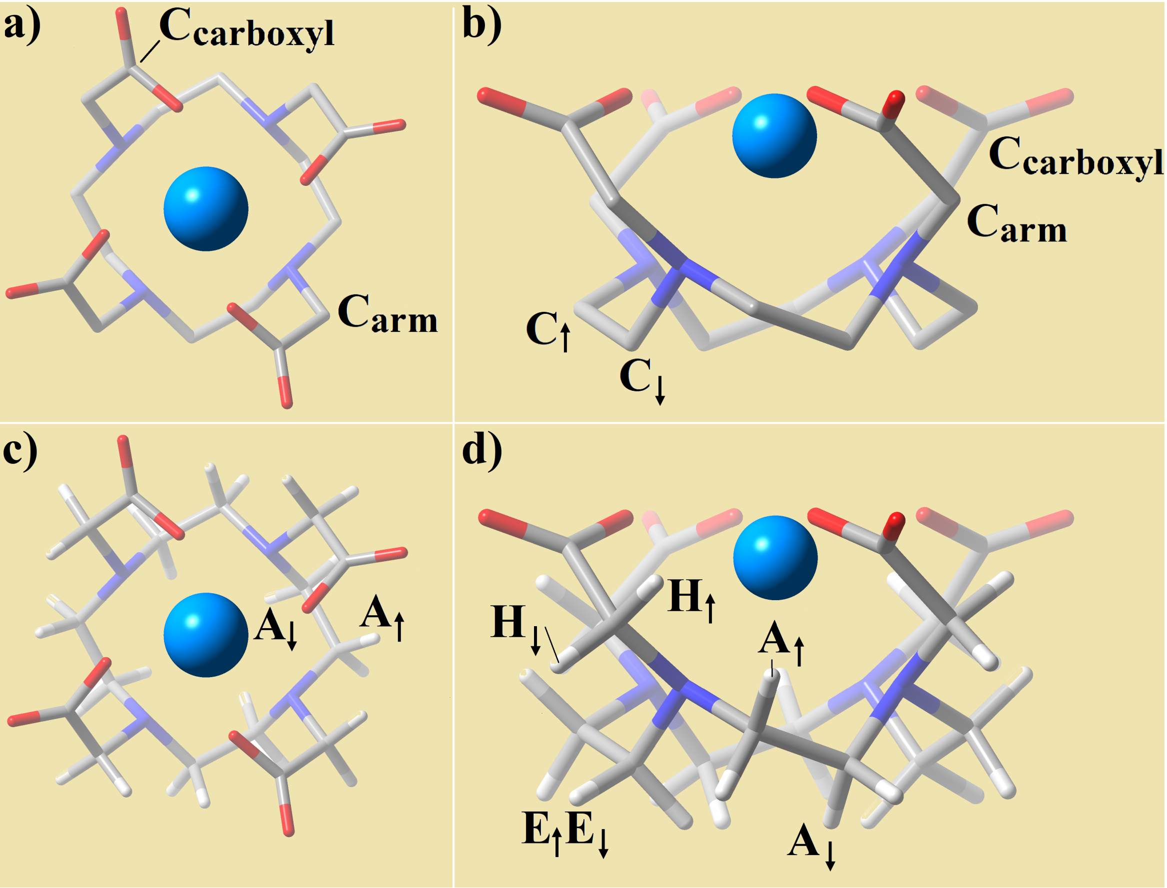

Figure 5.12: Labelling scheme for carbon and hydrogen atoms in U(DOTA), colour scheme as in Figure 5.1.

Table 5.1: Selected U–atom distances (Å) in U(DOTA).

U-$A_\uparrow$	3.72	U-$E_\uparrow$	4.51	U-$H_\downarrow$	3.68	U-$C_\uparrow$	3.49	U-C_{arm}	3.36
U-$A_\downarrow$	3.79	U-$E_\downarrow$	4.50	U-$H_\downarrow$	4.42	U-$C_\downarrow$	3.50	U-C_{carboxyl}	3.23

5.5.1 Comparison of calculated and experimental spectra

Figures 5.13 and 5.14 show the experimental ^{1}H NMR and ^{1}H-^{1}H COSY spectra for U(DOTA).[3] The resonance positions and their assignments from the work of Timmermann[3] are in Table 5.2, and the assignments follow the labelling given in Figure 5.8. The 2D COSY result implies that the signals at 18.39 and 37.86 ppm are due to the protons on C_{arm}, and this means that the signals at −0.61 and −6.00, −54.53 and 20.40 ppm are from the cyclen ring.

Timmermann's assignment of particular resonances to H atoms in the SAP structure of U(DOTA) was made through a Bleaney analysis (see Section 5.2) and using geometric data from [Eu(DOTA)]$^-$. That assignment was supported by the results

Table 5.2: Experimental and calculated ^{1}H NMR chemical shifts (ppm) for U(DOTA).

	Expt.^{3*}	Expt.^{4†}	DFT^{3‡}	CASSCF^{3‡}	This work^a	This work^b
$A_\uparrow$	20.40	38.54/5.77	-11.25	-16.87	19.29	22.09
$A_\downarrow$	-54.53	38.54/5.77	44.83	-15.57	-43.02	-54.50
$E_\uparrow$	-0.61	19.32/0.76	14.26	21.80	7.94	10.94
$E_\downarrow$	-6.42	19.32/0.76	16.02	4.57	7.87	12.06
$H_\uparrow$	37.86	21.74/-55.61	-30.30	-45.00	29.42	38.67
$H_\downarrow$	18.39	21.74/-55.61	-9.82	-15.57	14.44	14.56

[*] assignment as in reference 3 and supported by this work.

[†] assignment as in reference 4, at variance with this work.

[‡] calculations using DFT/CASSCF Zeeman matrix, respectively.

[a] calculation using NEVPT2-SOC matrices as in Section 5.3, $\tilde{S} = 1$, SAP.

[b] calculation using NEVPT2-SOC ITOs as in Section 5.3.1.

of some DFT and CASSCF calculations, which poorly reproduced the experimental chemical shifts, see Table 5.2.

Figure 5.15 compares the experimental results with the calculated ^{1}H pNMR shifts (including ZFS and PSO corrections) for the SAP conformer, by using the methods described in Section 5.3. The calculated ^{13}C pNMR shifts are also given, but no experimental data have yet been reported. These calculations correctly predict the sign of the ^{1}H pNMR shifts, and they confirm the assignment of the resonances at 37.86 and 18.39 ppm to the two H atoms, $H_\uparrow$ and $H_\downarrow$, bonded to C_{arm}, respectively. Experimental resonances at 20.40 and -54.53 ppm are also unambiguously assigned to the axial H atoms on the cyclen ring, $A_\uparrow$ and $A_\downarrow$, respectively. The remaining pair of resonances at -6.42 and -0.61 ppm are assigned to the equatorial positions, but the results of this calculation do not allow a clear distinction between $E_\uparrow$ and $E_\downarrow$.

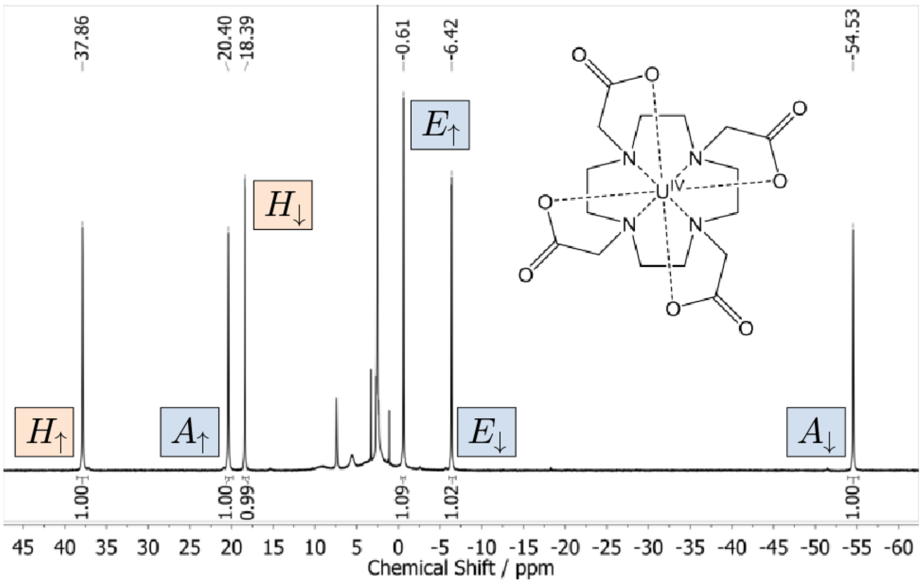

Figure 5.13: ^{1}H NMR spectrum[3] (400 MHz, 297 K) of the in situ complexation of UCl_4 with K_4DOTA in DMSO-d_6. Unnumbered resonances are from solvent or minor isomers, relative integrals are given above the chemical shift scale. Assignment shows the cyclen backbone signals in blue and the methylene unit of the acetate arms in orange, labelling scheme is as given in Figure 5.12.

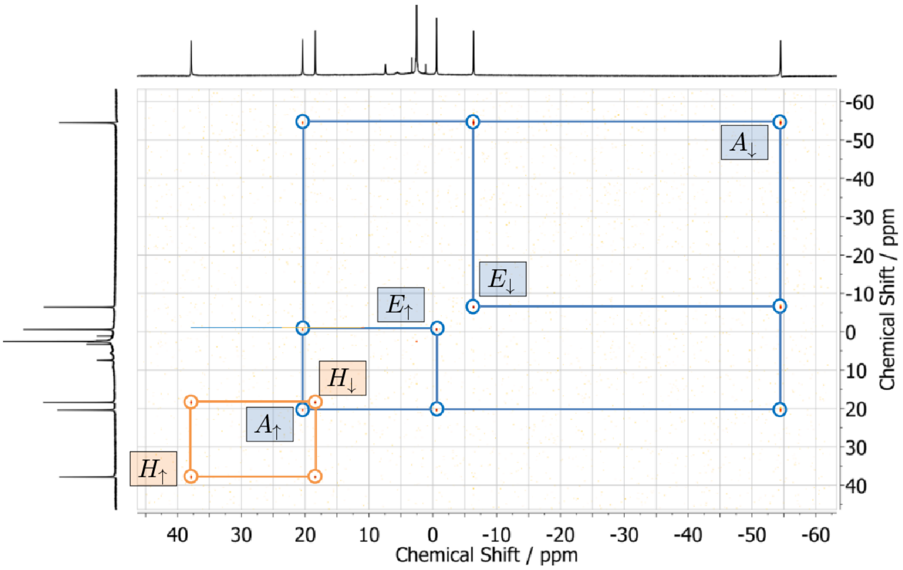

Figure 5.14: ^{1}H–^{1}H COSY[3] (400 MHz, 297 K) of U(DOTA) in DMSO-d_6 with its assignment showing the cyclen backbone signals in blue and the methylene unit of the acetate arms in orange, labelling scheme is as given in Figure 5.12.

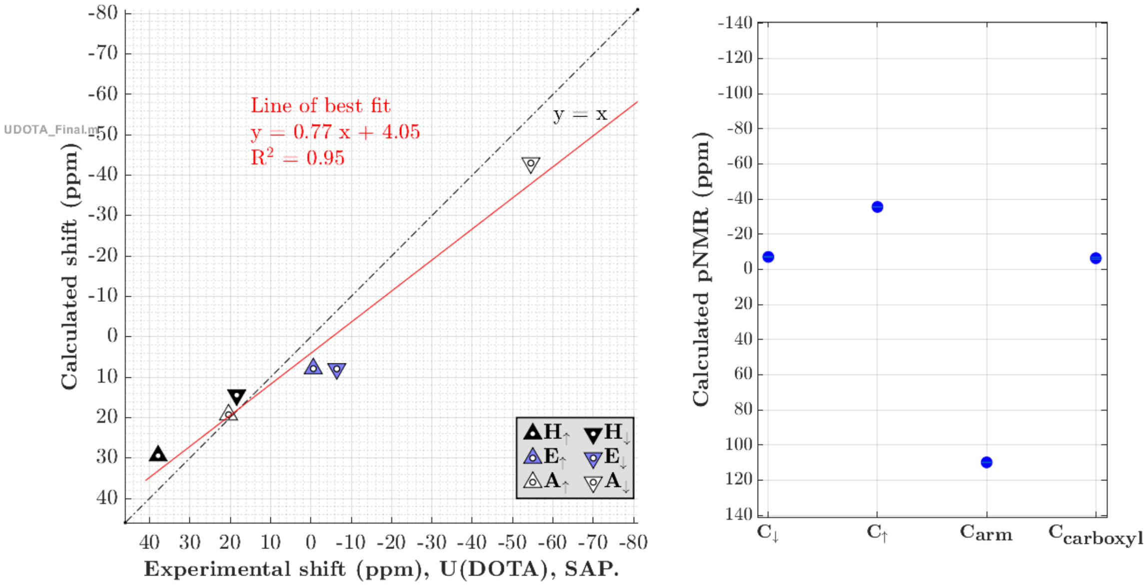

Figure 5.15: Left: Calculated ^{1}H pNMR shifts (ppm) vs. experimental shifts for U(DOTA), from reference[3] and given in Table 5.2. The line of best fit is indicated in red, and the dotted line indicates perfect correspondence. Right: Calculated ^{13}C pNMR shifts (ppm) for U(DOTA). Shifts are averaged over each set of chemically equivalent atoms, and the plotted error bars show 1 standard deviation in the averaging process. In this case the error bars are hidden by the marker.

Our assignments agree with Timmermann's work and are at variance with previously published competing assignments,[4] indicating the difficulty of assigning actinide pNMR results and the need for computational validation.

When considering the six resonances in Figure 5.11, the gradient of the line of best fit is only 0.77. We believe this scaling is due to three effects: Firstly, while the ground-state NEVPT2 spin-orbit free energies of the TSA conformer imply that it is barely present at 300 K, the SA-NEVPT2-SOC energies implies a Boltzmann population of 15%. Figure B.5 shows the calculated pNMR results for the TSA conformer. Calculating a Boltzmann weighted mix of the two conformers does not improve the gradient of the line of best fit, but it does allow the equatorial atoms to be distinguished. This is possible since, depending on both energetics and a lack of steric hinderance, NMR relaxation times can be relatively long compared to rapid interchange between conformers,[201,202] so the magnetic field experienced by the nuclei varies and is best represented by a Boltzmann average. This is similar to the NMR spectrum of cyclohexane which has a single signal for both conformers at temperatures about −70°C.[203] Spectra taken at lower temperatures should resolve the conformers.

Secondly the orbital shielding and hyperfine matrices are calculated at DFT level, and hence neglect the effects of static correlation. One approach to tackle the difficulty of obtaining accurate $\boldsymbol{\sigma}_{orb}$ is to substitute the results for a diamagnetic analogue. This is presented in Figure B.4, for Th(DOTA), this implies the same assignment however the gradient of the line of best fit is further reduced, implying that the correlation may be spurious. MP2 or CASSCF calculations on the orbital shielding term and/or fully repeating the analysis with a conductor-like polarizable continuum (CPCM) model[204] to represent solvent effects did not improve the correlation.

Thirdly, the method explicitly uses pseudospin, $\tilde{S} = 1$ as a parameter to calculate the paramagnetic shielding, and Figure 5.16 shows the NEVPT2-SOC energies for U(DOTA). The third excited state has a Boltzmann population of 4.3% at 300 K, and as such is energetically accessible. Calculations with a pseudospin of $\tilde{S} = 3/2$ were performed, and these generally overestimate the gradient of the line of best fit. From this we conclude that the magnetic behaviour of U(DOTA) cannot fully be captured with a single pseudospin value.

This led us to exploit the irreducible tensor operator method as described in Section 5.3.1. The revised values are shown in Figure 5.17. This figure shows the calculated values for the pure SAP conformer on the left, and the Boltzmann weighted values on the right. The correlation and the gradient of the line of best fit is 0.95, however the equatorial hydrogen values show poorer agreement with experiment. The right plot also shows the results for the TSA conformer (small symbols), as can be seen the conformer interconversion has a dramatic effect on the shifts of the equatorial hydrogen values (and on $H_{\uparrow}$). From this we believe that the variance of these computational results come from conformational interchange. The improved description of the Zeeman component built directly from the magnetic moment matrices is the main reason for better correlation, however the hyperfine coefficients are necessarily approximated. The method, whilst currently limited, shows considerable promise for quantitative use.

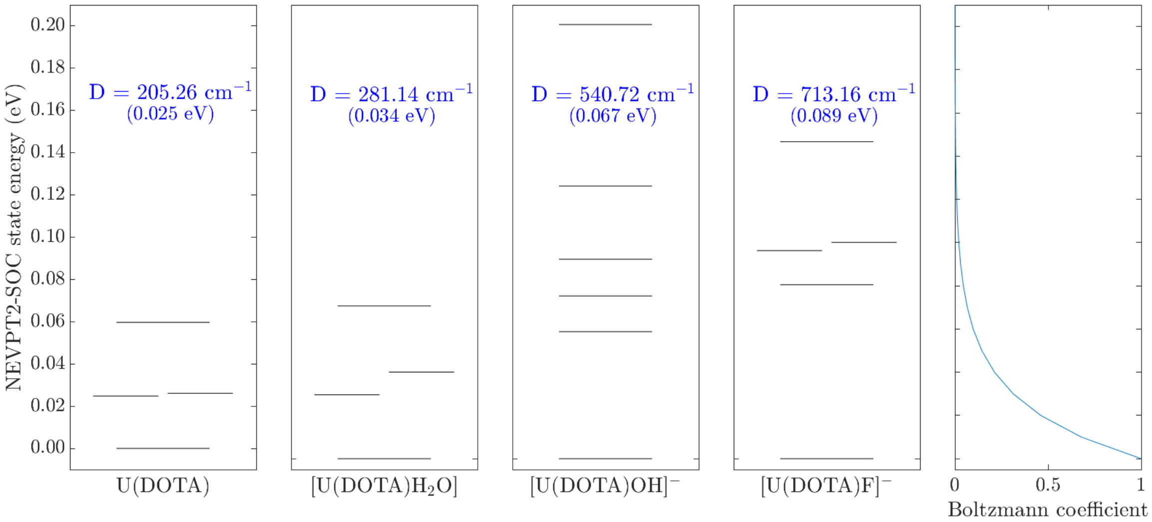

Figure 5.16: Left: NEVPT2-SOC state energies for U(DOTA) and the indicated substituted variant measured from the lowest SOC state in each case. Blue text shows the calculated D value in cm^{-1} (eV value in brackets). Right: The Boltzmann coefficient at 300 K (x-axis) for corresponding energy separation for the previous four energy level diagrams (y-axis).

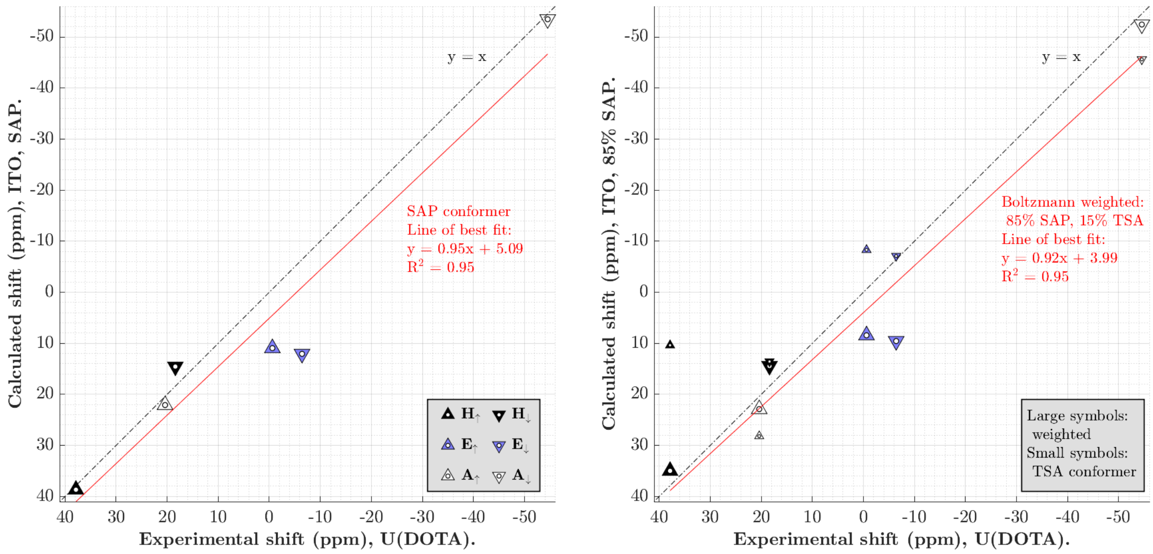

Figure 5.17: Left: Calculated ITO ^{1}H pNMR shifts (ppm) vs. experimental shifts for U(DOTA), from reference[3] and given in Table 5.2. The line of best fit is indicated in red, and the dotted line indicates perfect correspondence.
Right: Large symbols and line of best fit are the calculated ^{1}H pNMR shifts vs. experimental shifts (ppm) for U(DOTA), Boltzmann weighted (85% SAP, 15% TSA), small symbols indicate the TSA result.)

The method is accurate enough to confirm the disputed assignment of the remaining protons. The axial protons are the closest protons to the spin centre (3.8 and 3.7 Å for $A_\uparrow$ and $A_\downarrow$ respectively) and $A_\downarrow$ has the largest angle (157.5°) to the symmetry axis, as such the inverse square and $\cos^2\theta$ relationships used by Bleaney analysis would suggest that it has the largest pseudocontact contribution, as is the case here.

5.5.2 Unpaired electron spin density

Figure 5.18 shows contour plots of the spin density for U(DOTA) from the final CASCI/NEVPT2 calculation. The spherical distribution that occurs when the two unpaired electrons are evenly distributed is distorted by the ligands producing indentations facing the ligands and an axial indent on the nitrogen side of the molecule. This reflects a reduction in spatial density due to same-spin electron repulsion. Table B.5 shows the Löwdin atomic charges and spin densities.[17] The spin density of the uranium atom is transferred to the ligand oxygen (0.0034 Bohr^{-}3) and nitrogen atoms (0.0008 Bohr^{-}3). The larger U-O spin density has a combination of σ and π symmetry, whereas the U-N spin density is purely σ. Hence, the spin density is transferred through the carboxylic π-system, resulting in an increased spin density on the carboxyl carbons (0.0008) compared to the other carbon atoms and this leads to a significantly increased contact contribution. Overall the spin density around the uranium atom resembles that of an inverted apple.

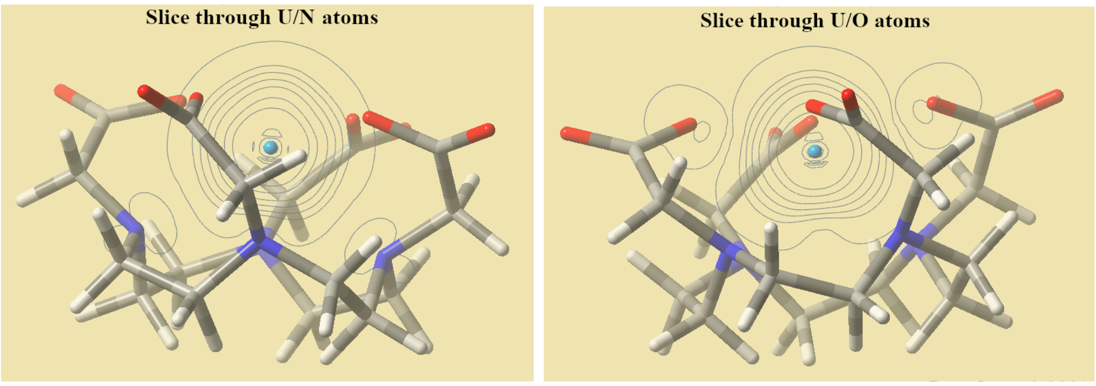

Figure 5.18: SA-NEVPT2(2,7) Spin density contour plots for U(DOTA).

5.5.3 Components of the pNMR shift.

Figure 5.19 shows a breakdown of the components of the total chemical shielding. Except for $A_{\downarrow}$ and the carboxyl carbon, the orbital contribution is dominant. The pseudocontact shifts are much smaller (^{1}H: –0.3 to 0.7 ppm. Unsaturated ^{13}C: 0.3 to 1.5 ppm, carboxyl ^{13}C: –11 ppm). As a consistency check, Figure 5.20 shows a comparison between the pseudocontact values obtained using the calculated magnetic susceptibility tensor (298 K) and geometrical parameters, *i.e.* Eq. 5.4, and the main calculation, *i.e.* Eq. 5.8.

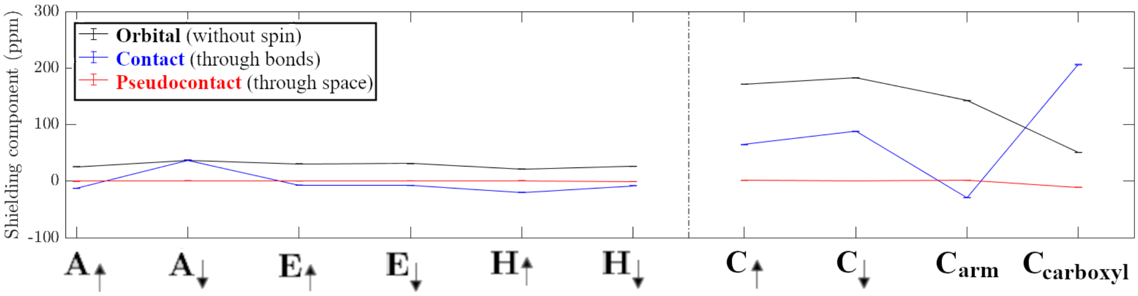

Figure 5.19: Calculated ^{1}H and ^{13}C pNMR components for U(DOTA). Shifts are averaged over each set of chemically equivalent atoms, and error bars show 1 standard deviation in these results, the error bars have similar thickness to the marker.

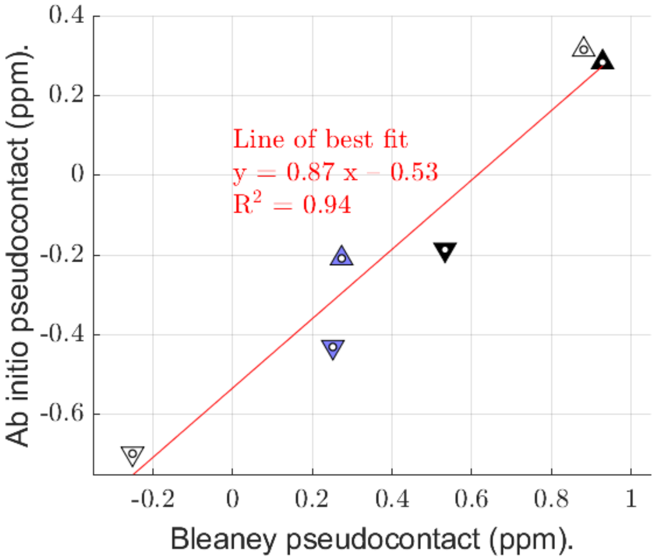

Figure 5.20: Calculated U(DOTA) pseudocontact shifts compared with those calculated using the Bleaney relationship and the susceptibility tensor (Eq. 5.4).

5.6 Axially substituted U(DOTA) complexes

Dovrat et al. reported[5] a series of spectrophotometric and NMR titrations of U(DOTA), alongside an electrospray induced mass spectrometric study of selected solutions and the single crystal X-ray diffraction structure of $[U(DOTA)F]^-$ co-crystallised with LiOH and $[Na(OH_2)]^+$. The ^{1}H chemical shifts for the axial adducts with H_2O, F^- and OH^- are in Table 5.4. The authors support their assignments with ^{1}H-^{1}H COSY data (SI of ref. 5), and they claim to identify both the SAP and TSA isomers of $[U(DOTA)H_2O]$.

Figure 5.21 shows the changes in selected geometrical parameters following axial substitution. For the water ligand, there is a very slight contraction of the DOTA ligand (the angle of the constituent atoms to the C_4 axis decreases by 0-2°), but the substitution of the anionic ligands cause a larger expansion of the DOTA ligand (corresponding increase is 2-6°). The axial substitution of water breaks the symmetry of the molecule, but the C_4 symmetry is maintained for $[U(DOTA)OH]^-$ and $[U(DOTA)F]^-$, with the former hydroxyl ligand lying on the symmetry axis. As a check of the geometry optimisation process, a series of SA-CASSCF(2,7)/NEVPT2 single point calculations were performed over a range of U–F^- distances. The resulting NEVPT2-SOC energies are shown in Figure 5.22. The minimum distance was determined by fitting the distances from the single point calculations to a sixth order polynomial and the fitted value, 2.056 Å was consistent with the optimised value of 2.043 Å.

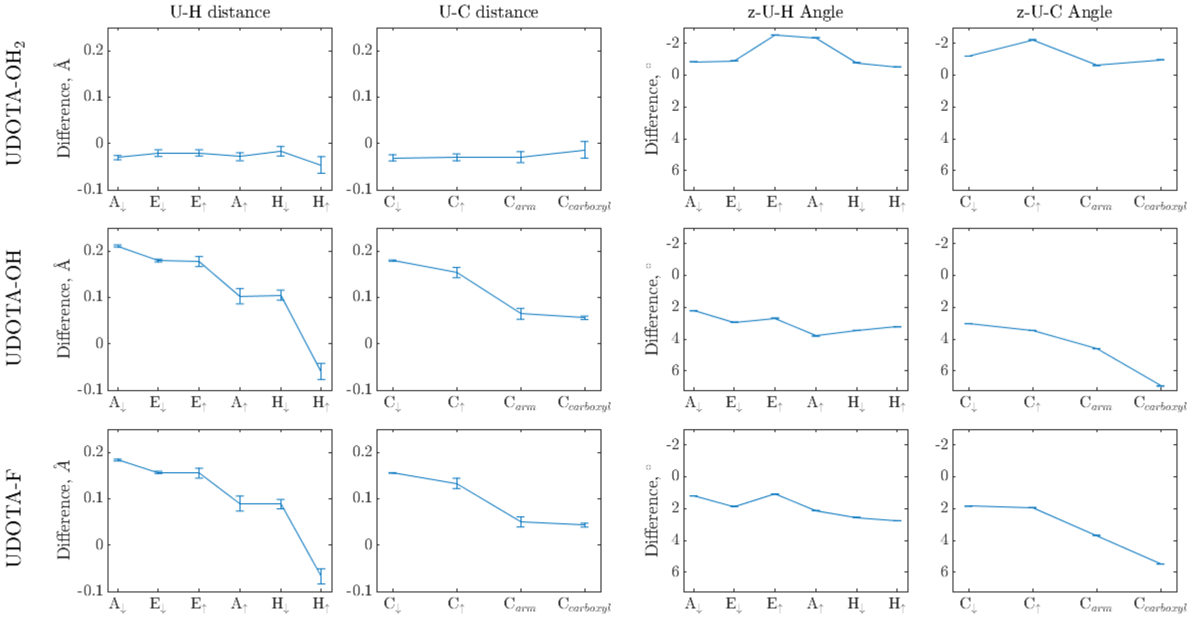

Figure 5.21: Change in geometrical parameters of the DOTA ligand from those of U(DOTA) with axial ligand binding.

From the spectrochemical series[205] the strength of ligand binding can be ordered as $F^- < OH^- < H_2O$, mirroring the decreasing polarisation of a dative bond from F^- to H_2O to a transition metal, however the strength of purely ionic bonding is reversed. We will adopt the order H_2O, OH^-, F^-, and this discussion will focus on the effect of adding increasingly polarising ligands, which should have increasing charge density

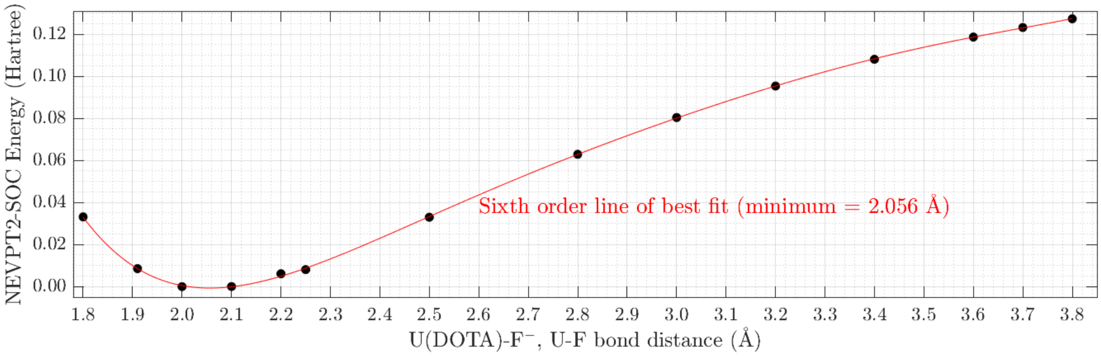

Figure 5.22: Potential energy curve for U–F$^-$ separation for $[U(DOTA)F]^-$. SA-NEVPT2-SOC energies (17 triplet, 8 singlet states included) presented. Red line indicates line of best fit to a sixth-order polynomial.

on the ligand atom, *i.e.* starting from the unsubstituted U(DOTA), then adding H_2O, OH^- and finally the F^- ligand.

Zeeman and ZFS parameters from these calculations are presented in Table 5.3. The principal values of the g matrix (*i.e.* the square roots of the eigenvalues of the Abragam-Bleaney tensor,[120] $\mathbf{gg}^T$), are presented as a parallel and perpendicular components, $g_{\|}$ and $g_{\perp}$. Excepting $[U(DOTA)OH]^-$, where the eigenvalues are all different, the Abragam-Bleaney tensor is oblate (*i.e.* $g_{\|} < g_{\perp}$), but becomes less oblate as increasingly electronegative ligands are added along the C_4 symmetry axis, with the exception of the hydroxyl ligand which has an anomalously low $g_{\perp}$ and significantly unequal $g_{\perp}$ components. ZFS increases as the ligand becomes more polarising as seen by the increasing D value. The addition of the neutral water ligand increases D from 205 to 281 cm^{-1} and the tensor is more rhombic (E/D increases from 0.00 to 0.15). In both cases the anisotropy axis (the axis of easy magnetisation) lies along the symmetry axis.

The addition of the negative ligands has a profound effect on the PAS of the Zeeman tensor. Figure 5.23 shows the principal components of the ZFS tensor for U(DOTA) and $[U(DOTA)F]^-$, with the anisotropy axis labelled D_3. The anisotropy axis is given by eigenvectors of the largest eigenvalue of the ZFS tensor. As can be seen the anisotropy axis of $[U(DOTA)F]^-$ is rotated by 90° relative to the symmetry axis (this is also the case for $[U(DOTA)OH]^-$). This corresponds to the effect of SOC on the model spin. The principal axis of the pseudospin is dependent on the direction of the magnetic field.[121] For U(DOTA), if a magnetic field is applied along the symmetry axis the angle between the principal axis of the pseudospin and the true spin is 0.01°, whereas for $[U(DOTA)F]^-$ this angle is 18.95°. The rotation of the pseudospin results in the rotation of the ZFS tensor. A similar effect has been observed experimentally for $Na[DyDOTA(H_2O)]\cdot 4H_2O$.[206]

Table 5.3: Magnetic parameters for U(DOTA) and its substituted variants.

Zeeman	$g_{\parallel}$	$g_{\perp_1}$	$g_{\perp_2}$	$g_{\parallel}$	$\lvert g_{\perp}\rvert$
U(DOTA)	0.467	2.115	2.115	0.467	2.115
[U(DOTA)H_2O]	0.472	1.984	2.173	0.472	2.081
[U(DOTA)OH]$^{-}$‡	0.094	0.173	2.726	N/A	N/A
[U(DOTA)F]$^{-}$	0.492	1.806	1.966	0.492	1.887

ZFS	D (cm^{-1})	E	E/D	anisotropy axis
U(DOTA)	204.56	0.08†	0.0004	C_4 axis
[U(DOTA)H_2O]	281.14	42.24	0.1503	C_4 axis
[U(DOTA)OH]$^{-}$	540.72	66.76	0.1235	90° to C_4 axis
[U(DOTA)F]$^{-}$	713.22	63.62	0.0892	90° to C_4 axis

$g_{\perp_1}$ and $g_{\perp_2}$ represent the 'x' and 'y' principal values. The perpendicular is the average of the two.

† This is not zero as would be expected for a purely C_4 molecule due to a combination of the slight rotation of the pseudospin due to SOC shifting the anisotropy axis slightly off center and computational errors due to the precision of the model geometry.

‡ The anomalous asymmetry for the [U(DOTA)OH]$^{-}$ g-values is an artifact of the Abragam-Bleaney symmetrisation of the g-matrix, g^{OH^-}. Due to spin-orbit coupling there are large asymmetric components, *e.g.* the difference in the off-diagonal elements $g_{21}^{\mathrm{OH}^-} - g_{12}^{\mathrm{OH}^-} = 0.9020 > g_{33}^{\mathrm{OH}^-}$. Therefore, in this case the symmetrisation fails. These PAS values are illustrative, and the methods used in this work do not rely on these values.

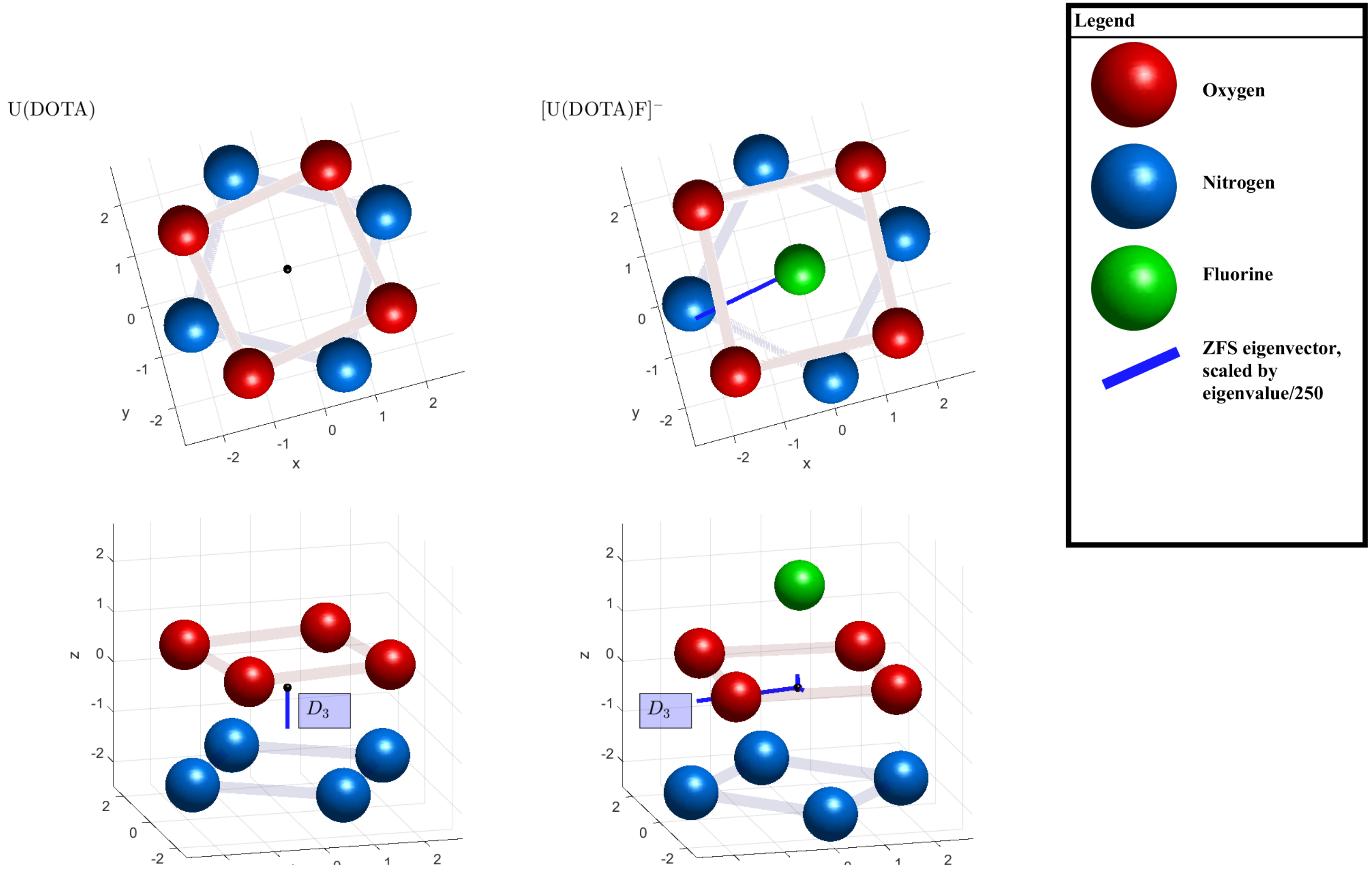

Figure 5.23: Principal axes of the ZFS tensor for U(DOTA)and $[U(DOTA)F]^-$: The anisotropy axis labelled is labelled by D_3. Carbon and Hydrogen atoms are not shown for clarity. Axes are in Angstrom.

Spin density surfaces for [U(DOTA)X], where X is the axial ligand (X = none, H_2O, OH^-, F^-) are presented in Figure 5.24. The effect of substitution on the spin density is to invert the observed apple shape. Löwdin atomic charges and spin populations from the NEVPT2 calculation are given in the supplementary information Tables B.7-B.8). All axial ligands donate beta spin density from the molecule (*i.e.* the ligand atom has overall alpha spin density), however while the water ligand transfers electron density to the uranium atom (ligand metal charge transfer, LMCT), the alpha spin density of the DOTA ligand atoms is almost unchanged (the largest changes are to the ligand nitrogen, 0.0014 to 0.0013 Bohr^{-3} and $C_{\downarrow}$, 0.0024 to 0.0020 Bohr^{-3}). This is consistent with the similarity between the ^{1}H pNMR of U(DOTA)and [U(DOTA)H_2O]. The charge transfer is greatest for the neutral water ligand, where the Löwdin charge on the uranium atom is -0.02 (U(DOTA) 0.17), and least for the more polar U-F bond, where the Löwdin charge is 0.09.

The addition of the anionic axial ligands has a more profound effect on the uranium atom's Löwdin spin density, with the donation of the beta spin density reducing the (alpha) spin density from 1.60 to 1.33 Bohr^{-3} for both the hydroxyl and fluoride ligand. This also reduces the spin density, and thereby the contact shift for these molecules, and the contraction of the experimental ^{1}H pNMR shifts as shown in the following section. Figure 5.25 shows a contour plot of the spin density for [U(DOTA)F]$^-$.

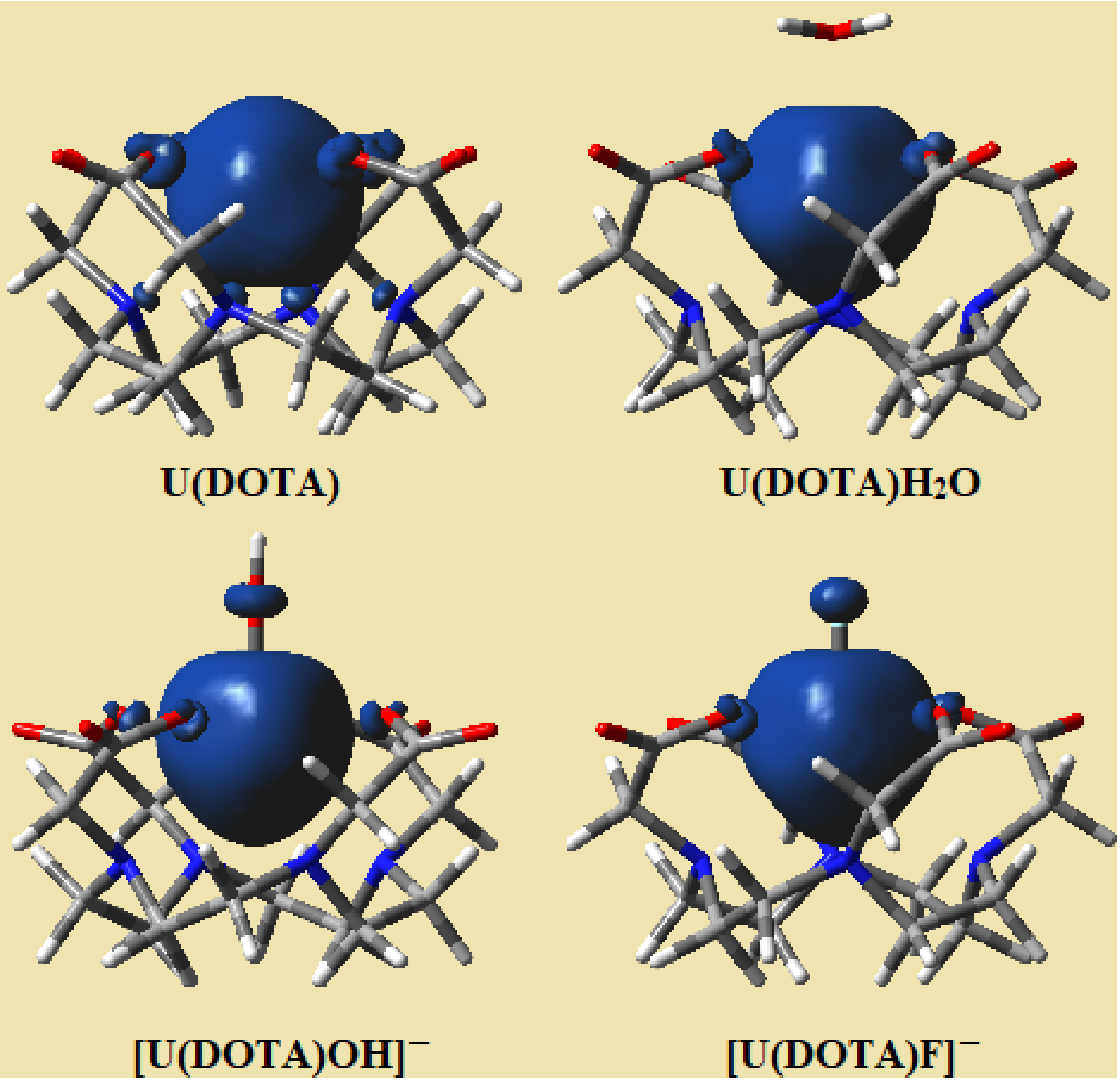

Figure 5.24: SA-NEVPT2(2,7)-SOC Spin density surfaces for [U(DOTA)X], where X = none, H_2O, OH^- and F^-, isovalue 0.0001 a.u.

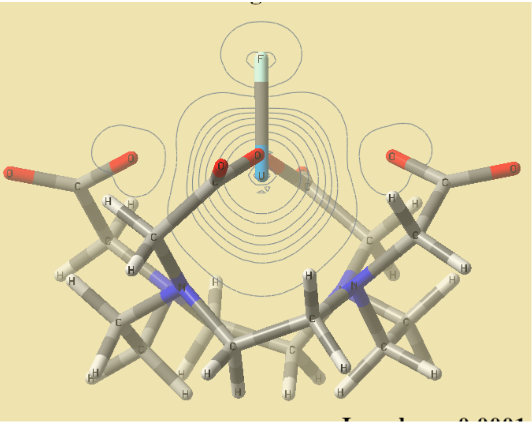

Figure 5.25: SA-NEVPT2(2,7)-SOC Spin density contour plots for $[U(DOTA)F]^-$, isovalue = 0.0001 a.u.

5.6.1 ^{1}H pNMR shifts

Table 5.4 summarises our main results for U(DOTA) and the three axially substituted complexes. The calculated components of the ^{1}H and ^{13}C chemical shifts, *i.e.* orbital, contact and pseudocontact components, the corresponding chemical shielding and the resulting chemical shift relative to TMS (tetramethylsilane) are presented in the SI (Tables B.11 to B.12).

Table 5.4: Experimental and calculated ^{1}H NMR chemical shifts (ppm) for axially substituted U(DOTA). $\Delta\delta$ indicates the spread of values.

	$H_{\uparrow}$	$A_{\uparrow}$	$H_{\downarrow}$	$E_{\downarrow}$	$E_{\uparrow}$	$A_{\downarrow}$	$\Delta\delta$
U(DOTA)							
Experiment[3]	37.86	20.40	18.39	−0.61	−6.42	−54.53	93.39
Calc., $\tilde{S} = 1$, SAP	26.52	19.00	14.00	−9.00	−8.00	−43.00	69.54
Calc., $\tilde{S} = 1$, 85% SAP†	29.07	19.97	13.54	5.59	6.14	−43.56	72.67
Calc., $\tilde{S} = 3/2$	49.76	32.99	23.71	15.64	15.17	−82.67	132.43
Calc., ITO, SAP	38.00	22.09	14.56	12.06	10.94	−54.50	92.50
Calc., ITO, 85% SAP†	34.94	22.88	14.43	8.42	9.56	−52.44	87.38
[U(DOTA)H_2O]							
Experiment[5]	38.40	21.70	19.30	0.70	−5.80	−56.70	95
Calc., $\tilde{S} = 1$	37.15	17.16	12.75	7.76	6.75	-39.42	66.57
Calc., $\tilde{S} = 3/2$	45.50	28.83	20.54	14.65	12.94	-75.28	120.78
$[U(DOTA)OH]^-$							
Experiment[5]	−1.40	1.80	3.30	7.80	8.70	5.4	10.00
Calc., $\tilde{S} = 1$	−2.10	3.40	5.02	5.40	6.21	6.28	8.38
Calc., $\tilde{S} = 3/2$	−12.58	4.42	8.54	9.34	13.10	40.46	53.04
$[U(DOTA)F]^-$							
Experiment[5]	9.90	10.20	16.60	4.40	1.80	−22.0	39.00
Calc., $\tilde{S} = 1$	4.95	5.12	5.48	4.72	4.09	−2.28	7.23
Calc., $\tilde{S} = 2$	12.30	11.69	14.95	10.80	9.13	−21.21	36.16

The assignment of protons for U(DOTA) follows reference 3. Reference 5 does not distinguish between the three pairs, so the assignment of substituted U(DOTA) species follows reference 5, but uses the calculated values to split pairs. † Boltzmann weighted, 85% SAP, 15% TSA.

Figure 5.26 shows the calculated result for the pNMR of [U(DOTA)H_2O] assuming a pseudospin of $\tilde{S} = 1$, however the NEVPT2-SOC state energies (Figure 5.16) shows that there are four levels within 0.1 eV with a Boltzmann population at 300 K exceeding 2%, therefore there are four levels that are energetically accessible. Figure 5.27 shows the corresponding qualitative plot for $\tilde{S} = 3/2$.

Similarly for [U(DOTA)F]$^-$ there are five levels within 0.15 eV, implying a pseudospin $\tilde{S} = 2$ may be more appropriate. Figure 5.28 shows the corresponding plot. This produces a much improved correlation, but the improved result may derive from a fortuitous cancellation of errors. It is also noticeable that the large magnetic anisotropy perpendicular to the C_4 axis causes considerable differences in predicted pNMR for formally equivalent centres, assuming a C_4 symmetry and this effect is averaged out.

For [U(DOTA)OH]$^-$ the experimental pNMR was recorded at a pH of 12.7, and the effect of such an environment is beyond the scope of this work, however the considerably smaller g-value along the symmetry axis (0.094) when compared to the other species results in a much smaller calculated range (8.8 ppm), which is in accordance to the experimental value of 10 ppm, and this reduced range means the approximations used in this approach are proportionally much more significant, the calculated and experimental values are within a few ppm of each other, but the correlation is reduced to $R^2 = 0.70$.

All assignments are consistent with published COSY data (SI of reference 5), and are able to reliably distinguish between $A_\uparrow/A_\downarrow$, $E_\uparrow/E_\downarrow$ and $H_\uparrow/H_\downarrow$.

Figure 5.29 shows the qualitative effect of the ^{1}H pNMR shifts for the axial substitution of the fluorine ligand. Due to the increased spin, the calculated contact shifts and pseudocontact shifts increase, however these are in opposition. The net effect is the contraction in the range of the pNMR results that is seen experimentally.

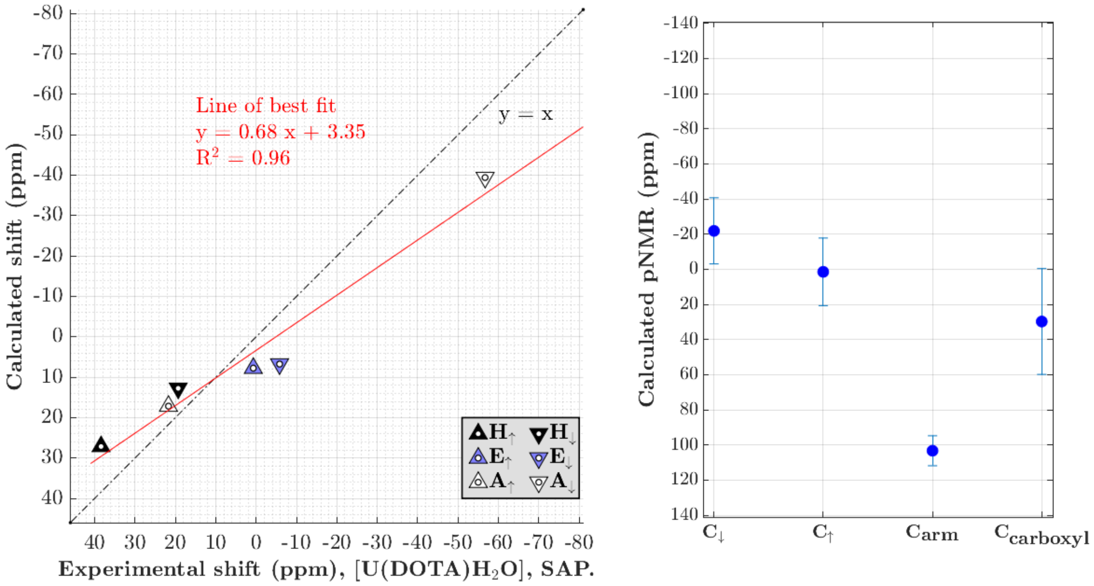

Figure 5.26: Left: Calculated vs. experimental ^{1}H pNMR shifts (ppm) for axially substituted [U(DOTA)H_2O]. The line of best fit is indicated in red, and the dotted line indicates perfect correspondence.
Right: Calculated ^{13}C pNMR shifts (ppm) for [U(DOTA)H_2O]. Shifts are averaged over each set of chemically equivalent atoms, and error bars show 1 standard deviation in these results.

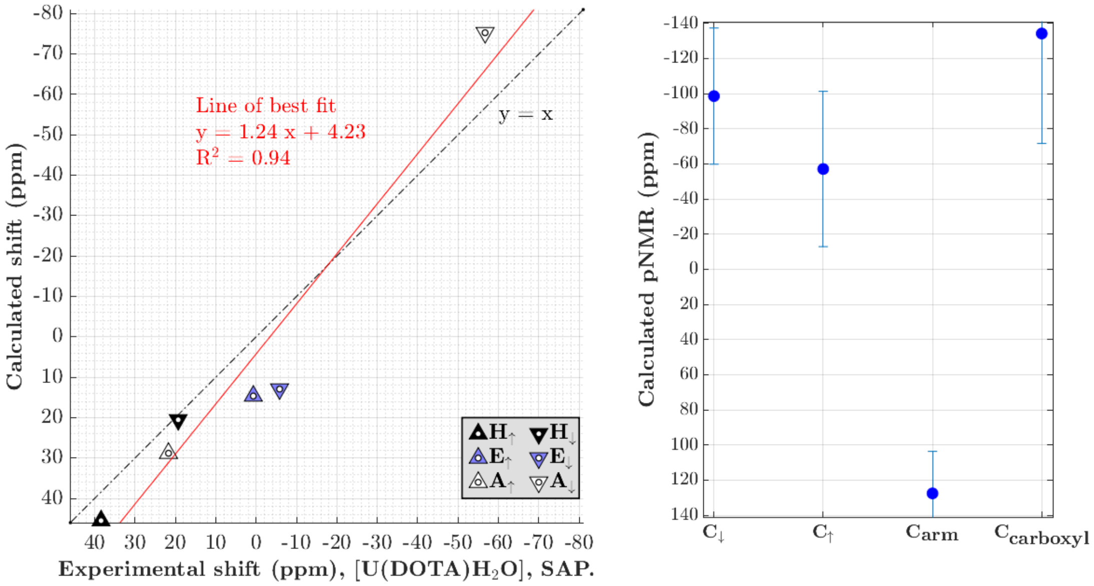

Figure 5.27: Left: Calculated (qualitative) vs. experimental ^{1}H pNMR shifts (ppm) for axially substituted [U(DOTA)H_2O], assuming $\tilde{S} = 3/2$. The line of best fit is indicated in red, and the dotted line indicates perfect correspondence.
Right: Calculated ^{13}C pNMR shifts (ppm) for [U(DOTA)H_2O], $\tilde{S} = 3/2$. Shifts are averaged over each set of chemically equivalent atoms, and error bars show 1 standard deviation in these results.

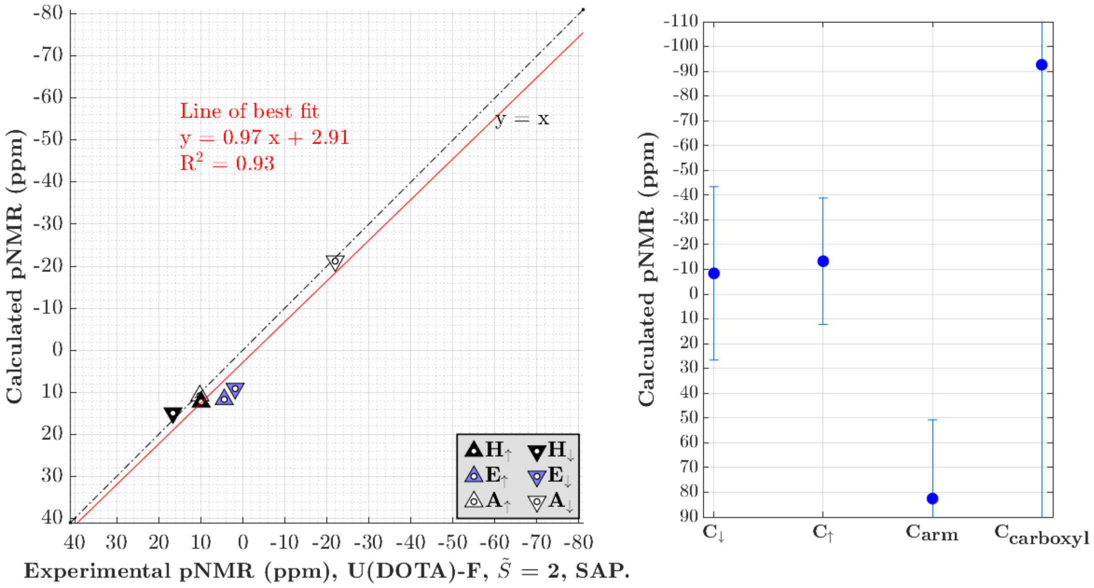

Figure 5.28: Left: Calculated (qualitative) vs. experimental ^{1}H pNMR shifts (ppm) for axially substituted $[\mathrm{U(DOTA)F}]^{-}$, assuming $\tilde{S} = 2$. The line of best fit is indicated in red, and the dotted line indicates perfect correspondence.
Right: Calculated ^{13}C pNMR shifts (ppm) for $[\mathrm{U(DOTA)F}]^{-}$, $\tilde{S} = 2$. Shifts are averaged over each set of chemically equivalent atoms, and error bars show 1 standard deviation in these results.

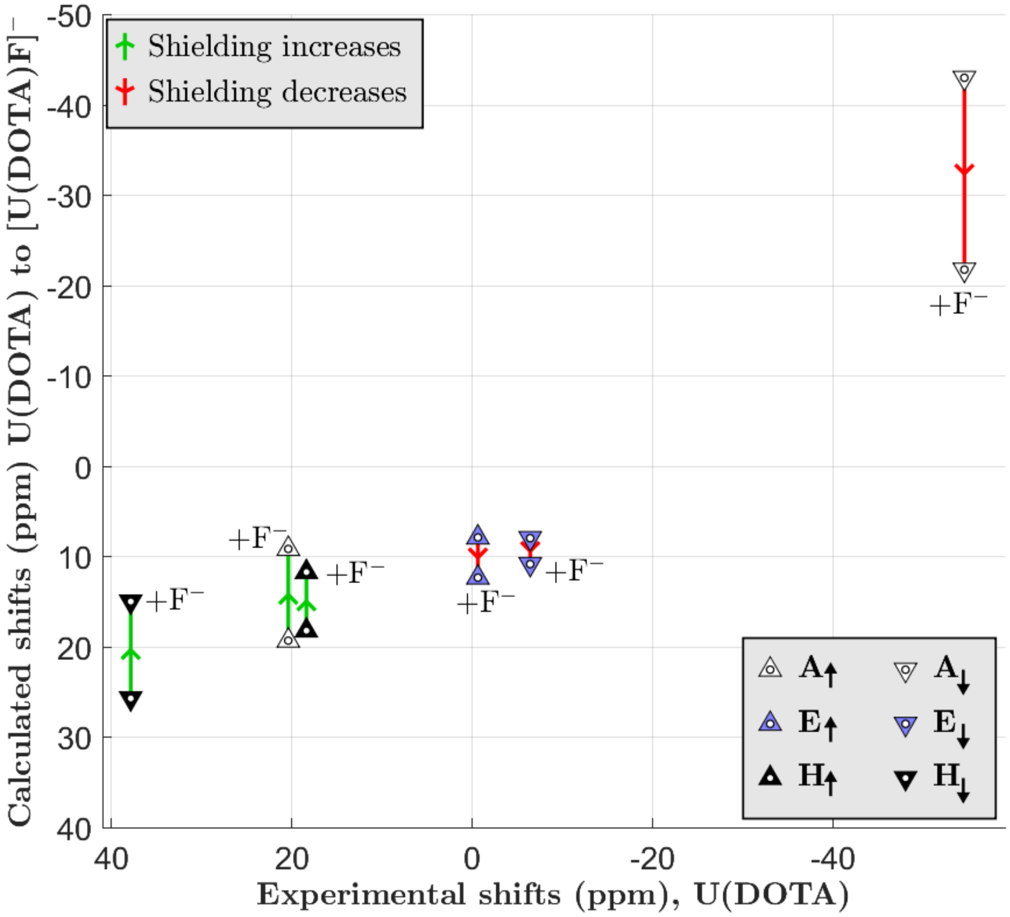

Figure 5.29: Effect of axial substitution of a F$^-$ ligand on the calculated ^{1}H shifts (ppm) of U(DOTA). +F$^-$ indicates the [U(DOTA)F]$^-$, $\tilde{S} = 2$, result. Green arrows indicate an increase in shielding (shift decreases) following axial substitution, red arrows indicate a decrease in shielding.

5.7 Calculated ^{13}C shifts

Figures 5.15, 5.22 and 5.24 shows the predicted ^{13}C pNMR shifts for the SAP conformers and the CH$_2$ link (C$_{arm}$) is predicted to be the most deshielded (highest), as the contact shift is deshielding, whereas the remaining three carbon centres are adjacent to ligand atoms with increased spin density. The drop in orbital shielding for the carboxyl group is balanced by the larger spin density in the carboxyl π-system producing a large contact shift.

Figure 5.30 shows the effect of axial substitution on the components of the calculated ^{13}C shifts of U(DOTA). The effect on the orbital shielding is minor, and the effect of the pseudocontact contribution is dominated by the rotation of the anisotropy axis, causing a sign change for the carboxyl carbon as they dip below the magic angle.

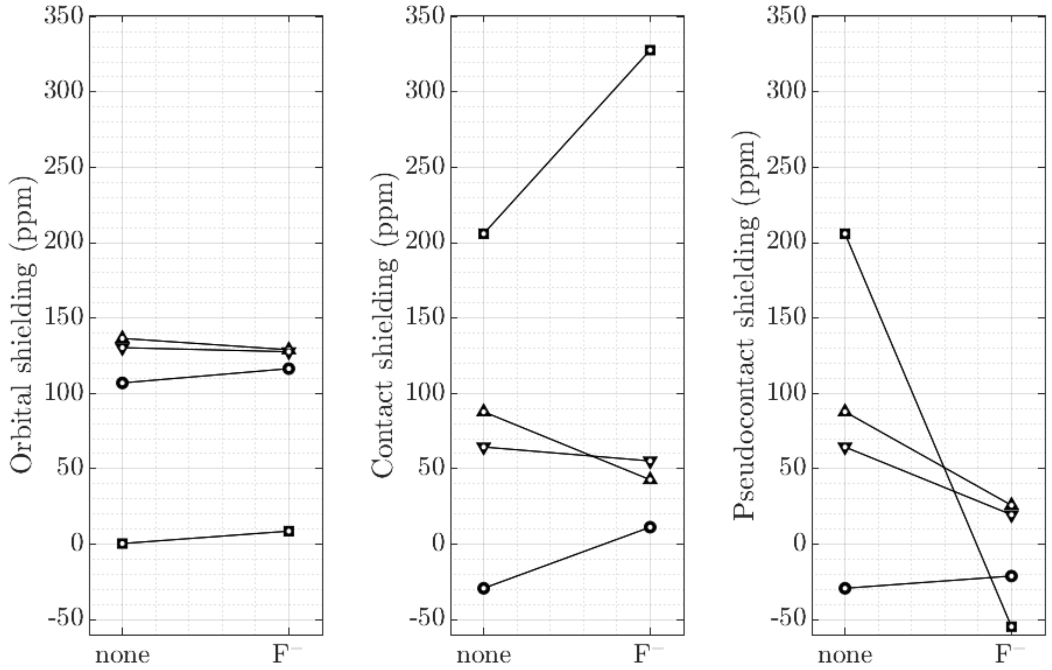

Figure 5.30: Effect of axial substitution of a F$^-$ ligand on the components of the calculated ^{13}C shifts of U(DOTA), using the [U(DOTA)F]$^-$, $\tilde{S} = 2$, result. Triangles indicate $C_\uparrow$, $C_\downarrow$, circles indicate C_{arm} and squares indicate C_{carboxyl}.

The contact contributions of $C_\uparrow$ and $C_\downarrow$ are decreased when the fluoride ligand binds, and as the uranium - carbon distance increases (see Figure 5.17), with a stronger effect on the former (distance increase is slightly larger), weakening the alpha spin on the adjacent ligand nitrogen from 14.02 to 9.17 $\times 10^{-4}$ Bohr^{-3}. This results in a reduction in the Löwdin alpha spin density from 2.21 to 1.31 $\times 10^{-4}$ Bohr^{-3} for $C_\uparrow$ and 2.04 to 1.41 $\times 10^{-3}$ Bohr^{-3} for $C_\uparrow$. Since this is a probe of covalency, it indicates the covalency of the uranium - nitrogen ligand bond is reduced. This in addition to the reduction of other interactions due to distance increase implies an overall weakening of this bond. Conversely the significantly increased contact contribution of $C_{carboxyl}$ does not correlate with a reduction in the Löwdin alpha spin density. This may reflect the need to consider the TSA conformer and model the motion of the molecule, and for the group of four chemically equivalent carboxyl carbon atoms, It could also be the flawed separation of the contact and pseudocontact components from $\boldsymbol{\sigma}_p$, by labelling the former as resulting from the isotropic part of the hyperfine interaction.

The majority of the uncertainty in the shift averaging for formally equivalent chemical shifts in $[U(DOTA)F]^-$ is from the pseudocontact contribution. For instance for the $C_\uparrow$ shift the single standard deviation for the four signals is 0.50 ppm for the orbital shift (128.96 ppm), 1.93 ppm for the contact shift (42.70 ppm) and 36.65 ppm for the pseudocontact shift (25.77 ppm). This is consistent with the geometrical variation caused by the anisotropy axis being at right angles to the symmetry axis. This is not the case with U(DOTA) which has an anisotropy axis along the symmetry axis: The largest standard deviation is 0.52 ppm (contact shift of C_{arm}) with the pseudocontact uncertainty only 0.02 (the shifts are too small to be visible in Figure 5.15).

5.8 Conclusions and future work

In this paper we have assigned the ^1H pNMR shifts for U(DOTA) and for a range of axially substituted derivatives and explored the magnetic effects of such a substitution. Of particular interest was the observed 90° shift in the anisotropy axis following axial substitution by the anionic ligands and this causes formally equivalent protons to not be magnetically equivalent in a static frame. We have also been able to qualitatively predict the corresponding ^{13}C pNMR shifts and look forward to comparing these to future experiments.

Because of the magnetic subtleties of U(DOTA) and its derivatives, we believe that development needs to be done on more elaborate computational approaches combining static and dynamic correlation corrections for calculating magnetic matrices and to explicitly calculate the matrices necessary to build the higher order terms in the ZFS expansion.

Chapter 6

Computational assignment of pNMR shifts for a selection of substituted actinocenes

6.1 Preface

For simplicity, this project was originally conceived to avoid the use of symmetry. Geometry optimisation was performed for 20 actinocenes and lanthanocenes, $M(COT)_2$ and $[M(COT)_2]^-$, { M = Nd–Gd, U–Cm }, at a density functional theory (DFT) level, with the in-house aZORA scalar relativistic correction.[27,28] These formulae correspond to formal oxidation states of +3 and +4.[*]

The optimised structures were approximately D_{8h}, but density functional theory (DFT) was found to poorly correspond to the experimental ring separations for $U(COT)_2$ and $Np(COT)_2$ due to the highly multi-configurational nature of the ground state. From this we concluded that the deviation from the eclipsed structure was an artifact, and adopted a Z-matrix formulation for the molecules, which locked the molecule in the eclipsed configuration, and was controlled by four parameters. Defining the COT centroid as a dummy atom, X, the four geometrical parameters were: the centroid-metal distance, r_{MX}, the centroid-carbon distance r_{XC}, the centroid-hydrogen distance, r_{XH}, and the metal-centroid-hydrogen angle A_{MXH}.

CASSCF calculations without the use of symmetry produced excessive mixing of the f_π and f_ϕ which are formally orthogonal in D_{8h}, and we concluded that using symmetry would produce better starting orbitals and resulting in a more physically representative wavefunction.

---

[*] The formal oxidation state is often poorly defined for complexes with strong multi-configurational nature. For instance, cerrocene, $Ce(COT)_2$ has a formal oxidation state of +4, but forms a molecular Kondo state with significant donation to the metal f_δ orbital, and is better represented as a mixture of states, dominated by a +3 oxidation state.[207,208]

Computational packages such as ORCA only implement a small range of typically abelian symmetry groups, and as discussed in Section 6.3.2, the highest symmetry available to represent uranocene is the D_{2h} group. This has eight irreducible representations, four of which are gerade $a_g, b_{1g}, b_{2g}, b_{3g}$ and the remaining four have the corresponding ungerade symmetries. For uranocene, in practice the four lowest energy states all have overall gerade symmetry, corresponding to the product of two ungerade f orbitals. Similarly the four lowest states of neptunacene have overall ungerade symmetry, corresponding to the product of three ungerade f orbitals. This pattern continues for species with odd/even numbers of electrons. Hence only four states need to be considered for single point calculations.

Partial optimisations in D_{8h} symmetry were performed for a range of fixed centroid-metal distances at the DFT/aZORA level (*i.e.* r_{XC}, r_{XH} and A_{MXH} were allowed to vary) for each of the metallocenes, and NEVPT2 single point energies for the first eight states were calculated for each geometry and each of the four relevant irreducible representations. This was necessary because the ground state of the NEVPT2 calculation is not necessarily the ground state of the CASSCF calculation due to the dynamic correlation correction. The results of these optimisations are shown in the appendix (Table C.1) as is a sample potential energy curve for the ${}^5Ag_g$ states of $[\mathrm{Np(COT)_2}]^-$ (Figure C1). From this we concluded that the symmetric DFT/aZORA full optimisation ring-metal separations were accurate (within 0.02 Å) in all cases except for $\mathrm{U(COT)_2}$, $[\mathrm{U(COT)_2}]^-$, and $\mathrm{Np(COT)_2}$.

On reflection, the lack of experimental data for these species was concerning; the methods that we are using are correct to within a few ppm in most cases, but as the previous chapter showed, there are exceptions, especially when strong spin-orbit coupling (SOC) causes the pseudospin to be poorly represented by a single value. Hence modelling pNMR remains qualitative, although the ITO approach shows considerable promise for quantitative prediction.

For now, we felt that it was more appropriate to focus on a range of substituted uranocenes and neptunocenes where experimental data exist, Hence the paper largely focuses on calculating the ^{1}H pNMR for $\mathrm{U(COT)_2}$, $\mathrm{Np(COT)_2}$, $[\mathrm{U(COT)_2}]^-$ and $[\mathrm{Np(COT)_2}]^-$ and the substituted analogues with a single substituent (either methyl, tert-butyl or trimethylsilyl) on each ring. These have C_{2h} symmetry, but this was not exploited for the substituted species, because it did not significantly reduce the unwanted orbital mixing.

As an operational note, when projecting a smaller basis to a larger basis, as presented in the methodology used in the previous chapter (Figure 5.3), ORCA does not reliably preserve the symmetry of the orbitals. Furthermore ORCA is limited by the number of states that can be included in the QDPT-SOC calculation.

The CASSCF states of uranocene are unstable to state-averaging,[209] and mixing spin states exacerbates this, hence only triplet states were included in the state averaging process. Higher spin-states are included in the NEVPT2 QDPT-SOC. The state-averaging is done in two halves. Firstly, in the symmetric form for a constrained number of states,[†] then using these orbitals as the starting point, then for the unsymmetric form, for all states with NEVPT2 energies below 0.5 eV and with level shifting to protect the active space.[32]

Less problematic, but of note, when determining the symmetry group of a molecule, ORCA counts dummy atoms, so the cartesian geometry form of the optimised Z-matrix is used.

This chapter presents the text from a paper in very early preparation. References have been merged with those in this thesis.

[†] Figure A3 shows an excerpt from an earlier calculation based on a 1eV cut-off.

Computational Assignment of pNMR shifts for a selection of substituted actinocenes.

Authors:

A. W. Lloyd, J. J. W. McDouall, D. Collison.

Affilation:

Department of Chemistry, The University of Manchester,
Oxford Road, Manchester, UK

Author contributions:

Draft preparation AWL, reviewing and editing JJWM, DC, AWL
Computational experiments AWL.

6.2 Abstract

This work studies and predicts the ^{1}H paramagnetic nuclear magnetic resonance spectra (pNMR) of a range of actinocenes and substituted actinocenes, based on the 1,3,5,7-cyclooctatetraene, $(COT)^{2-}$ ligand. We partially optimised the geometry of these molecules by keeping the ring-metal separation at the experimental value of the unsubstituted molecule, where available, or at the minimum of a NEVPT2 potential energy curve (PEC) where not. The PEC is formed from the single-point NEVPT2-SOC energies for a series of partially optimised geometries, each with a fixed ring-metal separation. Orbital and hyperfine matrices were generated via DFT, and we used state-averaged NEVPT2-SOC calculations to produce the Zeeman and ZFS matrices. Symmetry is exploited for the three unsubstituted species, but not for the disubstituted ones.

Previous published assignments were made using a Bleaney model of the pseudocontact and assuming a completely flat COT ring. Our calculations show that there is a small (6.7°) bend of the hydrogen atoms towards the uranium atom which improves the overlap in the η_f and η_d bonding system, and this result is confirmed by a NEVPT2 PEC. A third order decomposition of the magnetic moment matrices by irreducible tensor operators (ITOs) allows a more accurate result for the ^{1}H shift for the U^{III} complex, $[U(COT)_2]^-$ to be made. For the disubstituted species, the rotation

of the zero-field-splitting (ZFS) tensor to the new symmetry axis casts doubt on the previous assumption that the addition of alkyl groups is only a slight perturbation of the chemical shifts.

6.3 Introduction

The radioactivity and toxicity of many actinide species can make them difficult to study experimentally, especially in cases of short lived species and/or highly penetrating radiation. However the wide range of applications that exploit actinides, such as the use of ^{227}Ac compounds in radiotherapy[210] or in industrial, low carbon, nuclear energy production coupled with the need to process and to safely contain waste products drives commercial interest. Furthermore a large and potentially fertile area of chemistry is relatively unexplored. In principle, computational chemistry not only offers exploration and prediction of chemical species that are otherwise difficult to study, but can improve our understanding of their nature and properties. For instance, 95% of the radioactivity of waste from nuclear power occurs from 3% of its volume.[211] This waste consists of radionuclides with very different half-lives and decay processes. Different radionuclides present different storage challenges. Improving chemical extraction methods would lead to more recycling of fissile material and better waste separation and management. Many extraction processes exploit metal-ligand selectivity, *i.e.* for lanthanide and actinide species, this selectivity is dependent on the nature of the metal-ligand bond and is a matter of considerable research interest.

The computational study of actinides presents considerable challenges. The high atomic number of actinide nuclei implies that core electrons must move more quickly than in lighter atoms. For a hydrogenic atom, the virial theorem implies that the magnitude of the root-mean square of the speed of the electron equals the atomic number (in atomic units).[39] The speed of light being approximately 137 a.u (or $1/\alpha$ where α is the fine-structure constant). Hence the core electrons in the actinides move at speeds that are a significant fraction of that of light and relativistic effects in actinides must be modelled suitably. Relativistic effects can be split into spin-free effects and spin-orbit effects. The preponderance of unpaired electrons in f element species leads to a complex open shell structure (and significant paramagnetic nature) and results in the occurrence of many degenerate or near-degenerate low lying excited states. This latter concern means that multi-configurational approaches must be employed to model the electronic structure appropriately. Finally, dynamic correlation must also be modelled to achieve chemical accuracy. As ever the complexity of any approach must be balanced by its computational cost, and this requires compromises to make calculations tractable. Improving the efficiency of high-level techniques is ongoing, but currently available approaches allow semi-quantitative results to be produced on a reasonable timescale.

Spectroscopy has always provided a valuable analytical tool for probing the nature of chemical systems, and for diamagnetic species, decades of developments have made nuclear magnetic resonance spectroscopy almost routine for non-biological species. Conventionally to minimise environmental effects the chemical resonance shift δ of a chemically distinct atom is reported in terms of the observed shift σ^{exp} from a reference shift, σ^{ref}:

$$\delta = \sigma^{\mathrm{ref}} - \sigma^{\mathrm{exp}}, \tag{6.1}$$

where all quantities are measured in ppm (parts per million). By definition, a paramagnetic molecule has a spin-dipole. In the absence of an external magnetic field, the overall dipole of a macroscopic ensemble is zero, however the dipole interacts with the field used in the NMR experiment. The resulting observed shift is typically split into two components, the orbital shift that would be observed in the absence of the unpaired electron(s), σ^{orb}, and a correction for the effect of the spin-dipole, σ^{para}. So we can write:

$$\sigma^{\mathrm{exp}} = \sigma^{\mathrm{orb}} + \sigma^{\mathrm{para}}. \tag{6.2}$$

The latter correction is the more difficult to model computationally. The nature of the paramagnetic correction can give valuable insight into the chemical environment of the nucleus probed and in recent times there has been significant interest and advances in the calculation of σ^{para}. σ^{para} can be further split into a contact term σ^{c} that derives from spin polarisation at the nucleus and a pseudocontact term σ^{pc} that results from interactions between spin-dipoles.

$$\sigma^{\mathrm{para}} = \sigma^{\mathrm{c}} + \sigma^{\mathrm{pc}} \tag{6.3}$$

σ^{c} and σ^{pc} are often associated with through-bond and through-space interactions, respectively. In the context of f element compounds the relative magnitudes of these quantities can be used to motivate a discussion of relative covalency in 4f and 5f systems.

This study compares the predicted ^{1}H pNMR values from nine actinocene species to published spectra[212–214] and furthermore predicts ^{13}C values. This will support future studies of the actinocenes as well as a comparison with their formally isoelectronic lanthanocenes. Figure 6.1 shows the 1,3,5,7-cyclooctatetraene dianion, $(\mathrm{COT})^{2-}$, and uranocene, the first molecule in this study. Figure 6.2 shows the species under investigation. With the exception of the uranocene molecule and its anion, all species in this study have a single substituent group that is identical on both rings.

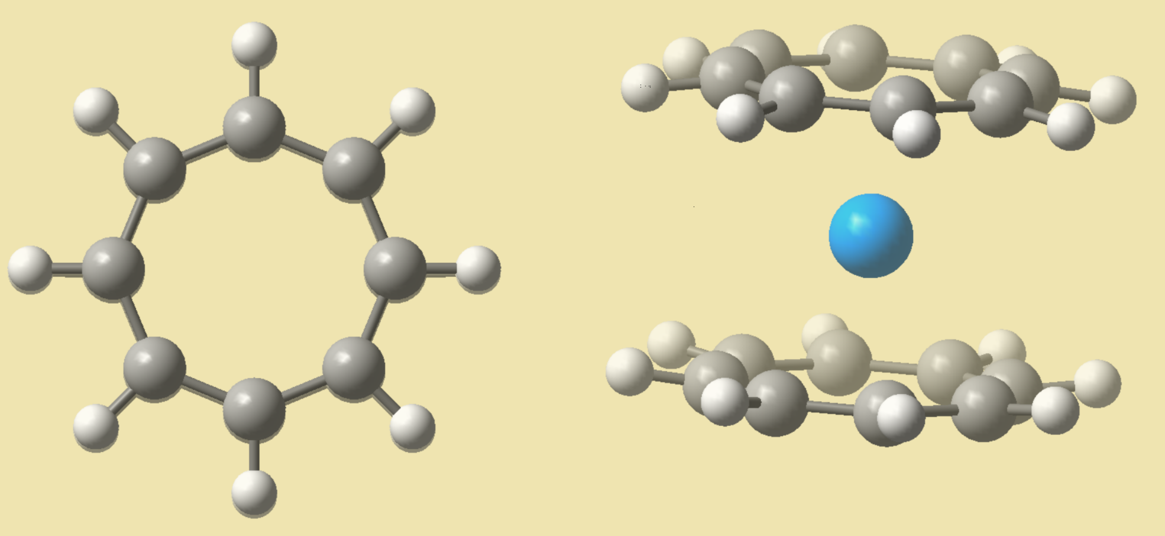

Figure 6.1: Left: the 1,3,5,7-cyclooctatetraene (COT^{2-}) dianion, Right: Uranocene. The blue sphere is the central uranium atom, carbon atoms are in grey, hydrogen atoms are in white.

The four conformers of disubstituted uranocenes are shown in Figure 6.3 and labelled by the lower position, *i.e.* 1:5' has the upper substituent diametrically opposed to the lower one. Following a study of the pNMR of 1,1'-ditert-butyluranocene, Luke *et al.* considered the 1:5' conformer to have the highest population[213] based on the presence of an alkyl group having a deshielding effect on a proton on the opposite ring, and further supported by the pNMR spectra having four aromatic signals with one signal of half-intensity, which would preclude the 1:2' and 1:4' conformers from dominating. As a result, this study focuses on the 1:5' conformer, but a more thorough investigation would consider the remaining three conformers, and ideally consider the rotation of the ring between conformers.

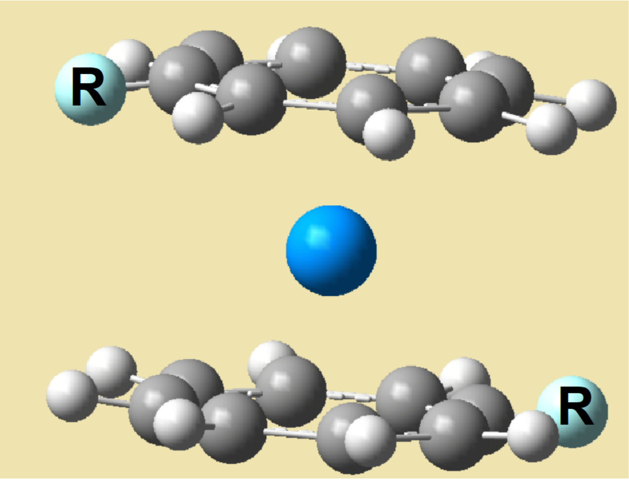

	An	Ox.State.	R-
1	**U**	**IV**	**H**
2	**U**	**IV**	**CH_3**
3	**U**	**IV**	**$C(CH_3)_3$**
4	**U**	**III**	**H**

Figure 6.2: The molecules studied in this work, Actinide is in blue, colour scheme is otherwise as in Figure 6.1.

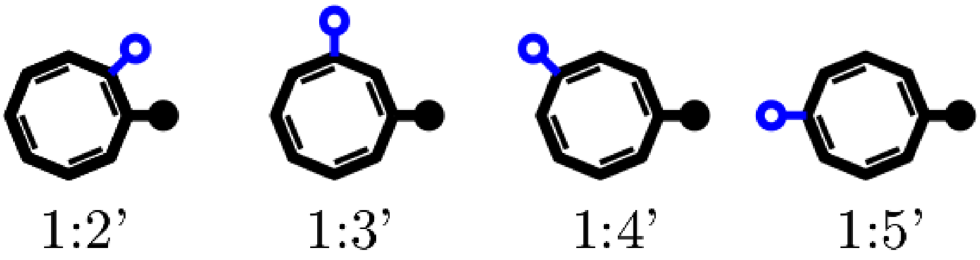

Figure 6.3: The four conformers of disubstituted uranocenes, top view. Top substituent shown by filled circle (and static), lower substituent shown by hollow blue circle.

6.3.1 Uranocene

1,3,5,7-Cyclooctatetraene (COT) is the first even annulene after benzene, i.e. [8]-annulene, and its planar form is predicted to be anti-aromatic, forming a triplet state with its two non-bonding π-orbitals singly occupied. However the species adopts a D_{2d} boat conformation[215] so no π-conjugation occurs. The addition of two electrons to form a dianion $(C_8H_8)^{2-}$ results in a D_{8h} planar configuration[216] and the $4n + 2$ Hückel rule implies aromatic character. The dianion can be prepared directly and can also act as an organometallic ligand.[217]

Figure 6.4 shows a molecular π-orbital energy level diagram for the COT dianion. The progression of the MOs from having zero to four vertical nodal planes mirrors the MOs of benzene: The lowest π orbital is a delocalised double torus ($a_{2\mathrm{u}}$), the vertical planes of the highest b_{1u} orbital separate each pair of ring atoms. The two degenerate

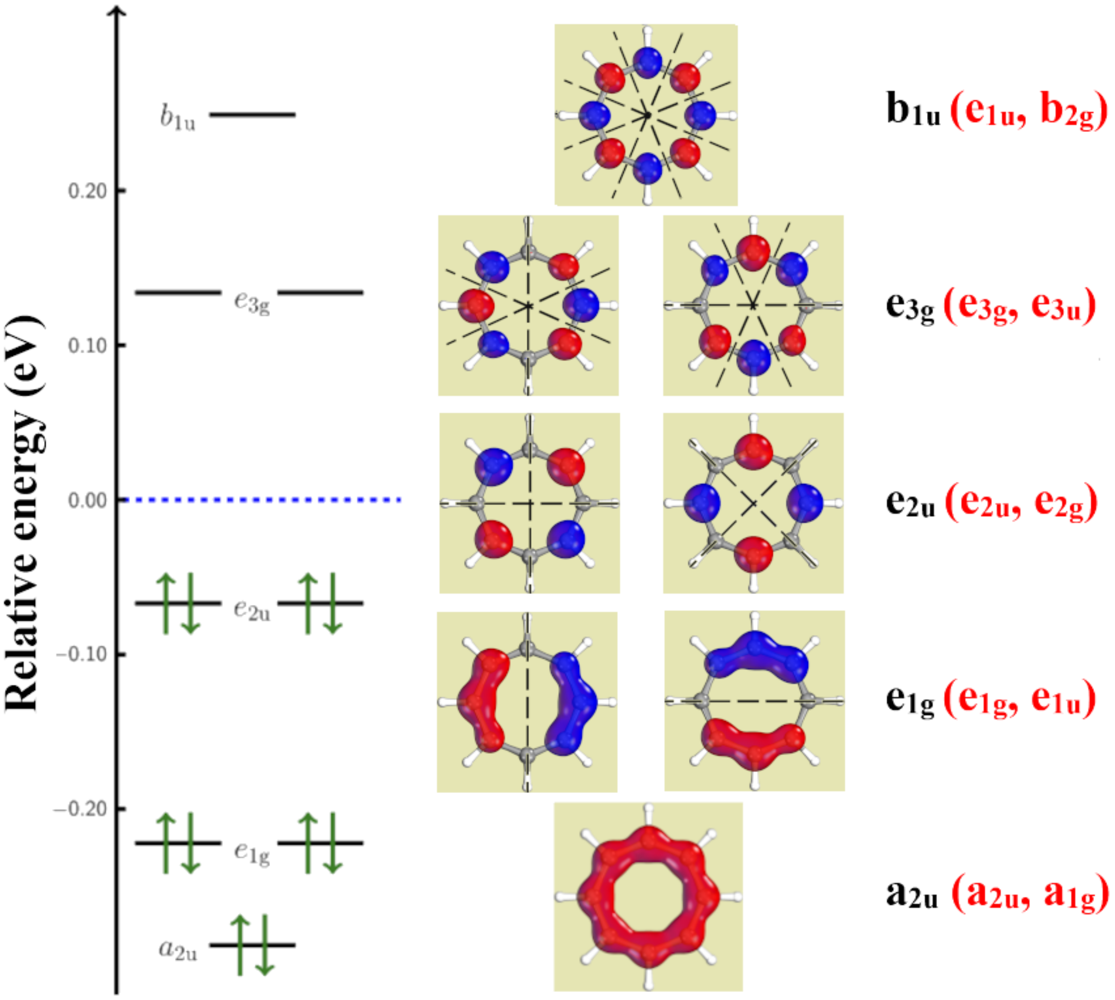

Figure 6.4: π MO energy level diagram for COT^{2-}. Canonical orbitals from an RKS/PBE0/def2-tzvp calculation. Dashed lines show nodal planes. The symmetry labels are given in black for D_{8h}, and in red for two stacked eclipsed rings (as in uranocene).

highest occupied molecular orbitals (HOMOs, e_{2u}) have two perpendicular vertical planes, and it is the interaction of these ligand orbitals with the metal d_δ and f_δ orbitals that characterise the η bond that stabilises the molecules under investigation. Figure 6.5 shows the symmetry labels for the d and f orbitals, so that the overlap between these and the ligand orbitals can be assessed.

The planar dianion is a common ligand in the organometallic chemistry of f-block elements and the nature of its bonding has been debated for some years.[218] The archetypal actinocene, uranocene U(COT)$_2$ was prepared by Strietwieser in 1968.[219] Synthesis of Np(COT)$_2$ and Pu(COT)$_2$ by Karraker followed,[220] along with Th(COT)$_2$ and Pa(COT)$_2$ by Streitwieser a few years later[221,222] The electronic structure of Th(COT)$_2$, U(COT)$_2$, Pu(COT)$_2$ and Cm(COT)$_2$ ($5f^0$, $5f^2$, $5f^4$ and $5f^6$ respectively)

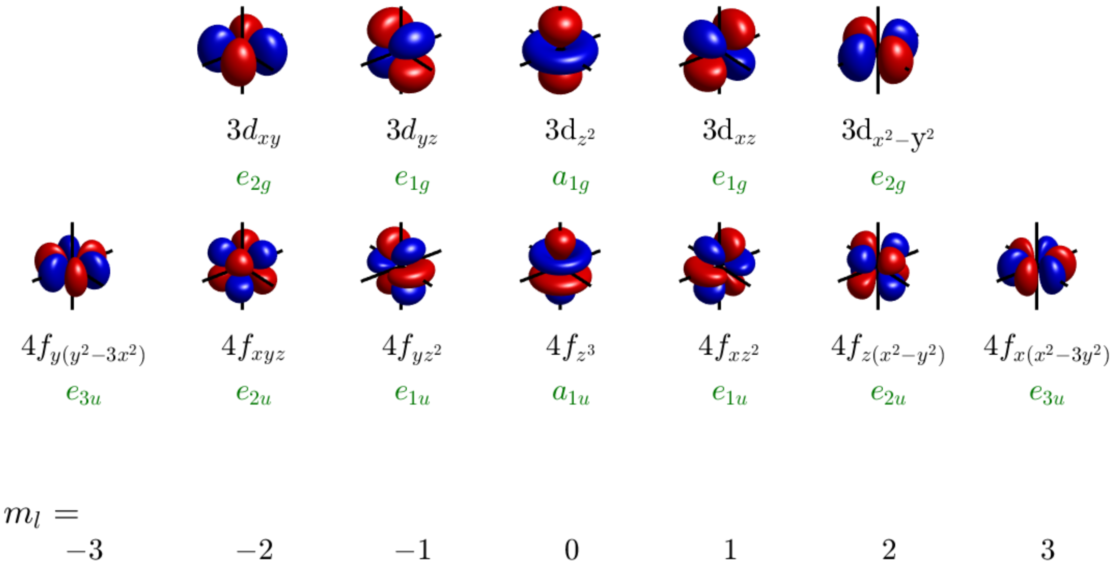

Figure 6.5: Symmetry labels for D_{8h}, d and f orbitals.

have been studied extensively,[208,209,218] species with an even number of f electrons having more representation in computational and experimental studies,[218,223] and to our knowledge, no computational predictions of pNMR results have been made.

6.3.2 Symmetry

Symmetry is only exploitable in a small percentage of molecules – most polyatomic molecules have no symmetry elements. Available electronic structure packages are not able to fully exploit the rare D_{8h} point group. In practice, subduction to a lower point group is used ($D_{8h} \rightarrow D_{4h} \rightarrow D_{2h}$, Altmann and Herzig, p. 46)[224] and this is the approach seen in much of the literature.[208,209,218,225] The D_{2h} point group has a relativity simple character table (see Appendix Table C.3) which is an Abelian group with eight irreducible representations that are all non-degenerate. For comparison the D_{8h} point group[‡] is a non-Abelian group with 14 irreducible representations, six of which are doubly degenerate, this presents a much more significant challenge for computation.

The use of lower point group allows mixing of orbitals that are formally orthogonal in D_{8h}.[209] In practice, the actual symmetry of the system should force most integrals to be zero, and as such, a calculation with a lower symmetry (or without symmetry)

[‡] http://symmetry.jacobs-university.de/cgi-bin/group.cgi?group=608&option=4

often produces the same result as one that exploits the full symmetry (or a subgroup of said symmetry).

Figure 6.6 shows the subduction from D_{8h} to D_{2h} for the gerade symmetries, constructed from the tables in reference 224.

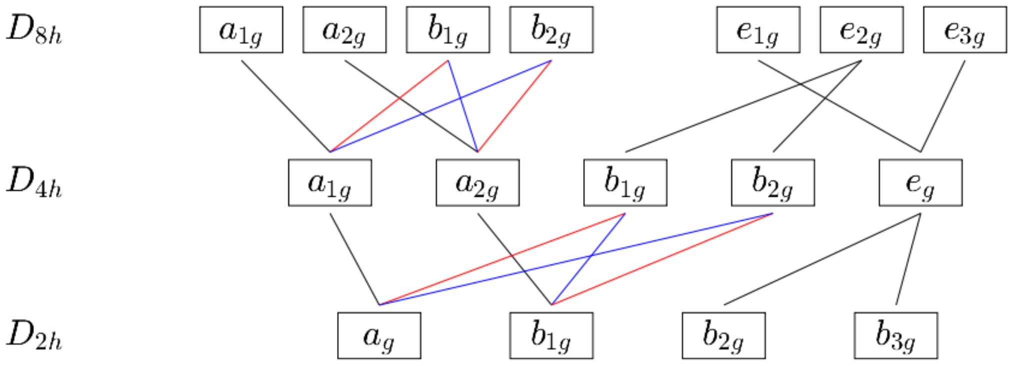

Figure 6.6: Descent of symmetry from D_{8h} to D_{2h} via D_{4h} for the gerade symmetry elements. ungerade elements follow the same pattern. Both the D_{8h} and D_{4h} groups have two possible descents and correlations consistent with both are shown in black. Red and blue lines show correlations unique to a single subduction.

6.4 The pseudospin approach to paramagnetic NMR

If a magnetic field $\mathbf{B}$ is applied to an isolated nucleus with nuclear spin I and magnetogyric ratio γ_{nuc}, then it is energetically favourable for the associated permanent magnetic moment to align with the field. This results in the nuclear energy level being lowered by $\gamma_{\text{nuc}}I|\mathbf{B}|$. A similar effect occurs when a magnetic field is applied to an isolated electron where the energy is lowered by $g_e\mu_B|\mathbf{B}|$; where $\mu_B = e\hbar/2m_e = \frac{1}{2}$a.u. is the Bohr magneton.

For an isolated closed shell atom, the applied magnetic field induces an effective current via circulating electrons that produces an opposing magnetic field. This effect is represented by $\boldsymbol{\sigma}^{\text{orb}}$, the chemical shift tensor. This effect is the orbital shielding, and the Hamiltonian corresponding to this interaction is given by $\gamma_{\text{nuc}}\mathbf{B}\cdot\boldsymbol{\sigma}^{\text{orb}}\cdot\mathbf{I}_{\text{nuc}}$. For a diamagnetic molecule, there are additional interactions, such as the direct nuclear dipole-dipole coupling, indirect nuclear spin-spin coupling and for nuclei with spin $> 1/2$, the quadrupole coupling interactions represented by the tensors $\mathbf{D}_{KL}, \mathbf{J}_{KL}$ and $\mathbf{Q}_K$ respectively, leading to a spin Hamiltonian of the form:

$$\mathcal{H}_{\texttt{NMR}} = -\gamma_K \sum_{K}^{\text{nuclei}} \mathbf{B} \cdot (1 - \boldsymbol{\sigma}_K) \cdot \mathbf{I}_K + \sum_{K}^{\text{nuclei}} \mathbf{I}_K \cdot \mathbf{Q}_K + \sum_{K,L<K}^{\text{nuclei}} \mathbf{I}_K \cdot (\mathbf{D}_{KL} + \mathbf{K}_{KL}) \cdot \mathbf{I}_L. \quad (6.4)$$

In this work higher order effects $\mathbf{D}_{KL}, \mathbf{J}_{KL}$ and $\mathbf{Q}_K$ are ignored. For a system with unpaired electrons, there is a permanent magnetic moment associated with the electronic spin. It is energetically favourable for the associated (reversed) magnetic moment to align with an applied magnetic field and the resulting (thermally averaged) dipole must be accounted for. The corresponding paramagnetic NMR spin Hamiltonian is given by:[102,108–110]

$$\mathcal{H}_{\texttt{pNMR}} = -\gamma_K \sum_{K}^{\text{nuclei}} \mathbf{B} \cdot (1 - \boldsymbol{\sigma}_K) \cdot \mathbf{I}_K + \mu_B \mathbf{B} \cdot \mathbf{g} \cdot \widetilde{\mathbf{S}} + \sum_{K}^{\text{nuclei}} \widetilde{\mathbf{S}} \cdot \mathbf{A}_K \cdot \mathbf{I}_K + \widetilde{\mathbf{S}} \cdot \mathbf{D} \cdot \widetilde{\mathbf{S}}, \quad (6.5)$$

where $\widetilde{\mathbf{S}}$ is the effective spin, or pseudospin which is discussed in the previous section. The Zeeman coupling matrix (often referred to as the $\mathbf{g}$ tensor, although it is not a true tensor) represents the interaction between the effective spin and the magnetic field. The zero-field-splitting (ZFS) tensor $\mathbf{D}$ represents the interaction between electronic spin dipoles, and is only non-zero when the electronic spin is greater than 1/2. Spin-orbit coupling (SOC) has a significant effect on these quantities. The hyperfine coupling constant matrix $\mathbf{A}$ represents the interaction between the nuclear and electronic spin dipoles. The leading SOC effect is second order, referred to as the paramagnetic spin-orbit (PSO) effect and results from nuclear-spin and electron-orbit interactions. For light atoms this can often be ignored, but is much more significant for heavy atoms or light atoms directly bonded to heavier atoms; the heavy-atom light-atom (HALA) effect. The magnitude of this effect is not always intuitive, so PSO corrections are needed in such cases. As an example the sign of A_{iso} for the protons of the closely related molecule $[\text{U(CHT)}_2]^-$, where CHT is the 1,3,5-cycloheptatriene trianion has been experimentally determined to be negative,[123,124] and this appears to be due to a spin-orbit induced PSO mechanism. While the formal oxidation state of the central atom is +5, *i.e.* U(V), the covalency of the metal-ligand η bond means that the compound has significant f^3 character corresponding to an oxidation state of +3.[124]

6.4.1 Orbital shielding, $\boldsymbol{\sigma}$

We calculated the orbital shielding matrices using the ORCA 4.2.1 package, using unrestricted Kohn-Sham DFT and the PBE0 functional. We also utilised gauge-including atomic orbitals (GIAO).[33,142,226] Scalar relativistic effects were modelled using the Douglas–Kroll–Hess approach to second-order (DKH2)[172,173] with picture change transformations included. In all cases def-TZVP basis sets where used for light atoms and a segmented all-electron relativistically corrected (SARC) basis set[30,31] with a g polarisation function on the uranium atom for the metal.[†]

6.4.2 Hyperfine coupling matrix, A

Hyperfine parameters were calculated using ORCA 4.2.1, UKS/PBE0 and the zero-order regular approximation (ZORA) for the scalar relativistic correction. For the nuclei of interest, the basis was extended by three additional large exponent s functions to better model the nuclear cusp following the methodology described in reference 2. Picture change transformations were applied. We have previously used the DKH2 approach for the calculation of hyperfine parameters, but the second-order PSO correction is a computationally expensive quantity and applying these corrections was faster using the ZORA method than the DKH2 method.

6.4.3 CASSCF and active space selection

For a multiconfigurational system with low lying excited states of differing multiplicity and significant spin-orbit coupling, there is no reliable single reference approach to calculate the Zeeman coupling and ZFS matrices. A multi-reference technique is essential, such as the CASSCF method.[60,61]

Unfortunately there is no prescriptive procedure to selecting the active space, so we will discuss and justify the selection process that we adopted in this work. In the following discussion a CASSCF calculation with N_e active electrons and N_o active orbitals is abbreviated CASSCF(N_e, N_o). One approach is to perform an unrestricted Kohn-Sham (UKS) calculation and form the corresponding natural orbitals.[227] As a first step, we may select the orbitals with UNO occupation numbers lying between 0.02–1.98; this approach can produce very small active spaces,[63] and this approach

---

[†] TVZP quality with $29s20p16d12f1g/$
$21s13p10d7f1g$ uncontracted/contracted gaussian functions for a uranium atom.

would imply a CASSCF(2,2) calculation, *i.e.* two singly occupied f orbitals, with only a single configuration for $S = 1$ and no $S = 2$ configuration possible, this clearly is not suitable for studying properties dependent on interactions between electronic states, such as the Zeeman matrix.

Figure 6.7 shows the crystal field splitting for an uranium atom in a D_{8h} field and reference 209 presents a combination of this with the energy levels of the two COT^{2-} rings. The energy of the f orbitals are between the π_2 bonding and π_3 antibonding orbitals, and the d orbitals straddle the π_3 orbitals (d_σ below, d_π and d_δ above). Figure 6.8 shows the candidate orbitals for the active space from a CASSCF(10,13) calculation using quasi-restricted orbitals (QROs)[41] from the UKS/UNO calculation with symmetry labels for D_{2h}, QROs were more suitable starting orbitals than UNOs due to reduced mixing between formally orthogonal orbitals and less delocalisation: most notably f_π and f_ϕ orbitals which have e_{1u} and e_{3u} symmetry respectively in D_{8h} but have $b_{2u}, (l = -1$ or $l = -3)$ or $b_{3u}, (l = 1$ or $l = 3)$ symmetry in D_{2h}. The gerade and ungerade π_0 molecular orbitals can interact with the d_σ and f_σ, but the ring orbitals are very low lying, so the interaction is limited, and the π_0 orbitals can be excluded from the active space. A similar argument holds for the π_4 orbitals. The interactions between the π_1 orbitals with d_π or f_π,[§] and π_3 with f_ϕ or f_ϕ molecular orbitals are marginally stronger.

As previously stated, the π_{2g} orbitals interact strongly with the d_δ orbitals and the π_{2u} orbitals interact strongly with the f_δ. This results in the η-bonding that stabilises the molecule, The first bonding pair represents a weak $\eta : \pi{-}\mathrm{d}_\delta$ bond, with the electron density primarily on the ring orbitals. The orbitals on the ring are similar to those predicted for the two HOMOs for the two planar COT dianions. The second bonding pair represents a weak $\eta : \pi{-}\mathrm{f}_\delta$ bond, again with the electron density residing primarily on the ring orbitals. The corresponding antibonding orbitals are dominated by the metallic orbitals and are labelled as η_d^* and η_f^* orbitals respectively. These along with the remaining d and f orbitals are candidates for a (10,16) active space.

[§] Some studies include one of the the pairs of π_1[209]

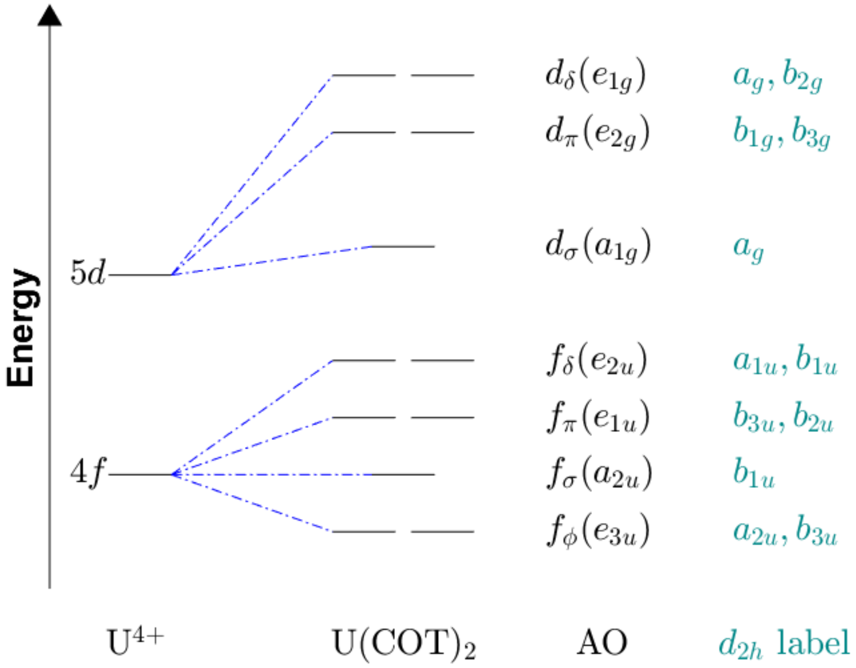

Figure 6.7: Crystal field splitting of a f-block element induced by a D_{8h} field. (D_{2h} labels are in green.)

This active space was sufficient to build the metal-centroid potential energy curve (PEC) for $UCOT_2$, but SA-NEVPT2-SOC(10,16) calculations proved to be too expensive. However looking at the excited states of this calculation showed that very few CSFs contained d_σ and d_π orbitals. These corresponded to high energy excitations, and as a result these were removed to give the main active space. Removing these leaves b_{2g} and b_{3g} unrepresented in the one-electron orbitals, but studies that include b_{2g} and b_{3g} in the active space orbitals imply minimal involvement.[209] This leaves a thirteen orbital active space (the eight η orbitals, f_σ, f_π and f_π orbitals). This is the active space that this work uses.

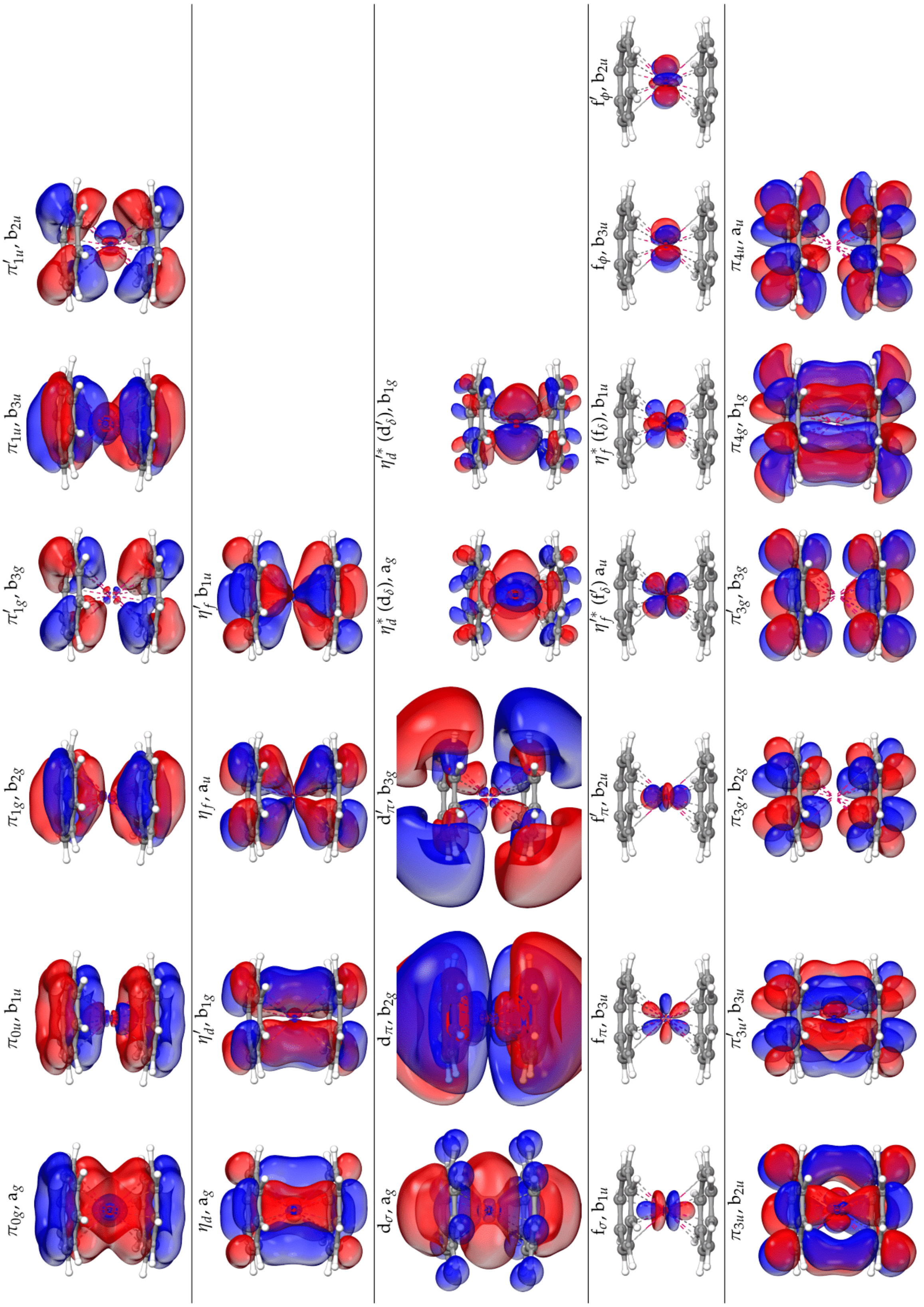

Figure 6.8: Candidate orbitals for the active space of uranocene taken from a CASSCF(10,13) calculation. The active space used in this work was the eight η_d and η_f bonding and antibonding orbitals, and the five remaining f orbitals (f_σ, f_π and f_ϕ). Symmetry labels are for D_{2h}.

To further justify our selection, we used the iterative configuration expansion (ICE)[200] method. This method uses a truncated form of the CI wavefunction, selects the most important components and iteratively improves the wavefunction. Figure 6.9 shows the orbital occupation that results from a CASSCI-ICE(22,60) with the active space coloured; blue for the η_d orbitals, red for the η_f orbitals and green for the remaining f orbitals. As can be seen, orbitals outside the active space have occupations below 0.02 (unoccupied) or above 1.92 (occupied).

Kerridge has studied a number of lanthanocene and actinocene compounds under D_{2h} symmetry[208,209,228] and varies the active space according to computational demands of the species. All calculations assume that the carbon and hydrogen atoms are in the same plane and exploit symmetry to ensure that the eight irreps are spanned. For uranocene, the inclusion of the f_σ orbital creates an unphysical imbalance in the orbital energies because it can mix with the b_{1u} η_f orbital in D_{2h} (but not in D_{8h}). Similar comments are the case for the d_σ orbital which can mix with the a_g η_0 orbital, however the former orbital is present in some of the excited states in the CASSCF(10,16) calculations, and may be magnetically important, so it is retained. This means that the D_{2h} CASSCF orbital energies differ from that which would be present in the true D_{8h} symmetry.

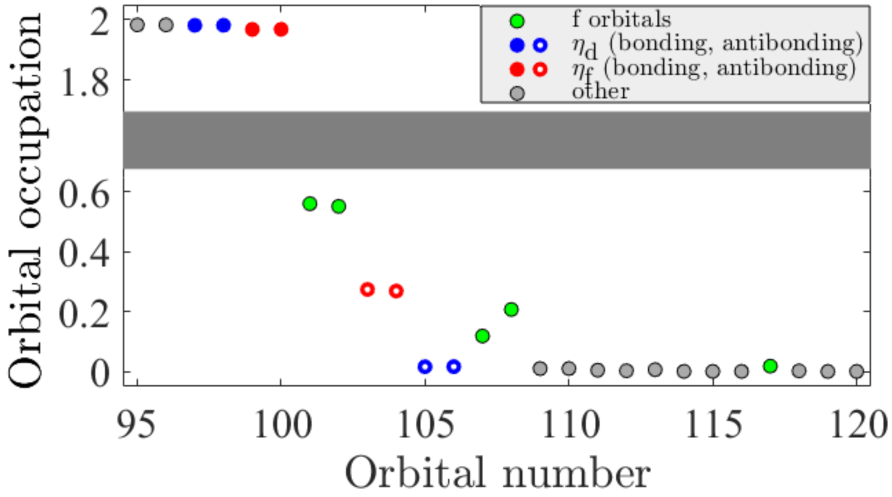

Figure 6.9: Orbital occupation numbers from a CASCI-ICE(22,60) calculation on $U(COT)_2$, using the QROs from a DFT/PBE0 calculation (basis as in text).

.

6.4.4 The Zeeman matrix and the ZFS tensor

Single reference approaches to calculating the **g** matrix[149,176] are only effective in systems that lack near degeneracies and where spin-orbit coupling is weak enough that it can be applied as a first-order perturbation. This is typically not true for *f* element species. We used a multiconfigurational approach, specifically state-averaged CASSCF (SA-CASSCF) calculations described in the following section, with DKH2 used to model scalar relativistic effects. Again the heavy elements used a SARC basis set and the remaining elements use def2-TZVP basis.

The best SA-CASSCF state averaging over the three interacting spin states (since the SOC operator can couple states with $\Delta S = 0, \pm 1$) and most appropriate pseudospin was obtained via the following process:

1. A series of SA-CASSCF calculations at the dominant spin state to establish the optimum number of these states to include. This is typically gauged by the convergence of the g-matrix, and an energy cut-off. This study originally used a cut-off of 2 eV, but this was adjusted to a cut-off of 0.5 eV from the ground state due to the known state-averaging instability of actinocenes.[209]

2. A CASCI calculation using the orbitals from the optimum number of SA roots (single spin), but including additional $\Delta S = 0, \pm 1$ roots. From this, we establish which $\Delta S = \pm 1$ to include in the calculation from the relative energies. Figure 6.10 shows an example for $U(COT)_2$, with the red line showing the 2 eV cut-off for SOC inclusion. The first $S = 2$ root occurs 4 eV above the first $S = 1$ root, so these are excluded.

3. A CASCI/NEVPT2-SOC calculation using the orbitals in the previous calculation with additional roots.

Dynamic correlation was modelled using a final NEVPT2 calculation.[69] The effective Hamiltonian approach[32,59] was used for both matrices.

In an attempt to make the pseudospin choice more quantitative, we are using Boltzmann populations (at 300 K) to assess the energy level separations, implying that the effective pseudospin is temperature dependent (increasing the temperature makes more states accessible).

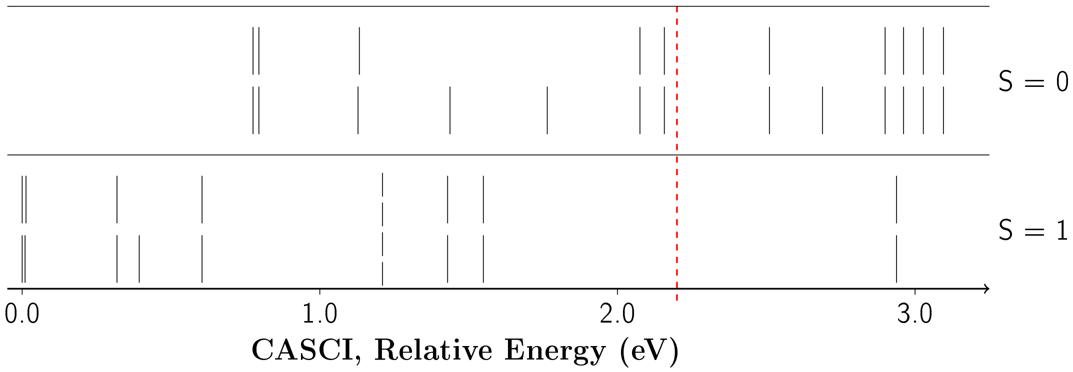

Figure 6.10: Example of (unsymmetrical) CASSCF state selection for $U(COT)_2$. This shows a CASCI/NEVPT2 calculation following a SA-CASSCF calculation with 18 $S = 1$ roots. Red dotted line shows the 2 eV energy level cut-off for SOC inclusion. Symmetrical root selection diagrams are given in Appendix C.

6.5 Results

6.5.1 Geometry optimisation

Following our previous work,[2,28] we initially attempted to optimise the geometry of uranocene using GAUSSIAN 09[169] via unrestricted density functional theory with the PBE0 functional[55] and a SARC basis set with a single set of g polarisation functions on the uranium atom[30] and a def2-TZVP basis set on the lighter atoms. Scalar relativistic effects were included by using an in-house program interfaced to GAUSSIAN that implements an atomic (one centre) form of the zeroth-order regular approach in its analytic form (aZORA).[27] This has the advantage of removing the gauge dependence issue and enables the use of analytic gradients.

The optimisation produced a ring-metal separation of 1.85 Å, which compared unfavourably with the experimentally measured result of 1.926 Å. CASPT2 calculations by Kerridge[218] produce a much closer result of 1.907 Å. This could imply that single-reference techniques cannot be used to fully optimise the geometry. To investigate this we optimised a series of seven actinocenes ($AnCOT_2$: An = Th–Cm).

Figure 6.11 shows the calculated DFT/aZORA ring-metal separations compared to the aforementioned paper's CASPT2 data. We judged that excluding uranocene and neptunacene, the DFT/aZORA results were competitive. The considerable multi-configurational nature of the ground-state of uranocene and neptunacene means that they cannot be fully optimised by DFT.

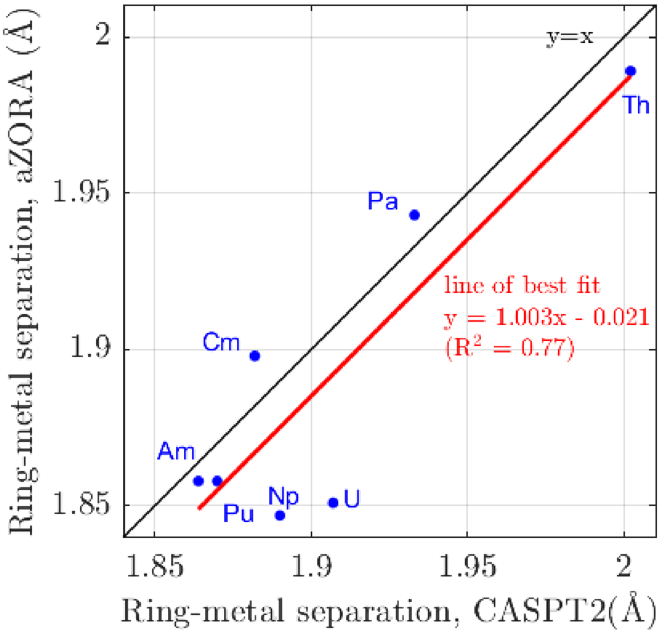

Figure 6.11: Performance of DFT/aZORA for optimising An(COT)$_2$, An = Th-Cm, compared against CASPT2 results,[218] black line shows perfect correlation, red line shows line of best fit (including U(COT)$_2$ and Np(COT)$_2$.

Hence partial optimisations using D_{8h} symmetry were performed for each complex, fixing the experimental ring-metal separation (*i.e.* ring centroid to metal distance) and allowing the distance between the ring-centroid and the carbon and hydrogen atoms to vary along with the metal-centroid-hydrogen angle. Equivalent partial optimisations at the DFT/aZORA level were performed for a range of fixed centroid-metal distances for $[\mathrm{U(COT)_2}]^-$ (1.85 – 2.05 Å, in increments of 0.01Å). The NEVPT2 single point energies for the first eight states for each of the $A_u, B_{1u}, B_{2u}, B_{3u}$ irreducible representations of the molecule were calculated for an 11 electron, 13 orbital active space (the choice of active space is discussed in Section 6.4.3). The ground spin-free state had A_u symmetry and the corresponding potential energy curve is plotted in Figure 6.12. The minimum of the line of best fit (sixth-order polynomial) was found to occur at centroid-metal distance 1.9980 Å. The corresponding DFT/aZORA optimisation gave a value of 1.9486 Å, was considered insufficently accurate and all following optimisations for U(III) are partial DFT/aZORA optimisations with our NEVPT2 centroid-metal distance. A similar calculation for $[\mathrm{Np(COT)_2}]^-$ (S.I. Figure C.1) produces a value of 1.9310 Å (NEVPT2), while the DFT/aZORA result was 1.9486 Å (DFT): this DFT result was considered trustworthy.

The geometry of all species were optimised via a constrained Z-matrix enforcing the D_{8h} symmetry of the ring carbon atoms. Parallel optimisations excluding symmetry led to eclipsed conformations in all cases, with the ring carbons showing only minor deviations from D_{8h}, plausibly a single-determinant artifact. We also observed a bending of the C-H bond towards the metal. Similar bending has been observed for substituents, and this is speculated to increase η overlap with the ring π system and d and f orbitals without compromising the aromaticity of the ring.[223]

A NEVPT2 potential energy curve for U(COT)$_2$ against the angle was constructed to confirm the accuracy of the partial optimisation, and to confirm that it was not an artifact of using DFT. This is shown in Figure 6.13. The partially optimised X-C-H angle was 6.7°, while the NEVPT2 fitted value was 6.5°, so we judged that the partial optimisation was reliable.

Substituted species typically have the same eclipsed C-H conformation as the unsubstituted analogues, but the substituted groups do not face each other, hence the symmetry is reduced to C$_{2h}$. Experimental measurements imply that the uranium-ring distance is invariant to substitution,[213] justifying the partial optimisation strategy. The spin multiplicity for all single-reference calculations corresponds to the electronic configuration of the free ion, *i.e.* An$^{\mathrm{IV}}$.

For 1,1'-dimethyluranocene, each methyl group is known to bend towards the uranium atom, and it is explained that “the change in hybridization of the ring carbons” achieves better overlap with the uranium f_δ and d_δ orbitals.[223] For 1,1'-ditert-butyluranocene, the tert-butyl group bends away from the uranium due to van der Waals repulsion between the bulky group and the opposite annulene-H atom.[223] The partially optimised geometries agree with this result, the X-C-C angle bends 2.0° towards the uranium atom for the methyl substituent and 2.8° away from the uranium atom for the tert-butyl group (the experimental range for this bending was estimated as between 0.5-6.5° for the staggered four-fold methyl substituted uranocene (1,1',3,3',5,5',7','8)-octamethyl uranocene.[223])

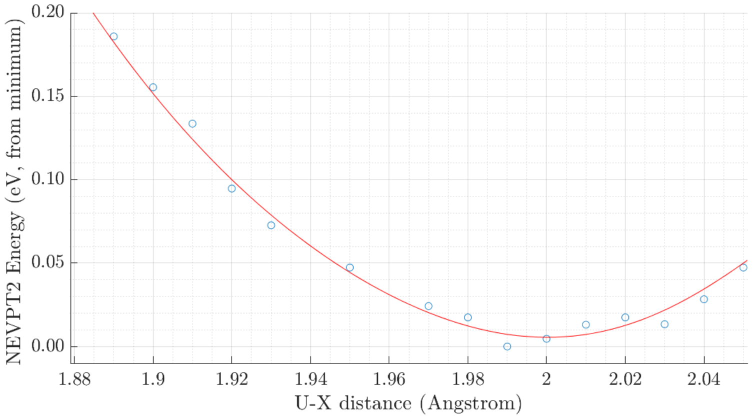

Figure 6.12: Potential energy curve for variation in U-X distance for , where X indicates the centroid of the COT ring. Ground state NEVPT2 energies with a (10,13) active space. Red line indicates line of best fit to a sixth-order polynomial.

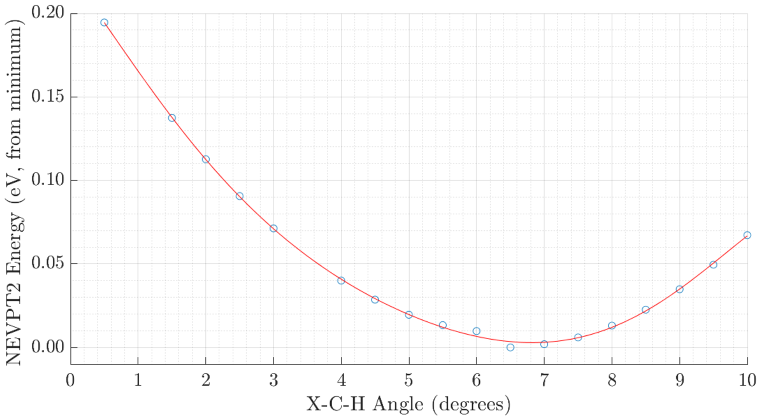

Figure 6.13: Potential energy curve for variation in X-C-H angle for uranocene, where X indicates the centroid of the COT ring. Ground state NEVPT2 energies for uranocene with a (10,13) active space. Red line indicates line of best fit to a sixth-order polynomial.

6.5.2 pNMR of neutral uranocenes

Edelstein[212] *et al.* measured the NMR spectral resonance of uranocene in deuterated tetrahydrofuran (THF-d_8) sealed under argon over temperatures ranging from 198 to 353 K, using the dianion (COT^{2-}) as the reference. Restandardising to tetramethylsilane (TMS), the single shift was measured to occur at -36.63 ppm (30°C), while we calculated a shift of -38.66 ppm (30°C). The paper used the Bleaney formula[194,197] to estimate the pseudocontact shift at 302 K to be 8.6 ppm, with the contact and pseudocontact shifts acting to shield the proton. The Bleaney relationship gives an angular dependence of the pseudocontact contact shift as proportional to $(3\cos^2\theta - 1)$, where θ is the angle of the proton to the anisotropy axis. Due to the assumption that the protons were coplanar with the carbon ring, this result was flawed and we calculated a pseudocontact shift of 12.86 ppm. The contact shift (32.69 ppm) is larger than the pseudocontact , which corresponds to the significant alpha spin density on the ring protons (Löwdin alpha spin density of 0.000059 Bohr^{-3}).

Figure 6.14 compares the calculated temperature dependence for the ^{1}H pNMR of uranocene against the experimental temperature dependence. In both cases the relationship is nearly linear with respect to reciprocal temperature, although the calculated gradient is larger than the experimental one. This difference may be a result of the single reference calculation of the hyperfine matrices not fully representing the spin-orbit mediated interaction, or due to conformational interchange. The magnetic susceptibility of uranocene follows[213] the Curie–Weiss law (*i.e.* it is inversely proportional to $(T - T_c)$ where T is the temperature and T_c is the curie temperature), and the proton NMR shows a corresponding linear relationship with the inverse temperature.

Paramagnetic NMR of substituted uranocenes are well documented in Luke and Streitwieser's summary of NMR studies of neutral uranocenes.[213] The 1,1'-substituted methyl and tert-butyl uranocene compounds were prepared in d_8-toluene and measured against tetramethylsilane (TMS). Both spectra produced five singlet peaks, with the six methyl protons and the two 5'- protons identified by integration. Tentative assignments were made by assuming that the central uranium atom locally experiences C_8 symmetry, and the differences in chemical shifts are entirely due to differences in contact shift. Further deuterium labelling studies were able to identify the 4' proton,

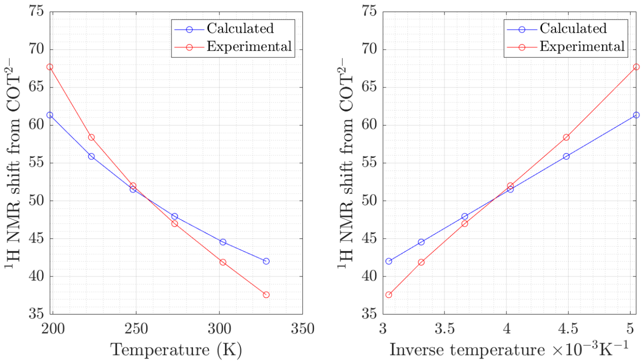

Figure 6.14: Calculated temperature dependence of the ^{1}H pNMR resonance for $U(COT)_2$ vs. the experimental temperature dependence. Shift is measured from that of COT^{2-}.[212]

but argues the 2',3' ordering on kinetic studies and the likely populations of the conformers. However the principal axis of the ZFS tensor is predicted to lie along the C_{2h} axis, hence the pseudocontact term, while smaller in magnitude oscillates. Figure 6.15 compares the calculated proton NMR with the experimental NMR. Assignments are from the calculation, and correctly identify the methyl and 5'- protons. Our results agree with the assignment of the 4' protons, but swap the 2' and 3' protons.

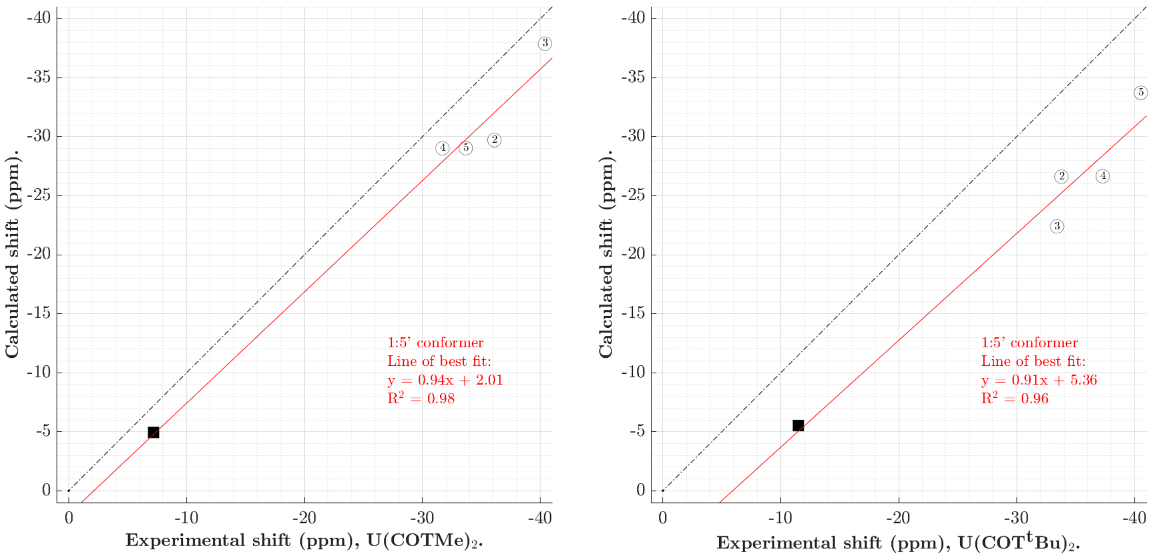

Figure 6.15: Left: Calculated qualitative ^{1}H pNMR shifts (ppm) vs. experimental shifts (ppm) for U(COTMe)$_2$, assuming $\tilde{S} = 3/2$. The line of best fit is indicated in red, and the dotted line indicates perfect correspondence. Black square indicates the methyl hydrogen, numbers indicate position relative to substituent.
Right: Calculated qualitative ^{1}H pNMR shifts (ppm) vs. experimental shifts (ppm) for U(COTtBu)$_2$, assuming $\tilde{S} = 3/2$. The line of best fit is indicated in red, and the dotted line indicates perfect correspondence. Black square indicates the methyl hydrogen, numbers indicate position relative to substituent.

6.5.3 pNMR of anionic uranocenes

Eisenberg[214] *et al.* prepared potassium bis([8]annulenediyl)uranate(III), $K^+[U(COT)_2]^-$ and obtained the ^{1}H NMR spectrum from a solution in d_8-THF, obtaining a single peak at −31.80 ppm relative to TMS (20°). We calculated this paramagnetic NMR shift using the `PNMRshift` program made available from Autschbach's group,[131,134,135] however because the calculated ZFS tensor was nearly axial, the SOC states were a pair of Kramers' doublets separated by 0.08 eV, indicating a perfect model pseudospin of 3/2 (in this case equal to the true spin), this provided our first opportunity to use the van den Heuvel and Soncini ITO approach[1] to third order in a real molecule. This was achieved in Matlab by combining the $\{\mathbf{L}_x, \mathbf{L}_y, \mathbf{L}_z\}$ and $\{\mathbf{S}_x, \mathbf{S}_y, \mathbf{S}_z\}$ to form the corresponding $\boldsymbol{\mu}$ matrix in the spin-orbit free (SOF) CASSCF states, parsing the spin-orbit state descriptions to rotate $\boldsymbol{\mu}$ into the NEVPT2-SOC basis and truncating the result into a 4×4 complex matrix. This was then used to generate first- and third-order Zeeman ITO coefficients ($g_{z0}^{(1)}$ the $g_{z0}^{(3)}$) and the first-order hyperfine analogue, with the remaining third order coefficient obtained by assuming that the ratio of the Zeeman coefficients is the same as that of the hyperfine coefficients. This process is described in ref 1. Autschbach's PNMRshift program gives a predicted shift of −27.06 ppm, while the ITO decomposition gave a result of −29.86 ppm. The latter is clearly closer to the experimental value. As a technical note, the ZFS tensor was only recovered at the NEVPT2-SOC level, the corresponding state-averaged CASSCF-SOC calculation returns a zero ZFS tensor due to orbital degeneracies.

6.6 Conclusions

In this paper we have studied four molecules, and made qualitative predictions of their ^{1}H pNMR shifts. These predictions only slightly differ from earlier models, which used the Bleaney model and an assumption that the hydrogen atoms are coplanar with the carbon atoms. Nonetheless due to the small differences in shifts, our predictions remain tentative. The ITO model of van den Heuvel and Soncini shows considerable promise if higher order hyperfine terms can be produced.

Chapter 7

Conclusions and future work

The main purpose of this work, was to facilitate the qualitative assignment and prediction of pNMR shifts in actinide complexes and to move towards quantitative prediction.

Chapter 4 successfully assigned the ^{1}H, ^{13}C and ^{28}Si pNMR of five f^3 actinide complexes. It also demonstrated and measured the importance of modelling zero-field splitting (ZFS) by a simple zero-field splitting model, using an empirical pseudospin of $\tilde{S} = S = 3/2$. The only lanthanide compound that is detailed in this thesis presented a more significant challenge due to its closely spaced shifts. A simple approach to modelling ZFS was implemented, however it has been superseded by an open source package from Autschbach's group, `pNMRShift`, freely available from `https://github.com/jautschbach/pnmr-shift`.

In Chapter 5 we improved our approach and resolved the ^{1}H pNMR shifts for U(DOTA) which have had competing suggested assignments. A complication was the effects of conformer interchange, especially on the assignment of the equatorial protons in U(DOTA) and its derivatives. Of particular interest was the observed 90° shift in the anisotropy axis following axial substitution by the anionic ligands and this causes formally equivalent protons to not be magnetically equivalent in a static frame. We have also been able to qualitatively predict the corresponding ^{13}C pNMR shifts and look forward to comparing these to future experiments. This included the first use of our new MATLAB (and C++) code that uses the Irreducible Tensor Operator (ITO) approach. This approach is limited due to the lack of availability for the matrix representations of the three $\hat{\boldsymbol{\mathcal{F}}}^{I}$ operators, and attempts to generalise the approach are ongoing.

The final research chapter started working on actinocenes, with the uranium atom existing in a highly symmetrical environment. Four actinocenes were briefly studied and assigned with the first use of an improved variant of our ITO program. While the program is currently limited, it is, in principle an exact decomposition of paramagnetic NMR shift contribution, since it has no theoretical limit on the order of operators used.

Other than the application of ZFS, it would be considerably better to generate orbital and hyperfine matrices that explicitly include both static and dynamic correlation, *e.g.* SC-NEVPT2, and we believe that once the ITO approach is generalised, in many cases, this will be the largest remaining source of error. However, it must be noted that the factorial scaling of the CASSCF approach greatly limits the size of the active space, and this is a further constraint on the quality of the wavefunction used. To generalise pNMR prediction to more complex actinide species will need to use approaches that allow more flexibility, such as RASSCF, and the application of dynamic correlation via perturbation theory.

Bibliography

[1] W. Van den Heuvel and A. Soncini, *Phys. Rev. Lett.*, 2012, **109**, 073001.

[2] A. W. Lloyd, H. M. Moylan and J. J. W. McDouall, *Magnetochem.*, 2019, **5**, 3.

[3] V. M. Timmermann, *PhD Thesis, ^{1}H NMR and Emission Spectroscopy of Lanthanide and Uranium(IV) Coordination Complexes*, Faculty of Science and Engineering, School of Chemistry, The University of Manchester, 2018.

[4] G. T. Kent, G. Wu and T. W. Hayton, *Inorganic Chemistry*, 2019, **58**, 8253–8256.

[5] G. Dovrat, M.-C. Illy, C. Berthon, A. Lerner, M. H. Mintz, E. Maimon, R. Vainer, Y. Ben-Eliyahu, Y. Moiseev, P. Moisy, A. Bettelheim and I. Zilbermann, *Chem. - A Euro. J.*, 2020, **26**, 3390–3403.

[6] P. W. Atkins and R. S. Friedman, *Molecular Quantum Mechanics*, Oxford University Press, Oxford, 3rd edn., 1997, p. 37.

[7] J. L. Lagrange, A. Boissonnade and V. N. Vagliente, *Analytical Mechanics: Translated from the Mecanique analytique*, Springer, Netherlands, 1997.

[8] I. M. Gelfand and G. V. Fomin, *Calculus of Variations*, Dover Publications Inc, New York, 2003, p. 240.

[9] R. E. Moss, *Advanced Molecular Quantum Mechanics*, John Wiley & Sons, Inc., New York, 1973.

[10] E. Noether, *Nachrichten von der Gesellschaft der Wissenschaften zu Göttingen, Mathematisch-Physikalische Klasse*, 1918, 235.

[11] P. W. Atkins and J. de Paula, *Physical Chemistry*, Oxford University Press, Oxford, 2006, p. 351.

[12] N. Bohr, *Zeitschrift für Physik.*, 1920, **2**, 241.

[13] D. R. Hartree, *Mathematical Proceedings of the Cambridge Philosophical Society*, 1928, **24**, 89.

[14] P. A. M. Dirac, *Principles of Quantum Mechanics*, Oxford University Press, London, 1948.

[15] K. A. Stroud and D. J. Booth, *Advanced Engineering Mathematics*, Red Globe Press (Macmillan Education Ltd), London, 2020.

[16] T. Kato, *Communications on Pure and Applied Mathematics*, 1957, **10**, 151–177.

[17] A. Szabo and N. S. Ostlund, *Modern Quantum Chemistry: Introduction to Advanced Electronic Structure Theory*, Dover Publications Inc, New York, 1996.

[18] C. A. Weatherford and H. W. Jones, *ETO Multicenter Molecular Integrals*, D. Reidel Publishing Company, London, 1982.

[19] E. R. Davidson and D. Feller, *Chem. Rev.*, 1986, **86**, 681.

[20] S. F. Boys, *Proc. R. Soc. A*, 1950, **200**, 542.

[21] B. P. Pritchard, D. Altarawy, B. Didier, T. D. Gibson and T. L. Windus, *J. Chem. Info. Modeling*, 2019, **59**, 4814.

[22] F. Weigend, F. Furche and R. Ahlrichs, *The Journal of Chemical Physics*, 2003, **119**, 12753.

[23] F. Weigend and R. Ahlrichs, *Phys. Chem. Chem. Phys.*, 2005, **7**, 3297.

[24] K. N. Kirschner, D. Reith and W. Heiden, *Soft Materials*, 2020, **18**, 200.

[25] M. Bursch, J.-M. Mewes, A. Hansen and S. Grimme, *Angew. Chem.2022,134,*, 2022, **134**, e202205.

[26] E. Y. Pankratyev, A. R. Tulyabaev and L. M. Khalilov, *J. Comput. Chem.*, 2011, **32**, 1993–1997.

[27] H. M. Moylan and J. J. W. McDouall, *Chem. - A Eur. J.*, 2017, **23**, 7798.

[28] H. M. Moylan and J. J. W. McDouall, *Trends Phys. Chem.*, 2018, **17**, 25.

[29] D. A. Pantazis, X. Y. Chen, C. R. Landis and F. Neese, *J. Chem. Theory Comput.*, 2008, **4**, 908.

[30] D. A. Pantazis and F. Neese, *J. Chem. Theory Comput.*, 2009, **5**, 2229.

[31] D. A. Pantazis and F. Neese, *J. Chem. Theory Comput.*, 2011, **7**, 677.

[32] F. Neese, *ORCA — An Ab Initio, DFT and Semiempirical SCF-MO Package (Manual)*, Max-Planck-Institute for Chemical Energy Conversion, 4th edn., 2020, p. 595.

[33] F. London, *Phys. Radium*, 1937, **8**, 397.

[34] C. J. Cramer, *Essentials of Computational Chemistry: Theories and Models*, John Wiley & Sons Ltd, Chichester, UK, 2nd edn., 2004, p. 190.

[35] C. C. J. Roothaan, *Rev. Mod. Phys.*, 1951, **23**, 69.

[36] G. G. Hall, *Proc. R. Soc. Lond. A*, 1951, **205**, 541.

[37] B. N. Plakhutin and E. R. Davidson, *The Journal of Chemical Physics*, 2014, **140**, 014102.

[38] T. Koopmans, *Physica*, 1934, **1**, 104–113.

[39] J. J. W. McDouall, *Computational Quantum Chemistry*, Royal Society of Chemistry, Cambridge, 2013.

[40] J. Autschbach, *J. Chem. Educ.*, 2012, **89**, 1032.

[41] F. Neese, *J. Am. Chem. Soc.*, 2006, **128**, 10213.

[42] D. Sherrill, *Non-Dynamical (Static) Electron Correlation: Bond Breaking in Quantum Chemistry*, `https://www.youtube.com/watch?v=coGVX7HCCQE`, 2020, [Georgia Institute of Technology, Atlanta, GA 30332-0400. Online; accessed 08-March-2023].

[43] C. L. Benavides-Riveros, N. N. Lathiotakis and M. A. L. Marques, *Phys. Chem. Chem. Phys.*, 2017, **19**, 12655.

[44] F. Sottile and L. Reining, *Density Functional Theory*, `https://www.coursera.org/learn/density-functional-theory/home/info`, 2023, [A Coursera course by École Polytechnique, Palaiseau, France. Online; accessed 08-March-2023].

[45] R. G. Parr and W. Yang, *Density-Functional Theory of Atoms and Molecules (International Series of Monographs on Chemistry)*, Oxford University Press, USA, 1994.

[46] A. Schindlmayr and R. W. Godby, *Phys. Rev. B*, 1995, **51**, 10427–10435.

[47] P. Hohenberg and W. Kohn, *Phys. Rev.*, 1964, **136**, B864–B871.

[48] W. Kohn and L. J. Sham, *Phys. Rev.*, 1965, **140**, A1133.

[49] D. M. Ceperley and B. J. Alder, *Phys. Rev. Lett.*, 1980, **45**, 566.

[50] A. D. Becke, *Phys. Rev. A*, 1988, **38**, 3098.

[51] C. Lee, W. Yang and R. G. Parr, *Phys. Rev. B*, 1988, **37**, 785.

[52] J. P. Perdew, K. Burke and M. Ernzerhof, *Phys. Rev. Lett.*, 1996, **77**, 3865.

[53] J. Tao, J. P. Perdew, V. N. Staroverov and G. E. Scuseria, *Phys. Rev. Lett.*, 2003, **91**, 146401.

[54] J. P. Perdew and K. Schmidt, *AIP Conference Proceedings*, 2001, **577**, 1.

[55] C. Adamo and V. Barone, *J. Chem. Phys.*, 1999, **110**, 6158.

[56] V. Vetere, C. Adamo and P. Maldivi, *Chemical Physics Letters*, 2000, **325**, 99–105.

[57] N. Iché-Tarrat and C. J. Marsden, *The Journal of Physical Chemistry A*, 2008, **112**, 7632–7642.

[58] P. Tecmer, A. S. P. Gomes, U. Ekström and L. Visscher, *Phys. Chem. Chem. Phys.*, 2011, **13**, 6249.

[59] J. Autschbach and T. Ziegler, *Coord. Chem. Rev.*, 2003, **238-239**, 83.

[60] P. A. Malmqvist and B. O. Roos, *Chem. Phys. Lett.*, 1989, **155**, 189.

[61] J. Olsen, *Int. J. Quantum Chem.*, 2011, **111**, 3267.

[62] E. R. Davidson, *J. Comput. Phys.*, 1975, **17**, 87.

[63] D. M. Rogers, C. Wells, M. Joseph, V. J. Boddington and J. J. W. McDouall, *J. Mol. Struct. THEOCHEM*, 1998, **434**, 239.

[64] B. G. Levine, A. S. Durden, M. P. Esch, F. Liang and Y. Shu, *J. Chem. Phys.*, 2021, **154**, 090902.

[65] Y. Shu, E. G. Hohenstein and B. G. Levine, *J. Chem. Phys.*, 2015, **142**, 024102.

[66] B. Huron, J. P. Malrieu and P. Rancurel, *J. Chem. Phys.*, 1973, **58**, 5745.

[67] J. Zobel, J. Nogueira and L. González, *Chem. Sci.*, 2017, **8**, 1482.

[68] C. Angeli, R. Cimiraglia, S. Evangelisti, T. Leininger and J.-P. Malrieu, *J. Chem. Phys.*, 2001, **114**, 10252.

[69] C. Angeli, B. Bories, A. Cavallini and R. Cimiraglia, *J. Chem. Phys.*, 2006, **124**, 054108.

[70] C. Angeli, M. Pastore and R. Cimiraglia, *Theo. Chem. Acc.*, 2007, **117**, 743.

[71] K. G. Dyall, *J. Chem. Phys.*, 1995, **102**, 4909.

[72] C. Angeli, C. J. Calzado, R. Cimiraglia and J.-P. Malrieu, *J. of Chem. Phys.*, 2006, **124**, 234109.

[73] P. A. M. Dirac and R. H. Fowler, *Proceedings of the Royal Society of London. Series A, Containing Papers of a Mathematical and Physical Character*, 1929, **123**, 714–733.

[74] A. Sommerfeld, *Annalen der Physik*, 1916, **356**, 1.

[75] D. A. McQuarrie, *Quantum Chemistry*, Oxford University Press, 1983.

[76] M. J. Winter, *The Orbitron*, `https://winter.group.shef.ac.uk/orbitron/`, University of Sheffield, Sheffield, Accessed: 2020-03-29.

[77] J. Autschbach, *Philos. Trans. A. Math. Phys. Eng. Sci.*, 2014, **372**, 20120489.

[78] M. Reiher and A. Wolf, *Relativistic Quantum Chemistry*, Wiley-VCH, Weinheim, Germany, 2015, p. 1.

[79] P. A. M. Dirac, *Proc. R. Soc. A Math. Phys. Eng. Sci.*, 1928, **117**, 610.

[80] E. Comay, *Apeiron*, 2005, **12**, 26.

[81] J. D. Bjorken and S. D. Drell, *Relativistic Quantum Chemistry*, McGraw-Hill, New York, 1964.

[82] E. van Lenthe, E. J. Baerends and J. G. Snijders, *J. Chem. Phys.*, 1993, **99**, 4597.

[83] P. A. M. Dirac and R. H. Fowler, *Proc. Royal Soc. London. A*, 1930, **126**, 360.

[84] A. Einstein, *Annalen Physik*, 1905, **323**, 639.

[85] C. G. Darwin, *London Edinburgh Dublin Phil. Mag. J. Sci.*, 1920, **39**, 537.

[86] L. L. Foldy and S. A. Wouthuysen, *Phys. Rev.*, 1950, **78**, 29.

[87] C. M. Marian, in *Rev. Computat. Chem.*, Wiley-Blackwell, New York, 2001, p. 99.

[88] M. Blume and R. E. Watson, *Proc. R. Soc. A Math. Phys. Eng. Sci.*, 1962, **270**, 127.

[89] M. Blume and R. E. Watson, *Proc. R. Soc. A Math. Phys. Eng. Sci.*, 1963, **271**, 565.

[90] J. E. Peralta and G. E. Scuseria, *The Journal of Chemical Physics*, 2004, **120**, 5875–5881.

[91] *SMT359 Book2: Electromagnetism, Electomagnetic fields*, ed. S. Freake, Open University Press, Milton Keynes, 2006, p. 7.

[92] University of Manchester, *EasySpin documentation, Spin operators and matrices*, `https://easyspin.org/easyspin/documentation/index.html/`, University of Manchester, Manchester, Accessed: 2023-03-12.

[93] A. W. Lloyd, *MPhil Thesis, Implementation of Spin-Orbit Coupling in a Slater Determinant Basis with Applications to Spin-Dependent Properties.*, Faculty of

Science and Engineering, School of Chemistry, The University of Manchester, 2018.

[94] J. E. Harriman, *Theoretical foundations of electron spin resonance*, Academic Press, 1978.

[95] M. Reiher and A. Wolf, *Relativistic Quantum Chemistry*, Wiley-VCH Verlag & Co. KGaA, Boschstr. 12, 69469 Weinheim, Germany, 2014, pp. 1–737.

[96] J. J. Sakurai, *Modern Quantum Mechanics, Revised Edition*, Cambridge University Press, Cambridge, UK, 1995, vol. 63, p. 93.

[97] K. Kanazawa, K. Matsuda, S. Mitsudo, T. Idehara and S. Honda, *EPR in the 21st Century*, Elsevier Science Ltd, Amsterdam, 2002, pp. 168–173.

[98] H. A. Buckmaster, *Canadian Journal of Physics*, 1962, **40**, 1670.

[99] D. Smith and J. H. Thornley, *Proc. Phys. Soc.*, 1966, **89**, 779.

[100] E. W. Weisstein, *Wigner 3j-Symbol.*

[101] P. Zeeman, *London, Edinburgh, Dublin Phil. Mag. J. Sci.*, 1897, **43**, 226.

[102] A. Abragam and B. Bleaney, *Electron Paramagnetic Resonance of Transition Ions*, Oxford University Press, Oxford, 1970.

[103] B. Odom, D. Hanneke, B. D'Urso and G. Gabrielse, *Phys. Rev. Lett.*, 2006, **97**, 030801.

[104] D. Hanneke, S. Fogwell and G. Gabrielse, *Phys. Rev. Lett.*, 2008, **100**, 120801.

[105] J. C. Facelli, *Prog. Nucl. Magn. Reson. Spectrosc.*, 2011, **58**, 176.

[106] K. S. Krane, *Introductory nuclear physics*, John Wiley & Sons, Inc., New York, 1988.

[107] W. A. van Wijngaarden and J. Li, *Z. Phys. D – Atoms, Molecules and Clusters*, 1994, **32**, 67.

[108] M. H. L. Pryce, *Proc. Phys. Soc. Sect. A*, 1950, **63**, 25.

[109] A. Abragam and M. H. L. Pryce, *Proc. R. Soc. A Math. Phys. Eng. Sci.*, 1951, **205**, 135.

[110] H. M. McConnell and D. B. Chesnut, *J. Chem. Phys.*, 1958, **28**, 107.

[111] M. Bühl and T. van Mourik, *WIREs Computational Molecular Science*, 2011, **1**, 634–647.

[112] R. McWeeny, *Methods of Molecular Quantum Mechanics*, Academic Press, London, 2nd edn., 1989.

[113] W. G. Richards, H. P. Trivedi and D. L. Cooper, *Spin-orbit coupling in molecules*, Oxford University Press, Oxford, 1981, p. 4.

[114] B. A. Heß, C. M. Marian, U. Wahlgren and O. Gropen, *Chem. Phys. Lett.*, 1996, **251**, 365.

[115] S. Koseki, M. W. Schmidt and M. S. Gordon, *J. Phys. Chem.*, 1992, **96**, 10768.

[116] S. Koseki, M. S. Gordon, M. W. Schmidt and N. Matsunaga, *J. Phys. Chem.*, 1995, **99**, 12764.

[117] S. Koseki, M. W. Schmidt and M. S. Gordon, *J. Phys. Chem. A*, 1998, **102**, 10430.

[118] K. F. Riley, M. P. Hobson and S. J. Bence, *Mathematical Methods for Physics and Engineering*, Cambridge University Press, Cambridge University, 2010, p. 930.

[119] D. Ganyushin and F. Neese, *J. Chem. Phys.*, 2013, **138**, 104113.

[120] M. Gerloch and R. F. McMeeking, *J. Chem. Soc. Dalt. Trans.*, 1975, **0**, 2443.

[121] L. F. Chibotaru and L. Ungur, *J. Chem. Phys.*, 2012, **137**, 64112.

[122] L. F. Chibotaru, in *Advances in Chemical Physics Volume 153*, Wiley-Blackwell, New York, 2013, p. 397.

[123] D.-C. Sergentu, F. Gendron and J. Autschbach, *Chem. Sci.*, 2018, **9**, 6292.

[124] Y. Qiao, G. Ganguly, C. H. Booth, J. A. Branson, A. S. Ditter, D. J. Lussier, L. M. Moreau, D. R. Russo, D.-C. Sergentu, D. K. Shuh, T. Sun, J. Autschbach and S. G. Minasian, *Chem. Commun.*, 2021, **57**, 9562.

[125] N. F. Ramsey, *Phys. Rev.*, 1950, **77**, 567.

[126] N. F. Ramsey, *Physica*, 1951, **17**, 303.

[127] W. Van den Heuvel and A. Soncini, *J. Chem. Phys.*, 2013, **138**, 054113.

[128] S. Moon and S. Patchkovskii, in *Calc. NMR EPR Parameters*, ed. M. Kaupp, M. Bühl and V. G. Malkin, Wiley-VCH Verlag GmbH & Co. KGaA, Weinheim, FRG, 2004, p. 325.

[129] R. J. Kurland and B. R. McGarvey, *J. Magn. Reson.*, 1970, **2**, 286.

[130] A. Soncini and W. Van den Heuvel, *J. Chem. Phys.*, 2013, **138**, 021103.

[131] B. Martin and J. Autschbach, *J. Chem. Phys.*, 2015, **142**, 054108.

[132] J. Vaara, S. A. Rouf and J. Mares, *J. Chem. Theory Comput.*, 2015, **11**, 4840.

[133] T. O. Pennanen and J. Vaara, *Phys. Rev. Lett.*, 2008, **100**, 133002.

[134] B. Martin and J. Autschbach, *Phys. Chem. Chem. Phys.*, 2016, **18**, 21051–21068.

[135] J. Autschbach, S. Patchkovskii and B. Pritchard, *J. Chem. Theory Comput.*, 2011, **7**, 2175.

[136] B. L. Silver, *Irreducible Tensor Methods. An Introduction for Chemists*, Academic Press Inc., 1976.

[137] H. M. Moylan, *PhD Thesis, Computational Prediction of Paramagnetic NMR Chemical Shifts in f-Element Complexes*, Faculty of Science and Engineering, School of Chemistry, The University of Manchester, 2017.

[138] N. Tsoureas, O. T. Summerscales, F. G. N. Cloke and S. M. Roe, *Organomet.*, 2013, **32**, 1352.

[139] C. A. P. Goodwin, F. Tuna, E. J. L. McInnes, S. T. Liddle, J. McMaster, I. J. Vitorica-Yrezabal and D. P. Mills, *Chem. — A Eur. J.*, 2014, **20**, 14579.

[140] V. Parsonnet, J. Driller, D. Cook and S. A. Rizvi, *PACE - Pacing Clin. Electrophysiol.*, 2006, **29**, 195.

[141] P. B. Iveson, C. Rivière, D. Guillaneux, M. Nierlich, P. Thuéry, M. Ephritikhine and C. Madic, *Chem. Commun.*, 2001, 1512.

[142] T. Helgaker, M. Jaszunski and K. Ruud, *Chem. Rev.*, 1999, **99**, 293.

[143] M. Kaupp and F. H. Köhler, *Coord. Chem. Rev.*, 2009, **253**, 2376.

[144] S. Patchkovskii, J. Autschbach and T. Ziegler, *J. Chem. Phys.*, 2001, **115**, 26.

[145] I. Bertini, C. Luchinat and G. Parigi, *Prog. Nucl. Magn. Reson. Spectrosc.*, 2002, **40**, 249.

[146] F. Gendron, K. Sharkas and J. Autschbach, *J. Phys. Chem. Lett.*, 2015, **6**, 2183.

[147] F. Gendron and J. Autschbach, *J. Chem. Theo. and Comput.*, 2016, **12**, 5309.

[148] J. Vaara, *Sci. Technol. At. Mol. Condens. Matter Biol. Syst.*, 2013, **3**, 41.

[149] H. Bolvin and J. Autschbach, in *Relativistic Methods for Calculating Electron Paramagnetic Resonance (EPR) parameters*, ed. W. Liu, Springer, Berlin, Heidelberg, 2017, p. 725.

[150] J. Autschbach, in *Annu. Rep. Comput. Chem.*, Elsevier, Amsterdam, 2015, vol. 11, ch. 1, p. 3.

[151] R. Ditchfield, *Mol. Phys.*, 1974, **27**, 789.

[152] G. Schreckenbach and T. Ziegler, *J. Phys. Chem.*, 1995, **99**, 606.

[153] M. Filatov, *Chem. Phys. Lett.*, 2002, **365**, 222.

[154] M. Reiher, *Theor. Chem. Acc.*, 2006, **116**, 241.

[155] J. Autschbach, N. Govind, R. Atta-Fynn, E. J. Bylaska, J. W. Weare and W. A. de Jong, in *Comput. Methods Lanthan. Actin. Chem.*, John Wiley & Sons Ltd, Chichester, UK, 2015, p. 299.

[156] F. Neese, *J. Chem. Phys.*, 2001, **115**, 11080.

[157] M. Kleinschmidt, J. Tatchen and C. M. Marian, *J. Chem. Phys.*, 2006, **124**, 124101.

[158] M. J. Klein, *Am. J. Phys.*, 1952, **20**, 65.

[159] H. Bolvin, *ChemPhysChem*, 2006, **7**, 1575.

[160] O. Vahtras, M. Engström and B. Schimmelpfennig, *Chem. Phys. Lett.*, 2002, **351**, 424.

[161] F. Neese, *J. Chem. Phys.*, 2007, **127**, 164112.

[162] F. Neese, *Mol. Phys.*, 2007, **105**, 2507.

[163] E. Malkin, M. Repisky, S. Komorovsky, P. Mach, O. L. Malkina and V. G. Malkin, *J. Chem. Phys.*, 2011, **134**, 044111.

[164] S. A. Rouf, J. Mares and J. Vaara, *J. Chem. Theo. Comput.*, 2017, **13**, 3731.

[165] J. Autschbach, *Sci. Technol. At. Mol. Condens. Matter Biol. Syst.*, 2013, **3**, 69.

[166] T. O. Pennanen and J. Vaara, *J. Chem. Phys.*, 2005, **123**, 174102.

[167] S. A. Rouf, J. Mares and J. Vaara, *J. Chem. Theory Comput.*, 2015, **11**, 1683.

[168] H. Liimatainen, T. O. Pennanen and J. Vaara, *Can. J. Chem.*, 2009, **87**, 954.

[169] M. J. Frisch, G. W. Trucks, H. B. Schlegel, G. E. Scuseria, M. A. Robb, J. R. Cheeseman, G. Scalmani, V. Barone, G. A. Petersson, H. Nakatsuji, X. Li, M. Caricato, A. Marenich, J. Bloino, B. G. Janesko, R. Gomperts, B. Mennucci, H. P. Hratchian, J. V. Ort and D. J. Fox, *Gaussian 09, Revision B.01*, 2010.

[170] K. Wolinski, J. F. Hinton and P. Pulay, *J. Am. Chem. Soc.*, 1990, **112**, 8251.

[171] F. Neese, *WIREs Comput. Mol. Sci.*, 2018, **8**, e1327.

[172] B. A. Heß, *Phys. Rev. A*, 1985, **32**, 756.

[173] G. Jansen and B. A. Hess, *Phys. Rev. A*, 1989, **39**, 6016.

[174] B. Sandhoefer, S. Kossmann and F. Neese, *J. Chem. Phys.*, 2013, **138**, 104102.

[175] D. M. Chipman, *Theor. Chim. Acta*, 1992, **82**, 93.

[176] G. Schreckenbach and T. Ziegler, *J. Phys. Chem. A*, 1997, **101**, 3388.

[177] F. Neese, *J. Chem. Phys.*, 2005, **122**, 034107.

[178] A. V. Luzanov, E. N. Babich and V. V. Ivanov, *J. Mol. Struct.*, 1994, **311**, 211.

[179] L. S. Natrajan, N. M. Khoabane, B. L. Dadds, C. A. Muryn, R. G. Pritchard, S. L. Heath, A. M. Kenwright, I. Kuprov and S. Faulkner, *Inorg. Chem.*, 2010, **49**, 7700.

[180] L. F. Chibotaru and L. Ungur, *Phys. Rev. Lett.*, 2012, **109**, 246403.

[181] Z. Kolarik, U. Mullich and F. Gassner, *Solvent Extr. Ion Exch.*, 1999, **17**, 1155.

[182] S. A. Cotton, *Lanthanide and Actinide Chemistry*, Wiley-Blackwell, Hoboken, NJ, USA, 2nd edn., 2006, p. 263.

[183] W. J. Evans, K. J. Forrestal and J. W. Ziller, *Angew. Chem. Int. Ed.*, 1997, **36**, 774.

[184] C. J. Windorff and W. J. Evans, *Organomet.*, 2014, **33**, 3786.

[185] N. A. Siladke, J. W. Ziller and W. J. Evans, *Zeitschrift fur Anorg. und Allg. Chemie*, 2010, **9**, 3387.

[186] R. J. Kahan, J. H. Farnaby, N. Tsoureas, F. G. N. Cloke, P. B. Hitchcock, M. P. Coles, S. M. Roe and C. Wilson, *J. Organomet. Chem.*, 2018, **857**, 110.

[187] G. M. Clore and J. Iwahara, *Chem. Rev.*, 2009, **109**, 4108.

[188] K. A. Pace, V. V. Klepov, A. A. Berseneva and H.-C. zur Loye, *Chem. — A Eur. J.*, 2021, **27**, 5835.

[189] A. Leoncini, J. Huskens and W. Verboom, *Chem. Soc. Rev.*, 2017, **46**, 7229.

[190] N. Viola-Villegas and R. P. Doyle, *Coord. Chem. Rev.*, 2009, **253**, 1906.

[191] W. A. Volkert and T. J. Hoffman, *Chem. Rev.*, 1999, **99**, 2269.

[192] G. Sgouros, L. Bodei, M. R. McDevitt and J. R. Nedrow, *Nature Rev. Drug Disc.*, 2020, **19**, 589.

[193] A. J. Pell, G. Pintacuda and C. P. Grey, *Prog. Nucl. Mag. Reson. Spectrosc.*, 2018, **111**, 1.

[194] D. Parker, E. A. Suturina, I. Kuprov and N. F. Chilton, *Acc. Chem. Research*, 2020, **53**, 1520.

[195] K. W. H. Stevens, *Proc. Phys. Soc.*, 1952, **65**, 1670.

[196] B. Bleaney, *J. Mag. Res.*, 1972, **8**, 91.

[197] A. M. Funk, K.-L. N. A. Finney, P. Harvey, A. M. Kenwright, E. R. Neil, N. J. Rogers, P. Kanthi Senanayake and D. Parker, *Chem. Sci.*, 2015, **6**, 1655.

[198] R. M. Golding and P. Pyykkö, *Mol. Phys.*, 1973, **26**, 1389.

[199] A. Souza and M. Couto dos Santos, *Chem. Phys. Lett.*, 2012, **521**, 138.

[200] F. Neese, F. Wennmohs, U. Becker and C. Riplinger, *J. Chem. Phys.*, 2020, **152**, 224108.

[201] J. K. M. Sanders and B. K. Hunter, *Modern NMR Spectroscopy: A Guide for Chemists*, Oxford University Press, Oxford, 1993.

[202] A. Steigel, in *NMR Basic Principles and Progress*, ed. P. Diehl, E. Fluck and R. Kosfeld, Springer, Berlin, Germany, 1978.

[203] R. T. Morrision and R. N. Boyd, *Organic Chemistry*, Allyn & Bacon, Boston, Massachusetts., 5th edn., 1983.

[204] J. Tomasi, B. Mennucci and R. Cammi, *Chem. Rev.*, 2005, **105**, 2999.

[205] N. N. Greenwood and A. Earnshaw, *Chemistry of the Elements*, Pergamon Press, Oxford, 2006.

[206] M.-E. Boulon, G. Cucinotta, J. Luzon, C. Degl'Innocenti, M. Perfetti, K. Bernot, G. Calvez, A. Caneschi and R. Sessoli, *Angew. Chem. Internat. Ed.*, 2013, **52**, 350.

[207] R. Coates, *PhD Thesis, Oxidation State Ambiguities in Cerium Organometallics — A Computational Approach*, University College London, 1998.

[208] A. Kerridge and N. Kaltsoyannis, *Comptes Rendus Chimie*, 2010, **13**, 853.

[209] A. Kerridge and N. Kaltsoyannis, *J. Phys. Chem. A*, 2009, **113**, 8737.

[210] M. G. Ferrier, E. R. Batista, J. M. Berg, E. R. Birnbaum, J. N. Cross, J. W. Engle, H. S. La Pierre, S. A. Kozimor, J. S. Lezama Pacheco, B. W. Stein, S. C. E. Stieber and J. J. Wilson, *Nature Commun.*, 2016, **7**, 12312.

[211] World Nuclear Association, *What is Nuclear Waste, and what do we do with it?*, https://world-nuclear.org/nuclear-essentials/what-is-nuclear-waste-and-what-do-we-do-with-it.aspx, accessed January 28, 2022.

[212] N. Edelstein, G. Lamar, F. Mares and A. Streitwieser, *Chem. Phys. Lett.*, 1971, **8**, 399.

[213] W. D. Luke and A. J. Streitwieser, *ACS Symp. Ser.*, 1980, **131**, 1.

[214] D. C. Eisenberg, A. Streitwieser and W. K. Kot, *Inorg. Chem.*, 1990, **29**, 10.

[215] K. H. Claus and C. Krüger, *Acta Cryst. Sec. C*, 1988, **44**, 1632.

[216] A. Y. Sokolov, D. B. Magers, J. I. Wu, W. D. Allen, P. v. R. Schleyer and H. F. Schaefer, *J. Chem. Theo. Computat.*, 2013, **9**, 4436.

[217] F. T. Edelmann, in *Comprehensive Organometallic Chemistry III From Fundamentals to Applications: Complexes of Scandium, Yttrium and Lanthanide Elements*, Elsevier, Oxford, 2006, p. 1.

[218] A. Kerridge, *RSC Adv.*, 2014, **4**, 12078.

[219] A. Streitwieser and U. Mueller-Westerhoff, *J. Am. Chem. Soc.*, 1968, **90**, 7364.

[220] D. G. Karraker, J. A. Stone, E. R. Jones and N. Edelstein, *J. Am. Chem. Soc.*, 1970, **92**, 4841.

[221] D. F. Starks and A. Streitwieser, *J. Am. Chem. Soc.*, 1973, **95**, 3423.

[222] D. F. Starks, T. C. Parsons, A. Streitwieser and N. Edelstein, *Inorg. Chem.*, 1974, **13**, 1307.

[223] A. Streitwieser and S. Kinsley, *NATO ASI Series (Series C: Math. Phys. Sci.)*, 1985, **155**, 1.

[224] S. L. Altmann and P. Herzig, *Point-Group Theory Tables*, University of Vienna, Vienna, 2011.

[225] N. Kaltsoyannis and A. Kerridge, in *Chemical Bonding of Lanthanides and Actinides*, John Wiley & Sons, Ltd, Weinheim, Germany, 2014, ch. 11, p. 337.

[226] R. Ditchfield, *J. Chem. Phys.*, 1972, **56**, 5688.

[227] P. Pulay and T. P. Hamilton, *J. Chem. Phys.*, 1988, **88**, 4926.

[228] A. Kerridge, *Dalton Trans.*, 2013, **42**, 16428.

Appendix A: Supplementary Information for Chapter 4

Table 1. EPR data for [Nd L$^{\mathrm{Py}}$]$^{3+}$. Atom numbering of protons refers to Figure 1 of the main text. Hyperfine values averaged over chemically equivalent atoms.

D/cm^{-1}		-19.830		
(E/D)		0.127		
g_{iso}		-0.938		
Eigenvalues of g		-1.349	-1.290	-0.1740
H$^{(1)}$	A_{iso}/MHz	-0.0079		
	A_{SD}/MHz	-0.1886		
		-0.0041	0.0898	
		-0.0101	-0.0007	0.9880
H$^{(2)}$	A_{iso}/MHz	-0.0248		
	A_{SD}/MHz	-0.4386		
		-0.0172	0.2210	
		-0.0298	0.0020	0.2177
H$^{(3)}$	A_{iso}/MHz	-0.0744		
	A_{SD}/MHz	0.4201		
		0.0485	-0.2463	
		0.1290	0.0469	-0.1737
H$^{(4)}$	A_{iso}/MHz	-0.0190		
	A_{SD}/MHz	-0.0230		
		0.0071	0.0023	
		0.0101	-0.0060	0.0207
H$^{(5)}$	A_{iso}/MHz	0.0219		
	A_{SD}/MHz	-1.6432		
		-0.0743	0.8657	
		-0.1018	0.0118	0.7774
H$^{(6)}$	A_{iso}/MHz	-0.0274		
	A_{SD}/MHz	-0.5400		
		-0.0203	0.2800	
		-0.0325	0.0032	0.2601
H$^{(7)}$	A_{iso}/MHz	-0.0033		
	A_{SD}/MHz	-0.6485		
		-0.0246	0.3262	
		-0.0332	-0.0041	0.3223
H$^{(8)}$	A_{iso}/MHz	-0.1960		
	A_{SD}/MHz	0.3921		
		0.0191	-0.1946	
		0.0273	-0.0010	-0.1974
H$^{(9)}$	A_{iso}/MHz	0.0010		
	A_{SD}/MHz	2.1094		
		0.0866	-1.0539	
		0.1217	0.0043	-1.0555
H$^{(10)}$	A_{iso}/MHz	-0.1548		
	A_{SD}/MHz	0.4669		
		0.0224	-0.2310	
		0.0325	0.0028	-0.2360

Table 2. EPR data for tris(2,6-bis(5,6-dialkyl-1,2,4-triazin-3-yl)pyridine) uranium(III), U(MeBTP)$^{3+}$. Atom numbering of protons refers to Figure 3 of the main text. Hyperfine values averaged over chemically equivalent atoms.

D/cm^{-1}		**20.751**		
(E/D)		**0.219**		
g_{iso}		**-1.182**		
Eigenvalues of g		**-1.027**	**-1.242**	**-1.291**
$\mathrm{H}^{(1)}$	**A_{iso}/MHz**	**0.8704**		
	A_{SD}/MHz	**0.0846**		
		0.0047	**-0.0390**	
		-0.0054	**0.0018**	**-0.0456**
$\mathrm{H}^{(2)}$	**A_{iso}/MHz**	**-0.2220**		
	A_{SD}/MHz	**0.2522**		
		0.0062	**-0.1287**	
		-0.0077	**-0.0027**	**-0.1234**
$\mathrm{H}^{(3)}$	**A_{iso}/MHz**	**-0.3817**		
	A_{SD}/MHz	**-0.4027**		
		0.0011	**0.1810**	
		-0.0012	**-0.0113**	**0.2217**
$\mathrm{H}^{(4)}$	**A_{iso}/MHz**	**-1.1959**		
	A_{SD}/MHz	**-0.5767**		
		-0.0403	**0.2391**	
		0.0402	**-0.0285**	**0.3375**

Table 3. EPR data for tris(pentamethylcyclopentadienyl) uranium (III), U(C$_5$Me$_5$)$_3$. Hyperfine values averaged over chemically equivalent atoms.

D/cm^{-1}		**289.808**						
(E/D)		**0.021**						
g_{iso}		**-0.605**						
Eigenvalues of g		**0.725**	**-1.265**	**-1.276**				
H	**A_{iso}/MHz**	**0.0454**						
	A_{SD}/MHz	**0.0216**						
		-0.0077	**-0.0429**					
		0.0360	**0.0165**	**-0.0644**				
C Ring	**A_{iso}/MHz**	**-0.4868**						
	A_{SD}/MHz	**0.1243**			**A_{PSO}/MHz**	**-0.4864**	**0.1280**	**-0.0726**
		-0.1138	**-0.3193**			**0.0968**	**-0.6695**	**-0.0156**
		-0.0723	**-0.0185**	**-0.4436**		**-0.0725**	**-0.0194**	**0.7318**
C Methyl	**A_{iso}/MHz**	**0.6527**						
	A_{SD}/MHz	**0.0389**			**A_{PSO}/MHz**	**-0.0265**	**0.0012**	**-0.0002**
		0.0003	**0.0398**			**-0.0010**	**-0.0261**	**0.0009**
		0.0004	**-0.0004**	**-0.0787**		**-0.0007**	**0.0010**	**0.0832**

Table 4. EPR data for $\mathrm{U(N(SiMe^{t}Bu_2)_2)_3}$. Hyperfine values averaged over chemically equivalent atoms.

D/cm^{-1}	**-89.051**		
(E/D)	**0.212**		
g_{iso}	**-0.849**		
Eigenvalues of g	**-0.137**	**-0.892**	**-1.888**
A_{iso}/MHz	**-0.9381**		
A_{SD}/MHz	**-0.0477**		
	0.0069	**-0.1151**	
	-0.1508	**-0.0015**	**0.1630**

Table 5. EPR data for Tris(trimethylsilyltetramethylcyclopentadienyl)uranium(lll), $\mathrm{U(C_5Me_4SiMe_3)_3}$. Hyperfine values averaged over chemically equivalent atoms.

D/cm^{-1}	**29.714**		
(E/D)	**0.125**		
g_{iso}	**-0.739**		
Eigenvalues of g	**-0.272**	**-0.676**	**-1.291**
A_{iso}/MHz	**-0.5841**		
A_{SD}/MHz	**0.0385**		
	-0.1520	**0.0928**	
	-0.1803	**-0.0902**	**-0.1313**

Table 6. EPR data for $\mathrm{U(\eta\text{-}C_5Me_4Et)(\eta\text{-}(1,4\text{-}C_8H_6(Si^{i}Pr_3)_2)}$. Hyperfine values averaged over chemically equivalent atoms.

D/cm^{-1}	**-178.253**		
(E/D)	**0.182**		
g_{iso}	**-1.162**		
Eigenvalues of g	**-0.549**	**-0.769**	**-2.172**
A_{iso}/MHz	**-0.4951**		
A_{SD}/MHz	**0.0490**		
	-0.1016	**-0.0799**	
	-0.0646	**-0.1165**	**0.0310**

Appendix B: Supplementary Information for Chapter 5

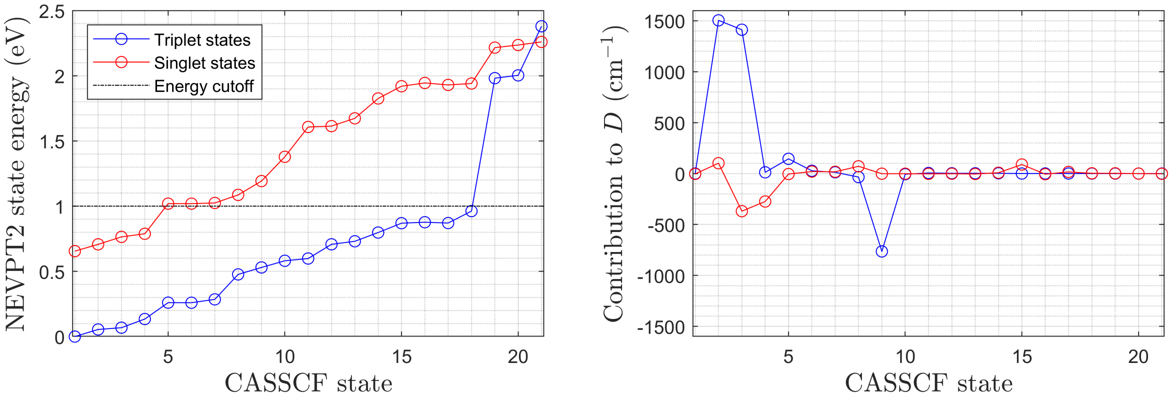

Figure B.1: 18 triplet, 4 singlet SA-NEVPT2 individual state energies (eV from lowest state) for [U(DOTA)H_2O] and their contributions to the ZFS D parameter (SARC/def-TZVP basis).

.

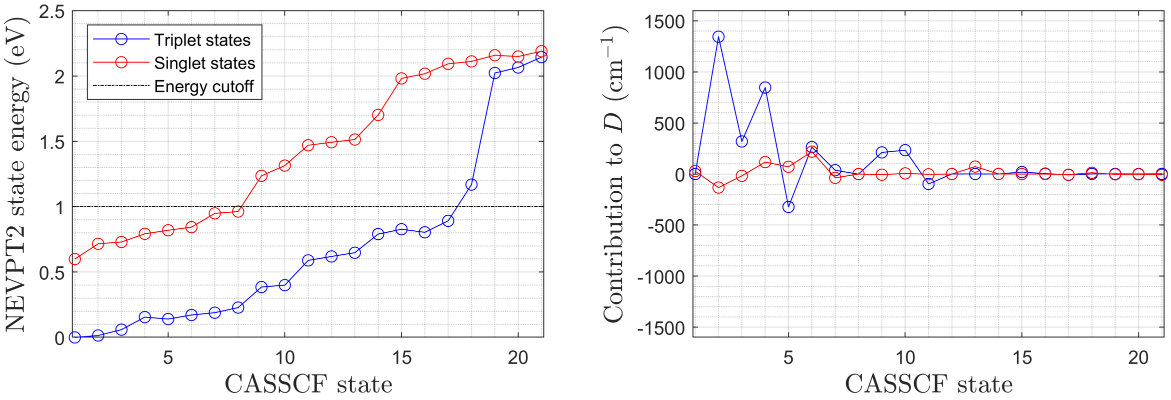

Figure B.2: 17 triplet, 8 singlet SA-NEVPT2 individual state energies (eV from lowest state) for [U(DOTA)OH]$^-$ and their contributions to the ZFS D parameter (SARC/def-TZVP basis).

.

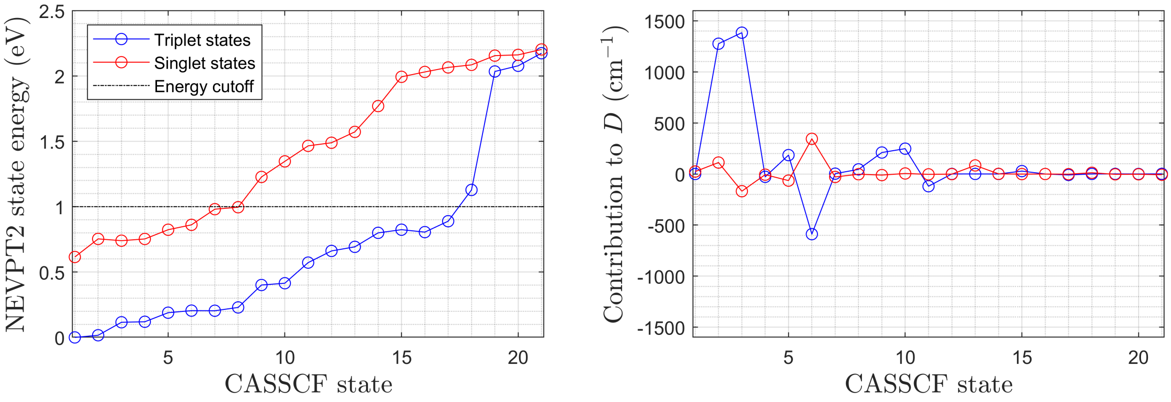

Figure B.3: 17 triplet, 8 singlet SA-NEVPT2 individual state energies (eV from lowest state) for $[U(DOTA)F]^-$ and their contributions to the ZFS D parameter (SARC/def-TZVP basis).

.

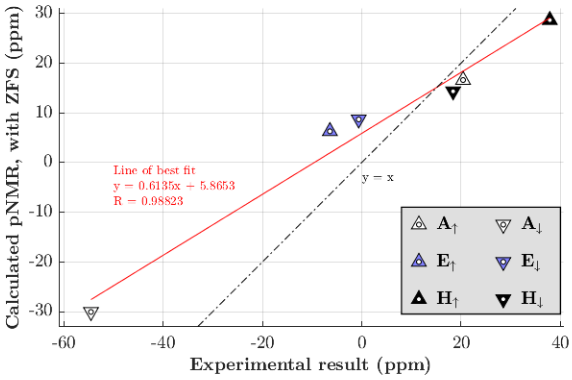

Figure B.4: Calculated ^{1}H pNMR results vs. experimental[3] results for U(DOTA) using $\boldsymbol{\sigma}_{\mathrm{orb}}$ from Th(DOTA). The line of best fit is indicated in red, and the dotted line indicates perfect correspondence. Labelling as in Figure 5.12.

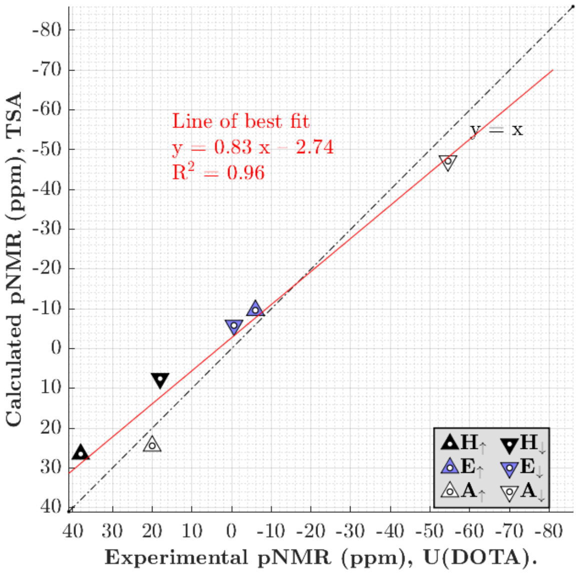

Figure B.5: Calculated ^{1}H pNMR results for TSA conformer vs. experimental[3] results for U(DOTA). The line of best fit is indicated in red, and the dotted line indicates perfect correspondence. Labelling as in Figure 5.12.

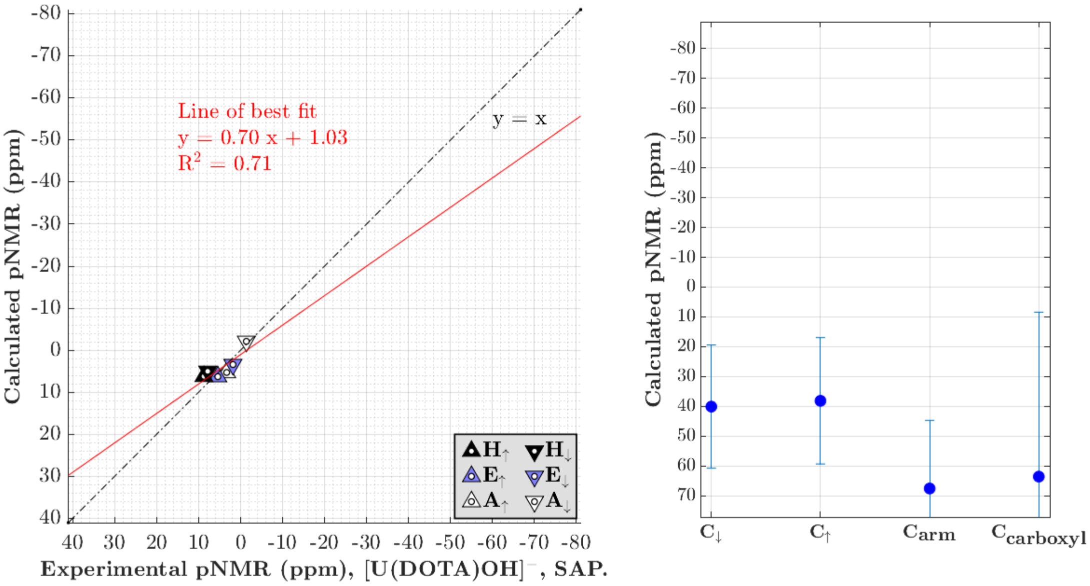

Figure B.6: Calculated ^{1}H pNMR results vs. experimental results for $[U(DOTA)OH]^{-}$. The line of best fit is indicated in red, and the dotted line indicates perfect correspondence.

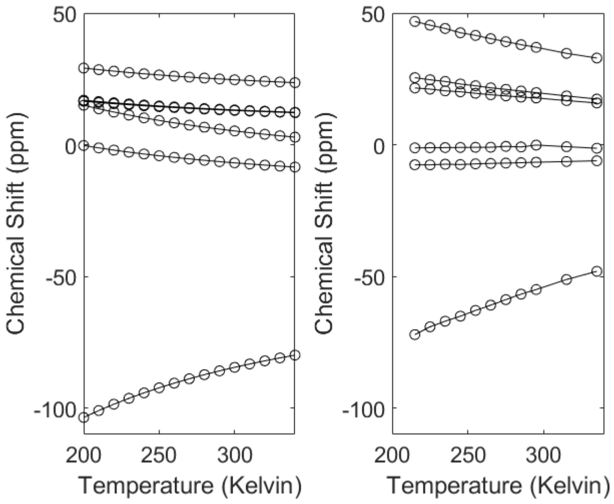

Figure B.7: U(DOTA). Temperature dependence of proton shifts, calculated (right) and experimental (left).

Table B.1: Geometry of U(DOTA)

SAP				TSA			
U	-0.001818	-0.001439	-0.590939	U	4.843922	1.704684	1.807434
N	0.568505	-2.044395	1.071704	N	2.530238	0.999585	2.511674
N	2.052954	0.571406	1.056681	N	3.712394	3.629222	3.000229
N	-0.563167	2.056342	1.056577	N	4.666983	3.690293	0.242712
N	-2.047809	-0.559580	1.072123	N	3.492860	1.092090	-0.244277
O	-2.979972	-3.131542	-1.211890	O	4.070888	-1.216027	4.869891
O	1.723293	-1.231943	-1.247155	O	4.840440	0.570294	3.772208
O	1.224208	1.722476	-1.258198	O	6.681666	4.071985	4.945053
O	-1.730228	1.223471	-1.248691	O	6.299042	2.921519	3.086352
O	-1.231219	-1.731126	-1.236908	O	8.172130	3.301416	-0.402432
O	3.124843	-2.979871	-1.228105	O	6.673057	1.923730	0.468199
O	2.973322	3.122669	-1.255204	O	5.210809	-0.433782	1.099249
O	-3.131064	2.972049	-1.238408	O	5.940485	-1.528566	-0.718740
C	1.197840	-3.038889	0.184705	C	2.725269	-0.320622	3.156817
H	1.737653	-3.814468	0.755175	H	2.767841	-1.032815	2.442775
H	0.402087	-3.525231	-0.399753	H	2.043736	-0.619689	3.648504
C	2.135022	-2.408046	-0.847290	C	1.993703	1.947979	3.543589
C	1.497813	-1.610401	2.125810	H	2.495221	1.706390	4.337491
H	1.977175	-2.490729	2.596344	H	0.865324	1.688428	3.695480
H	0.911622	-1.124508	2.920547	C	2.254558	3.379550	3.186569
C	2.586654	-0.665445	1.649328	H	1.743851	3.520552	2.254869
H	3.216114	-1.162287	0.900130	H	1.989073	3.870811	3.946021
H	3.252064	-0.437051	2.504129	C	4.421482	3.745975	4.288949
C	2.403593	2.134127	-0.868026	H	4.282481	3.062521	4.775938
C	3.041310	1.198921	0.161571	H	4.264017	4.625215	4.619350
H	3.523651	0.402006	-0.424626	C	3.922958	4.909015	2.251737
H	3.820847	1.739806	0.725603	H	4.866073	5.199999	2.474093
C	1.626004	1.503047	2.111599	H	3.227267	5.586182	2.536728
H	2.509524	1.983342	2.575140	C	3.757069	4.738376	0.773545
H	1.145385	0.918738	2.910922	H	3.980336	5.568220	0.360153
C	0.678051	2.591010	1.639092	H	2.822827	4.436614	0.469764
H	1.169730	3.218533	0.884867	C	6.053547	4.200414	0.133100
H	0.455904	3.258528	2.493894	H	6.423908	4.652158	0.829917
C	-1.196994	3.043076	0.164127	H	6.163199	4.768911	-0.626353
H	-1.733817	3.823700	0.730530	C	4.216723	3.260103	-1.100815
H	-0.404237	3.524216	-0.428654	H	5.055868	2.837996	-1.581540
C	-2.139497	2.403345	-0.857494	H	4.012636	3.951640	-1.534564
C	-1.487202	1.631620	2.119103	C	3.090768	2.272193	-1.035048
H	-0.897068	1.152773	2.915207	H	2.740313	1.975820	-1.847740
H	-1.964245	2.516072	2.584223	H	2.290981	2.739205	-0.595035
C	-2.578425	0.682522	1.656487	C	4.387304	0.215544	-1.039745
H	-3.211687	1.172708	0.906111	H	5.000046	0.763385	-1.456270
H	-3.239482	0.461763	2.516658	H	3.927084	-0.224525	-1.565881
C	-2.408324	-2.139530	-0.836572	C	2.285961	0.311641	0.155022
C	-3.040780	-1.195077	0.187824	H	1.662425	0.458031	-0.610694
H	-3.526215	-0.403463	-0.402977	H	2.592457	-0.664594	0.375812
H	-3.817339	-1.730875	0.760746	C	1.613954	0.906183	1.371712
C	-1.615257	-1.481829	2.132998	H	0.872619	0.565803	1.534564
H	-2.496303	-1.958004	2.605409	H	1.196171	1.877029	1.221387
H	-1.130456	-0.890434	2.924544	C	3.963460	-0.338584	4.018052
C	-0.669753	-2.573922	1.665116	C	5.915138	3.584317	4.104175
H	-1.165292	-3.207891	0.918847	C	7.045135	3.056234	0.036015
H	-0.443288	-3.234030	2.524524	C	5.238583	-0.671779	-0.180076

Table B.2: Geometry of [U(DOTA)H_2O]

U	0.000000	0.000000	0.000000
N	-0.209497	2.134615	-1.696036
N	-2.196393	-0.118634	-1.627409
N	0.051013	-2.117855	-1.725451
N	2.049781	0.137295	-1.787873
C	-1.240608	1.904954	-2.716633
C	-2.483075	1.205481	-2.199342
C	-2.000450	-1.102405	-2.701799
C	-1.290801	-2.371731	-2.268808
C	1.007628	-1.878293	-2.815528
C	2.288288	-1.182466	-2.389406
C	1.771773	1.133832	-2.831526
C	1.089473	2.395999	-2.334652
C	-0.588860	3.239597	-0.802048
C	-3.274347	-0.538850	-0.719667
C	0.493574	-3.230461	-0.871160
C	3.184290	0.551741	-0.947566
C	-1.602476	2.833676	0.268646
C	-2.836163	-1.600412	0.289665
C	1.588340	-2.820942	0.115314
C	2.798508	1.620451	0.077445
O	-1.451397	1.601330	0.676073
O	-1.587253	-1.476318	0.647785
O	1.456730	-1.587864	0.528009
O	1.574586	1.478967	0.512615
O	-2.418637	3.619014	0.685162
O	-3.615034	-2.422220	0.707916
O	2.446921	-3.595649	0.456377
O	3.578980	2.473601	0.419312
H	-0.794753	1.309421	-3.527434
H	-1.543109	2.866059	-3.176759
H	-3.213575	1.126484	-3.027949
H	-2.966943	1.817229	-1.427360
H	-1.427012	-0.619989	-3.507406
H	-2.976460	-1.378610	-3.146833
H	-1.242676	-3.059286	-3.135703
H	-1.879891	-2.892348	-1.503171
H	0.504139	-1.276678	-3.587141
H	1.274740	-2.835859	-3.304054
H	2.951022	-1.099818	-3.272912
H	2.830758	-1.799710	-1.661991
H	1.144670	0.658268	-3.600652
H	2.711603	1.422292	-3.342028
H	0.973713	3.089029	-3.190682
H	1.731884	2.914373	-1.611968
H	-0.971771	4.110419	-1.362464
H	0.309500	3.550243	-0.247276
H	-4.163317	-0.893655	-1.270178
H	-3.567398	0.333075	-0.115256
H	0.832248	-4.097853	-1.464484
H	-0.360135	-3.544613	-0.251714
H	4.038035	0.905819	-1.551572
H	3.509336	-0.320198	-0.359598
O	-0.199962	0.007842	2.497951
H	-0.790985	0.765561	2.633880
H	-0.740608	-0.773507	2.689482

Table B.3: Geometry of $[U(DOTA)OH]^-$

U	0.000000	0.000000	0.000000
N	-0.847288	-1.954069	1.984299
N	-1.968398	0.849416	1.998631
N	0.852808	1.954328	1.983288
N	1.973965	-0.849526	1.994577
C	-1.685475	-1.389942	3.040049
C	-2.644479	-0.301319	2.590933
C	-1.387751	1.693230	3.039373
C	-0.296922	2.640335	2.569102
C	1.693193	1.389807	3.036916
C	2.651174	0.301222	2.585711
C	1.395432	-1.693736	3.036176
C	0.303592	-2.640653	2.567691
C	-1.617220	-2.853905	1.122995
C	-2.873975	1.612572	1.139828
C	1.620127	2.854248	1.120060
C	2.878111	-1.612281	1.133947
C	-2.570900	-2.101392	0.185896
C	-2.124505	2.543212	0.181897
C	2.569974	2.102360	0.178536
C	2.127042	-2.541903	0.176411
O	-2.074573	-1.011014	-0.280454
O	-1.043818	2.020458	-0.288257
O	2.071537	1.012476	-0.286536
O	1.044039	-2.019876	-0.289411
O	-3.676103	-2.558494	-0.047876
O	-2.566527	3.647282	-0.074990
O	3.674990	2.558597	-0.058033
O	2.565205	-3.648254	-0.077054
H	-1.025296	-0.985907	3.822895
H	-2.277367	-2.193053	3.529157
H	-3.252774	0.002082	3.470128
H	-3.355327	-0.704069	1.859185
H	-0.980554	1.038202	3.824895
H	-2.180300	2.297095	3.531624
H	0.012361	3.262171	3.436524
H	-0.699916	3.341269	1.827936
H	1.034597	0.985769	3.821116
H	2.286381	2.192610	3.525059
H	3.261372	-0.002392	3.463498
H	3.360481	0.704077	1.852533
H	0.989891	-1.039073	3.822876
H	2.188921	-2.297931	3.526467
H	-0.004438	-3.262677	3.435387
H	0.704959	-3.341365	1.825463
H	-2.191688	-3.594924	1.711423
H	-0.905014	-3.388065	0.475283
H	-3.604962	2.201111	1.727270
H	-3.417115	0.894998	0.505641
H	2.197214	3.594712	1.706717
H	0.905734	3.389051	0.475316
H	3.609957	-2.201213	1.719943
H	3.420442	-0.894583	0.499212
O	-0.010643	-0.005154	-2.036829
H	-0.052840	-0.015506	-2.988644

Table B.4: Geometry of $[U(DOTA)F]^-$

U	0.000000	0.000000	0.000000
N	-0.142886	2.154488	-1.948747
N	-2.155633	-0.106961	-1.920088
N	0.081676	-2.127874	-1.981325
N	2.095459	0.132501	-1.986507
C	-1.152740	1.912528	-2.976765
C	-2.411855	1.214067	-2.492433
C	-1.936887	-1.083336	-2.986141
C	-1.241313	-2.362547	-2.555062
C	1.058700	-1.873054	-3.037535
C	2.332743	-1.180668	-2.584334
C	1.842373	1.123244	-3.031474
C	1.161526	2.396449	-2.560852
C	-0.531466	3.260309	-1.072072
C	-3.250578	-0.522753	-1.039683
C	0.497765	-3.244680	-1.131460
C	3.218015	0.536764	-1.136196
C	-1.646483	2.864982	-0.100180
C	-2.852398	-1.680834	-0.115603
C	1.643555	-2.861589	-0.190921
C	2.849255	1.680853	-0.183052
O	-1.511393	1.664808	0.358114
O	-1.650744	-1.580657	0.336126
O	1.523892	-1.667261	0.286434
O	1.662407	1.573019	0.304662
O	-2.535912	3.646837	0.172150
O	-3.647455	-2.571597	0.121062
O	2.540866	-3.646923	0.042925
O	3.650974	2.568708	0.041551
H	-0.691918	1.309399	-3.773968
H	-1.450430	2.869669	-3.455884
H	-3.115490	1.144538	-3.349131
H	-2.919062	1.828889	-1.738917
H	-1.341900	-0.599773	-3.776003
H	-2.903927	-1.356084	-3.459661
H	-1.179703	-3.033562	-3.438272
H	-1.853843	-2.894162	-1.816656
H	0.573210	-1.260609	-3.812716
H	1.341063	-2.824244	-3.537336
H	3.008870	-1.099878	-3.461961
H	2.863264	-1.805474	-1.855443
H	1.222008	0.650420	-3.808196
H	2.793588	1.402718	-3.532414
H	1.072383	3.079664	-3.432294
H	1.797483	2.917714	-1.834936
H	-0.842067	4.154488	-1.645637
H	0.339756	3.516713	-0.449685
H	-4.154222	-0.804781	-1.612892
H	-3.494846	0.326880	-0.383634
H	0.789612	-4.131504	-1.725919
H	-0.353147	-3.508966	-0.484793
H	4.102538	0.827973	-1.734137
H	3.483889	-0.321841	-0.500571
F	0.032130	-0.015450	2.042523

Table B.5: U(DOTA) Löwdin atomic charges and spin densities from a 18 triplet, 4 singlet SA-NEVPT2 calculation. Labelling as in Figure 5.12.

	Atomic charge	Spin density	C	Atomic charge	Spin density	H	Atomic charge	Spin density
U	0.1672	1.599327	$C_{\uparrow}$	-0.2227	0.000221	$A_{\uparrow}$	0.1553	0.000006
O[†]	0.0294	0.005396	$C_{\downarrow}$	-0.2315	0.000237	$A_{\downarrow}$	0.1311	0.000012
O	0.0386	0.001402	C_{arm}	-0.1767	0.000284	$E_{\uparrow}$	0.1366	0.000025
N	0.1341	0.000356	$C_{carboxyl}$	-0.4796	0.001253	$E_{\downarrow}$	0.1389	0.000032
						$H_{\uparrow}$	0.1661	0.000014
						$H_{\downarrow}$	0.1388	0.000020

[†] DOTA ligand.

Table B.6: [U(DOTA)H_2O] Löwdin atomic charges and spin densities from a 17 triplet, 8 singlet SA-NEVPT2 calculation. Labelling as in Figure 5.12.

	Atomic charge	Spin density	C	Atomic charge	Spin density	H	Atomic charge	Spin density
U	-0.0219	1.599328	$C_{\uparrow}$	-0.2332	0.000228	$A_{\uparrow}$	0.1543	0.000007
O[†]	0.0209	0.005112	$C_{\downarrow}$	-0.2252	0.000204	$A_{\downarrow}$	0.1306	0.000013
O	0.0309	0.000356	C_{arm}	-0.1807	0.000283	$E_{\uparrow}$	0.1356	0.000023
N	0.1135	0.001297	$C_{carboxyl}$	-0.4866	0.001226	$E_{\downarrow}$	0.1378	0.000029
O[‡]	-0.0837	0.001420				$H_{\uparrow}$	0.1649	0.000016
H[‡]	0.2105	0.000180				$H_{\downarrow}$	0.1382	0.000022

[†] DOTA ligand, [‡] axial ligand.

Table B.7: $[\mathrm{U(DOTA)OH}]^-$ Löwdin atomic charges and spin densities from a 17 triplet, 8 singlet SA-NEVPT2 calculation. Labelling as in Figure 5.12.

	Atomic charge	Spin density	C	Atomic charge	Spin density	H	Atomic charge	Spin density
U	0.0376	1.329279	$\mathrm{C}_{\uparrow}$	-0.2398	0.000131	$\mathrm{A}_{\uparrow}$	0.1526	0.000005
$\mathrm{O}^{\dagger}$	0.0389	0.003260	$\mathrm{C}_{\downarrow}$	-0.2452	0.000140	$\mathrm{A}_{\downarrow}$	0.1247	0.000004
O	-0.0265	0.000235	C_{arm}	-0.5086	0.000199	$\mathrm{E}_{\uparrow}$	0.1237	0.000016
N	0.1279	0.000924	$\mathrm{C}_{carboxyl}$	0.0389	0.000843	$\mathrm{E}_{\downarrow}$	0.1272	0.000019
$\mathrm{O}^{\ddagger}$	-0.2540	0.006934				$\mathrm{H}_{\uparrow}$	0.1611	0.000013
$\mathrm{H}^{\ddagger}$	0.1584	0.000550				$\mathrm{H}_{\downarrow}$	0.1254	0.000020

† DOTA ligand, ‡ axial ligand.

Table B.8:]

$[\mathrm{U(DOTA)F}]^-$ Löwdin atomic charges and spin densities from a 17 triplet, 8 singlet SA-NEVPT2 calculation. Labelling as in Figure 5.12.

	Atomic charge	Spin density	C	Atomic charge	Spin density	H	Atomic charge	Spin density
U	0.0929	1.330255	$\mathrm{C}_{\uparrow}$	-0.2384	0.000131	$\mathrm{A}_{\uparrow}$	0.1531	0.000005
$\mathrm{O}^{\dagger}$	0.0388	0.003439	$\mathrm{C}_{\downarrow}$	-0.2441	0.000141	$\mathrm{A}_{\downarrow}$	0.1251	0.000005
O	-0.0190	0.000245	C_{arm}	-0.5040	0.000203	$\mathrm{E}_{\uparrow}$	0.1247	0.000015
N	0.1284	0.000917	$\mathrm{C}_{carboxyl}$	0.0388	0.000878	$\mathrm{E}_{\downarrow}$	0.1281	0.000018
F	-0.2382	0.005628				$\mathrm{H}_{\uparrow}$	0.1619	0.000014
						$\mathrm{H}_{\downarrow}$	0.1263	0.000020

† DOTA ligand.

Table B.9: Calculated pNMR shifts (ppm) for U(DOTA).

^{1}H results	$A_\uparrow$	$A_\downarrow$	$E_\uparrow$	$E_\downarrow$	$H_\uparrow$	$H_\downarrow$
Orbital shielding, σ_{orb}	25.34	36.84	30.61	30.88	21.37	26.07
$\tilde{S} = 1$						
Contact term, σ_c	−12.74	37.04	−7.10	−7.68	−19.93	−8.10
Pseudocontact term, σ_pc	−0.31	0.71	0.21	0.44	0.72	−0.82
Total shielding	12.29	74.60	23.71	23.64	2.16	17.14
Predicted shift†	19.29	−43.02	7.87	7.94	29.42	14.44
$\tilde{S} = 3/2$						
Contact term, σ_c	26.15	76.07	−14.60	−15.78	−40.92	−16.64
Pseudocontact term, σ_pc	−0.60	1.34	0.40	0.83	1.37	−1.56
Total shielding	−1.41	114.25	16.41	15.93	−18.18	7.87
Predicted shift†	32.99	−82.67	15.17	15.65	49.76	23.71
ITO Method						
Pseudocontact term, σ_pc	−15.85	48.21	−9.97	−11.36	−28.46	−9.05
Total shielding	9.49	85.05	20.64	19.52	−2.39	12.32
Predicted shift†	22.09	−53.47	10.94	12.06	38.67	14.56
Experimental shift	20.00	−54.50	−6.00	−0.60	38.00	18.00

†Shift from TMS reference.

^{13}C results	$C_\uparrow$	$C_\downarrow$	C_{arm}	$C_{carboxyl}$
Orbital shielding, σ_{orb}	136.51	130.34	106.96	0.39
$\tilde{S} = 1$				
Contact term, σ_c	87.82	64.43	−29.29	205.98
Pseudocontact term, σ_pc	0.28	1.39	1.50	−10.96
Total shielding	224.61	196.16	79.17	195.41
Predicted shift†	193.03	−164.58	−47.59	−163.83
$\tilde{S} = 3/2$				
Contact term, σ_c	180.30	132.25	−60.15	422.91
Pseudocontact term, σ_pc	0.56	2.66	2.86	−20.61
Total shielding	317.37	265.25	49.67	402.68
Predicted shift†	−128.34	−76.22	139.36	−213.65

†Shift from TMS reference.

Table B.10: Calculated pNMR shifts (ppm) for [U(DOTA)H_2O].

^{1}H results	$A_\uparrow$	$A_\downarrow$	$E_\uparrow$	$E_\downarrow$	$H_\uparrow$	$H_\downarrow$
Orbital shielding, σ_{orb}	25.89	35.81	30.87	30.59	22.32	35.55
$\tilde{S} = 1$						
Contact term, σ_c	−21.14	64.79	−13.90	−14.70	−34.27	−12.93
Pseudocontact term, σ_pc	−2.00	6.26	1.67	1.04	−1.97	−2.58
Total shielding	2.75	106.86	18.64	16.93	−13.92	11.04
Predicted shift†	28.83	−75.28	12.94	14.65	45.50	20.54
$\tilde{S} = 3/2$						
Contact term, σ_c	−26.15	76.07	−14.60	−15.78	−40.92	−16.64
Pseudocontact term, σ_pc	−0.60	1.34	0.40	0.83	1.37	−1.56
Total shielding	−1.41	114.25	16.41	15.93	−18.18	7.87
Predicted shift†	32.99	−82.67	15.17	15.65	49.76	23.71
Experimental shift	21.70	−56.70	−5.80	0.70	38.40	19.30

†Shift from TMS reference.

Table B.11: Calculated pNMR shifts (ppm) for [U(DOTA)OH]$^-$.

^{1}H results	$A_\uparrow$	$A_\downarrow$	$E_\uparrow$	$E_\downarrow$	$H_\uparrow$	$H_\downarrow$
Orbital shielding, σ_{orb}	28.59	26.31	29.33	29.22	33.00	29.75
$\tilde{S} = 1$						
Contact term, σ_{c}	0.92	−5.10	−7.14	−4.70	4.86	−0.08
Pseudocontact term, σ_{pc}	−3.23	12.47	3.11	3.65	−9.49	−3.11
Total shielding	26.29	33.69	25.30	28.18	25.37	26.56
Predicted shift†	5.29	−2.11	6.28	3.40	6.21	5.02
$\tilde{S} = 3/2$						
Contact term, σ_{c}	2.09	−11.56	−16.20	−10.66	11.02	−0.18
Pseudocontact term, σ_{pc}	−7.64	29.42	7.32	8.60	−22.54	−7.33
Total shielding	23.04	44.16	−8.88	27.16	18.48	22.24
Predicted shift†	8.54	−12.58	40.46	4.42	13.10	9.34
Experimental shift	3.30	−1.40	5.40	1.80	8.70	7.80

†Shift from TMS reference.

Table B.12: Calculated pNMR shifts (ppm) for [U(DOTA)F]$^-$.

^{1}H results	$A_\uparrow$	$A_\downarrow$	$E_\uparrow$	$E_\downarrow$	$H_\uparrow$	$H_\downarrow$
Orbital shielding, σ_{orb}	29.43	26.81	28.50	29.35	29.44	29.61
$\tilde{S} = 1$						
Contact term, σ_{c}	−4.86	−2.74	0.34	−4.56	4.93	−1.18
Pseudocontact term, σ_{pc}	2.28	9.79	−2.41	2.70	−7.75	−2.34
Total shielding	26.85	33.86	26.43	27.49	26.63	26.10
Predicted shift†	4.73	−2.28	5.15	4.09	4.95	5.48
$\tilde{S} = 2$						
Contact term, σ_{c}	−17.99	−10.15	1.24	16.90	18.26	−4.36
Pseudocontact term, σ_{pc}	8.45	36.10	−8.96	10.00	28.42	−8.63
Total shielding	19.89	52.76	20.78	22.45	19.28	16.63
Predicted shift†	11.69	−21.18	10.80	9.13	12.30	14.95
Experimental shift	10.02	−22.00	4.4	1.8	9.9	16.60

^{13}C results	$C_\uparrow$	$C_\downarrow$	C_{arm}	$C_{carboxyl}$
Orbital shielding, σ_{orb}	128.96	127.64	116.43	8.60
$\tilde{S} = 1$				
Contact term, σ_{c}	11.53	14.90	3.04	88.53
Pseudocontact term, σ_{pc}	6.95	5.26	−5.72	−16.21
Total shielding	147.44	147.80	113.75	80.92
Predicted shift†	41.59	41.23	75.28	108.11
$\tilde{S} = 2$				
Contact term, σ_{c}	42.70	55.19	11.24	327.82
Pseudocontact term, σ_{pc}	25.77	19.50	−21.19	−54.77
Total shielding	197.43	202.33	106.48	281.65
Predicted shift†	−8.40	−13.30	82.55	−92.62

†Shift from TMS reference.

Appendix C: Supplementary Information for Chapter 6

These are provisional results for the DFT/aZORA optimised geometries, with the original state averaging based on CASSCF (1 eV state averaging, 2 eV included in the Zeeman/ZFS calculation). NEVPT2 analogues with a more conservative scheme is progressing.

Table C.1: Geometrical parameters for the neutral and anionic actinocenes M(COT)$_2$ and [M(COT)$_2$]$^-$, showing the centroid-metal distance, r_{MX}, the centroid-carbon distance r_{XC}, the centroid-hydrogen distance, r_{XH}, and the metal-centroid-hydrogen angle A_{MXH}. Distances are in Angstrom, angles are in degrees.

	Neutral				Anion			
M	r_{MX}	r_{XC}	r_{XH}	A_{MXH}	r_{MX}	r_{XC}	r_{XH}	A_{MXH}
Nd	1.9637	1.8436	2.9347	178.38	1.9959	1.8452	2.9372	178.18
Pm	1.9297	1.8429	2.9342	178.41	1.9770	1.8444	2.9362	178.10
Sm	1.9397	1.8431	2.9347	178.53	1.9656	1.8441	2.9357	178.03
Eu	1.9386	1.8437	2.9354	178.57	1.9786	1.8447	2.9367	178.16
Gd	1.9047	1.8448	2.9358	178.39	1.9376	1.8453	2.9364	177.89
U	1.9240†	1.8422	2.9304	177.53	1.9980‡	1.8458	2.9364	177.77
Np	1.8900†	1.8412	2.9291	177.43	1.9486	1.8464	2.9375	177.89
Pu	1.8581	1.8423	2.9306	177.55	1.9290	1.8453	2.9364	177.86
Am	1.8578	1.8428	2.9321	177.79	1.9521	1.8457	2.9371	177.97
Cm	1.8982	1.8452	2.9354	178.14	1.9622	1.8466	2.9379	178.00

† Partial optimisation with experimental ring separation.

‡ Partial optimisation with NEVPT2 ring separation.

Table C.2: Metallocene Z-matrix. Parameters as in Table C1.

M							Constants	
X1	1	0.1					ninety	90.0
X2	1	rUX	2	ninety			a0	0.0
X3	1	rUX	2	ninety	3	line	a1	45.0
C	3	rXC	1	ninety	2	a1	a2	90.0
C	3	rXC	1	ninety	2	a3	a3	135.0
C	3	rXC	1	ninety	2	a4	a4	180.0
C	3	rXC	1	ninety	2	a5	a5	225.0
C	3	rXC	1	ninety	2	a6	a6	270.0
C	3	rXC	1	ninety	2	a7	a7	315.0
H	3	rXH	1	aXCH	2	a0	line	180.0
H	3	rXH	1	aXCH	2	a1		
H	3	rXH	1	aXCH	2	a2	Variables	
H	3	rXH	1	aXCH	2	a3	rUX	Distance metal to centroid, X2, X3
H	3	rXH	1	aXCH	2	a4	rXC	Distance centroid to carbon atom
H	3	rXH	1	aXCH	2	a5	rXH	Distance centroid to hydrogen atom
H	3	rXH	1	aXCH	2	a6	aXCH	Angle metal-centroid-hydrogen
H	3	rXH	1	aXCH	2	a7		
C	4	rXC	1	ninety	2	a0		
C	4	rXC	1	ninety	2	a1		
C	4	rXC	1	ninety	2	a2		
C	4	rXC	1	ninety	2	a3		
C	4	rXC	1	ninety	2	a4		
C	4	rXC	1	ninety	2	a5		
C	4	rXC	1	ninety	2	a6		
C	4	rXC	1	ninety	2	a7		
H	4	rXH	1	aXCH	2	a0		
H	4	rXH	1	aXCH	2	a1		
H	4	rXH	1	aXCH	2	a2		
H	4	rXH	1	aXCH	2	a3		
H	4	rXH	1	aXCH	2	a4		
H	4	rXH	1	aXCH	2	a5		
H	4	rXH	1	aXCH	2	a6		
H	4	rXH	1	aXCH	2	a7		

Figure A1. Lowest CASSCF(x,13) states by irrep. of the neutral lanthanocenes and actinocenes (individually state optimised).

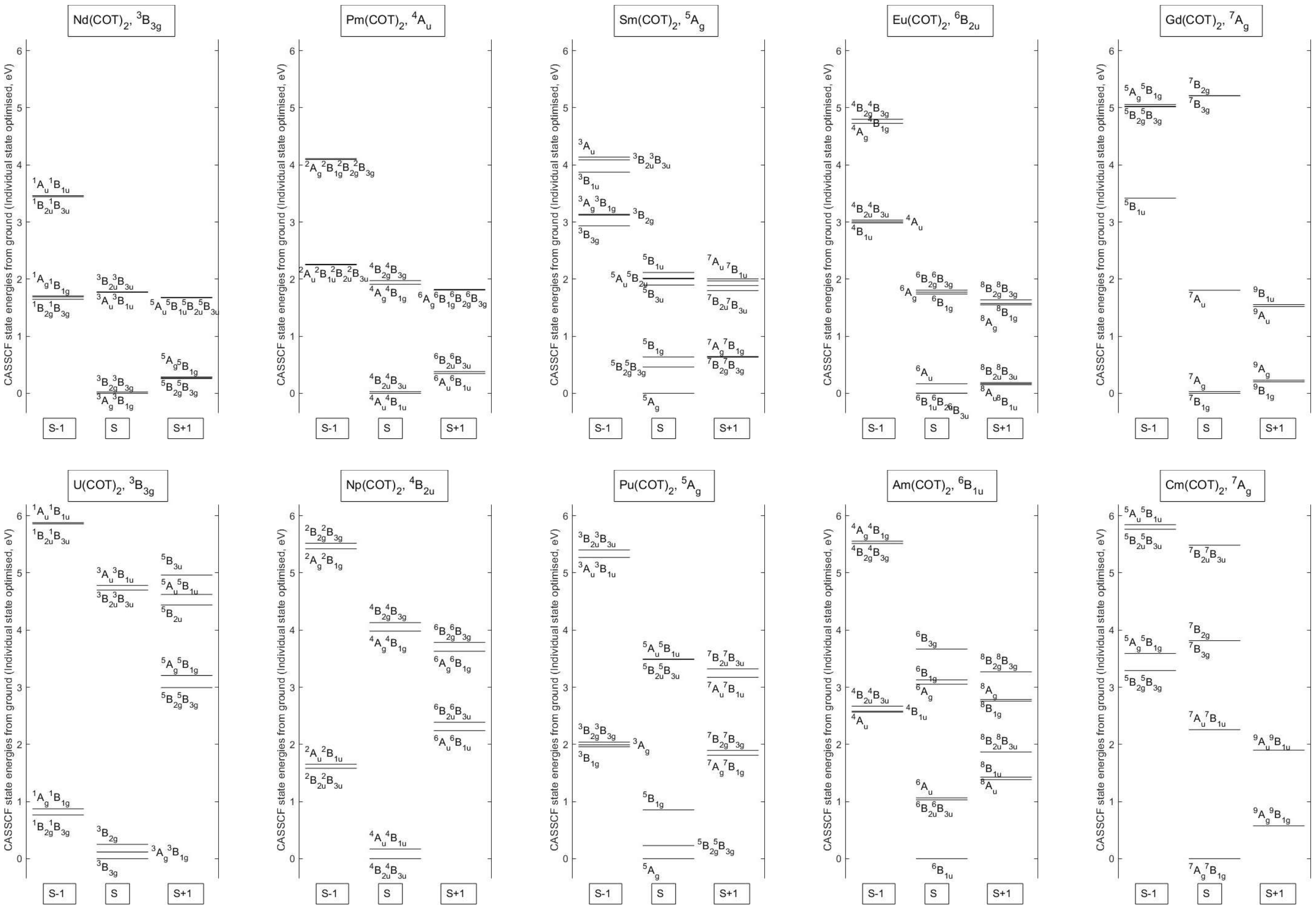

Figure A2. Lowest CASSCF(x,13) states by irrep. of the anionic lanthanocenes and actinocenes (individually state optimised).

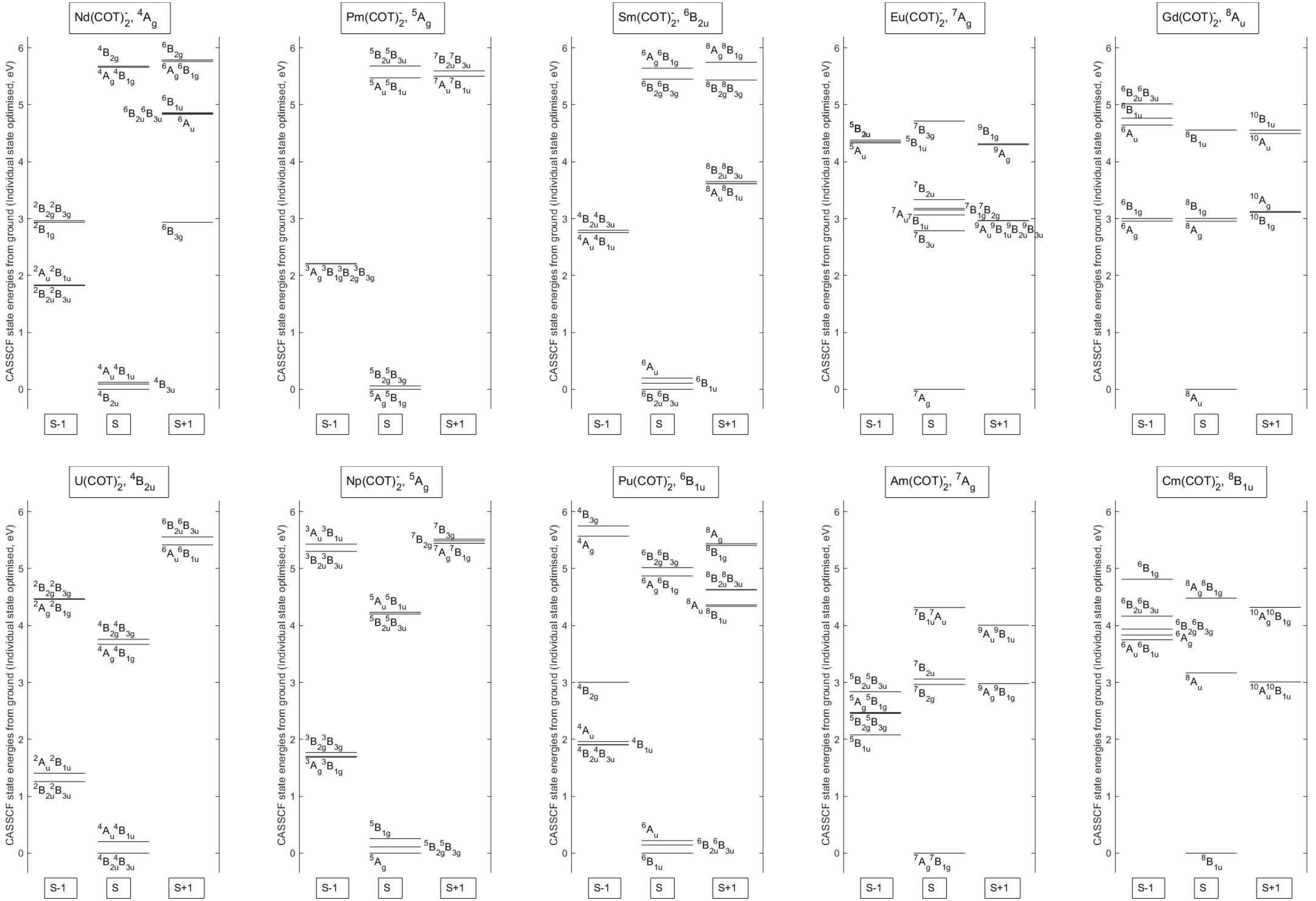

Figure A3. CASSCF(X,13) energies for neutral species, optimised to the lowest energy state of the stated irrep. SA line indicates the state averaging used to generate the spin free states for the final SOC calculation chosen by a cut-off of 2eV (red dotted line).

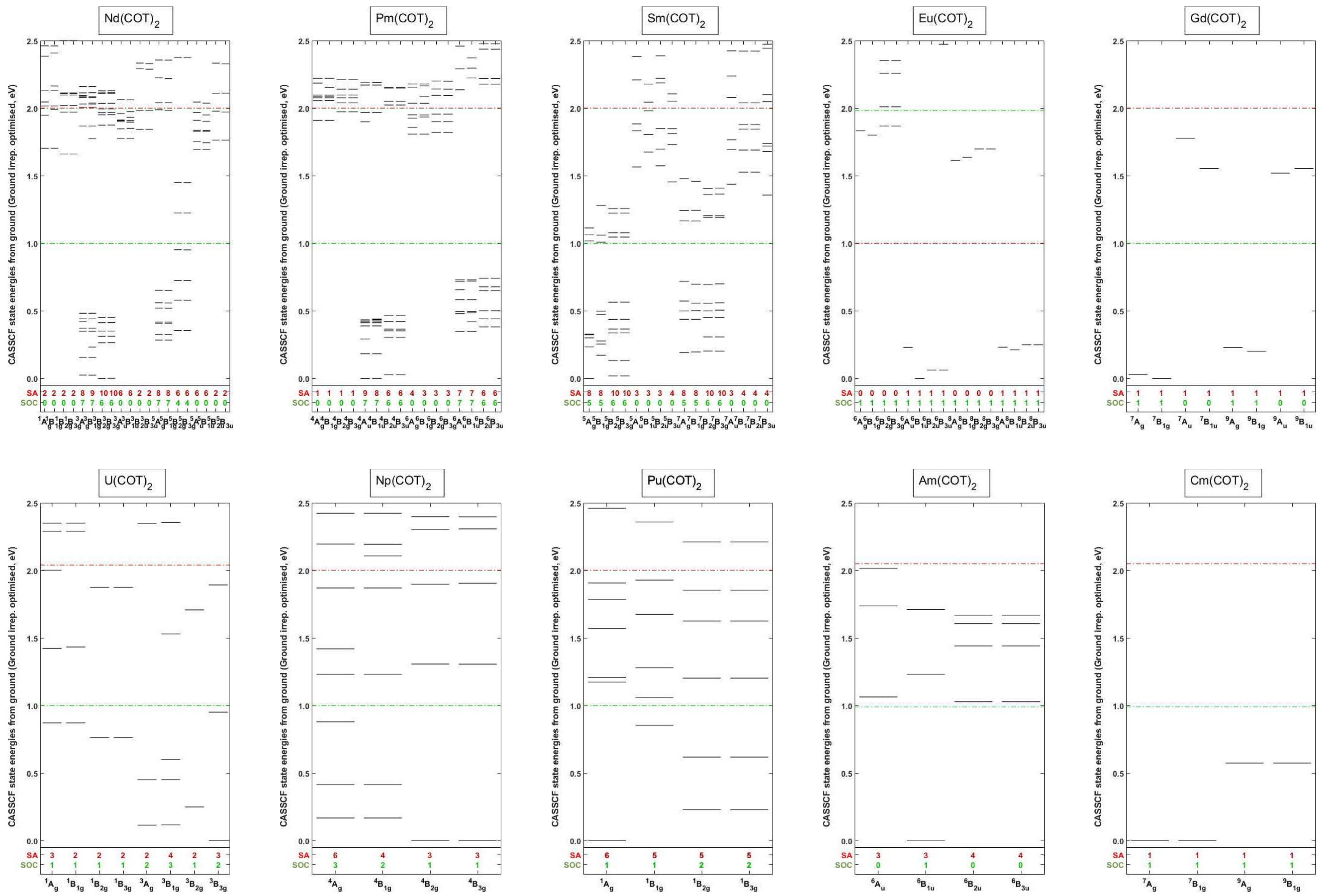

Figure A5. Canonical orbital energies of the neutral lanthanocenes and actinocenes.

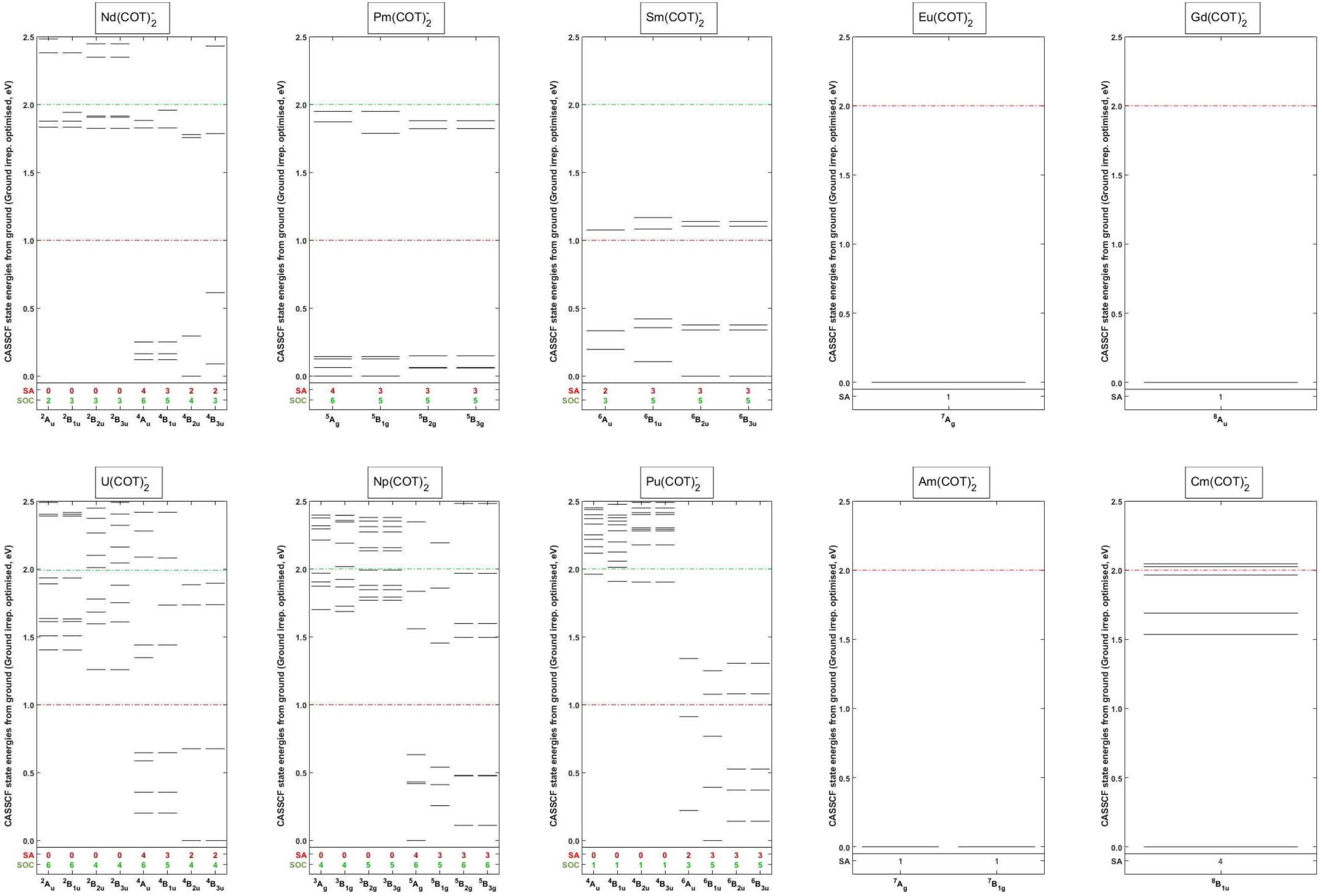

Figure A7. Canonical orbital occupations of the neutral lanthanocenes and actinocenes.

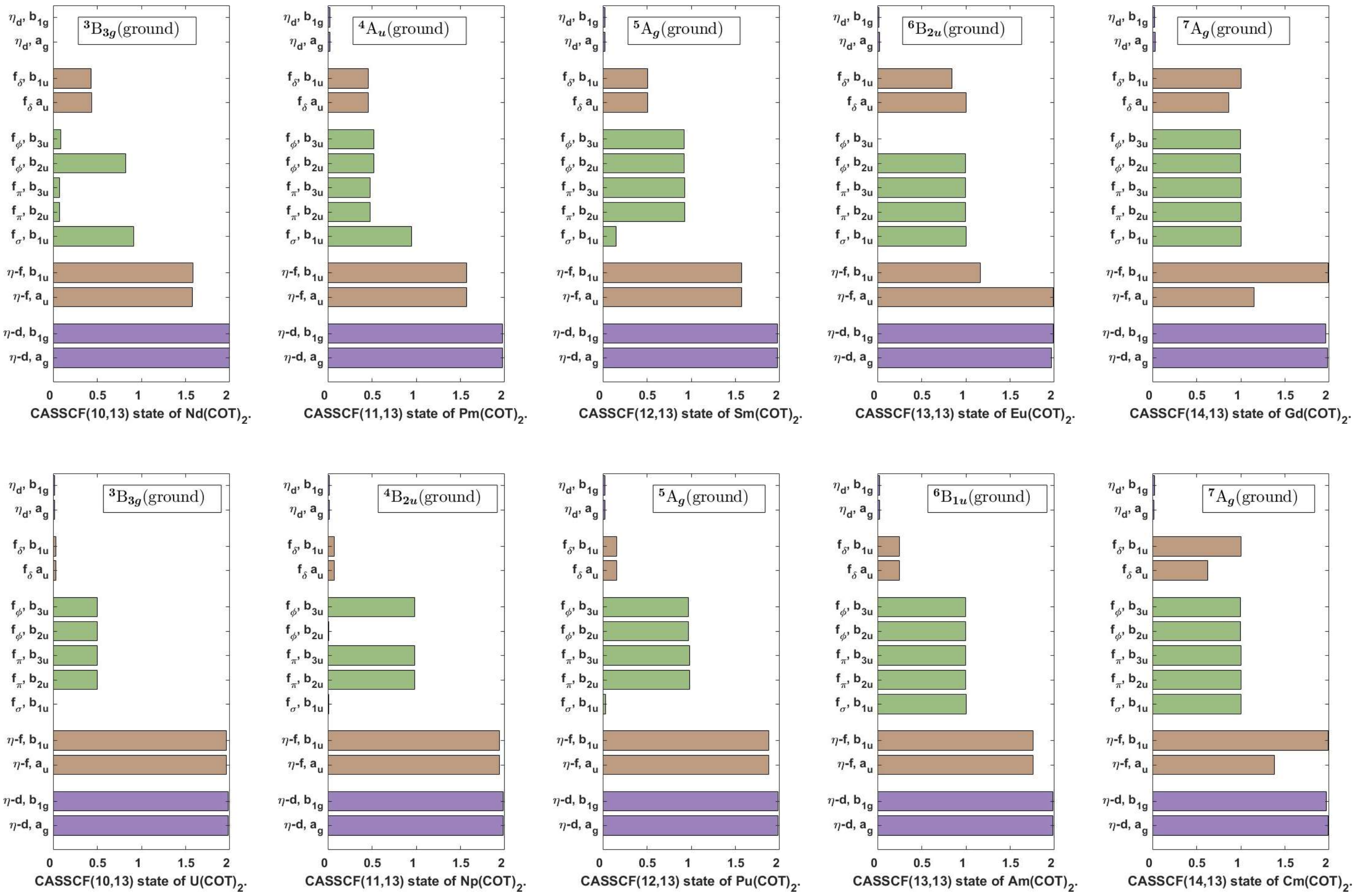

Figure A8. Canonical orbital occupations of the anionic lanthanocenes and actinocenes.

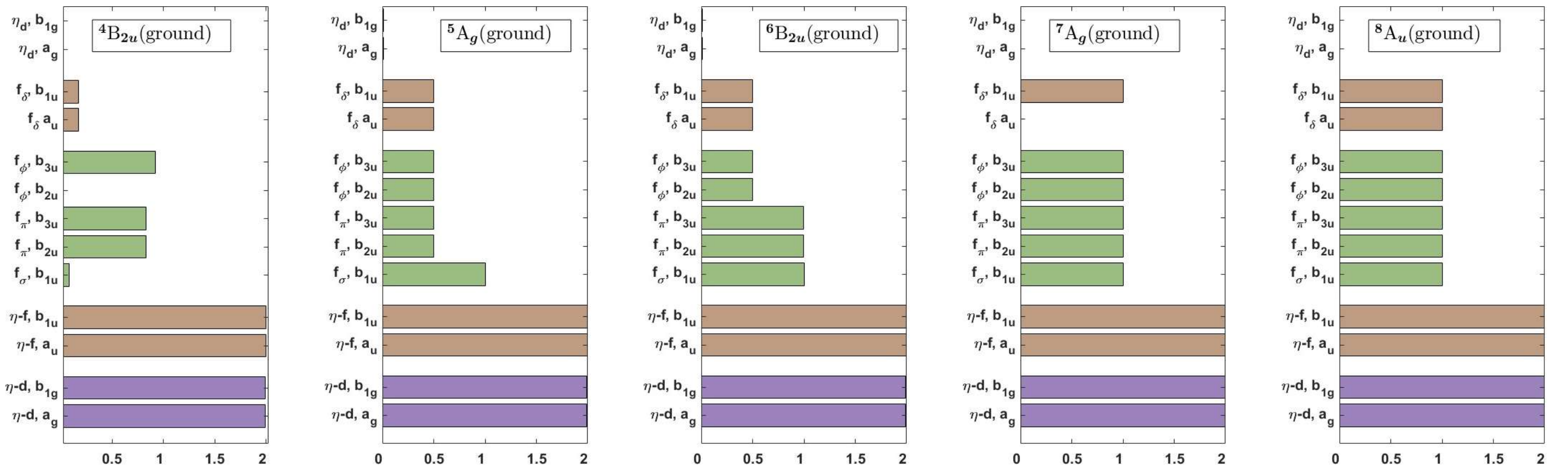

CASSCF(11,13) state of Nd(COT)$_2^-$. CASSCF(12,13) state of Pm(COT)$_2^-$. CASSCF(13,13) state of Sm(COT)$_2^-$. CASSCF(14,13) state of Eu(COT)$_2^-$. CASSCF(15,13) state of Gd(COT)$_2^-$.

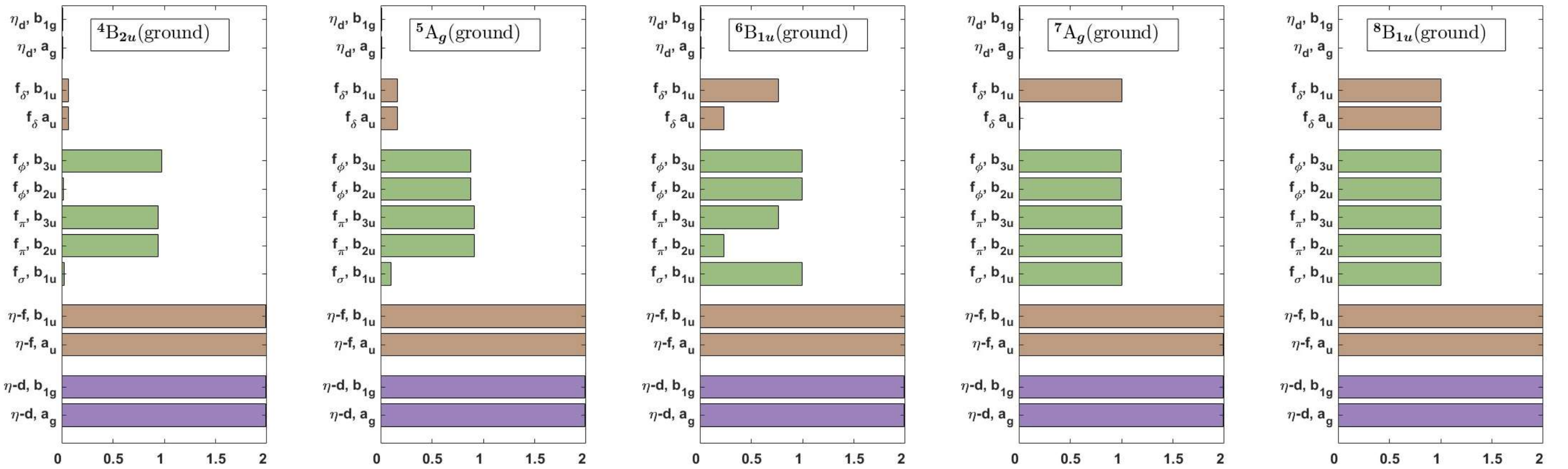

CASSCF(11,13) state of U(COT)$_2^-$. CASSCF(12,13) state of Np(COT)$_2^-$. CASSCF(13,13) state of Pu(COT)$_2^-$. CASSCF(14,13) state of Am(COT)$_2^-$. CASSCF(15,13) state of Cm(COT)$_2^-$.

Table C.3: Character table for point group D_{2h}.

D_{2h}	E	C_2(z)	C_{2h}(y)	C_{2h}(x)	i	σ_{xy}	σ_{xz}	σ_{yz}	Function order 1	 2	 3
A_g	+1	+1	+1	+1	+1	+1	+1	+1	-	x^2, y^2, z^2	-
B_{1g}	+1	+1	-1	-1	+1	+1	-1	-1	R_z	xy	-
B_{2g}	+1	-1	+1	-1	+1	-1	+1	-1	R_y	xz	-
B_{3g}	+1	-1	-1	+1	+1	-1	-1	+1	R_x	yz	-
A_u	+1	+1	+1	+1	-1	-1	-1	-1	-	-	xyz
B_{1u}	+1	+1	-1	-1	-1	-1	+1	+1	z	-	z^3, y^2z, x^2z
B_{2u}	+1	-1	+1	-1	-1	+1	-1	+1	y	-	yz^2, y^3, x^2y
B_{3u}	+1	-1	-1	+1	-1	+1	+1	-1	x	-	xz^2, xy^2, x^3

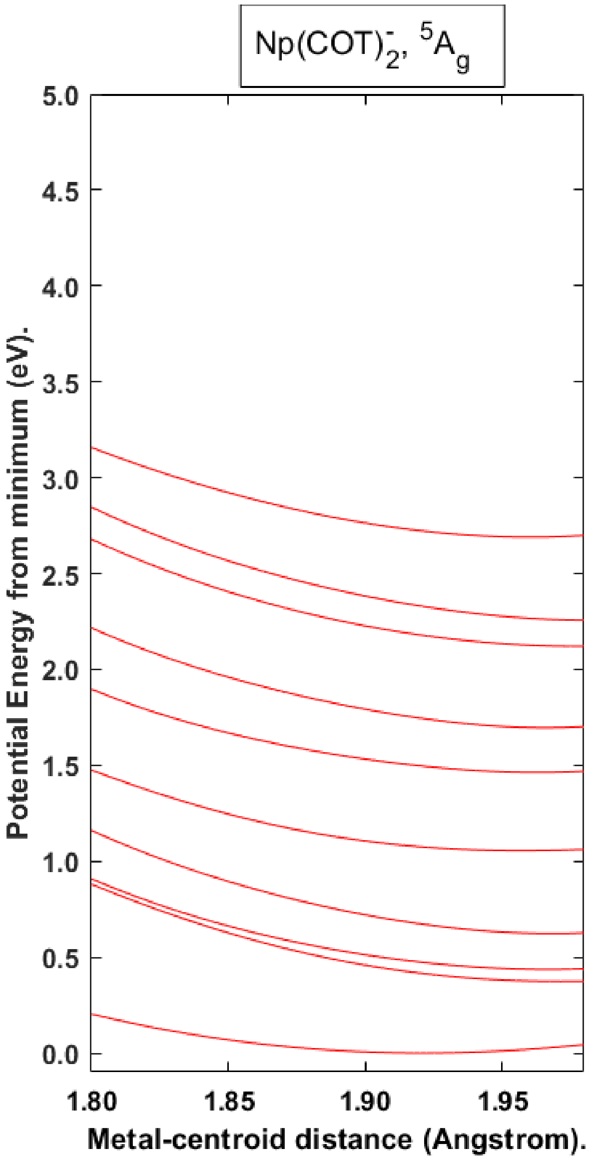

Figure C.1: ^5A_g Potential energy curve for the neptunium-centroid (of either COT ring) separation of $[\mathrm{Np(COT)_2}]^-$ NEVPT2(11,13).